The use of soil moisture - remote sensing products for large-scale groundwater modeling and assessment

Utrecht Studies in Earth Sciences

ISSN 2211-4335

Utrecht Studies in Earth Sciences 025

The use of soil moisture - remote sensing products for large-scale groundwater modeling and assessment

Edwin H. Sutanudjaja

Utrecht 2012

Department Physical Geography
Faculty of Geosciences - Utrecht University

Promotors:
Prof. Dr. Ir. M. F. P. Bierkens
Prof. Dr. S. M. de Jong
Prof. Dr. Ir. F. C. van Geer

Examination committee
Prof. Dr. A. P. J. de Roo, Utrecht University, The Netherlands & European Commission Joint Research Centre, Ispra, Italy
Prof. Dr. S. Kollet, Research Centre Jülich, Germany
Prof. Dr. Ir. T.N. Olsthoorn, Delft University of Technology, The Netherlands
Prof. Dr. Z. Su, University of Twente, The Netherlands
Prof. Dr. Dipl.-Ing. W. Wagner, Vienna University of Technology, Austria

This work was financially supported by the Netherlands Organization for Scientific Research NWO (contract: SRON GO-AO/10).

ISBN 978-80-6266-313-2

Cover design: Paula Amelia Tania Sutanudjaja.

Printed in the Netherlands by WPS, Zutphen.

The use of soil moisture - remote sensing products for large-scale groundwater modeling and assessment

Toepassing van bodemvocht remote sensing in grootschalige grondwatermodellering

(met een samenvatting in het Nederlands)

PROEFSCHRIFT

ter verkrijging van de graad van doctor aan de Universiteit Utrecht op gezag van de rector magnificus, prof. dr. G. J. van der Zwaan, ingevolge het besluit van het college voor promoties in het openbaar te verdedigen op vrijdag 14 december 2012 des middags te 4.15 uur

door

Edwin Husni Sutanudjaja

geboren op 16 juni 1981 te Cirebon, Indonesië

Promotoren: Prof. dr. ir. M. F. P. Bierkens
Prof. dr. S. M. de Jong
Prof. dr. ir. F. C. van Geer

Live as if you were to die tomorrow.
Learn as if you were to live forever.

Mahatma Gandhi

Contents

1 General Introduction **15**

1.1 Background 15

1.1.1 Common groundwater assessment methods 15

1.1.2 Spaceborne remote sensing for groundwater hydrology 16

1.2 Research objective: Integration ERS spaceborne remote sensing products into groundwater modeling 17

1.3 Remote sensing data and study area 20

1.3.1 ERS Soil Water Index 20

1.3.2 Rhine-Meuse basin 20

1.4 Research questions and outline 21

2 Correlation between ERS spaceborne microwave soil moisture time series and groundwater head dynamics **23**

2.1 Introduction 24

2.2 Study area and data 26

2.2.1 Rhine-Meuse basin 26

2.2.2 ERS Soil Water Index 28

2.2.3 Groundwater head data 29

2.3 Methodology 30

2.4 Results 32

2.5 Conclusion and discussion 38

3 Using ERS spaceborne microwave based soil moisture products to predict groundwater heads in space and time **41**

3.1 Introduction 42

3.2 Methodology 43
3.2.1 Groundwater head forecasting in time 43
3.2.2 Spatio-temporal prediction of groundwater head 46
3.3 Results 50
3.3.1 Groundwater head forecasting in time 50
3.3.2 Spatio-temporal prediction of groundwater head 60
3.4 Discussion 70
3.4.1 Groundwater head forecasting in time 70
3.4.2 Spatio-temporal prediction of groundwater head 71
3.5 Summary and conclusion 72

4 Large-scale groundwater modeling using global datasets 73

4.1 Introduction 74
4.2 Model description 75
4.2.1 General modeling procedure 75
4.2.2 PCR-GLOBWB land surface model 76
4.2.3 Groundwater model 77
4.3 Sensitivity analysis of aquifer properties 86
4.4 Results 88
4.5 Conclusions and discussion 96

5 The suitability of using ERS spaceborne soil moisture time series to calibrate a large-scale groundwater model 99

5.1 Introduction 100
5.2 Model structure: the online coupled groundwater-land surface model of PCR-GLOBWB-MOD 101
5.2.1 Activating capillary rises from the groundwater bodies 102
5.2.2 Local runoff and surface water routing 103

5.2.3 Groundwater model 104
5.3 Brute-force model calibration 105
5.3.1 General calibration strategy 105
5.3.2 Model parameters and runs 106
5.3.3 Model evaluation criteria 110
5.4 Results and discussion 112
5.4.1 Model evaluation using in-situ daily discharge measurement time series 115
5.4.2 Model evaluation using ERS Soil Water Index time series . . . 118
5.4.3 Defining calibration scenarios (developed based on Sects. 5.4.1 and 5.4.2) 128
5.4.4 Verification to observed groundwater head time series 134
5.5 Conclusions 137

6 Summary and outlook **139**

6.1 Introduction 139
6.2 Is there correlation between ERS Soil Water Index time series and groundwater head dynamics? 140
6.3 Can ERS Soil Water Index time series be used as the input of transfer function-noise models for predicting groundwater head in space and time? 140
6.4 Is it possible to build a large scale, physically-based and coupled land surface-groundwater model by using only global datasets? 141
6.5 Can ERS Soil Water Index time series be used to evaluate the performance of a large scale, physically-based and coupled land surface-groundwater model? 142
6.6 Outlook 142
6.6.1 Possible applications 143
6.6.2 Further research topics 144

Appendix A The land surface model of PCR-GLOBWB-MOD **147**

A.1 Interception 147

A.2 Snow pack 148

A.3 Direct or surface runoff 149

A.4 Vertical water exchange between soil and groundwater stores 150

A.5 Interflow or shallow sub-surface flow 151

A.6 Soil evaporation and plant transpiration 152

A.7 Baseflow and specific runoff from a land surface cell 154

A.8 Surface water bodies and surface water accumulation in the land surface model 154

Appendix B Climatological forcing data **155**

B.1 Period 1960–1999 155

B.2 Period 2000–2008 156

References **159**

Summary **173**

Samenvatting: Toepassing van bodemvocht remote sensing in grootschalige grondwatermodellering **175**

Ringkasan: Penggunaan data kelembaban tanah berdasarkan teknologi penginderaan jauh untuk pemodelan aliran air tanah skala makro **177**

Acknowledgements **179**

Dankwoord **180**

About the author **183**

List of publications **184**

1 General Introduction

1.1 Background

Groundwater plays an important role in the basic needs of human society, in developed as well as developing countries. It serves as a primary source of drinking water and it supplies water for agricultural and industrial activities. In liquid form, groundwater is the largest accessible source of freshwater (Gleick, 1996). It has an essential role in the environment. During times of drought, groundwater sustains water flows in streams, rivers, brooks and wetlands, and thus supports ecosystem habitat and biodiversity, while its large natural storage provides a buffer against water shortages.

Besides its importance, groundwater is known as a vulnerable resource. In many areas, groundwater is being consumed faster than it is naturally replenished (Rodell et al., 2009; Wada et al., 2010). Given increased population and heightened variability and uncertainty in precipitation due to climate change, the pressure upon groundwater resources is expected to intensify. Moreover, excessive groundwater extractions can accelerate land subsidence (Gambolati et al., 1974) and even significantly contribute to sea level rise (Wada et al., 2012). These issues make monitoring and predicting groundwater variabilities and changes imperative.

1.1.1 Common groundwater assessment methods

Monitoring and assessing groundwater states over large areas is difficult because it requires large amounts of data that are often prohibitively expensive to acquire on the ground. The most common and traditional way to obtain information about groundwater states is by measuring groundwater heads or groundwater levels in in-situ drilled observation wells. However, in-situ groundwater head measurements, which are usually sparsely distributed and not spatially continuous, have limited spatial support. Also, the spatial coverage of most of the groundwater head monitoring networks is limited. Large-extent groundwater head maps obtained by interpolation from point head measurements are therefore subject to large uncertainty. Consequently, large-scale groundwater assessments, especially at the sub-continental scale, comprising multiple aquifers, basins and countries, are still challenging.

Another way to gain insights into groundwater head behavior is by exploiting the underlying theoretical principles (e.g. based on physical laws of groundwater flow and/or statistical inferences of groundwater time series and their forcing time series). Using this knowledge, groundwater models can be built to simulate and predict groundwater head dynamics. Groundwater models plays an important role in groundwater

management, as they allow analyses of the past and present conditions, projection of evolution of groundwater system, as well as identification of the impacts of external factors, such as human intervention, increasing water demand and climate change (see e.g. Knotters and Bierkens, 2000; Scibek and Allen, 2006; Maxwell and Kollet, 2008; Olsthoorn, 2008; Oude Essink et al., 2010). They are thus essential tools for analyzing possible measures to counteract such impacts.

However, large-scale groundwater models, especially for aquifers and basins of multiple countries, are still rare, due to a lack of hydro-geological data to parameterize the model and a lack of groundwater head measurements to evaluate the model performance and calibrate the model. Some existing large-scale groundwater models, such as those for the Death Valley area, USA (D'Agnese et al., 1999), the Great Artesian Basin, Australia (Welsh, 2000, 2006), and the MIPWA region, the Netherlands (Snepvangers et al., 2008), are developed on the basis of highly detailed hydro-geological data (e.g. elaborate 3-D geological models) and supported by extensive groundwater head measurement networks (e.g. United States Geological Survey National Water Information System, USGS NWIS, `http://waterdata.usgs.gov/nwis/gw`, and Data and Information of the Subsurface of The Netherlands, DINOLoket, `http://www.dinoloket.nl`). Such information may be available in developed countries but is rarely found in other parts of the world.

1.1.2 Spaceborne remote sensing for groundwater hydrology

During the last decades, the application of satellite-based remote sensing in hydrological studies has received increased attention. Many studies have shown the usefullness of spaceborne remote sensing in large-scale hydrological analysis and modeling. Examples include mapping of land surface elevation (Lehner et al., 2008), precipitation (e.g. Kummerow et al., 2000), soil moisture (Njoku et al., 2003; Wagner et al., 1999b), snow cover (Dankers and de Jong, 2004; Immerzeel et al., 2009), land surface temperature (Wan and Li, 1997), evaporation (Bastiaanssen et al., 1998a,b; Su, 2002; Mu et al., 2007; Jung et al., 2010), as well as vegetation and drought indices (Myneni et al., 2002; de Jong and Jetten, 2007; Hansen et al., 2008; Zhao and Running, 2010). These examples show that satellite remote sensing is a viable source for information of hydrological land-surface related parameters, fluxes and state variables. Remote sensing holds a great promise for large-scale hydrology because it provides spatially and temporally exhaustive maps of surface properties covering large river basins and even the globe. The other main appeal of remote sensing methods is their spatial support. They provide average estimates over large areas (or footprints) that may range from a few square meters to thousands of square kilometers, depending on the method. This bypasses the need to infer areal averages from point data.

However, groundwater hydrology has been relatively late to embrace remote sensing applications. Up to now, only the Gravity Recovery and Climate Experiment (GRACE,

Tapley et al., 2004), a spaceborne gravity mission launched and operated by the National Aeronautics and Space Administration (NASA) since March 2002, has been acknowledged as a groundwater assessment tool, specifically for detecting changes of large groundwater storage. The twin satellites of GRACE — the distance of which changes in response to variations in the pull of gravity — can sense slight changes in Earth's gravity field and associated mass distribution, including changes in underground water masses. Hence, data from GRACE can show fluctuations in groundwater storage over time and highlight where groundwater is being depleted faster than replenished (e.g. Rodell et al., 2007; Swenson et al., 2008; Strassberg et al., 2009; Rodell et al., 2009). However, a major drawback of the GRACE mission is its coarse spatial resolution of 400 km, which makes it suitable for assessing continental or global groundwater storage dynamics but unsuitable for local to regional scale assessments. Recently, the European Space Agency (ESA) launched a gravity mission called the Gravity Field and Steady-state Ocean Circulation Explorer (GOCE, Drinkwater et al., 2003, 2007), which can deliver 100 km resolution products. Yet, its application for groundwater hydrology is still in its infancy (launched in March 2009) and might be constrained by its short mission period (only until December 2012). Therefore, the currently known possible applications of spaceborne remote sensing for groundwater assessment should still be considered limited.

The benefits of spaceborne remote sensing applications have been late to reach groundwater hydrology applications due to an obvious reason: groundwater movement take place beneath the surface and it cannot be directly sensed by spaceborne remote sensors. Yet, several scientists have argued that spaceborne remote sensing should hold tremendous potential to support groundwater assessments. For example, Jackson (2002) proposed to use remotely sensed soil moisture data to support groundwater studies. Becker (2006) reviewed that groundwater behavior can be inferred from remotely-sensed surface expressions, such as elevation, gravity anomaly, land surface temperature, vegetation and soil moisture. Moreover, in a recent application, Alkhaier et al. (2012b) showed that remotely sensed land surface temperature and evaporation correlate well with groundwater depth. In this study, we intend to show that spaceborne remote sensing based soil moisture products — reflecting wet and dry soil locations, and their temporal dynamics — may, albeit indirectly, inform about groundwater dynamics.

1.2 Research objective: Integration ERS spaceborne remote sensing products into groundwater modeling

This study aims to extend the application of spaceborne remote sensing based soil moisture products to groundwater quantity modeling and assessment. Given that groundwater (quantity) can hardly be measured directly from space, remote sensing applications for groundwater hydrology certainly depend upon their efficient integra-

tion with in-situ measurement data and theoretical models. This study is to explore the possibility of incorporating satellite-based soil moisture products for modeling groundwater head dynamics. This possibility is explored using two modeling techniques: time series modeling and physically-based groundwater modeling.

The first modeling technique, time series modeling, refers to a statistical approach to analyze and describe one or more time series. Time series models, which are often classified as empirical or "black-box" models, are data driven and used in order to describe causal relationships between input and output time series. The main advantage of empirical time series models is that only data on the input and output variables are required (Dooge, 1973; Hipel and McLeod, 1994; von Asmuth et al., 2002; Sivapalan et al., 2003), while physically-based models need additional information (e.g. soil physical properties). In this study, the attention is focused on a special class of time series models called transfer function-noise (TFN) models. Such time series models have been used in groundwater hydrology (see e.g. van Geer and Defize, 1987; Gehrels et al., 1994; Bierkens et al., 1999, 2001; Knotters and Bierkens, 2000, 2001), but using ground-measured precipitation (excess) time series as forcing input. In this study, **we explore the possibility of using spaceborne soil moisture time series (as input) in TFN models in order to predict groundwater head (as output)**.

A common and often-heard criticism of empirical time series models is that they merely exploit the statistical relation between the data without giving a physical explanation (Freeze and Harlan, 1969; Abbott et al., 1986a). In contrast, physically-based models are based upon physical descriptions and laws of such phenomena (e.g. Abbott et al., 1986b; McDonald and Harbaugh, 1988; Kollet and Maxwell, 2006; Miguez-Macho et al., 2007; Kollet and Maxwell, 2008; Lam et al., 2011). Yet, a physically-based groundwater model is difficult to apply because it contains many model parameters (e.g. aquifer transmissivities) that are not known (Stephenson and Freeze, 1974; Beven, 1993) and must be refined from limited field measurements and/or subjective assumptions. As a result, the parameters in a groundwater model must generally be calibrated so that the models can reproduce observations (Bakker et al., 1999; Olsthoorn and Kamps, 1996, 2006), i.e. observed groundwater head time series. Therefore, to develop a reliable groundwater model, (in-situ) field groundwater head measurements are needed. Consequently, if such head data are not available (as the case for many parts of the world), calibrating groundwater models is difficult and another kind of measurement, as a substitute, is thus needed. In this study, **we also investigate the possibility of using spaceborne soil moisture time series to calibrate physically-based groundwater models**. It is further noted that this is done in the context of exploring the possibility of setting-up groundwater models in data-poor environments. Thus, apart from calibrating groundwater models using remote sensing data, **we also explore whether we can build a physically-based groundwater model by using only globally-available datasets** (not using any locally-available detailed information).

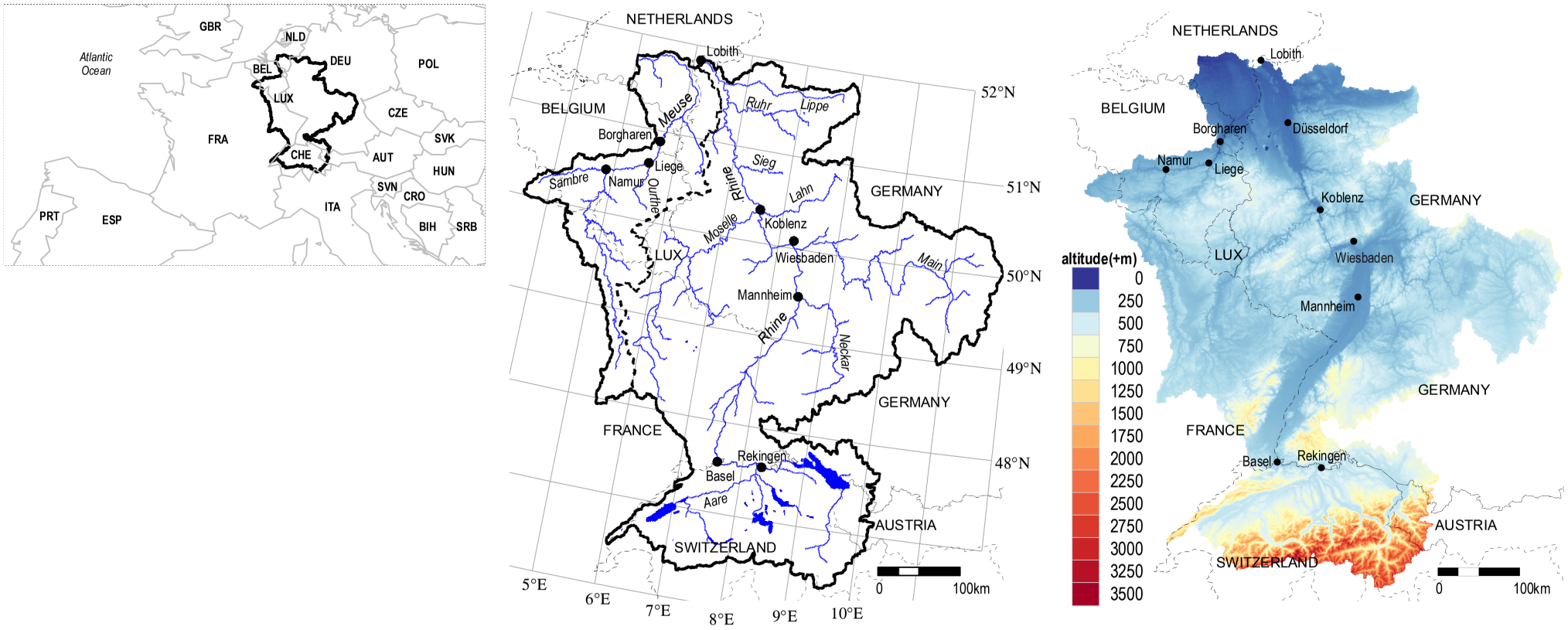

Figure 1.1 The combined Rhine-Meuse basin used as the study area. The map shown in the left part indicates the location of the study area in Europe, while the map in the right illusrates the topography based on the digital elevation map of HydroSHEDS (Lehner et al., 2008). For the map in the center, the bold black line indicates the extent of the model/study area while the bold dashed line indicates the approximate border between the Meuse and Rhine. The major rivers and large lakes are indicated in blue.

1.3 Remote sensing data and study area

1.3.1 ERS Soil Water Index

In this study, we focus on the spaceborne soil moisture product European Remote Sensing Soil Water Index (ERS SWI), which is a measure of the profile or average root zone soil moisture content (Wagner et al., 1999b). SWI time series are derived from the backscatter signals received by the scatterometers flown on board: the ERS-1 (1991-1995) and ERS-2 (1996-2007) satellites. These scatterometers, operating in the frequency of 5.3 GHz (C-band) and using vertical transmit and receive (VV) polarization, are active microwave instruments that send electromagnetic pulses to the surface of the earth and measure the signal scattered back. The measured backscatter signal is converted to Surface Soil Moisture (SSM) estimates by applying a change detection algorithm, accounting mainly for soil moisture and vegetation phenology (Wagner, 1998; Wagner et al., 1999a,b, 2007). To correct for the effects of plant growth and decay, the method uses the multi-incidence angle measurement capacity of the sensor to isolate the vegetation signature from the backscatter observations. The ERS SSM values are then retrieved by scaling each observation between dry and wet backscatter references representing the historically lowest and highest observed backscatter values. The SSM values, indicating soil moisture content in the first centimeters of topmost soil layer, are then convolved with an exponential low-pass filter model in order to derive ERS SWI time series, representing the first meter profile soil moisture content (Sect. 2.2.2).

The ERS SWI time series with a spatial and temporal resolution of 25-50 km and 10 days are more suitable for groundwater hydrology studies than SSM time series (25-50 km resolution and retrieved about 3-4 times per week) because the implemented low-pass filter removes high-frequency temporal signals representing individual rain events which are rarely found in (natural) groundwater head dynamics. The other advantage of using ERS SWI product (available from Vienna University of Technology: `http://www.ipf.tuwien.ac.at/radar/index.php?go=ascat`) is that its available long time series (1991-2007) are much longer than other soil moisture products, such as the ones from the missions of AMSR-E (Advanced Microwave Scanning Radiometer - Earth Observation System, launched in 2002 and switched of in 2011) and SMOS (Soil Moisture and Ocean Salinity, launched in 2009).

1.3.2 Rhine-Meuse basin

As a test-bed of this study, we used the Rhine-Meuse river basin, situated in the humid temperate zone of Western Europe (see Fig. 1.1 and Sect. 2.2.1). The Rhine-Meuse basin is selected because it is a well documented basin, which is not only supported by a good coverage of ERS SWI observations (see Fig. 2.2b), but also ample in-situ

groundwater head measurement time series (see Fig. 2.2a). We used more than 4 000 groundwater head time series (see Sects. 2.2.3, 4.3 and 5.3.3).

The large size of the study area, covering $\pm$ 200 000 km^2, makes it well-suited for large-scale hydrological studies. As the study area, the Rhine basin contains the upstream areas in the Alps of Austria and Switzerland and covers large areas in Germany with the outlet located in the town of Lobith in the Dutch eastern border. The Meuse basin used stretches from its headwaters, mainly in France and Belgium, until a point near Borgharen on the Dutch southern border. Note that the downstream area of the Rhine-Meuse basin, mainly in the Netherlands (see Fig. 1.1), is excluded because of strong anthropogenic water management practices occur in lower parts of the basin.

1.4 Research questions and outline

In the previous Sect. 1.2, the research objective is defined as to investigate the usefulness of remote sensing products for large-scale groundwater modeling and assessment. Following this objective and focusing on the satellite-based soil moisture product of ERS Soil Water Index (SWI), the main research questions are formulated as follows:

1. **Is there significant correlation between ERS Soil Water Index time series and groundwater head dynamics?** (Chapter 2)
2. **Can ERS Soil Water Index time series be used as the input for transfer function-noise models for predicting groundwater head?** (Chapter 3)
3. **Is it possible to build a large-scale, physically-based and coupled land surface-groundwater model using only global datasets?** (Chapter 4)
4. **Can ERS Soil Water Index time series be used to support the calibration of a large-scale groundwater model?** (Chapter 5)

The first and second questions are explored in the first part of this study, in which we used ERS SWI time series to predict groundwater head in space and time using an empirical transfer function-noise (TFN) model. This prediction is demonstrated mainly in Chapter 3 (2nd research question). However, before focusing on prediction, it is logical to first perform a statistical analysis to infer whether there is a relationship between ERS SWI time series and groundwater head dynamics (1st research question). This is explored in Chapter 2.

The third and fourth questions are explored in the second part of this study consisting of Chapters 4 and 5. In Chapters 4 (and also Sect. 5.2), we developed a large-scale and physically-based groundwater-land surface model called PCR-GLOBWB-MOD

by using only global datasets such that the model is portable for other areas in the world, including in data-poor areas (3rd research question). Subsequently, in Chapter 5, we explored the possibilities to calibrate the model using ERS Soil Water Index time series (4th research question).

The last chapter (Chapter 6) concludes with a summary of the answers to all four research questions and an outlook on prospective applications and further studies inspired by the findings in this study.

2 Correlation between ERS spaceborne microwave soil moisture time series and groundwater head dynamics

This chapter is adopted from:
Sutanudjaja, E. H., de Jong, S. M., van Geer, F. C., Bierkens, M. F. P., Using ERS spaceborne microwave soil moisture observations to predict groundwater heads in space and time, submitted to Remote Sensing of Environment.

Abstract

The aim of this chapter is to investigate whether the spaceborne microwave product of European Remote Sensing Soil Water Index (ERS SWI) — which provides spatio-temporal maps of the profile soil moisture content — correlates with in-situ observed groundwater head dynamics. As a test-bed, we use the Rhine-Meuse basin, where more than four thousand groundwater head measurement time series are available. Results show there is correlation between ERS SWI and groundwater head time series, with stronger correlation in areas with shallow groundwater. The correlation improves for most areas, including those with deep groundwater heads if the lag time — i.e. the response time of water from the upper soil part to the deeper groundwater bodies — is added to the correlation analysis. Following this finding, we hypothesize that ERS SWI time series may be used to predict groundwater head dynamics.

2.1 Introduction

Groundwater is a vulnerable water resource that, in many areas of the world, is consumed faster than it is naturally replenished (Wada et al., 2010). Due to global climate change, population growth and an ever increasing demand for fresh water, the pressure upon groundwater resources is expected to intensify in the future. These issues call for reliable monitoring and predicting groundwater changes over large areas. Currently, most groundwater assessments heavily depend on ground-based measurements of groundwater head that are often not available for large parts of the world and, if available, only as point-scale resolution data that are sparsely distributed and not spatially continuous. Consequently, large-scale groundwater resource assessments, especially at the sub-continental scale, comprising multiple aquifers, basins and countries, are still challenging.

During the last decades, many studies have investigated the possibilities of earth observation for hydrological purposes and spaceborne remote sensing is increasingly used for mapping and monitoring hydrological states and fluxes, such as precipitation (e.g. Kummerow et al., 2000), soil moisture (Njoku et al., 2003; Wagner et al., 1999b), snow cover (Dankers and de Jong, 2004; Immerzeel et al., 2009), land surface temperature (Wan and Li, 1997) and evaporation (Bastiaanssen et al., 1998a,b; Su, 2002; Mu et al., 2007; Jung et al., 2010). The advantage of remote sensing is its ability to provide spatially and temporally exhaustive maps of surface properties. Most spaceborne remote sensing missions cover the entire globe so that their data products are globally available. Thus, spaceborne remote sensing data can offer the spatial coverage and support that can not be provided by sparsely distributed point-scale ground-measured data. Yet, the applications of spaceborne remote sensing for groundwater hydrology are still limited (e.g. Alkhaier et al., 2012b). Up to now, only the Gravity Recovery and Climate Experiment (GRACE, Tapley et al., 2004), a space gravity mission launched and operated by the National Aeronautics and Space Administration (NASA) since March 2002, has been recognized as a groundwater assessment tool, specifically for detecting groundwater storage dynamics (Rodell et al., 2007; Swenson et al., 2008; Strassberg et al., 2009; Rodell et al., 2009). However, a major drawback of the GRACE mission is its coarse spatial resolution of 400 km, which makes it suitable for assessing large-scale groundwater storage dynamics but unsuitable for local to regional scale assessments. Recently, the European Space Agency (ESA) launched a gravity mission called the Gravity Field and Steady-state Ocean Circulation Explorer (GOCE, Drinkwater et al., 2003, 2007), which can deliver 100 km resolution products. However, its application is still in its infancy (launched in March 2009) and might be constrained by its short mission period (only until December 2012). Therefore, the current known possibilities of spaceborne remote sensing for groundwater assessment should be considered as limited.

Apart from gravity missions, other remote sensing applications remain problematic for groundwater assessment due to an obvious reason: current sensors are unable to sense

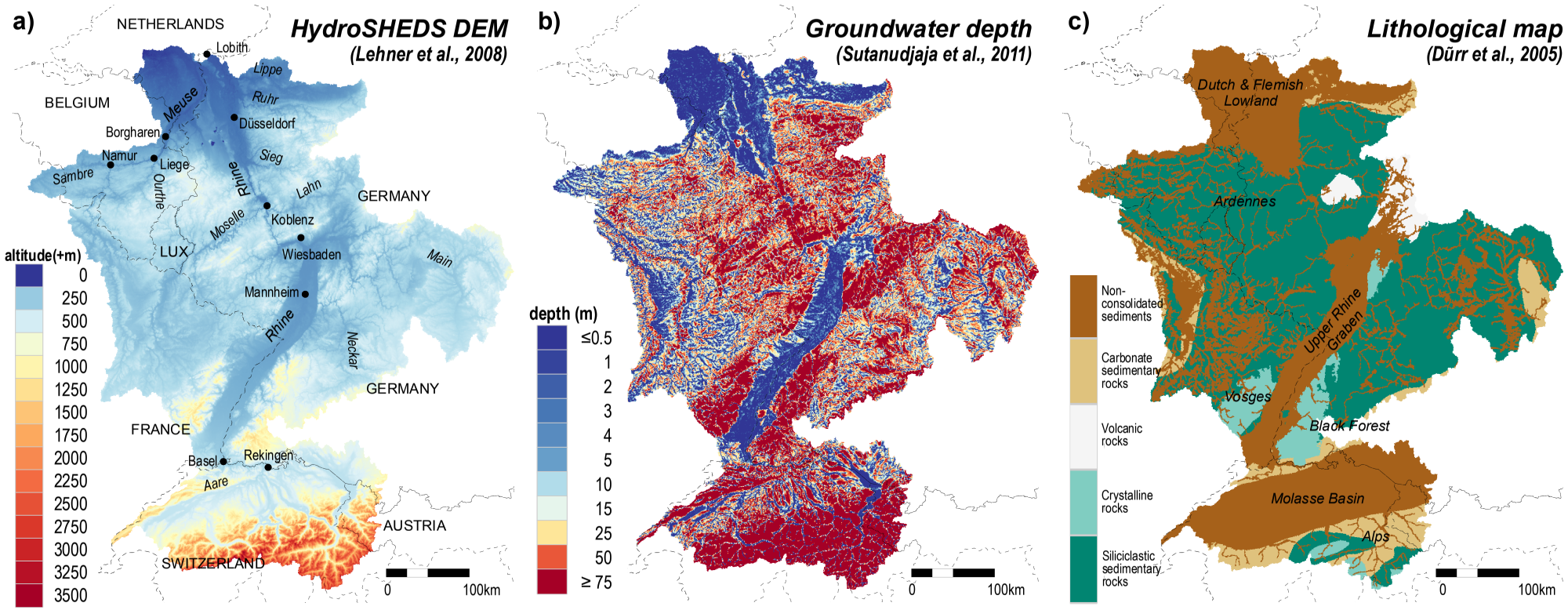

Figure 2.1 The study area in the Rhine-Meuse basin: (a) the 30 arc-second digital elevation map DEM of HydroSHEDS (Lehner et al., 2008); (b) the 30 arc-second groundwater depth average (1974-2008) based on the reference scenario in the model of Sutanudjaja et al. (2011, also in Chapter 4); (c) the lithological map of Dürr et al. (2005) that has been corrected based on (a) and (b).

sufficiently deep into the earth to directly sense groundwater dynamics. Despite this limitation, several scientists hypothesize that remote sensing should have tremendous potential for groundwater studies. Jackson (2002) reviewed the possibility of using microwave remote sensing for groundwater recharge estimates and related studies due to its capacity to map the spatial domain of surface soil moisture and to monitor its temporal dynamics. Becker (2006) proposed that groundwater behavior can be inferred from remotely-sensed surface expressions, such as elevation, land surface temperature, vegetation and soil moisture. The latter is the focus of this study, which argues that remote sensing based soil moisture products, reflecting wet soil locations, may correlate to groundwater heads and hence, albeit indirectly, inform about groundwater dynamics.

More specifically, the objective of this chapter is to investigate whether the time series of the remote sensing based soil moisture product referred as European Remote Sensing Soil Water Index (ERS SWI), introduced by Wagner et al. (1999b), correlate to in-situ measured groundwater head dynamics. In this chapter, we compare ERS SWI time series to groundwater head time series and analyze their correlation. This investigation complements other comparison studies found in the literature, such as comparisons of remotely-sensed soil moisture signals with ground-measured soil moisture data (e.g. Brocca et al., 2010), precipitation data (e.g. Wagner et al., 2003) and discharge data (e.g. Scipal et al., 2005).

2.2 Study area and data

2.2.1 Rhine-Meuse basin

As a test bed of this study, we use the combined Rhine-Meuse basin (total area: $\pm$ 200 000 km^2). It is a well documented basin containing locations of deep and shallow groundwater and is supported by a good coverage of ERS SWI observations and ample in-situ groundwater head measurements. The study area is situated in the humid temperate zone of Western Europe. The rivers flow through several countries: Austria, Switzerland, Liechtenstein, France, Luxembourg, Germany, Belgium and the Netherlands. The study area covers the Rhine basin from its source in the Alps in Switzerland until a point located in the town of Lobith in the Dutch eastern border, and the Meuse basin from its source in France until a point located about 150 km downstream from the town of Borgharen in the Dutch southern border. Note that, the downstream areas of the Rhine-Meuse basin, after the two aforementioned termination points, where strong anthropogenic water management practices occur, were excluded.

In its upstream part until the city of Basel in Switzerland, the River Rhine has a typical snow-melt driven regime, while in areas located more to the north in Germany and France, the river is mainly fed by rainfall. Consequently, the lower part of the

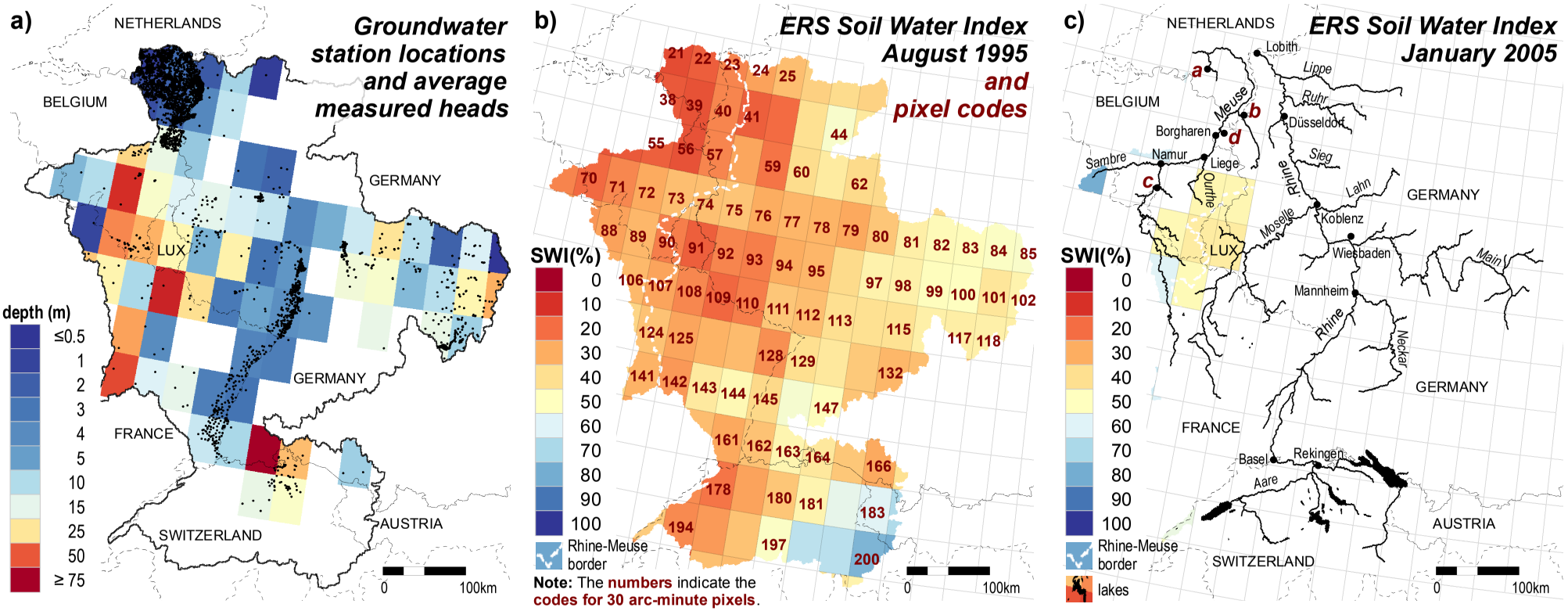

Figure 2.2 The locations of groundwater head stations used in this study and their average measured depths (a); and two fields of ERS SWI in August 1995 (b) and January 2005 (c). There are many missing data in Fig. 2.2c due to snow cover or frozen soils during the winter. Figure 2.2b includes the codes of half arc-degree pixels (30 arc-minute pixels) used in this study. Figure 2.2c includes points a, b, c, and d indicating the locations of the time series shown in Figs. 2.3 and 2.4.

River Rhine, such as at Lobith, has a combined rainfall-snow melt driven regime. The River Meuse can be considered as a rain-fed river as snow melt is not a major contributing factor to its discharge regime.

The topography of the study area is illustrated in Fig. 2.1a, which is based on the digital elevation model of HydroSHEDS (Lehner et al., 2008). Figure 2.1b provides the approximate average depths to groundwater heads in the study area. The estimates are based on the model of Sutanudjaja et al. (2011, see also Chapter 4). Although the model used to produce this map has some limitations, it allows us to distinguish between regions with deep and shallow groundwater areas. In Fig. 2.1b, the locations of the important shallow groundwater areas are indicated in blue. The largest and most important shallow groundwater bodies comprise the Upper Rhine Graben — straddling in the central Germany and in the border between France and Germany — and the delta area of The Netherlands — located in the north-western part of the study area. Figure 2.1b also shows small-scale aquifer structures near major tributary rivers, i.e. the Aare, Neckar, Main, Moselle, Lahn, Ruhr and Lippe rivers (Rhine basin), and the Sambre and Ourthe rivers (Meuse basin).

The hydro-geological condition of the basin is illustrated in the map shown in Fig. 2.1c. This map is the global lithological map of Dürr et al. (2005) that has been rectified in order to include small aquifer structures and an adjustment of the position of the Upper Rhine Graben, based on the digital elevation model of HydroSHEDS (Lehner et al., 2008) and the groundwater model of Sutanudjaja et al. (2011, see also Chapter 4). As shown in Fig. 2.1c, the upstream parts of the Meuse and Rhine basins are dominated by siliciclastic sedimentary rocks, such as in the Ardennes and Alps mountains, and non-consolidated sediments, such as in the Molasse Basin. In these upstream regions, some parts also consist of carbonate sedimentary rocks, which may include karst aquifer systems. Crystalline rock structures are mainly found in the Vosges and Black Forest mountainous areas. Between these two mountain ranges, a vast non-consolidated sediment pocket called the Upper Rhine Graben, is located and characterized by volcanic rock structures in its northern part. The lower part of the Rhine and Meuse basin, which forms the Dutch and Flemish lowlands, consists of non-consolidated sediments that are also found surrounding all major rivers of the Rhine-Meuse basin.

2.2.2 ERS Soil Water Index

Figure 2.2 illustrates the locations of the groundwater head stations and ERS SWI information. The coloured backgrounds of Fig. 2.2b and 2.2c are two snapshots of ERS SWI fields (in August 1995 and January 2005). Wagner et al. (1999b) claim that ERS SWI fields represent the profile soil moisture content in the first meter of the soil and their values range from 0% to 100% — respectively representing wilting point level and field capacity conditions. The ERS SWI time series are actually derived from the

ERS Surface Soil Moisture (SSM) time series. SSM values, retrieved about 3 to 4 times per week from the ERS scatterometers, represent soil moisture content in the top soil layer (< 5 cm, as discussed by Wagner et al., 1999b). SSM values are scaled between 0% and 100% — respectively representing zero soil moisture and saturation. The retrieval algorithm of SSM is based on a change detection approach of backscatters measured by active scatterometers accounting mainly for soil moisture and vegetation phenology (Wagner et al., 1999b, 2007). The backscatter measurements are corrected for the effects of vegetation phenology (Wagner et al., 1999a) and the time series of SSM are then retrieved by relating the vegetation-corrected backscatter time series to the dry and wet backscatter reference values determined by selecting their lowest and highest values within a 10-year period. Using these derived SSM time series, Wagner et al. (1999b) implemented the following exponential low-pass filter model to derive SWI time series:

$$\mathrm{SWI}_{t_{\mathrm{SWI}}} = \frac{\sum \mathrm{SSM}_{t_{\mathrm{SSM}}} \times e^{-(t_{\mathrm{SWI}} - t_{\mathrm{SSM}})/T}}{\sum e^{-(t_{\mathrm{SWI}} - t_{\mathrm{SSM}})/T}} \quad \text{for} \quad t_{\mathrm{SSM}} \leq t_{\mathrm{SWI}} \tag{2.1}$$

where t_{SWI} and t_{SSM} are the (daily) time indexes of SWI and SSM and T is the characteristic time length, taken as 20 days because it provided the best correlation to the field data (see Wagner, 1998; Wagner et al., 1999b, for an extensive description about the SSM and SWI retrieval algorithms).

Both ERS SSM and SWI fields are globally available since 1 August 1991. For this study, all available ERS SWI time series until 31 May 2007 were used. There are unfortunately missing data in the period 1 January 2001 to 12 August 2003 due to satellite problems (Wagner et al., 2003). Due to snow cover or frozen soil conditions, there are also often missing data during winter periods (as an example, see Fig. 2.2c).

In their original format, the ERS SWI time series are sampled and presented at about 25-50 km spatial resolution and 10-day temporal resolution. In this study, to reduce the number of missing values, these spatio-temporal maps were resampled to the monthly resolution (which is also the resolution of groundwater head time series used in this study) and to the resolution of 30 arc minutes (approximately equals to 50 km at the earth equator), as shown in Figs. 2.2b and c.

2.2.3 Groundwater head data

For this study, thousands of point-scale groundwater head time series collected from several parties in the Netherlands, Belgium, France, Germany and Switzerland, were used. The groundwater data used in this study must satisfy the following criteria. First, the groundwater head time series must be relatively recent (after 1992), represent long records (at least 5 years) and contains seasonal variation (i.e. in all years, there is at least one measurement datum for each season: winter, spring, summer and autumn). Moreover, based on the information provided by the data suppliers, we only selected the time series belonging to the very first top aquifer, where strong

correlation between remotely-sensed soil moisture SWI and groundwater time series can be expected. Furthermore, the time series that do not include information about station elevations were not used in the analysis because one of the aims of this study is to investigate the influence of the depths of groundwater heads. Finally, we used only groundwater head time series that contain at least 50 months during which SWI values are also available in order to ensure that sufficient pairs of both time series were available for analyses. Figure 2.2a illustrates the selected measurement stations in the study area.

The original temporal resolutions of the groundwater head time series vary among stations, from daily, monthly to quarterly or seasonal observations. In this study, all groundwater head time series were resampled to a monthly resolution in order to give them a uniform temporal resolution and to make them consistent to the temporal resolution of ERS SWI used.

2.3 Methodology

The objective of this chapter is to investigate whether the ERS Soil Water Index time series — symbolized as SWI_t — correlates to groundwater head time series — h_t. The index t is introduced as the time series index with a monthly resolution used throughout this chapter. For each groundwater head station, we calculated the cross correlation function CCF between the time series of h_t and corresponding SWI_t and identified the zero-lag cross correlation coefficient, $\rho_{\mathrm{lag}=0}$, the highest cross correlation coefficient, ρ_{best}, and its corresponding delay time, $\mathrm{lag}_{\mathrm{best}}$. Note that a delay time $\mathrm{lag}_{\mathrm{best}}$, indicating a forward shift of SWI_t time series, may be expected due to the response time between the water in upper soil layers and groundwater compartments. As an analogy of this delay time, Scipal et al. (2005) reported a similar successful approach of introducing a delay time while studying the relation between the catchment scale of ERS SWI time series and measured river discharge time series.

The correlation analysis was also performed on the time series of monthly anomalies (i.e. by beforehand removing the seasonal cycles of SWI_t and h_t time series). We first computed the seasonal means of both time series by calculating 12 monthly values (January to December) from all years where data are available. By substracting these monthly climatology means, we obtained the monthly anomaly time series of SWI_t and h_t. We then calculated its zero-lag cross correlation coefficient, symbolized as ρ_{ma0}, and the cross correlation coefficient ρ_{mab}, which was computed by considering $\mathrm{lag}_{\mathrm{best}}$ as the time delay. Here, to identify ρ_{mab}, it should be noted that we used the same $\mathrm{lag}_{\mathrm{best}}$ identified from the CCF of the original SWI_t and h_t time series.

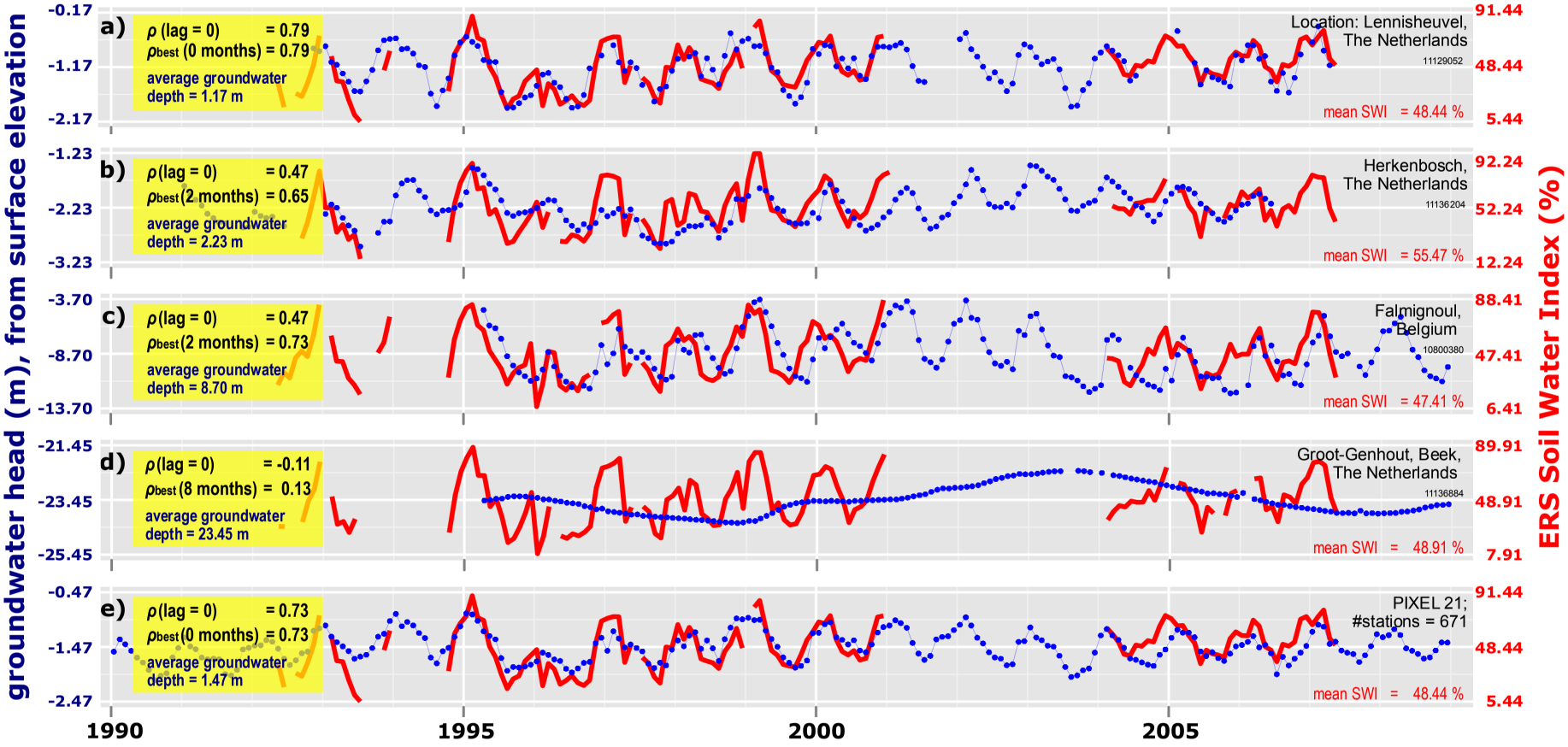

Figure 2.3 Comparisons between ERS SWI_t (red lines) and groundwater head h_t time series (blue dots) at several locations: Lennisheuvel, the Netherlands (a); Herkenbosch, the Netherlands (b); Falmignoul, Belgium (c); and Groot-Genhout, Beek, the Netherlands (d) (see Fig. 2.2c for the location of each point). The lowermost one (e) is the comparison between the time series of SWI_t and the upscaled h_t at the pixel 21 (see Fig. 2.2b for the pixel location).

There is a significant spatial support difference between the point-scale groundwater head measurement data and ERS SWI fields that have about 50 km resolution. Because of this scale discrepancy, our analysis was performed in two ways:

1. Direct comparison of **point-scale** groundwater head time series to remote sensing time series: A SWI_t time series of a 30-arc-minute pixel is compared to multiple point-scale head time series h_t. It implies that the result of this analysis, without upscaling of head data and without downscaling of remote sensing data, is conservative as the errors also include unresolved spatial variation within a 30 arc-minute pixel.

2. Comparison at the 30-arc-minute **pixel scale**: Here, we beforehand upscale (aggregate) the point-scale groundwater head time series to 30-arc-minute resolution. The upscaling and this analysis is only done for the 30-arc-minute pixels containing a minimum of 15 groundwater head measurement stations.

Note that all groundwater head h levels mentioned and used throughout this chapter are with respect to surface elevation and given a negative sign if groundwater head position is below surface level. In other words, h is defined as "groundwater depth", "depths to groundwater head" or "depths to water table".

2.4 Results

Figures 2.3a to d show some examples of graphical comparisons between the SWI_t and point-scale h_t time series at four different locations indicated in Fig. 2.2c. For each graph, the values of $\rho_{\text{lag=0}}$, ρ_{best} and the time delay lag_{best} are given in the yellow box on the left. For Figs. 2.3a to c, which are the examples of the locations with shallow groundwater heads, the correlations between two time series are obvious. Figures 2.3a to c clearly show that the soil moisture and groundwater head dynamics are correlated and react to the same seasonal hydrologic pattern. Figure 2.3a shows good correlation without any time lag, while Figs. 2.3b and 2.3c show correlation with a time lag of two months. However, Fig. 2.3d, which is an example of deep groundwater head, suggests no correlations between the fluctuations of SWI_t and h_t. The head time series in Fig. 2.3d do not show the seasonal pattern suggested by its soil moisture time series.

Figure 2.4 presents the monthly anomaly time series of SWI_t and h_t, plotted by beforehand removing seasonal variations of SWI_t and h_t. The yellow boxes contain the values of ρ_{ma0}, the zero-lag cross correlation coefficients, and ρ_{mab}, the cross correlation coefficients calculated with considering lag_{best} as the time delay. From Figs. 2.4a to c (with the exception of Fig. 2.4d), it is shown that the monthly anomaly time series of in-situ groundwater head observations correlate well to the ones of

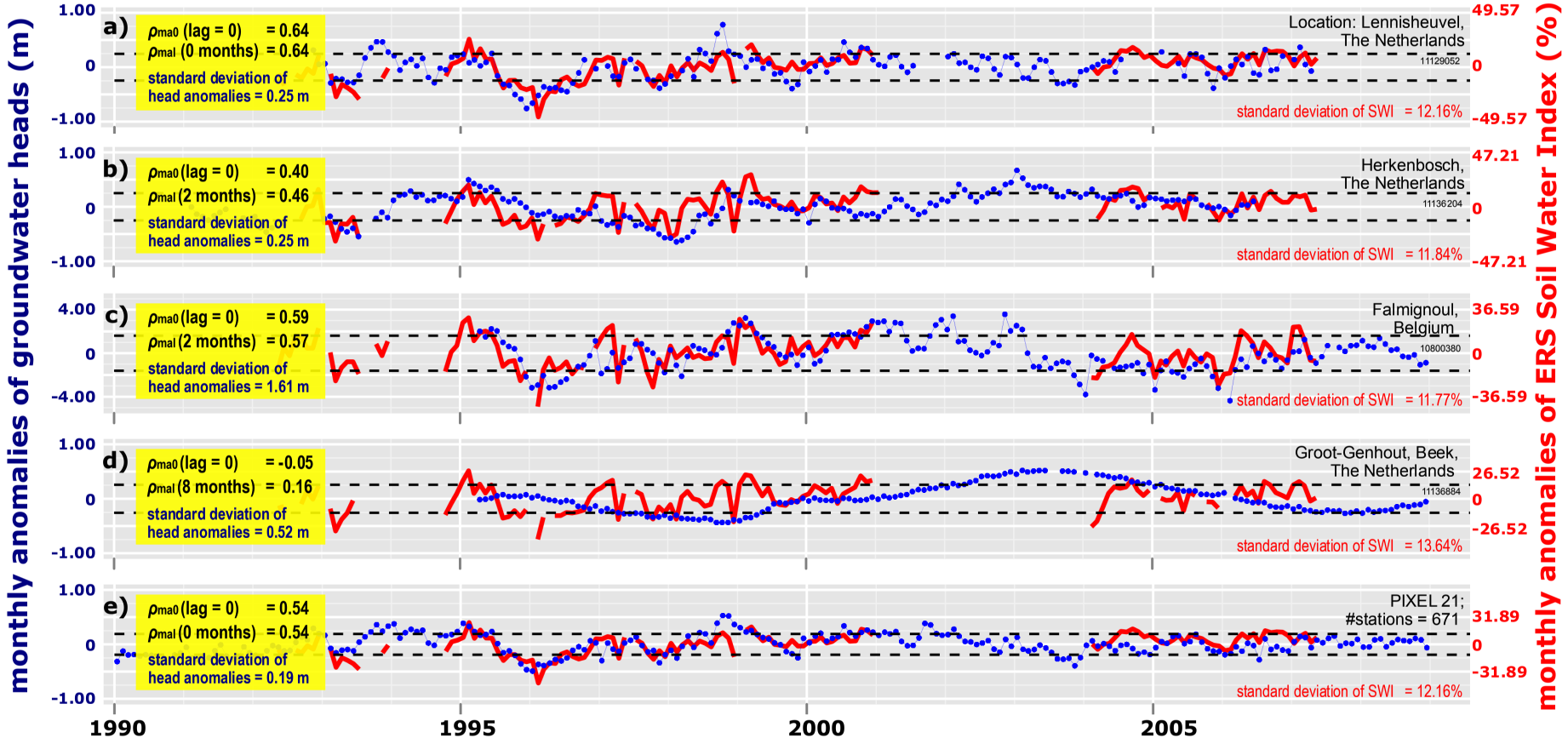

Figure 2.4 Comparisons between monthly anomaly time series of ERS SWI_t (red lines) and groundwater head h_t at several locations: Lennisheuvel, the Netherlands (a); Herkenbosch, the Netherlands (b); Falmignoul, Belgium (c); and Groot-Genhout, Beek, the Netherlands (d) (see Fig. 2.2c for the location of each point). The lowermost one (e) is the comparison between the monthly anomaly time series of SWI_t and the upscaled h_t at the pixel 21 (see Fig. 2.2b for the pixel location). The dashed line in each chart indicates the standard deviations of both monthly anomaly time series around the mean of zero.

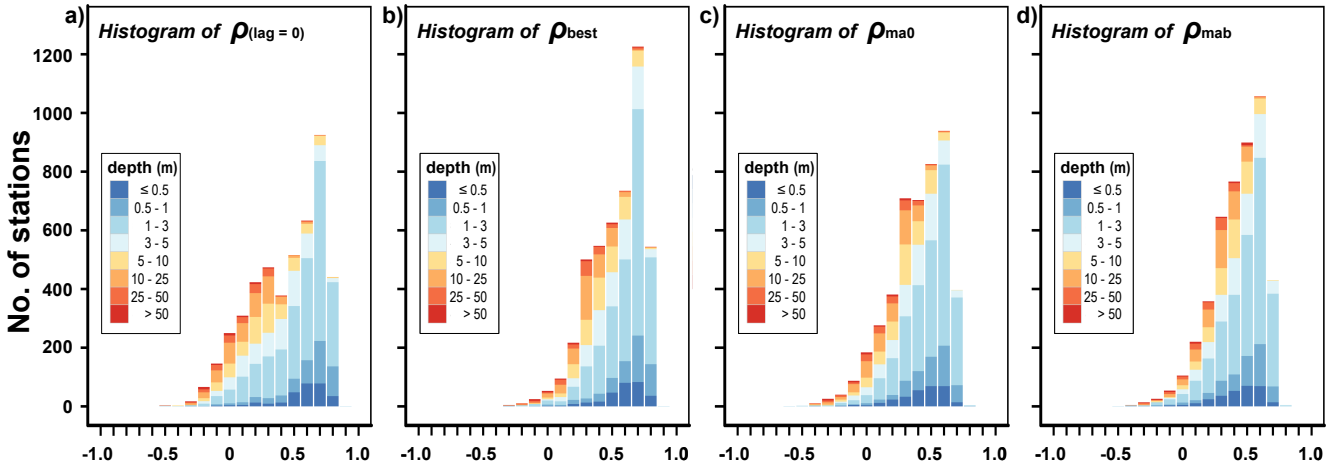

Figure 2.5 Histograms of correlations between SWI_t and h_t time series: zero-lag cross correlation coefficient, $\rho_{\mathrm{lag}=0}$ (a), and the highest one from cross correlation function, ρ_{best}, with time delay $\mathrm{lag}_{\mathrm{best}}$ (b). Also, we computed cross correlation coefficients between two monthly anomaly time series (i.e. by beforehand substracting their seasonal means, see Sect. 2.3): without considering delay, ρ_{ma0} (c), and with considering $\mathrm{lag}_{\mathrm{best}}$ as the time delay, ρ_{mab} (d). Note that the total number of stations is 4586.

remotely sensed soil moisture dynamics. This fact thus shows the ability of ERS SWI signals in explaining inter-annual groundwater head variations. In Fig. 2.4, the black dashed lines indicate the standard deviation intervals. Using these intervals, years can be identified with extreme wet and/or dry anomalies as indicated by observations above and/below the standard deviation interval lines. For examples, the extreme wet and/or dry periods can be identified during the years 1995-1996 in Figs. 2.4a and c and 1997-1998 in Fig. 2.4b. This extreme period identification is generally consistent from the points of views of soil moisture and head anomalies and, therefore, suggest a strong coupling between soil moisture and groundwater head inter-annual variation signals, specifically in shallow groundwater head areas. Such phenomena are not expected in areas with deep groundwater heads (see Fig. 2.4d for an example).

The values of $\rho_{\mathrm{lag}=0}$, ρ_{best}, ρ_{ma0} and ρ_{mab}, for all groundwater head station locations, are summarized in the histograms in Fig. 2.5. The histograms show that most of the groundwater head time series used in this study have good correlation to remotely sensed soil moisture signals. Without considering any time lags, Figs 2.5a and c show that there are 2285 (47 %) groundwater head stations having $\rho_{\mathrm{lag}=0} \geq 0.5$ and 1804 stations (39 %) with $\rho_{\mathrm{ma0}} \geq 0.5$. These figures are not only for stations with shallow groundwater heads, but also for some stations with deep groundwater heads (average groundwater heads are 5 m below surface levels). As seen in Figs. 2.5b and c, taking time lags into consideration improves correlation between SWI_t and groundwater

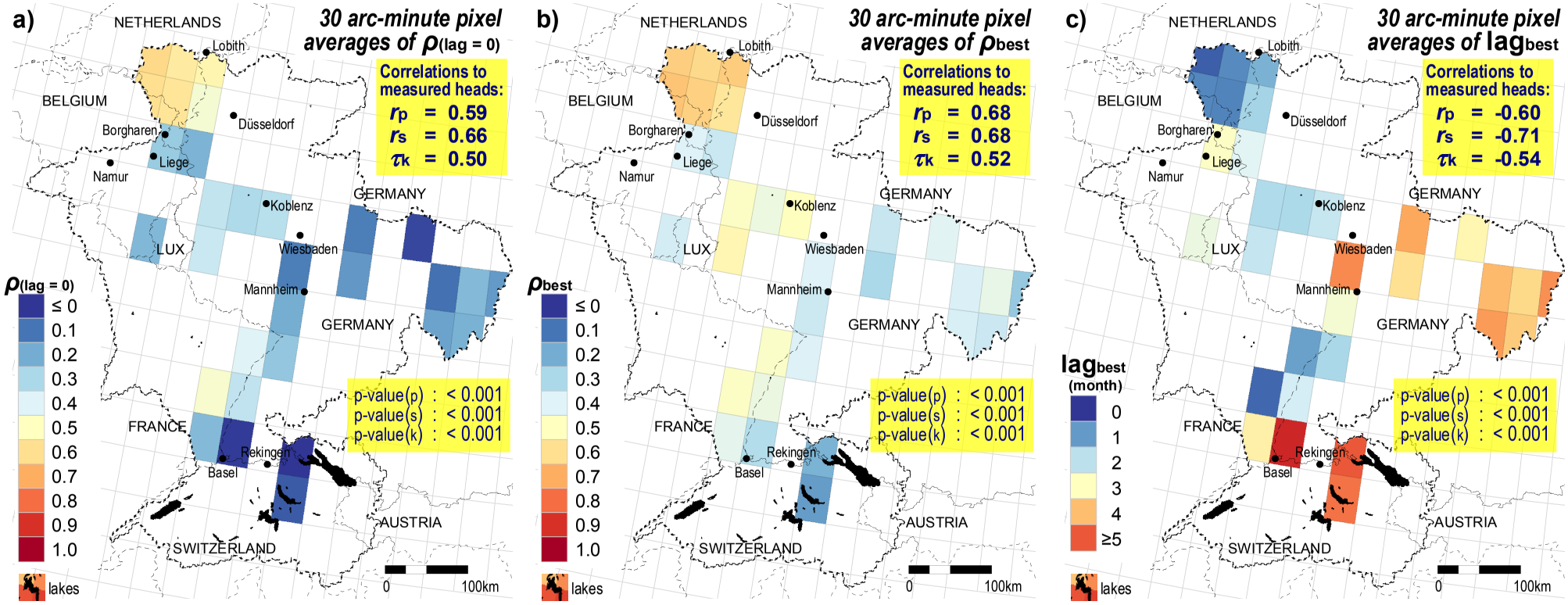

Figure 2.6 The 30 arc-minute pixel averages of the zero-lag cross correlation coefficients, $\rho_{\text{lag}=0}$ (a), the highest cross correlation coefficients, ρ_{best} (b), and their corresponding delay, lag_{best} (c). We show only the pixel average values calculated from at least 15 point-scale values. The yellow boxes contain the correlation coefficients of the field values to average measured heads (Fig. 2.2a): Pearson's correlation (r_{p}), Spearman's rho (r_{s}) and Kendall's tau (τ_{k}) coefficients.

head time series h_t. Considering time lags, there are 2835 (62 %) groundwater head stations with $\rho_{\text{best}} \geq 0.5$ and 1957 stations (43 %) with $\rho_{\text{mab}} \geq 0.5$.

Figures 2.6a and b present the spatial distribution of $\rho_{\text{lag=0}}$ and ρ_{best}, respectively. These correlation values in both figures are calculated based on point-scale values and averaged to 30 arc-minute pixel resolution. We only plotted average values for 30 arc-minute pixels that have at least 15 stations. Comparing the maps in Figs. 2.6a and b to average groundwater heads maps in Figs. 2.1b and 2.2a, it is apparent that most areas with shallow groundwater heads (e.g. the lowland areas in the Netherlands and Belgium) show strong correlation — even without accounting for any time lag — and weaker correlation is found in most areas with deep groundwater heads (Fig. 2.6a). Strong correlation for areas having deep groundwater heads become apparent only if the analysis accounts for a time lag (Fig. 2.6b) (e.g. at the Main catchment in the eastern part of the study area). We performed the correlation tests between the 30 arc-minute pixel scale values of $\rho_{\text{lag=0}}$ (from Fig. 2.6a) and ρ_{best} (from Fig. 2.6b) to the average measured groundwater heads (from Fig. 2.2a). Three different statistics tests were computed: Pearson's product-moment correlation test, Spearman's rho rank correlation test and Kendall's tau rank correlation test. The results are presented in the yellow boxes of Figs. 2.6a and 2.6b. Note that, as stated previously, the negative sign for groundwater heads refers to below surface levels. Here, as expected, we found a positive correlation between $\rho_{\text{lag=0}}$ and ρ_{best} values to average groundwater heads in all correlation test methods. It thus confirms that SWI_t signals have stronger correlation to h_t time series in shallower groundwater head areas, as they should be. In situation with deeper groundwater, the correlation between the dynamics of groundwater heads and soil moisture states is expected to be weaker, as SWI_t signals have been smoothed and dampened.

Figure 2.6c shows the spatial distribution of lag_{best} (calculated based on point-scale values and averaged to 30 arc-minute pixel scale if there are at least 15 stations). We also analyzed lag_{best} in connection to the groundwater table depth (Fig. 2.2a). Generally, we found that most areas with shallow groundwater heads (e.g. the Dutch and Flemish lowlands) have small lag_{best}, indicating short delays between SWI_t and h_t time series. Areas with deep groundwater heads (e.g. the eastern part of the study area) have high lag_{best}, indicating long transfer of groundwater pressure and/or travel times from the water in unsaturated zone to the deep saturated groundwater compartments. The Pearson's, Spearman's and Kendall's correlation tests were also conducted between the lag_{best} values in Fig. 2.6c and the average measured groundwater heads in Fig. 2.2a. As expected, all correlation tests provide a negative correlation between lag_{best} and average groundwater heads (assumed to be negative if below surface level), suggesting that longer delays between groundwater head and soil moisture time series are expected in areas with deeper groundwater heads.

Table 2.1 shows the results of the correlation analysis in which we beforehand upscaled point-scale groundwater head time series to 30-arc minute pixel scale time series. An example of the comparison between the SWI_t and the upscaled h_t time series is

Table 2.1 Results of the correlation analysis between the 30 arc-minute scale of SWI_t and upscaled groundwater head h_t time series. The information is ordered to average measured groundwater heads h_{avg}.

Pixel codes	Number of stations	h_{avg} (meter)	$\rho_{\mathrm{lag=0}}$	$\mathrm{lag}_{\mathrm{best}}$ (month)	ρ_{best}	ρ_{ma0}	ρ_{mab}
21	671	-1.47	0.73	0	0.73	0.54	0.54
38	336	-1.93	0.74	1	0.79	0.71	0.69
23	159	-2.30	0.56	2	0.71	0.55	0.61
39	851	-2.65	0.61	0	0.61	0.44	0.44
22	500	-2.85	0.71	0	0.71	0.64	0.64
145	39	-3.15	0.51	0	0.51	0.57	0.57
129	15	-3.47	0.29	1	0.40	0.39	0.46
144	33	-3.55	0.51	0	0.51	0.60	0.60
128	41	-3.77	0.49	1	0.52	0.51	0.47
40	312	-4.02	0.57	1	0.62	0.60	0.62
112	187	-4.15	0.24	2	0.43	0.31	0.32
95	142	-4.39	0.16	4	0.48	0.36	0.38
92	19	-5.82	0.40	2	0.51	0.43	0.45
162	25	-8.28	0.04	7	0.35	0.29	0.19
82	18	-8.40	-0.30	4	0.03	-0.26	-0.30
100	20	-8.58	-0.26	5	0.14	-0.13	-0.06
80	29	-9.26	-0.32	6	-0.14	-0.33	-0.20
57	20	-9.52	0.04	2	0.04	0.02	-0.03
77	27	-9.72	0.42	2	0.59	0.56	0.55
118	132	-9.90	-0.15	0	-0.15	-0.11	-0.11
161	50	-9.98	0.30	2	0.40	0.34	0.44
76	24	-10.62	0.38	2	0.48	0.43	0.41
75	21	-12.43	0.41	1	0.53	0.38	0.47
56	307	-13.02	0.10	1	0.18	0.12	0.12
97	42	-13.03	0.28	4	0.45	0.36	0.29
117	262	-13.57	0.03	1	0.03	-0.04	0.00
181	19	-14.64	0.04	6	0.12	0.15	-0.01
101	24	-18.75	0.02	4	0.08	0.06	0.06
102	19	-21.93	-0.22	6	-0.19	-0.23	-0.22
164	20	-22.93	0.00	8	0.38	0.04	0.28
90	22	-26.70	0.14	9	0.18	0.19	0.18
Correlations to h_{avg}							
Pearson's correlation coefficients	r_{p}		0.58	-0.71	0.60	0.58	0.55
	p-value		≤ 0.001	≤ 0.001	≤ 0.001	≤ 0.001	0.001
Spearman's rho coefficients	r_{s}		0.69	-0.61	0.69	0.67	0.65
	p-value		≤ 0.001	≤ 0.001	≤ 0.001	≤ 0.001	≤ 0.001
Kendall's tau coefficients	τ_{k}		0.52	-0.48	0.52	0.47	0.46
	p-value		≤ 0.001	≤ 0.001	≤ 0.001	≤ 0.001	≤ 0.001

given in Fig. 2.3e showing a good correlation between the asbolute or actual time series and Fig. 2.4e showing a good correlation between the monthly anomaly time series. From Table 2.1, in which we sorted the data based on average (upscaled) groundwater depth, we also find a tendency that areas with shallower water table depths have higher correlation between SWI_t and upscaled h_t time series (measured in $\rho_{\mathrm{lag=0}}$, ρ_{best}, ρ_{ma0} and ρ_{mab}), and longer delay ($\mathrm{lag}_{\mathrm{best}}$) are found in areas with deeper groundwater tables. The lower part of Table 2.1 contains the results of the correlation tests confirming this fact.

2.5 Conclusion and discussion

In this chapter, we investigated the correlation between groundwater head time series and ERS Soil Water Index (SWI) time series for the Rhine-Meuse catchment. We considered areas with shallow and deep groundwater depths and we studied the correlation between the ERS SWI and groundwater head time series by accounting for lag time, i.e. response time of water from the upper unsaturated soil zone to saturated groundwater bodies. Results show that there is correlation between the ERS SWI and groundwater head time series. This correlation is apparent for areas with shallow groundwater depth. Moreover, for most areas including the ones with deep groundwater depth, the correlation considerably improves if we account for the response time and add a time delay to the correlation analysis.

However, it should be noted that the analysis of these correlation properties and their causes is still limited and needs further investigation. The influence of vegetation and soil characteristics have not been explored yet. It is known that scatterometer signals can be heavily influenced and/or attenuated by the presence of vegetation (Wagner et al., 1999a, 2003). Related to the soil characteristics, the presence of a confining layer (if there is any) above the aquifer is expected to affect correlation between measured groundwater head and ERS SWI dynamics. Variations of soil physical properties (e.g. porosity and conductivity) and anthropogenic interventions should also be investigated. The analysis can also be further expanded by the improvement of the exponential model in Eq. 2.1 — proposed by Wagner et al. (1999b) for deriving the profile soil moisture content ERS SWI. This can be done, for example, by modifying and evaluating its chosen characteristic time length T — which was taken as 20 days (Wagner, 1998; Wagner et al., 1999b). Analyzing an improved SWI product, such as proposed by de Lange et al. (2008) — using a one dimensional water flow model and a differentiation of characteristic time lengths T based on soil texture to derive SWI, is another interesting subject for further study.

The correlation analysis in this study is limited by the monthly temporal resolution used. Explorations to higher temporal resolution remotely sensed soil moisture time series, e.g. using 10 day resolution of original ERS SWI and daily (1-3 day) resolution of original ERS surface soil moisture (SSM) time series, will be worthwhile. This

suggestion includes the idea to do a similar correlation analysis to other soil moisture products, such as those acquired by the Advanced Microwave Scanning Radiometer-Earth Observation System (AMSR-E, Njoku et al., 2003; de Jeu and Owe, 2003) and Soil Moisture and Ocean Salinity (SMOS, Kerr et al., 2001) missions.

Despite the aforementioned limitations, the results of our study are promising for spaceborne microwave remote sensing application to support large-scale groundwater assessments. The ERS SWI product (25-50 km spatial resolution) should thus be considered as an additional important higher resolution resource, next to GRACE that detects groundwater storage dynamics but only at a very coarse resolution (400 km). This finding is particularly relevant for groundwater modeling applications and offers possibilities for making groundwater head predictions. Due to the correlation between ERS SWI and field-measured shallow groundwater head time series — indicating that soil moisture and shallow groundwater head dynamics are correlated, predicting shallow groundwater head variations based on ERS SWI dynamics should be feasible. This possibility is demonstrated and discussed in Chapter 3.

3 Using ERS spaceborne microwave based soil moisture products to predict groundwater heads in space and time

This chapter is adopted from:
Sutanudjaja, E. H., de Jong, S. M., van Geer, F. C., Bierkens, M. F. P., Using ERS spaceborne microwave soil moisture observations to predict groundwater heads in space and time, submitted to Remote Sensing of Environment.

Abstract

The objective of this chapter is to investigate the possibility of using a spaceborne soil moisture time series called the European Remote Sensing Soil Water Index (ERS SWI) to predict groundwater heads. This is explored in two exercises, in which ERS SWI time series are used as the forcing input of a transfer function-noise (TFN) model. (1) In the first exercise, the focus is on forecasting in time. Here, the parameters of the TFN model are calibrated based on groundwater head time series in the period 1995-2000 by embedding the model in a Kalman filter algorithm. Once calibrated, the TFN forecasts are validated for the period 2004-2007 in order to assess their forecasting skill. (2) The focus of the second exercise is on spatio-temporal prediction. Here, the calibrated TFN model parameters from selected locations, derived in the first exercise, are used to fit regression models with a digital elevation map as input. With these regression models, TFN model parameters are spatially predicted. Subsequently, using these estimated parameters, spatio-temporal prediction of groundwater heads is made (also with the TFN model and ERS SWI time series) and evaluated against available observations. Results of both exercises are very promising. TFN model results can reproduce the observed groundwater head time series reasonably well, especially in shallow groundwater areas where soil moisture dynamics is the major cause of groundwater head fluctuations. This shows that ERS SWI products should be considered as an important source of information for the assessment of large-scale groundwater dynamics.

3.1 Introduction

Current groundwater monitoring heavily relies on ground-based measurement data. Such data are not available for large parts of the world and, if available, only as point-scale resolution data that are sparsely distributed in space. Consequently, large-scale groundwater resource assessment, especially at the sub-continental scale and comprising several aquifers, basins and countries, is still challenging. This challenge may be overcome by using spaceborne remote sensing products that can provide spatio-temporal soil moisture estimates — reflecting wet soil and shallow groundwater — and therefore may hold information about groundwater dynamics (Jackson, 2002; Becker, 2006). In Chapter 2, it is shown that, especially in shallow groundwater areas, the time series of field measured groundwater heads, are correlated to the time series of the spaceborne based soil moisture product called the European Remote Sensing Soil Water Index (ERS SWI Wagner et al., 1999b), which provides spatio-temporal maps of the upper profile soil moisture content. However, such soil moisture products that have better spatial coverage and support than point-scale field groundwater head data are hardly used for large-scale groundwater hydrology applications.

The objective of this chapter is to investigate whether time series of ERS SWI can be used to predict groundwater heads. In particular, the following research questions are investigated:

1. **Groundwater head forecasting in time**: Can ERS SWI time series be used for making temporal prediction (forecasts) of groundwater heads?
2. **Spatio-temporal groundwater head prediction**: Can ERS SWI time series be used for spatio-temporal prediction of groundwater heads, including at locations that are not supported by head measurements?

The aforementioned research questions serve to judge the usefulness of ERS SWI time series for predicting groundwater heads. In this study, we made use of transfer function-noise (TFN) models. TFN models are frequently used in groundwater hydrology, such as for decomposition of groundwater head time series into components corresponding to varying natural and anthropogenic causes (Gehrels et al., 1994; van Geer and Defize, 1987), filling in gaps of groundwater head measurement time series (Bierkens et al., 1999) and estimating groundwater heads (Knotters and Bierkens, 2000; Bierkens et al., 2001). Yet, in all of these applications, ground-measured precipitation (excess) time series were used as forcing input. In this chapter, the possibility to utilize remotely-sensed soil moisture time series of ERS SWI as TFN model input is explored.

As a test bed of this study, we use the Rhine-Meuse basin, where thousands of groundwater head time series are used. We use the monthly groundwater head and ERS SWI time series. The study area and the datasets used are described in Chapter. 2.2.

3.2 Methodology

3.2.1 Groundwater head forecasting in time

As the first exercise, we investigated the accuracy of temporal prediction of groundwater heads by using ERS SWI time series as input for a transfer function-noise model (TFN) model. Using SWI time series as input, a TFN model describing groundwater head is given by the following set of equations:

$$h_t = h_t^* + n_t \tag{3.1}$$

$$h_t^* = \sum_{i=1}^{r} \delta_i h_{t-i}^* + \sum_{j=0}^{s} \omega_j \mathrm{SWI}_{t-j-b} \tag{3.2}$$

$$(n_t - c) = \sum_{k=1}^{p} \phi_k (n_{t-k} - c) + a_t + \sum_{l=1}^{q} \theta_l a_{t-l} \tag{3.3}$$

where:

t	is the time step index, which is monthly based in this study
h_t	is the groundwater head at time step t
h_t^*	is the component of the head at time step t attributable to SWI
n_t	is the noise component at time step t
a_t	is a realization of a zero mean white noise process with variance σ_a^2
c	is the reference level or the expected value of n_t
δ_i	is the autoregressive parameter of lag i of a transfer model up to order r
ω_j	is the moving average parameter of lag j of a transfer model up to order s
ϕ_k	is the autoregressive parameter of lag k of a noise model up to order p
θ_l	is the moving average parameter of lag l of a noise model up to order q
b	is the delay between input and output

We assume that readers are familiar with the basic theory of single-output TFN models (see Box and Jenkins, 1976, for a detailed description). This study considers only a simple TFN model with $r = 1$, $s = 0$, $p = 1$, $q = 0$ and $b = 0$. This simple TFN model can be written in the following state and measurement equations of Kalman filter using the following vector notation:

$$\begin{bmatrix} h_t^* \\ n_t - c \end{bmatrix} = \begin{bmatrix} \delta_1 & 0 \\ 0 & \phi_1 \end{bmatrix} \begin{bmatrix} h_{t-1}^* \\ n_{t-1} - c \end{bmatrix} + \begin{bmatrix} \omega_0 \\ 0 \end{bmatrix} \mathrm{SWI}_t + \begin{bmatrix} 0 \\ 1 \end{bmatrix} a_t \tag{3.4}$$

$$y_t = \begin{bmatrix} 1 & 1 \end{bmatrix} \begin{bmatrix} h_t^* \\ n_t - c \end{bmatrix} + c + \epsilon_t \tag{3.5}$$

where y_t is a groundwater head measurement available at time t and ϵ_t is introduced as a zero mean (measurement) white noise with variance σ_ϵ^2. The state equation (3.4) consists of h_t^* describing the deterministic component related to the forcing input series, i.e. SWI_t, and $(n_t - c)$ providing the stochastic component independent of the

input series. The measurement equation (3.5) relates the model state, i.e. h_t^* and $(n_t - c)$, to the measurement y_t. The parameters in Eqs. 3.4 and 3.5 can be estimated using the Kalman filter application described in Berendrecht et al. (2003) (see also Bierkens et al., 1999). In the following, we briefly present this algorithm.

Using the following variables:

$$\mathbf{x}_t = \begin{bmatrix} h_t^* \\ n_t - c \end{bmatrix},\ \mathbf{A} = \begin{bmatrix} \delta_1 & 0 \\ 0 & \phi_1 \end{bmatrix},\ \mathbf{B} = \begin{bmatrix} \omega_0 \\ 0 \end{bmatrix},\ \mathbf{C} = \begin{bmatrix} 1 & 1 \end{bmatrix},\ \mathbf{D} = \begin{bmatrix} 0 \\ 1 \end{bmatrix},$$

the state and measurement equations are written in the general form:

$$\mathbf{x}_t = \mathbf{A}\mathbf{x}_{t-1} + \mathbf{B}\mathrm{SWI}_t + \mathbf{D}a_t \tag{3.6}$$
$$y_t = \mathbf{C}\mathbf{x}_t + c + \epsilon_t \tag{3.7}$$

We define $\bar{\mathbf{x}}_t$ as the time update — the prediction of $\mathbf{x}_t$ given observations up to and including time step $t-1$, $\hat{\mathbf{x}}_t$ as the measurement update — the prediction of $\mathbf{x}_t$ given observations up to and including time step t, $\mathbf{M}_t$ as the covariance matrices of the errors in the time update, $\mathrm{E}\left[(\mathbf{x}_t - \bar{\mathbf{x}}_t)(\mathbf{x}_t - \bar{\mathbf{x}}_t)^{\mathrm{T}}\right]$, and $\mathbf{P}_t$ as the covariance matrices of the errors in measurement update, $\mathrm{E}\left[(\mathbf{x}_t - \hat{\mathbf{x}}_t)(\mathbf{x}_t - \hat{\mathbf{x}}_t)^{\mathrm{T}}\right]$. Given the initial conditions $\hat{\mathbf{x}}_0$ and $\mathbf{P}_0$ for $t = 0$, the Kalman filter algorithm starts with the time update:

$$\bar{\mathbf{x}}_t = \mathbf{A}\hat{\mathbf{x}}_{t-1} + \mathbf{B}\mathrm{SWI}_t \tag{3.8}$$
$$\mathbf{M}_t = \mathbf{A}\mathbf{P}_{t-1}\mathbf{A}^{\mathrm{T}} + \mathbf{D}\sigma_a^2\mathbf{D}^{\mathrm{T}} \tag{3.9}$$

If at time step t, a measurement y_t is available, the measurement update is obtained as:

$$v_t = y_t - c - \mathbf{C}_t\bar{\mathbf{x}}_t \tag{3.10}$$
$$\sigma_{v,t}^2 = \mathbf{C}_t\mathbf{M}_t\mathbf{C}_t^{\mathrm{T}} + \sigma_\epsilon^2 \tag{3.11}$$
$$\mathbf{K}_t = \mathbf{M}_t\mathbf{C}^{\mathrm{T}}\left(\sigma_{v,t}^2\right)^{-1} \tag{3.12}$$
$$\hat{\mathbf{x}}_t = \mathbf{A}\bar{\mathbf{x}}_t + \mathbf{K}_t v_t \tag{3.13}$$
$$\mathbf{P}_t = (\mathbf{I} - \mathbf{K}_t\mathbf{C})\,\mathbf{M}_t \tag{3.14}$$

where v_t is the innovation (i.e. the difference between the observation and time update), $\sigma_{v,t}^2$ is the innovation variance, $\mathbf{I}$ and $\mathbf{K}_t$ are the identity and "Kalman gain" weighing matrices. If no observation is taken, it follows:

$$\hat{\mathbf{x}}_t = \bar{\mathbf{x}}_t \tag{3.15}$$
$$\mathbf{P}_t = \mathbf{M}_t \tag{3.16}$$

Assuming that the variance σ_ϵ^2 is very small ($\sigma_\epsilon^2 = 0$), the parameters δ_1 and ϕ_1 (defined in $\mathbf{A}$), ω_0 ($\mathbf{B}$), c and the variance σ_a^2 were estimated by optimizing a likelihood

function for the innovations, i.e. v_t and $\sigma^2_{v,t}$ of the Kalman filter (see Berendrecht et al., 2003, for an extensive explanation).

To run a TFN model, we need a time series input that does not contain missing values. For the estimation or the calibration of the model parameters, we used the period 1995-2000, while the period 2004-2007 were used for the validation. For both periods, there are only few missing values of SWI_t that were filled by linear interpolation.

The time step used in the Kalman filter time update is one month. For the calibration (1995-2000), we used all available head measurement data to obtain the measurement update. However, while validating the model (2004-2007), we ran the model with varying measurement update frequencies:

1. Using all available monthly measured heads for measurement updates.
2. Measurement updates in January, April, July and October (i.e. the measurement update interval is about 3 months).
3. Measurement updates in January, May and September (i.e. the measurement update interval is about 4 months).
4. Without any measurement updates.

In the experiments 1 to 3, the intention was to evaluate the forecasting skill of the derived TFN model for varying head observation frequencies applied in the real world. For the last experiment 4 (without measurement updates), the focus was on the evaluation of the calibrated deterministic parameters of the model (i.e. c, δ_1 and ω_0). For each case 1-4, using available measurement data in the validation period 2004-2007, we calculated the cross correlation coefficients ρ_{TF} (without considering any lag) between measured groundwater head data and predicted head time updates in order to evaluate timing agreements between observed and predicted head time series. Also, the mean error ME, as a measure of bias of predicted time updates, and the mean absolute error MAE, as a measure of accuracy of predicted time updates, were calculated.

All TFN model parameters are expected to be constant in time, including the reference level c. However, if such levels c, estimated in the calibration period 1995-2000, physically changed in the validation period 2004-2007 (e.g. due to land subsidence or human invervention), large biases ME and eventually large errors MAE are expected, especially for the runs without measurement updates (point 4). Hence, particularly for each validation run without measurement updates, we also calculated $\mathrm{MAE}_{\mathrm{ano}}$, which is the mean absolute error computed by beforehand removing the bias between the predicted and measured head time series. An indicator value of $\mathrm{MAE}_{\mathrm{ano}}$ could be justified as an unbiased measure of accuracy, without the influence of the estimated level c. Note, for the runs with measurement updates (points 1-3), in which we assumed that $\sigma^2_\epsilon = 0$, the performance indicators of ME and MAE of the validation and

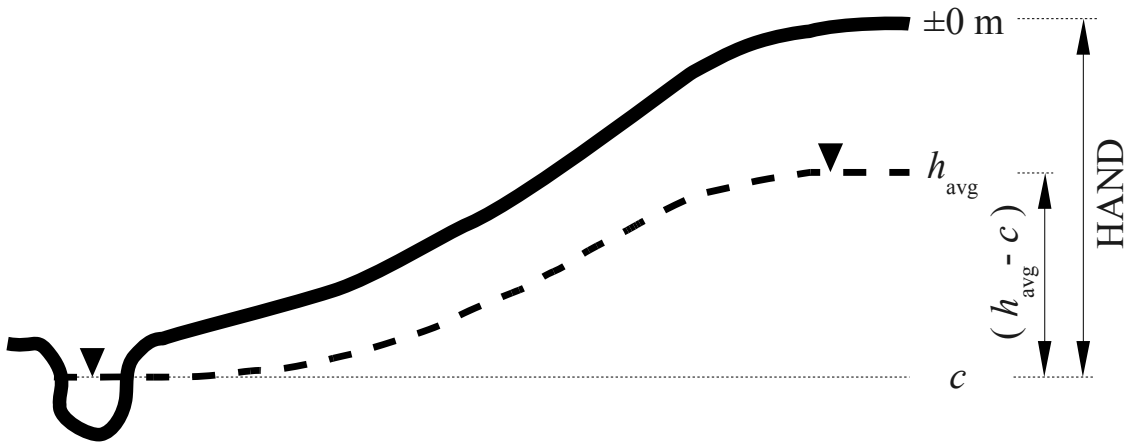

Figure 3.1 Illustration of the definition of HAND: a relative topography height above the nearest surface water bodies or stream networks. Also illustrated are the conventions used throughout the chapter, in which groundwater head levels (indicated as a dashed bold line) are considered with respect to surface elevation (continuous bold line) and given a negative sign if below surface. In the figure, h_{avg} is the average groundwater head level and c is the drainage level (fine dashed line).

evaluation period (2004-2007) are less sensitive to the estimated levels c due to the fact that any prediction would always be updated to measurements taken (following Eqs. 3.10 to 3.14).

In order to ensure that the model calibration and validation results were supported by enough data, this forecasting exercise was performed only for groundwater head time series that contain at least 40 months in 1995-2000 and at least 20 months in 2004-2007. As done in the correlation analysis exercise in the previous Chapter 2, the forecasting exercise was performed at both point scale (without aggregating head data) and pixel scale (by beforehand aggregating point-scale head time series to 30-arc-minute resolution).

3.2.2 Spatio-temporal prediction of groundwater head

In the second exercise of this study, the focus was on making spatio-temporal prediction of groundwater head h_t by using a transfer function model and SWI_t as input series. We constructed a simple spatio-temporal transfer function model (i.e. using Eqs. 3.1 to 3.3 with orders $r = 1$, $s = 0$, $p = 1$, $q = 0$ and $b = 0$) and evaluated its predictive skill at "non-visited locations" — where groundwater head data were assumed not to exist — and transfer function model parameters were estimated using a digital elevation model. The spatio-temporal model has a spatial resolution of $30'' \times 30''$ (approximately equal to $1\,\text{km} \times 1\,\text{km}$ at the equator) — which is the

resolution of the digital elevation model used for deriving model parameters — and operates at monthly temporal resolution. Constructing this spatio-temporal model involved the following steps.

First, from results of the (point-scale) temporal prediction exercise described in Sect. 3.2.1, we selected a limited number of stations with good validation results — i.e. those with prediction (without measurement updates) having $\mathrm{MAE}_{\mathrm{ano}}$ less than 10 cm and ρ_{TF} larger than 0.7. Subsequently, for each 30 arc-minute pixel containing the selected stations, we identified maximum three locations with the highest values of ρ_{TF} (of the validation runs without measurement updates). In these selected stations, we identified the average groundwater heads (h_{avg}) and TFN model parameters in the period 1995-2000 (particularly c, δ_1 and ω_0 derived from the calibration).

Next, we introduce a simplification of the phreatic groundwater head condition shown in Fig. 3.1: the shape of groundwater table follows the topography as a subdued replica (Hubbert, 1940; Tóth, 1962). The conceptualization in Fig. 3.1 was used to estimate average groundwater heads and TFN model parameters. In particular, we derived the regression models for estimating them by using the values identified in the selected stations (from the previous step) and a predictor variable referred as HAND (height above the nearest drainage) and calculated from a digital elevation model. Briefly, HAND (also illustrated in Fig. 3.1) is a relative topography height above the nearest pixel containing surface water bodies or stream networks, based on the drainage direction (see e.g. Rennó et al., 2008; Nobre et al., 2011). To calculate HAND, we used the digital elevation model of HydroSHEDS (Lehner et al., 2008), which is a global dataset such that the approach introduced here is portable to other areas in the world. We used the 30 arc-second river network map (RIV) of HydroSHEDS to identify pixels containing river/stream networks, together with the Global Lakes and Wetland Database (GLWD, Lehner and Döll, 2004) for identifying the locations of lakes, wetlands and other large surface water bodies (LAK). Based on the local drainage direction map (LDD) and the digital elevation map of HydroSHEDS (Lehner et al., 2008), the HAND field is calculated as follows:

$$\mathrm{HAND} = \mathrm{DEM}_{30''} - \mathrm{DEM}_{\mathrm{wat}} \tag{3.17}$$

where the subscript $30''$ indicates the spatial resolution and $\mathrm{DEM}_{\mathrm{wat}}$ is the assumed elevation of the nearest (based on $\mathrm{LDD}_{30''}$) surface water pixel (identified in LAK and RIV). To calculate $\mathrm{DEM}_{\mathrm{wat}}$, we applied a 3×3 window neighborhood moving average to 3 arc-second HydroSHEDS digital elevation map ($\mathrm{DEM}_{3''}$) and then assigned the resulting minimum value to the center of every 30 arc-second pixel. This filter was implemented in order to eliminate remaining artefacts found in the original digital elevation map (but still preserving important surface water course elevations).

The reference level c is estimated based on its physical definition as conceptualized in Fig. 3.1. For zero input values ($\mathrm{SWI}_t = 0$), i.e. a prolonged dry condition of soil moisture, Eqs. 3.1 to 3.3 suggest that the groundwater head would decline to a certain level that equals to c. In reality, this level is most likely the level of the

nearest drainage (see e.g. von Asmuth et al., 2002; von Asmuth and Knotters, 2004). Referring to the conceptualization in Fig. 3.1, the reference level c is approximated by:

$$c = -\text{HAND} \tag{3.18}$$

where the negative sign indicates a position below surface elevation. Note that the values of HAND are always greater than or equal to zero.

To estimate δ_1, we used the following regression model:

$$\delta_1 = e^{-C\times\left(1/\text{HAND}^D\right)} \tag{3.19}$$

where the regression coefficients are positive ($C > 0$ and $D > 0$) such that $0 \leq \delta_1 \leq 1$, as it should be from the physical point of view. The exponential function in Eq. 3.19 is similar to the relation proposed by Knotters and Bierkens (2000) in their ARX model, i.e. a form of TFN model with ϕ_1 equal to δ_1 and estimated as $\delta_1 = e^{-\Delta t/f\gamma}$ where Δt is a constant modeling time interval, γ is the resistance to the drainage or surface water network and f is the porosity. If the variation of f is assumed to be less important, it can be further anticipated that γ and HAND are positively correlated in order to reasonably suggest the model in Eq. 3.19.

To estimate ω_0, we investigate the steady state condition of the TFN model used, where the mean conditions of groundwater head state $h_t^* = h_{t-1}^* = h_{\text{avg}}^*$ is obtained by forcing the TFN model with mean soil moisture $\text{SWI}_t = \text{SWI}_{t-1} = \overline{\text{SWI}}_{\text{avg}}$. The steady state condition of the deterministic part of the TFN model (Eq. 3.2) is expressed as:

$$h_{\text{avg}}^* = \frac{\omega_0}{1-\delta_1} \times \overline{\text{SWI}}_{\text{avg}} \tag{3.20}$$

Since the expected value of the noise component n_t is c (Eq. 3.3), the steady state condition of the TFN model (Eq. 3.1) can be written as:

$$h_{\text{avg}} = \frac{\omega_0}{1-\delta_1} \times \overline{\text{SWI}}_{\text{avg}} + c \tag{3.21}$$

Therefore, the value of ω_0 is given as:

$$\omega_0 = \frac{(h_{\text{avg}} - c)}{\overline{\text{SWI}}_{\text{avg}}} (1-\delta_1) \tag{3.22}$$

Following the conceptualization in Fig. 3.1, the positions of groundwater heads h_{avg} above levels c can be estimated from the following power regression model:

$$(h_{\text{avg}} - c) = A \times \text{HAND}^B \tag{3.23}$$

which, with the regression coefficients $0 < A \leq 1$ and $0 < B < 1$, logically assumes that groundwater heads are close to drainage levels ($h_{\text{avg}} = c$) for areas located near stream networks (HAND = 0); and groundwater heads are above drainage levels

($h_{\text{avg}} > c$) for areas located higher above the flood plain (HAND $\gg 0$); but they are never above the surface elevation ($h_{\text{avg}} \leq 0$).

Using the regression models in Eqs. 3.19 and 3.23, the value of ω_0 in Eq. 3.22 can be estimated as follows:

$$\omega_0 = \frac{A \times \text{HAND}^B}{\text{SWI}_{\text{avg}}} \left[1 - e^{-C \times \left(1/\text{HAND}^D\right)}\right] \tag{3.24}$$

that logically suggests $\omega_0 \geq 0$ (Knotters and Bierkens, 2000), as it should be from a physical point of view.

The formulas suggested in Eqs. 3.18, 3.19 and 3.24 were used to estimate c, δ_1 and ω_0 for the entire study area. Using the estimates of these deterministic parameters, we made a spatio-temporal prediction of monthly groundwater heads (based on Eqs. 3.1 to 3.3) for the periods 1995-2000 and 2004-2007. Note, the estimation of the noise series (i.e. Eq. 3.3, including the parameter ϕ_1 and the variance σ_a^2) are not necessary in this spatio-temporal prediction exercise because we assume no groundwater head data are available (hence, a_t series can not be estimated) and their expected value are zero ($\text{E}\left[n_t - c\right] = 0$). As the initial condition for both periods 1995-2000 and 2004-2007, we used the estimate of h_{avg} based on the conceptualization in Eqs. 3.18 and 3.23 (see also Fig. 3.1):

$$h_{\text{avg}} = -\left[\text{HAND} - A \times \text{HAND}^B\right] \tag{3.25}$$

The predicted head (monthly) time series, which have a spatial resolution of 30-arc seconds, were evaluated by point-scale groundwater head measurements. We ignored the spatial scale discrepancy between them. For the period 1995-2000, the prediction was evaluated only at the measurement stations having at least 40 months of observation data, while the evaluation of the prediction time series in 2004-2007 was done only at the stations with at least 20 months of observations. For both periods, as done in the temporal forecasting exercise explained in Sect. 3.2.1, we measured the cross correlation coefficient ρ_{TF}, the bias ME, the mean absolute error MAE between the predicted and measured time series, and the mean absolute error between two anomaly time series MAE_{ano}. Note that, for this exercise, the calculation of MAE is not preferred because we expect a large bias ME mainly due to the uncertainty of the estimated levels c. Clearly, their estimates are limited by the 30-arc-second spatial resolution of the HydroSHEDS DEM used in this study. Also, the accuracy of HydroSHEDS DEM, which is a derivation product of Shuttle Radar Topography Mission (SRTM) DEM (`http://www2.jpl.nasa.gov/srtm/`), should be considered limiting since the target value of the SRTM standard accuracy is 16 m. Moreover, our approach is limited by the simplification that water tables are subdued replica of topography. In reality, other factors, such as anthropogenic influence, hydro-geological conditions and recharge also play roles (see e.g. Haitjema and Mitchell-Bruker, 2005).

3.3 Results

3.3.1 Groundwater head forecasting in time

Figures 3.2a to d present comparisons between point-scale measured and time update predicted time series calculated from the TFN model at four locations. In each figure, the prediction performance, indicated in ρ_{TF}, ME and MAE (evaluated to the measurements in the period 2004-2007), is presented in the yellow box on the left side, while the calibrated parameters (c, ω_0, δ_1, ϕ_1 and σ_a) are shown on the right side. Note that, as stated previously in Sect. 3.2.1, for all time series used in this prediction exercise, we assume that $\sigma_\epsilon = 0$, i.e. the measurement noise is very small and neglected. For the examples shown in Figs. 3.2a to d, the model can predict the observed groundwater head time series very well, not only in the examples with shallow groundwater (Figs. 3.2a to c), but also for the location with deep groundwater (Fig. 3.2d). The good prediction performance found here is partly due to the regular measurement updates in the prediction. In each example shown in Fig. 3.2, three prediction time series with varying measurement update intervals were plotted: with every-one month update (indicated as red lines and resulted from the calibration run 1995-2000 and the validation run 2004-2007), with every three-month update (yellow lines, validation run 2004-2007) and with every four-month update (black lines, validation run 2004-2007). From these plots, as expected, the prediction performance generally decreases if longer measurement update intervals are used.

In Figs. 3.3a to d, we plotted the point-scale prediction time series without any measurement updates. The prediction time series (indicated as red lines) were presented together with their 95% prediction interval (indicated as black lines) estimated from the noise component (i.e. $\pm 1.96\sqrt{\sigma_a/1-\phi_1^2}$). Without measurement updates, the model can still shows good prediction, as indicated in Figs. 3.3a to c. However, Fig. 3.3d shows a poor or even very bad prediction for an example of deep groundwater and indicates that the used SWI_t time series does not contribute for predicting deep groundwater head dynamics.

From the calibrated parameters ω_0, which determines the relations between groundwater heads and SWI_t input series (see Eqs. 3.2 and 3.8), we can judge the usefulness of SWI_t for groundwater head prediction. A higher value of ω_0 indicates that there is strong influence of SWI_t to groundwater head dynamics. The value of ω_0 in the example in Fig. 3.3d (and Fig. 3.2d) is very small ($\omega_0 \approx 0$), especially if it is compared to the ones in the other examples (Figs. 3.3a to c and Figs. 3.2a to c). This small value of ω_0 indicates that the influence of soil moisture dynamics is very small on groundwater head dynamics. It is clear that the good prediction shown in Fig. 3.2d are mainly due to the measurement updates (Eqs. 3.10 to 3.14) and could not be produced if no measurement updates were taken, as shown in Fig. 3.3d. Nevertheless, this is not entirely true for the shallow groundwater head examples in Figs. 3.2a to c, in which SWI_t input series (in addition to the measurement updates) play an impor-

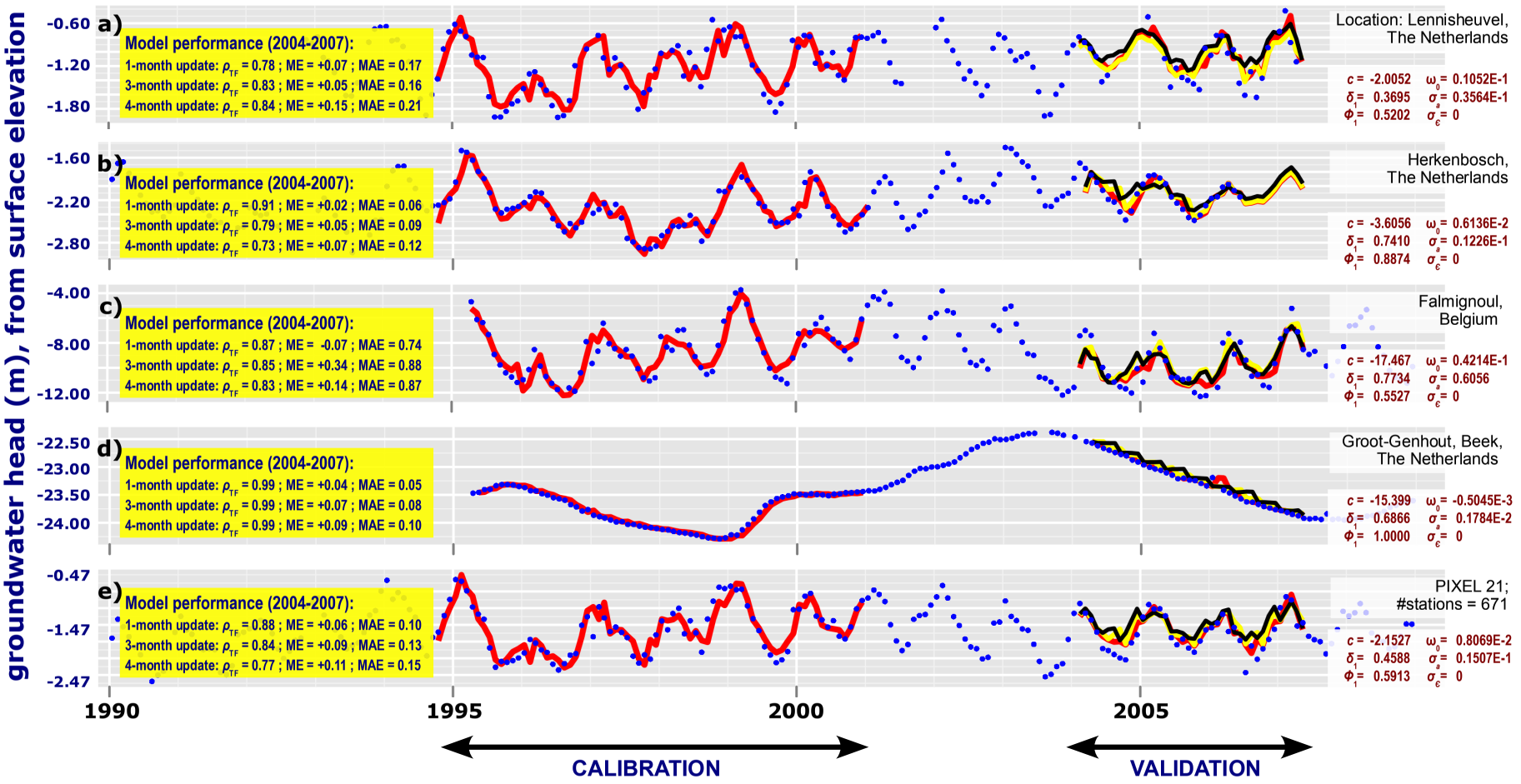

Figure 3.2 Comparisons between the time update predicted and measured groundwater head time series (blue dots) at several locations: Lennisheuvel, the Netherlands (a); Herkenbosch, the Netherlands (b); Falmignoul, Belgium (c); and Groot-Genhout, Beek, the Netherlands (d) (see Fig. 2.2c for the location of each point). The red, yellow and black lines represent the prediction time series with respectively one-month, three-month and four-mouth measurement update intervals. The lowermost one (e) is the comparison for the upscaled h_t at the pixel 21 (see Fig. 2.2b for the pixel location).

tant role for providing reliable groundwater head predictions. For the examples in Figs. 3.3a to c, the model can still provide good predictions even if no measurement updates are used.

When forecasting without measurement update, Fig. 3.3a provides an example of good prediction for both calibration (1995-2000) and validation (2004-2007) periods. However, in the examples shown in Figs. 3.3b and c, the prediction performance deteriorates during the validation, mainly due to the prediction biases (ME), most likely attributable to the changing levels or trends of c. Figure 3.3b is an example with a positive trend, as indicated by the fact that its average measured groundwater head in 2004-2007 is higher than the one in 1995-2000), while Fig. 3.3c has a negative trend of c.

In Figs. 3.4 to 3.6, we presented the histograms summarizing the performance indicators ρ_{TF}, ME and MAE of the predictions with every one-month (Fig. 3.4), three-month (Fig. 3.5) and four-month (Fig. 3.6) measurement updates. For the ones without measurement updates, the results are summarized in the histograms in Fig. 3.7. All of them were based on the validation run 2004-2007. As expected, they suggest that more prediction time series with higher correlations ρ_{TF} and smaller biases ME and errors MAE are obtained if shorter measurement update intervals are used.

Yet, the results for the case without measurement update still provide reasonably good prediction in term of reproduction of the dynamics, as suggested in the histogram of the timing agreement indicators ρ_{TF} in Fig. 3.7a (in which there are 1730 (63%) locations with $\rho_{\mathrm{TF}} > 0.5$ and 974 (35%) locations with $\rho_{\mathrm{TF}} > 0.7$). In term of prediction biases, there are several locations with large biases, as suggested in the histogram in Fig. 3.7c (in which there are 659 (24%) locations with $|\mathrm{ME}| > 0.5$ m). These biases are most likely attributable to the changing levels of c or the inability to estimate c in case of a lack of relationship between groundwater and soil moisture dynamics (see the previous discussion). Such biases ME certainly affect the prediction accuracy measured in MAE, as shown in its histogram in Fig. 3.7d (with 766 (24%) point-scale forecasts having MAE > 0.5 m). If these biases were removed, the prediction would have a much higher accuracy, as indicated in the histogram of the unbiased error $\mathrm{MAE}_{\mathrm{ano}}$ shown in Fig. 3.7d (in which there are only 303 (11%) points with $\mathrm{MAE}_{\mathrm{ano}} > 0.5$ m).

The performance indicators ρ_{TF}, ME and MAE of point-scale predictions with measurement updates (in 2004-2007) are summarized in the 30 arc-minute pixel fields presented in Fig. 3.8 (updated every one months), Fig. 3.9 (updated every three months) and Fig. 3.10 (updated every four months). From the fields of ρ_{TF} (Figs. 3.8a, 3.9a and 3.10a), including the results of their correlation tests to average measured heads (Fig. 2.2a), it follows that all forecasts generally have equally good performance, regardless their locations in shallow or deep groundwater areas. This good performance is partly due to the recurring measurement updates. The same applies for the fields of ME (Figs. 3.8b, 3.9b and 3.10b). Nonetheless, the fields of MAE

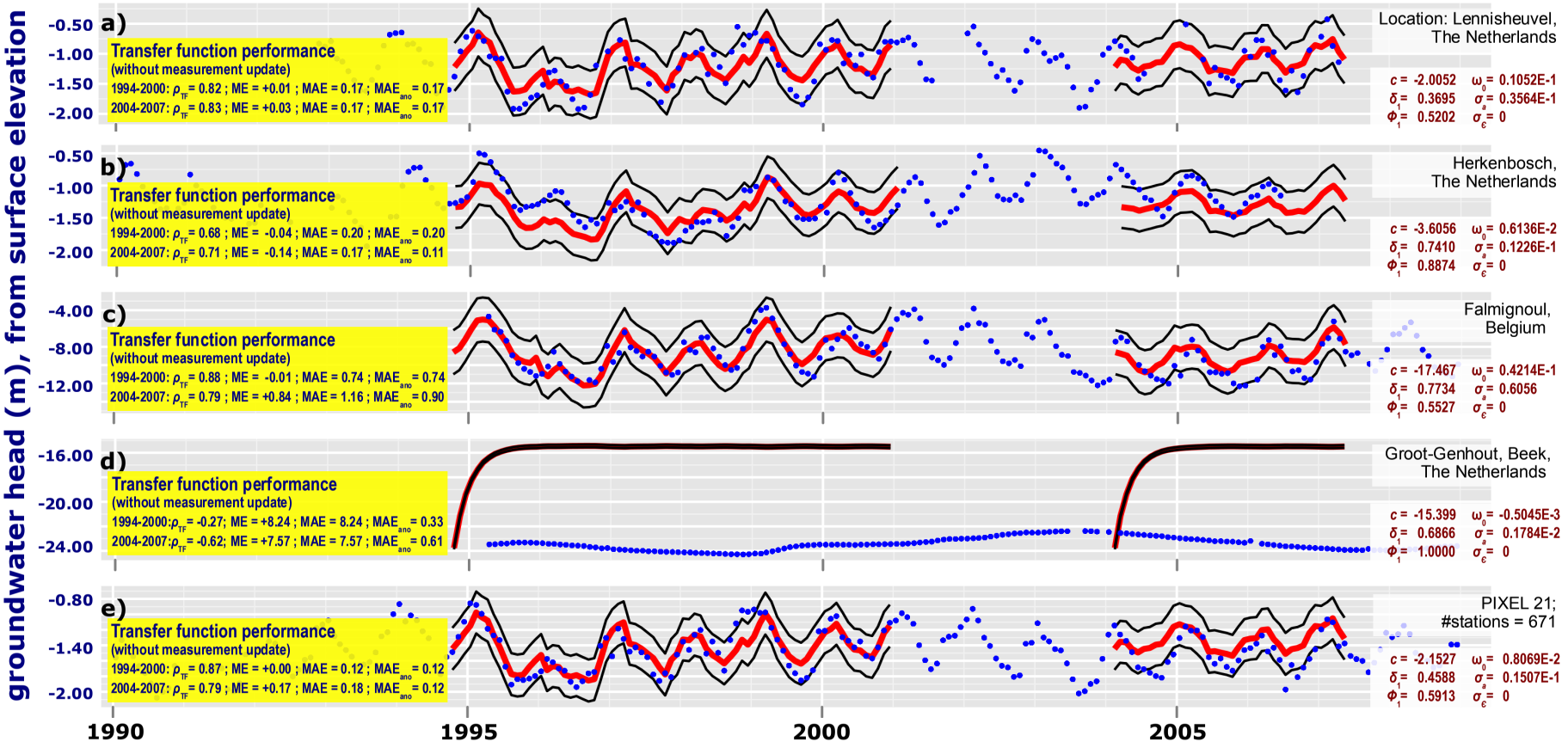

Figure 3.3 Comparisons between predicted and measured groundwater head time series (indicated by blue dots) at several locations: Lennisheuvel, the Netherlands (a); Herkenbosch, the Netherlands (b); Falmignoul, Belgium (c); and Groot-Genhout, Beek, the Netherlands (d) (see Fig. 2.2c for the location of each point). Here, the predicted time series, indicated by red lines, are resulted from transfer function without any measurement update and noise component of the TFN model, while the black lines illustrate the confidence interval of the prediction. The lowermost one (e) is the comparison for the upscaled h_t at the pixel 21 (see Fig. 2.2b for the pixel location).

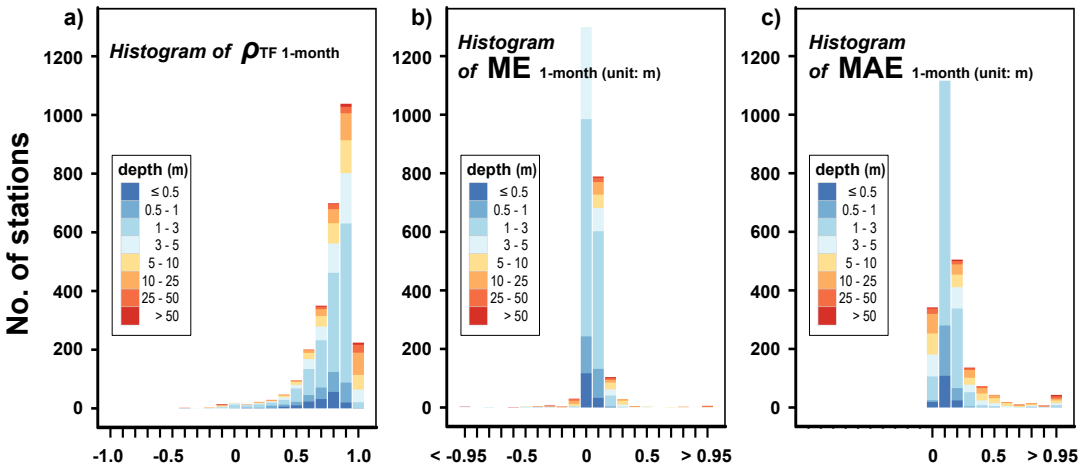

Figure 3.4 Histograms of TFN model performance measured in ρ_{TF} (a), ME (b) and MAE (c) for the prediction with every one-month measurement update. Note that these are based on the validation run 2004-2007, the total number of stations is 2761 and a positive ME value indicates that an average prediction is larger than an average measurement time series.

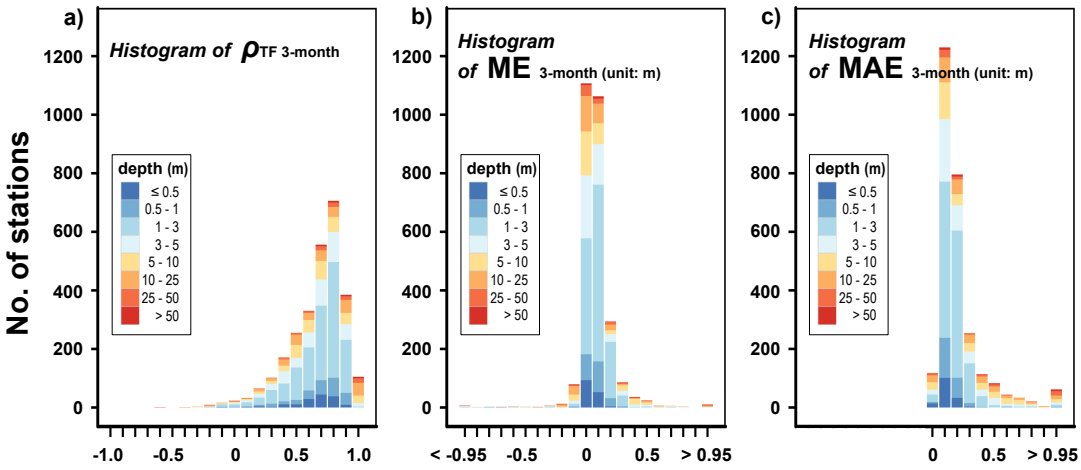

Figure 3.5 Histograms of TFN model performance measured in ρ_{TF} (a), ME (b) and MAE (c) for the prediction with every three-month measurement update. Note that these are based on the validation run 2004-2007, the total number of stations is 2761 and a positive ME value indicates that an average prediction is larger than an average measurement time series.

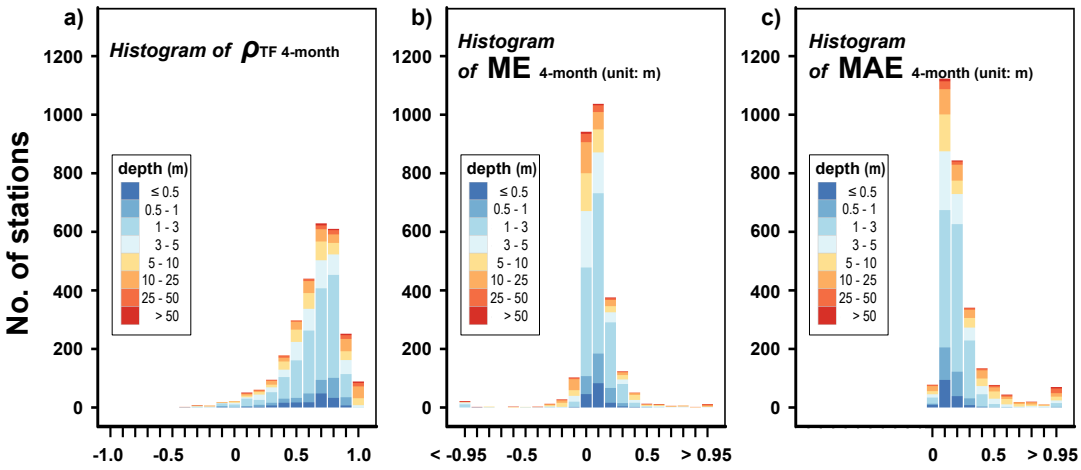

Figure 3.6 Histograms of TFN model performance measured in ρ_{TF} (a), ME (b) and MAE (c) for the prediction with every four-month measurement update. Note that these are based on the validation run 2004-2007, the total number of stations is 2761 and a positive ME value indicates that an average prediction is larger than an average measurement time series).

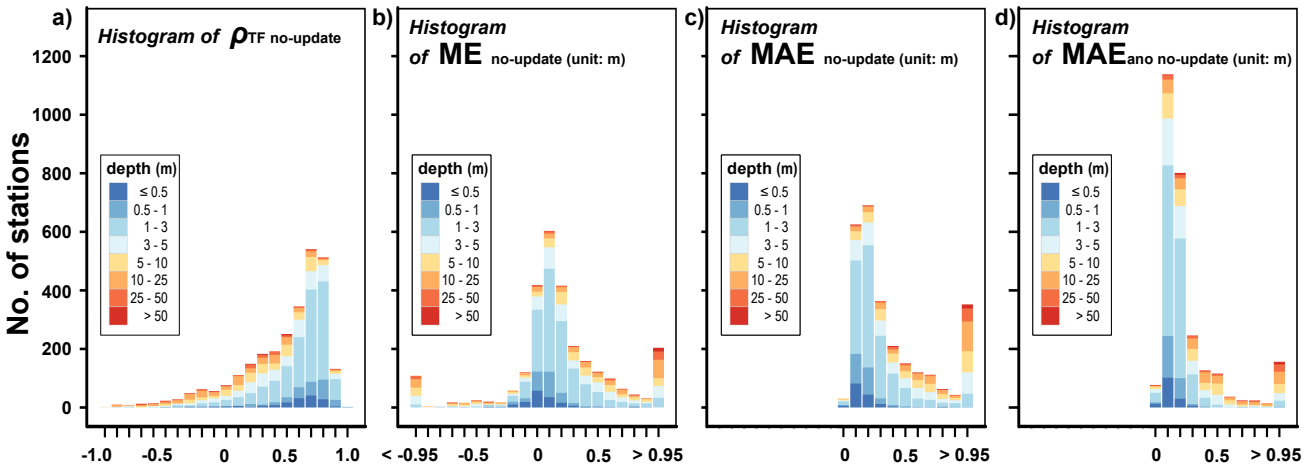

Figure 3.7 Histograms of TFN model performance measured in ρ_{TF} (a), ME (b), MAE (c) and $\mathrm{MAE}_{\mathrm{ano}}$ (d), for the predictions without measurement updates. Note that these are based on the validation runs 2004-2007, the total number of stations is 2761 and a positive ME value indicates that an average prediction is larger than an average measurement time series.

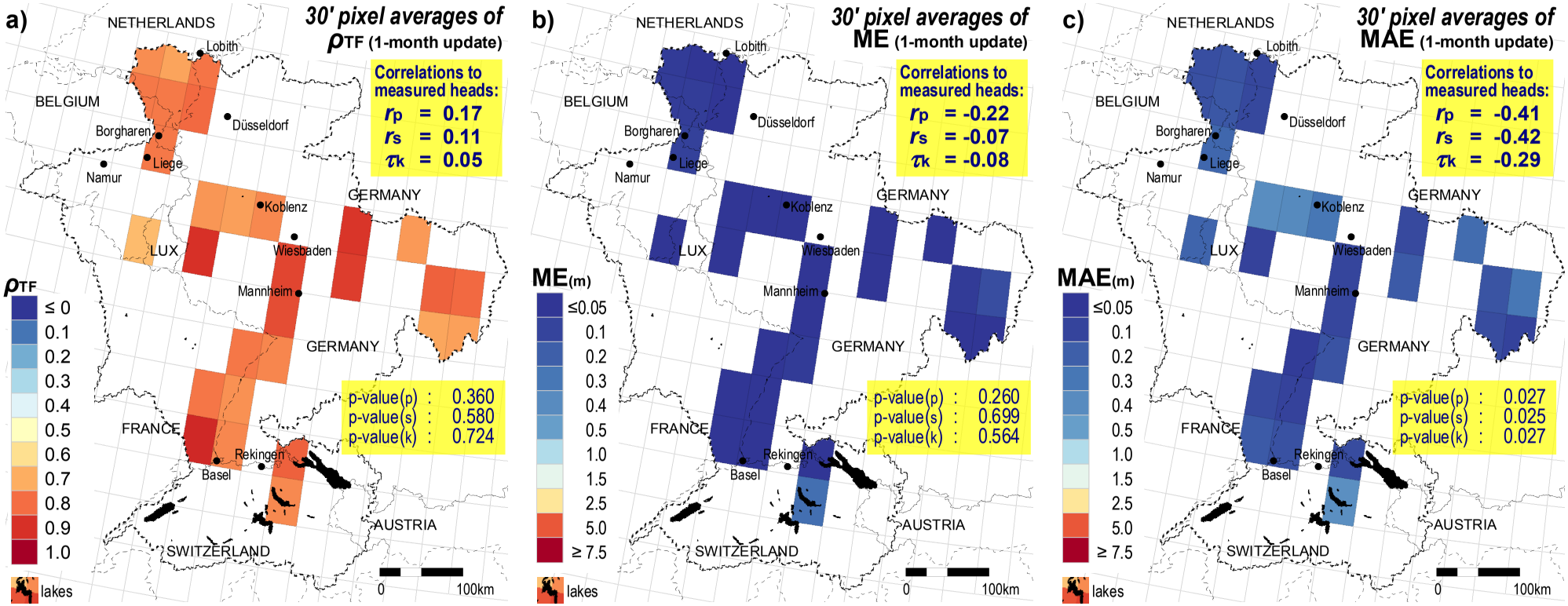

Figure 3.8 30 arc-minute pixel averages of TFN model performance measured in ρ_{TF}, ME (unit: m) and MAE (unit: m) for the prediction with updates every month. We show only the pixel average values calculated from at least 15 point-scale values. The upper yellow boxes contain the correlation coefficients of the field values to average measured heads (Fig. 2.2a): Pearson's correlation (r_{p}), Spearman's rho (r_{s}) and Kendall's tau (τ_{k}) coefficients. The lower yellow boxes contain their corresponding p-values.

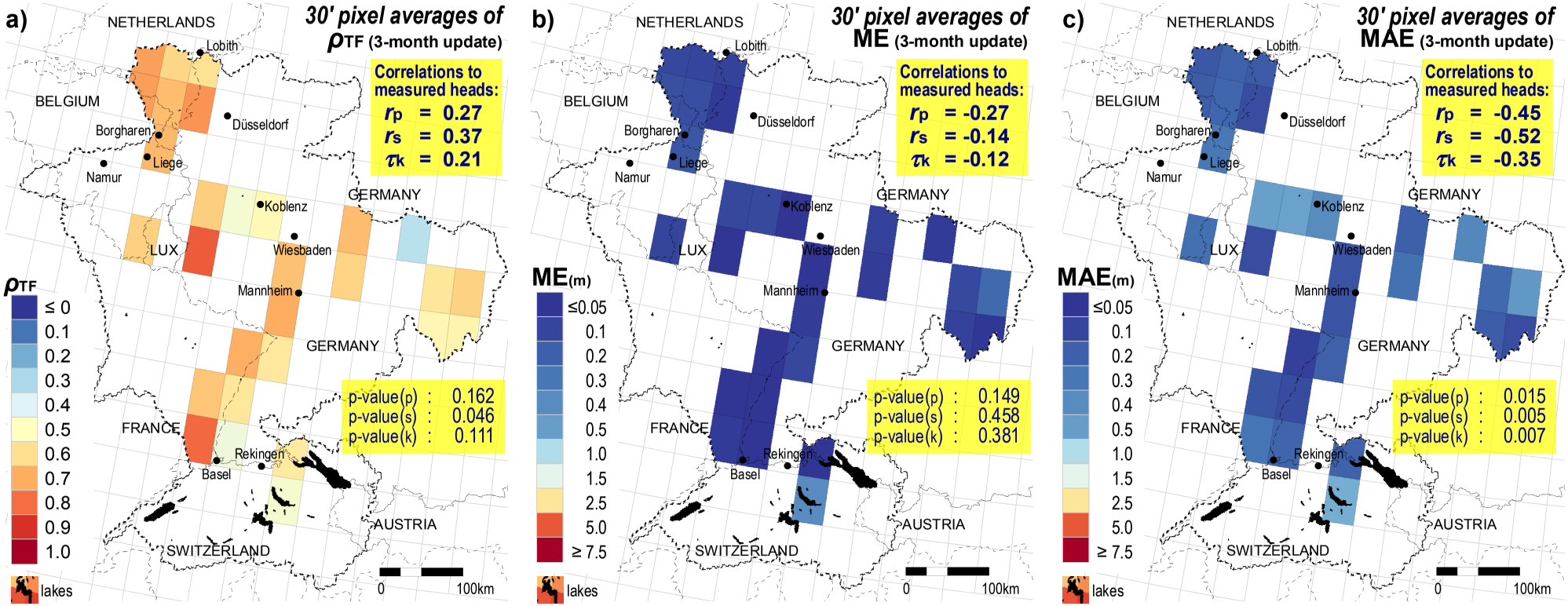

Figure 3.9 30 arc-minute pixel averages of TFN model performance measured in ρ_{TF}, ME (unit: m) and MAE (unit: m) for the prediction with updates every three months. We show only the pixel average values calculated from at least 15 point-scale values. The upper yellow boxes contain the correlation coefficients of the field values to average measured heads (Fig. 2.2a): Pearson's correlation (r_{p}), Spearman's rho (r_{s}) and Kendall's tau (τ_{k}) coefficients. The lower yellow boxes contain their corresponding p-values.

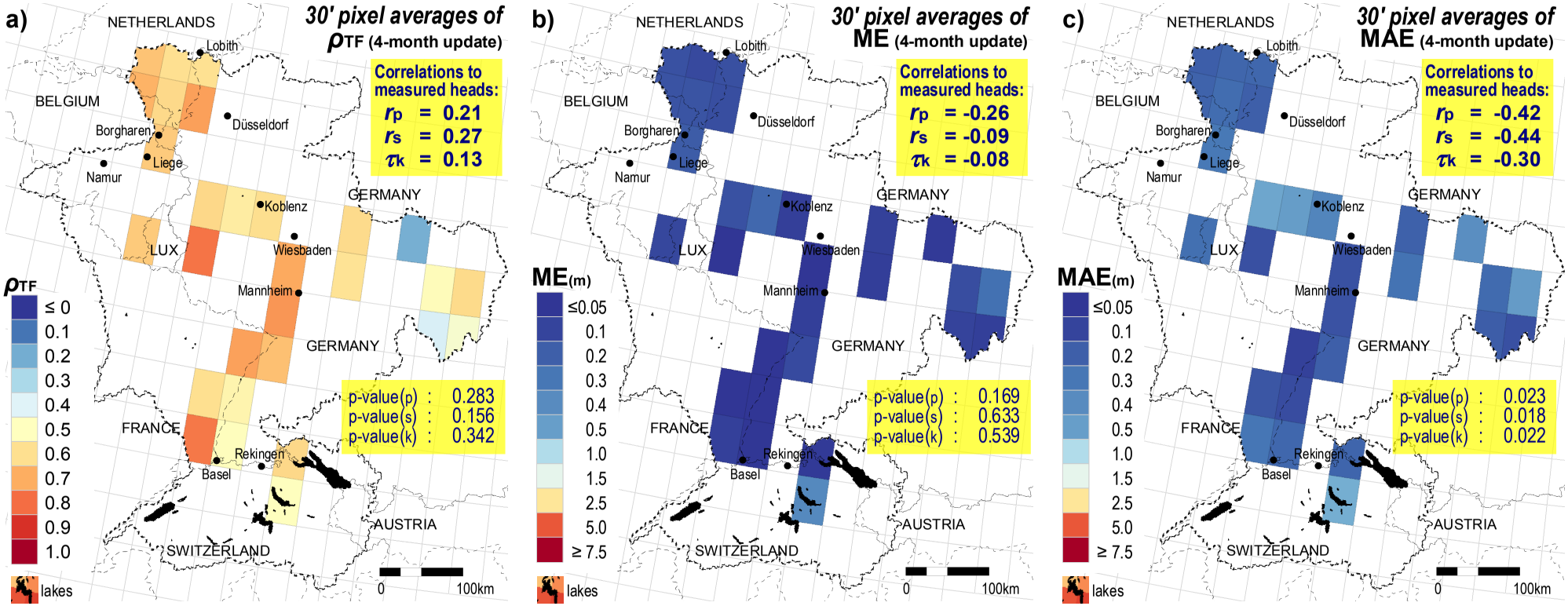

Figure 3.10 30 arc-minute pixel averages of TFN model performance measured in ρ_{TF}, ME (unit: m) and MAE (unit: m) for the prediction with updates every four months. We show only the pixel average values calculated from at least 15 point-scale values. The upper yellow boxes contain the correlation coefficients of the field values to average measured heads (Fig. 2.2a): Pearson's correlation (r_{p}), Spearman's rho (r_{s}) and Kendall's tau (τ_{k}) coefficients. The lower yellow boxes contain their corresponding p-values.

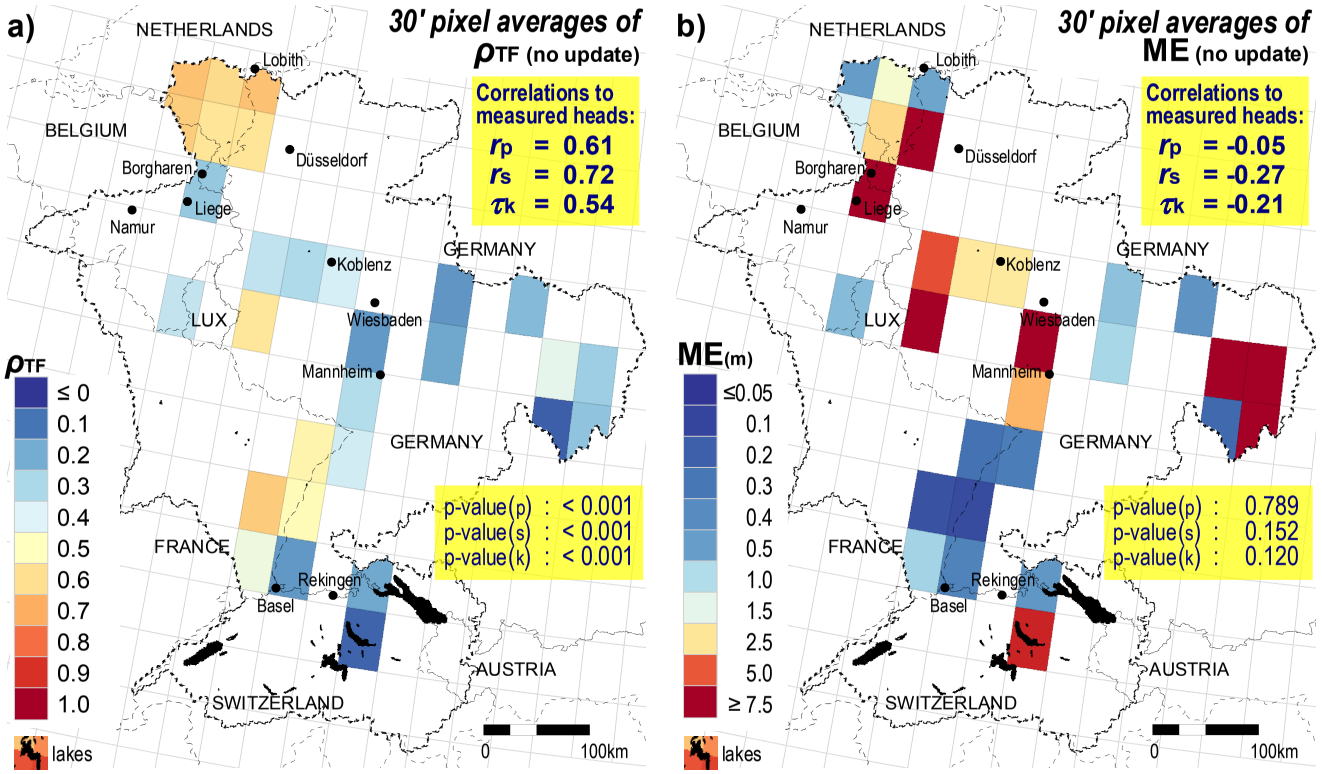

Figure 3.11 30 arc-minute pixel averages of TFN model performance measured in ρ_{TF} and ME (unit: m). We show only the pixel average values calculated from at least 15 point-scale values. The upper yellow boxes contain the correlation coefficients of the field values to average measured heads (Fig. 2.2a): Pearson's correlation (r_{p}), Spearman's rho (r_{s}) and Kendall's tau (τ_{k}) coefficients. The lower yellow boxes contain their corresponding p-values.

(Figs. 3.8c, 3.9c and 3.10c) and the their correlation tests to average measured heads (Fig. 2.2a) suggest that predictions are to be better in areas with shallower groundwater.

For the prediction without measurement update, the prediction performance is summarized in the 30 arc-minute fields of ρ_{TF} and ME in Fig. 3.11, and MAE and $\mathrm{MAE}_{\mathrm{ano}}$ in Fig. 3.12. For the fields of ME and MAE that are very similar to each other, it is obvious that the prediction errors measured in MAE are mainly attributable to the prediction biases ME. If these biases were corrected, the predictions would have much better accuracy, as indicated in the map of $\mathrm{MAE}_{\mathrm{ano}}$ presented in Fig. 3.12a.

From Fig. 3.11, it follows that the head predictions without measurement updates are generally better for shallower groundwater areas. This fact is obvious from the field of ρ_{TF} in Fig. 3.11a, specifically from its correlation tests to average groundwater heads (Fig. 2.2a) that suggest significant positive correlations (i.e. the timing agreements between the predicted and measured time series are much better in shallower groundwater areas). A similar conclusion can also be drawn for the field of $\mathrm{MAE}_{\mathrm{ano}}$ in Fig. 3.12, in which the correlation tests of the field values to average heads (Fig. 2.2a) indicate negative correlations (i.e. smaller prediction errors are expected in shallower groundwater areas).

Table 3.1 lists the results of the temporal forecasting exercise at the 30 arc-minute pixel scale (at which we beforehand upscaled groundwater head time series to 30-arc minute pixel scale time series). An example of comparing the predicted and measured time series of the upscaled h_t is given in Fig. 3.2e for the prediction with measurement update, and in Fig. 3.3e for the prediction without measurement update. The results of the 30 arc-minute scale prediction are consistent with the results found in the point scale prediction. Table 3.1, in which we sorted the data based on average (upscaled) measured heads, shows that better predictions are generally found in shallower groundwater head areas and worse predictions are obtained in deeper groundwater head areas. The lower part of Table 3.1 shows the correlation test results confirms this.

3.3.2 Spatio-temporal prediction of groundwater head

The fitted regression models for estimating the parameters δ_1 and $(h_{\mathrm{avg}} - c)$ are given in Figs. 3.13a and b, respectively. The background color illustrates the number of groundwater head stations with values in each bin — i.e. the values of HAND and the calibrated values of δ_1 and $(h_{\mathrm{avg}} - c)$ as obtained from the previous "temporal forecasting" exercise (Sect. 3.3.1). The points (indicated by plus signs '+') are the values used in fitting regression lines (indicated by yellow lines). They are taken from 40 stations located in 18 different 30 arc-minute pixels (maximum 3 stations in a 30 arc-minute pixel). Using the calibrated parameters from these selected stations, the regression analyses provided the following regression coefficients: for Eq. 3.23 and

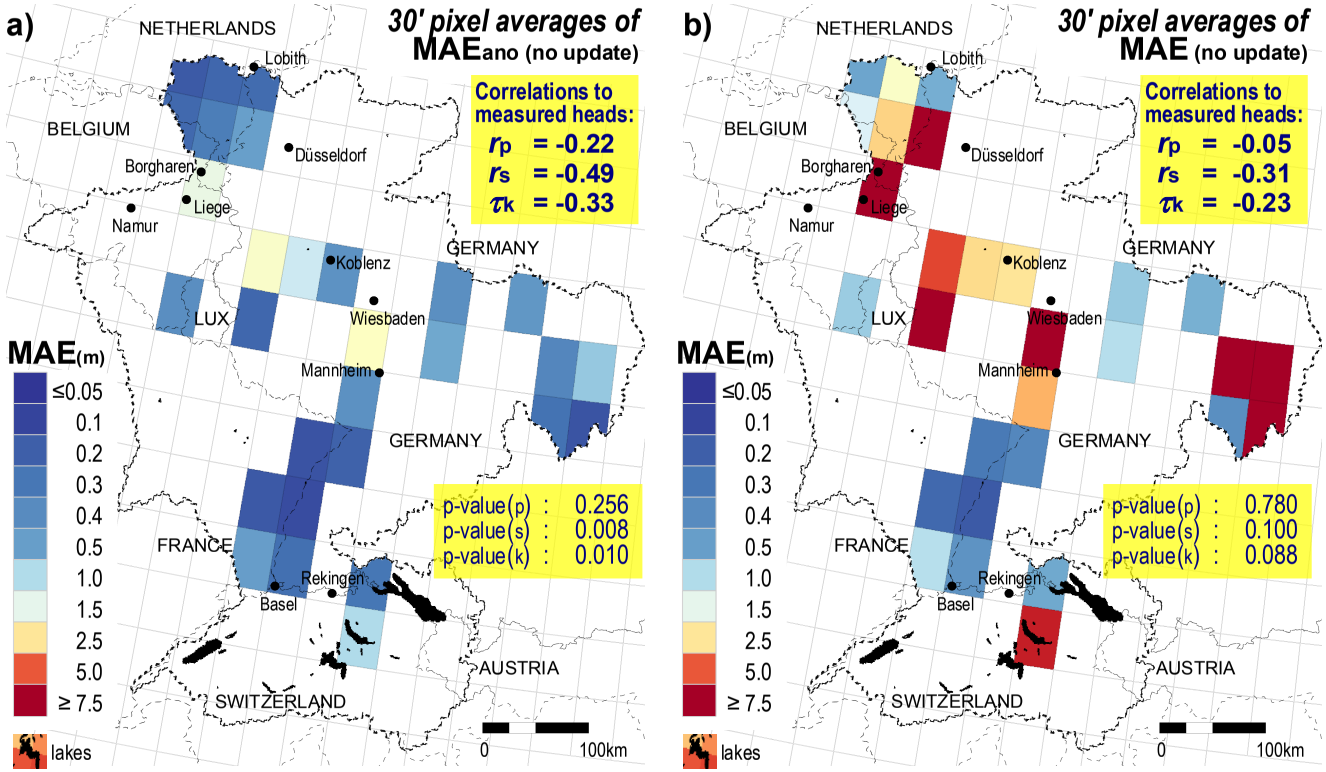

Figure 3.12 30 arc-minute pixel averages of TFN model performance measured in $\mathrm{MAE}_{\mathrm{ano}}$ (unit: m) and MAE (unit: m) for the prediction without any measurement updates. We show only the pixel average values calculated from at least 15 point-scale values. The upper yellow boxes contain the correlation coefficients of the field values to average measured heads (Fig. 2.2a): Pearson's correlation (r_{p}), Spearman's rho (r_{s}) and Kendall's tau (τ_{k}) coefficients. The lower yellow boxes contain their corresponding p-values.

Table 3.1 Results of the temporal forecasting of the 30 arc-minute scale h_t time series. The information is ordered to average groundwater head h_{avg}.

Pixel codes	Number of stations	h_{avg} (m)	1-month updates ρ_{TF}	ME (m)	MAE (m)	3-month updates ρ_{TF}	ME (m)	MAE (m)	4-month updates ρ_{TF}	ME (m)	MAE (m)	no measurement updates ρ_{TF}	ME (m)	MAE (m)	MAE_{ano} (m)
21	671	-1.47	0.88	0.06	0.10	0.84	0.09	0.13	0.77	0.11	0.15	0.79	0.17	0.18	0.12
38	336	-1.93	0.90	0.06	0.10	0.80	0.12	0.16	0.73	0.10	0.15	0.65	0.04	0.15	0.15
23	159	-2.30	0.67	0.01	0.12	0.60	0.01	0.12	0.74	0.07	0.12	0.72	0.01	0.11	0.11
39	851	-2.65	0.88	0.04	0.10	0.79	0.08	0.14	0.77	0.11	0.17	0.80	0.39	0.39	0.13
22	500	-2.85	0.86	0.05	0.10	0.85	0.08	0.13	0.82	0.08	0.14	0.87	0.32	0.32	0.11
145	39	-3.15	0.70	0.01	0.07	0.71	0.00	0.08	0.62	0.02	0.08	0.73	0.12	0.14	0.08
129	15	-3.47	0.59	0.06	0.13	0.46	0.07	0.16	0.59	0.07	0.14	0.49	0.28	0.29	0.15
144	33	-3.55	0.84	0.00	0.12	0.72	0.01	0.16	0.70	0.01	0.16	0.75	0.06	0.17	0.17
128	41	-3.77	0.87	0.01	0.05	0.80	0.01	0.06	0.84	0.02	0.05	0.78	0.25	0.25	0.06
40	312	-4.02	0.64	0.00	0.08	0.86	0.04	0.07	0.44	0.00	0.12	0.77	0.23	0.23	0.07
112	187	-4.15	0.87	0.08	0.10	0.65	0.12	0.15	0.71	0.14	0.16	0.41	0.43	0.44	0.12
95	142	-4.39	0.54	0.03	0.15	0.44	0.12	0.20	0.52	0.03	0.15	0.10	0.00	0.20	0.20
92	19	-5.82	0.94	0.00	0.06	0.89	0.00	0.08	0.89	0.01	0.09	0.80	0.03	0.12	0.11
162	25	-8.28	0.76	0.02	0.13	0.42	0.04	0.19	0.52	0.06	0.19	-0.17	0.19	0.25	0.21
82	18	-8.40	0.80	0.00	0.27	0.25	0.01	0.48	-0.09	0.05	0.55	-0.15	1.78	1.78	0.72
100	20	-8.58	0.82	0.21	1.24	0.75	0.38	1.58	0.73	0.23	1.57	-0.08	0.73	1.39	1.78
80	29	-9.26	0.58	0.00	0.25	0.67	0.07	0.24	0.51	0.05	0.34	0.39	1.35	1.35	0.28
57	20	-9.52	0.40	0.23	1.00	0.54	0.31	1.13	0.44	0.66	1.37	-0.11	2.07	2.54	1.21
77	27	-9.72	0.79	0.03	0.25	0.48	0.03	0.36	0.65	0.05	0.30	0.52	0.17	0.37	0.34
118	132	-9.90	0.90	0.28	1.07	0.83	0.60	1.66	0.72	0.69	1.97	0.33	7.41	7.41	2.59
161	50	-9.98	0.85	0.03	0.23	0.80	0.03	0.28	0.88	0.13	0.25	0.87	0.44	0.50	0.34
76	24	-10.62	0.73	0.03	0.24	0.47	0.07	0.33	0.60	0.15	0.28	0.45	0.51	0.61	0.37
75	21	-12.43	0.76	0.04	0.27	0.57	0.16	0.40	0.46	0.05	0.43	0.24	0.10	0.54	0.55
56	307	-13.02	0.71	0.19	0.66	0.39	0.39	0.87	0.41	0.44	0.87	-0.39	0.09	0.89	0.87
97	42	-13.03	0.31	0.05	0.34	0.16	0.17	0.39	-0.14	0.12	0.41	0.13	0.48	0.56	0.36
117	262	-13.57	0.50	0.20	1.25	0.49	0.00	1.40	0.47	0.02	1.37	-0.19	3.51	3.51	1.62
181	19	-14.64	0.63	0.02	0.30	0.27	0.08	0.45	0.44	0.06	0.35	-0.07	0.47	0.57	0.43
101	24	-18.75	0.30	0.19	1.08	0.18	0.80	1.22	0.34	0.85	1.23	-0.05	4.14	4.14	1.26
102	19	-21.93	0.44	0.11	0.48	0.38	0.05	0.54	0.06	0.15	0.68	-0.48	16.66	16.66	0.76
164	20	-22.93	0.70	0.02	0.56	0.57	0.03	0.85	0.04	0.14	1.43	0.34	1.26	1.61	1.44
90	22	-26.70	-0.10	0.04	6.54	0.20	0.67	5.94	0.05	1.19	6.41	0.14	4.41	5.98	5.81
Correlations to h_{avg}															
Pearson	r_{p}		0.67	-0.24	-0.62	0.64	-0.47	-0.65	0.70	-0.57	-0.67	0.62	-0.56	-0.60	-0.68
	p-value		≤ 0.001	0.193	≤ 0.001	≤ 0.001	0.007	≤ 0.001	≤ 0.001	0.001	≤ 0.001	≤ 0.001	0.001	≤ 0.001	≤ 0.001
Spearman	r_{s}		0.55	-0.22	-0.81	0.62	-0.28	-0.80	0.68	-0.43	-0.79	0.63	-0.62	-0.80	-0.81
	p-value		0.002	0.23	≤ 0.001	≤ 0.001	0.131	≤ 0.001	≤ 0.001	0.016	≤ 0.001	≤ 0.001	≤ 0.001	≤ 0.001	≤ 0.001
Kendall	τ_{k}		0.42	-0.14	-0.60	0.44	-0.20	-0.6	0.50	-0.28	-0.57	0.43	-0.43	-0.58	-0.61
	p-value		0.001	0.279	≤ 0.001	≤ 0.001	0.111	≤ 0.001	≤ 0.001	0.029	≤ 0.001	0.001	≤ 0.001	≤ 0.001	≤ 0.001

Eq. 3.19 (and Eq. 3.24): $A = 0.4137$, $B = 0.2432$, $C = 1.6832$ and $D = 0.5183$. As shown in Figs. 3.13, the regression models with HAND as predictor variable and constrained in their form by physical considerations are clearly limited in their ability to describe the spatial variability of δ_1 and $(h_{\text{avg}} - c)$.

Despite the limitation of the regression models used, the derived transfer function models are able to reproduce observed groundwater head variations reasonably well of a subset of locations. An example of a reasonable prediction is given in Fig. 3.14a. In this example, the timing agreement between the predicted and measured head time series is relatively good, both for the periods 1995-2000 ($\rho_{\text{TF}} = 0.82$) and 2004-2007 ($\rho_{\text{TF}} = 0.80$). In term of MAE_{ano}, the prediction errors are also still reasonable for both periods ($\text{MAE}_{\text{ano}} = 0.21$ m for the period 1995-2000 and $\text{MAE}_{\text{ano}} = 0.20$ m for the period 2004-2007). Note that, in this exercise, the actual MAE errors are not considered since we have expected prediction biases (as discussed in Sect. 3.2.2).

In the next example in Fig. 3.14b, we show a model prediction result for a location with HAND = 0. In areas with HAND = 0, Eqs. 3.18, 3.19 and 3.24 give $c = 0$, $\delta_1 = 0$, $h_{\text{avg}} = 0$ and $\omega_0 = 0$. Consequently, the transfer function model in these areas simulates only a constant value (which is the initial condition $h_{\text{avg}} = 0$). Clearly, this example provides a weakness of the approach for locations that are very close to open surface water bodies (i.e. rivers and lakes).

For the prediction example shown in Fig. 3.14c, it is found that the timing agreements between the predicted and measured head time series are reasonably well (see the yellow box on the right), for both periods 1995-2000 ($\rho_{\text{TF}} = 0.82$) and 2004-2007 ($\rho_{\text{TF}} = 0.80$). However, the prediction errors MAE_{ano} are large ($\text{MAE}_{\text{ano}} = 1.52$ m for the period 1995-2000 and $\text{MAE}_{\text{ano}} = 1.56$ m for the period 2004-2007). Clearly, the amplitude of the predicted groundwater head time series is off for the periods 1995-2000 and 2004-2007, as the model is not able to reproduce the measured large amplitude. However, it might be possible that the large extreme amplitude (almost 5 m) of the measurement time series is caused by an extreme local phenomenon or even a spurious measurement error (e.g. using a wrong unit while documenting the measurement data and/or station surface elevation). Note that, in the previous temporal forecasting exercise in Sect. 3.3.1 (see Fig. 3.11c), this extreme groundwater head fluctuation could "properly" be simulated due to the implementation of the calibration procedure.

For the prediction given in Fig. 3.14d, which is an example of a deep groundwater head location, we should not expect that the derived transfer function model can produce a reasonable prediction performance. Clearly, the predictions in both periods 1995-2000 and 2004-2007 are equally bad as indicated in their performance indicators.

Figure 3.15 summarizes the prediction performance in the histograms of ρ_{TF} and MAE_{ano}, for the periods 1995-2000 and 2004-2007. For 1995-2000 (Fig. 3.15b), there are 2369 (54%) stations with $\text{MAE}_{\text{ano}} \leq 0.25$ m. For 2004-2007 (Fig. 3.15d), we

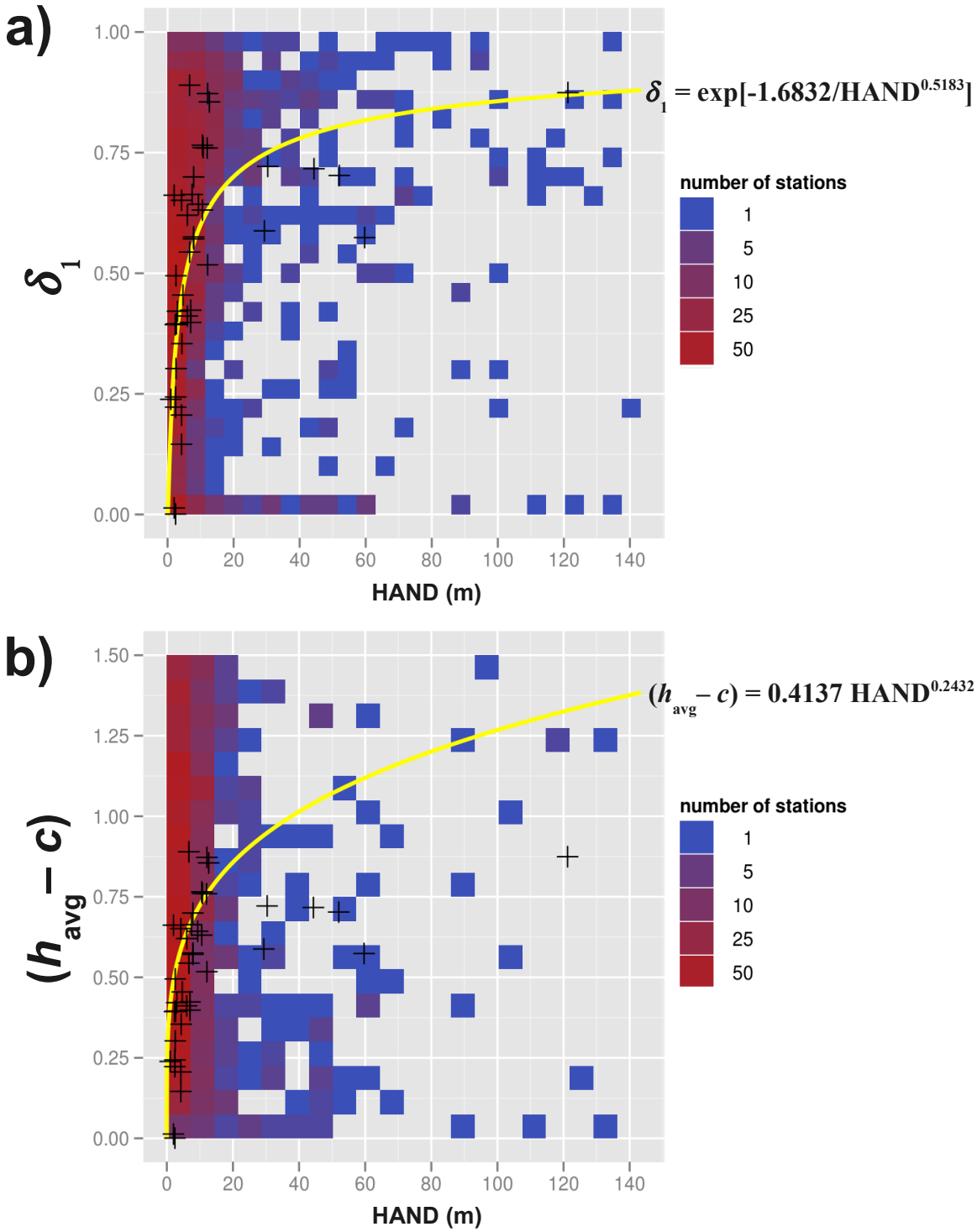

Figure 3.13 Regression models for estimating δ_1 (a); and $(h_{\text{avg}} - c)$ (b), based on the digital elevation model (HAND, see Sect. 3.3.2). The points (indicated by '+') are the values used in fitting regression lines (yellow lines). The background illustrates the number of head stations with values (in each bin) of HAND and the calibrated δ_1 and $(h_{\text{avg}} - c)$ as obtained from the exercise in Sect. 3.3.1.

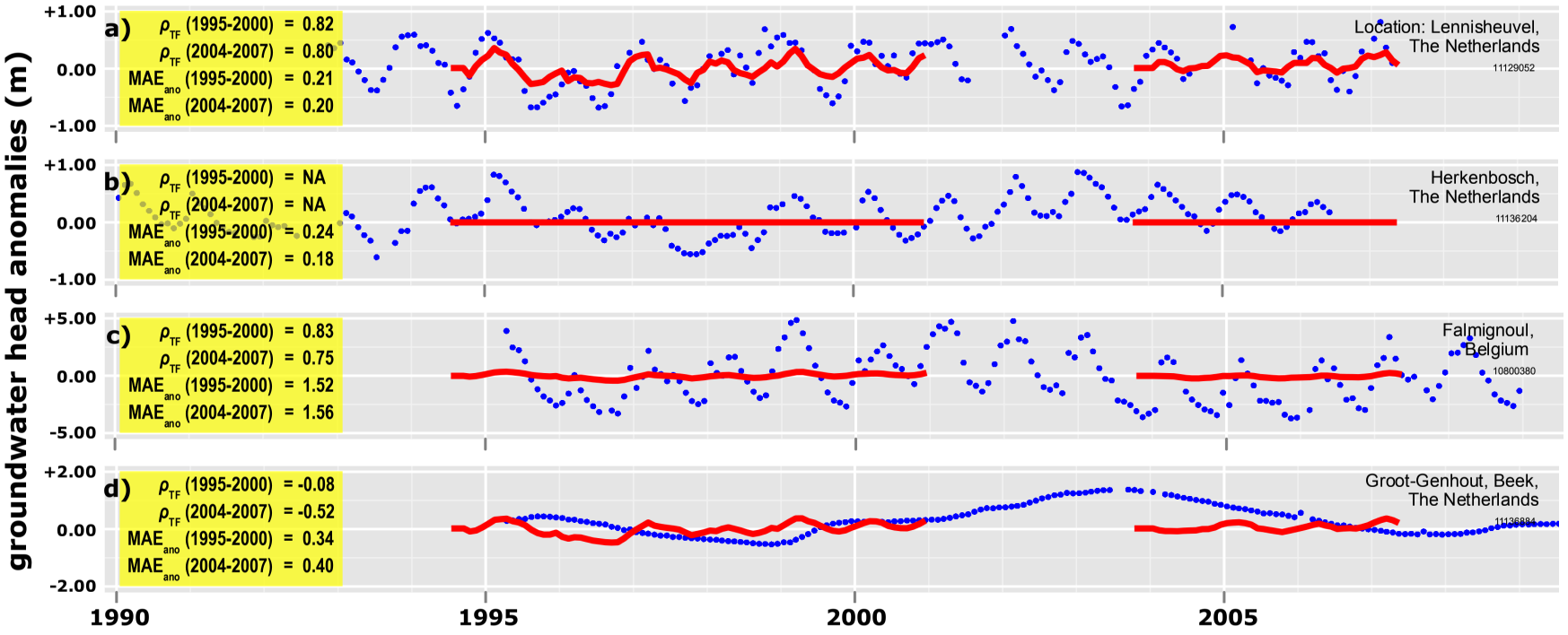

Figure 3.14 Comparisons between spatio-temporal predictions of groundwater heads (red lines) and observations (blue dots) at several locations: Lennisheuvel, the Netherlands (a); Herkenbosch, the Netherlands (b); Falmignoul, Belgium (c); and Groot-Genhout, Beek, the Netherlands (d) (see Fig. 2.2c for the location of each point). Here, each predicted time series is a result of a transfer function with parameters estimated by using a digital elevation model.

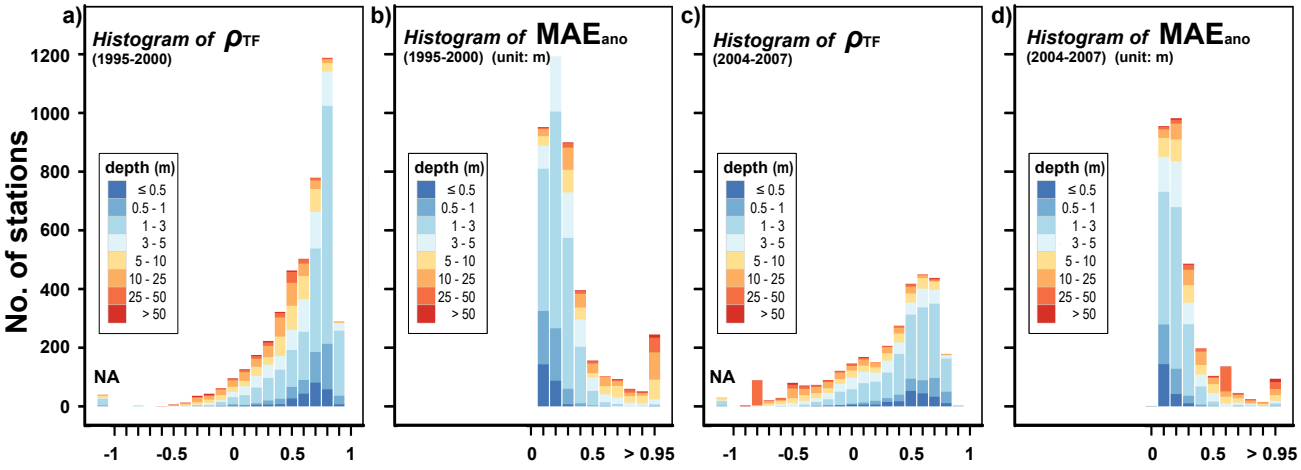

Figure 3.15 Histograms of spatio-temporal prediction performance with transfer function with parameters estimated using a digital elevation model: ρ_{TF} for the periods 1995-2000 (a) and 2004-2007 (c); and $\mathrm{MAE}_{\mathrm{ano}}$ (unit: m) for the periods 1995-2000 (b) and 2004-2007 (d). There are 4387 stations used for the period 1995-2000 and 2925 stations used for the period 2004-2007. Note that the histograms of ρ_{TF} also contain the "NA" bars for ρ_{TF} that cannot be calculated in the pixels with HAND = 0.

have 1901 (65%) stations with $\mathrm{MAE}_{\mathrm{ano}} \leq 0.25$ m. In the case of ρ_{TF}, for 1995-2000 (Fig. 3.15a), there are 3011 (69%) predictions with $\rho_{\mathrm{TF}} > 0.5$ and 1923 (44%) prediction with $\rho_{\mathrm{TF}} > 0.7$; while for 2004-2007 (Fig. 3.15c), there are 1376 stations (47%) with $\rho_{\mathrm{TF}} > 0.5$ and 585 stations (20%) with $\rho_{\mathrm{TF}} > 0.7$. Although the results for ρ_{TF} are better in 1995-2000 (which is expected as it is the calibration period of the previous temporal forecasting exercise), the prediction performance in 2004-2007 of this spatio-temporal modeling exercise is reasonable and comparable to the results of the previous temporal forecasting exercise presented in Sect. 3.3.1 (in which the model parameters were properly calibrated). This fact can be observed by comparing the histograms of ρ_{TF} and $\mathrm{MAE}_{\mathrm{ano}}$ of the previous temporal forecasting exercise (Fig. 3.7a and d, without measurement update) to the ones obtained here (Figs. 3.15c and d). Note that this is after bias-correction, so that the results are comparable in terms of the ability to predict groundwater head variation, not its absolute or actual level.

In Figs. 3.16a to c and Fig. 3.17a, the prediction performance indicators ρ_{TF}, ME, MAE, and $\mathrm{MAE}_{\mathrm{ano}}$ of the period 1995-2000 are summarized at 30 arc-minute resolution. Clearly, the spatio-temporal prediction method is not able to estimate the absolute value of groundwater levels (as indicated by ME and MAE in Figs. 3.16b and c). However, head variation in terms of timing (as indicated by ρ_{TF} in Fig. 3.16a) and amplitude (as indicated by $\mathrm{MAE}_{\mathrm{ano}}$ in Fig. 3.17a) is reasonably well predicted. The correlation tests between the field values and average groundwater heads (Fig. 2.2a)

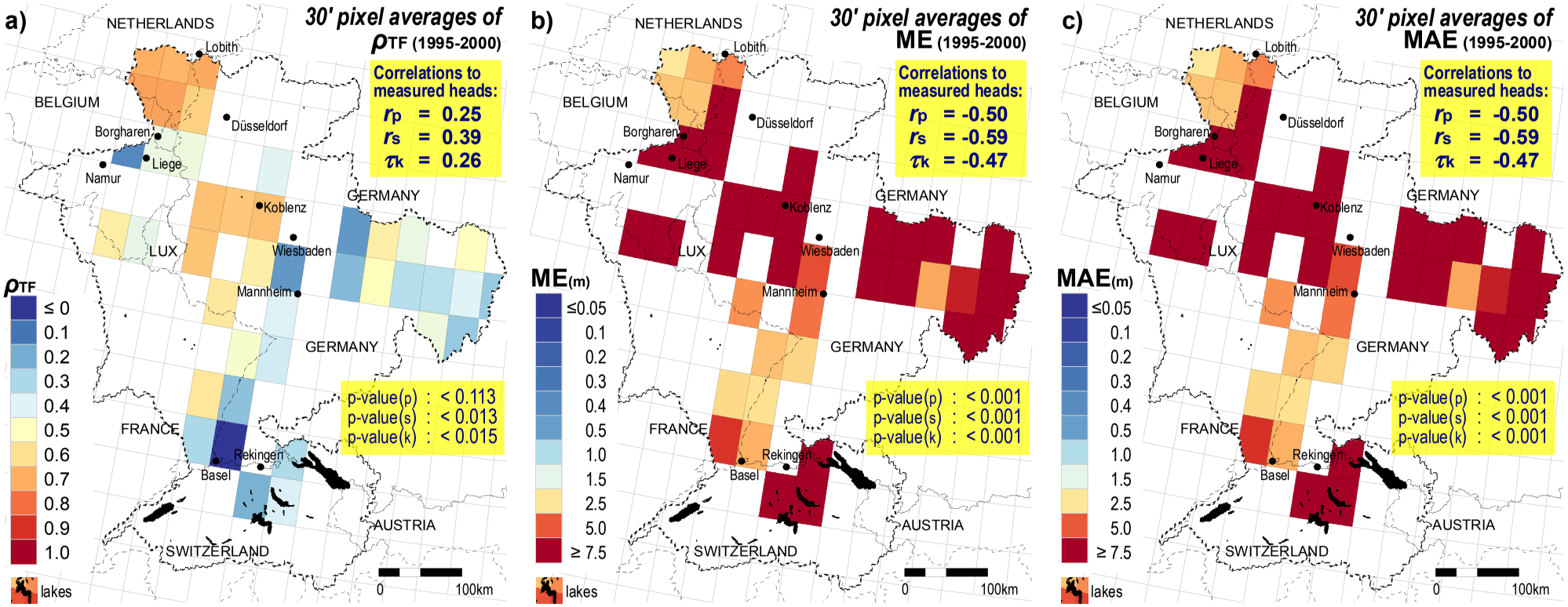

Figure 3.16 30 arc-minute pixel averages of TFN model performance measured in ρ_{TF} (a), ME (b) and MAE (c) for the spatio-temporal prediction in the period 1995-2000 with transfer function with parameters estimated using a digital elevation model. We show only the pixel average values calculated from at least 15 point-scale values. The upper yellow boxes contain the correlation coefficients of the field values to average measured heads (Fig. 2.2a): Pearson's correlation (r_{p}), Spearman's rho (r_{s}) and Kendall's tau (τ_{k}) coefficients. The lower yellow boxes contain their corresponding p-values.

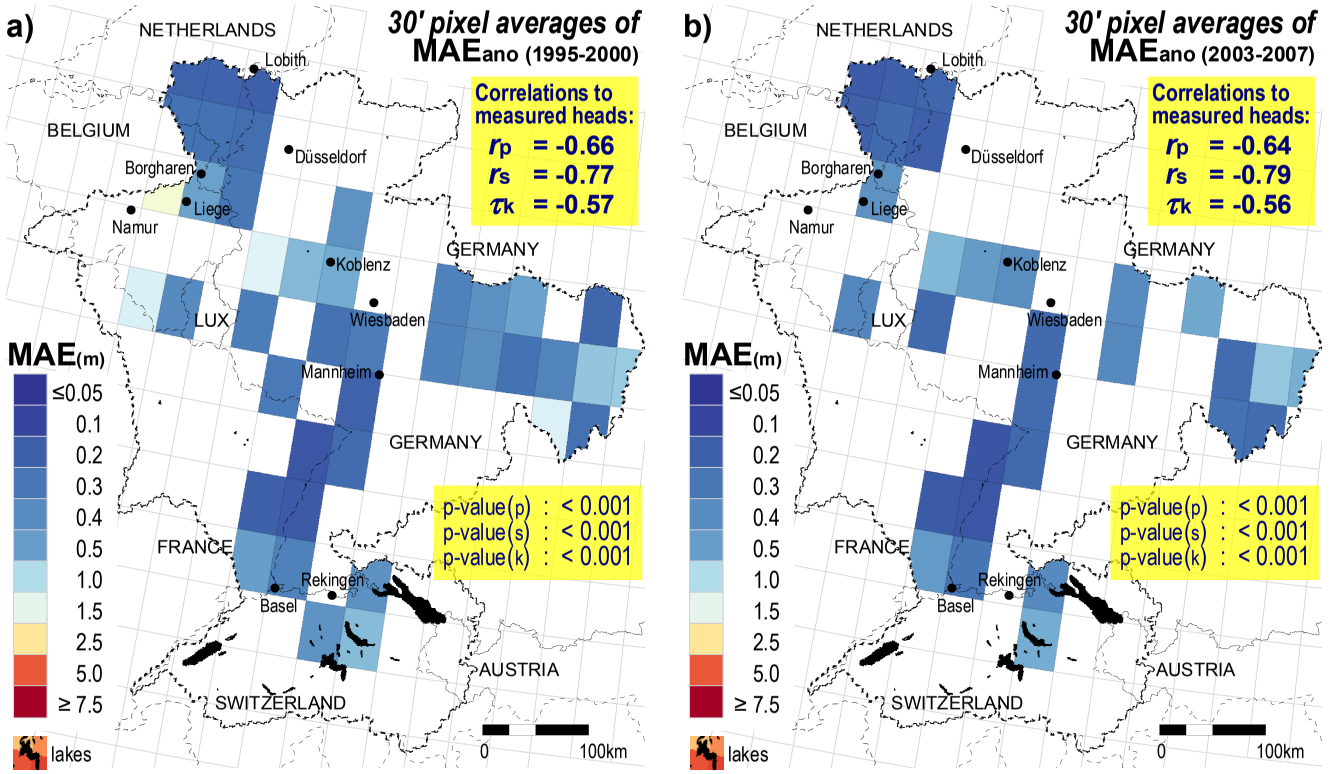

Figure 3.17 30 arc-minute pixel averages of TFN model performance measured in $\mathrm{MAE}_{\mathrm{ano}}$ (unit: m) for spatio-temporal predictions with transfer function parameters estimated using a digital elevation model: for the periods 1995-2000 (a) and 2004-2007 (b). We show only the pixel average values calculated from at least 15 point-scale values. The upper yellow boxes contain the correlation coefficients of the field values to average measured heads (Fig. 2.2a): Pearson's correlation (r_{p}), Spearman's rho (r_{s}) and Kendall's tau (τ_{k}) coefficients. The lower yellow boxes contain their corresponding p-values.

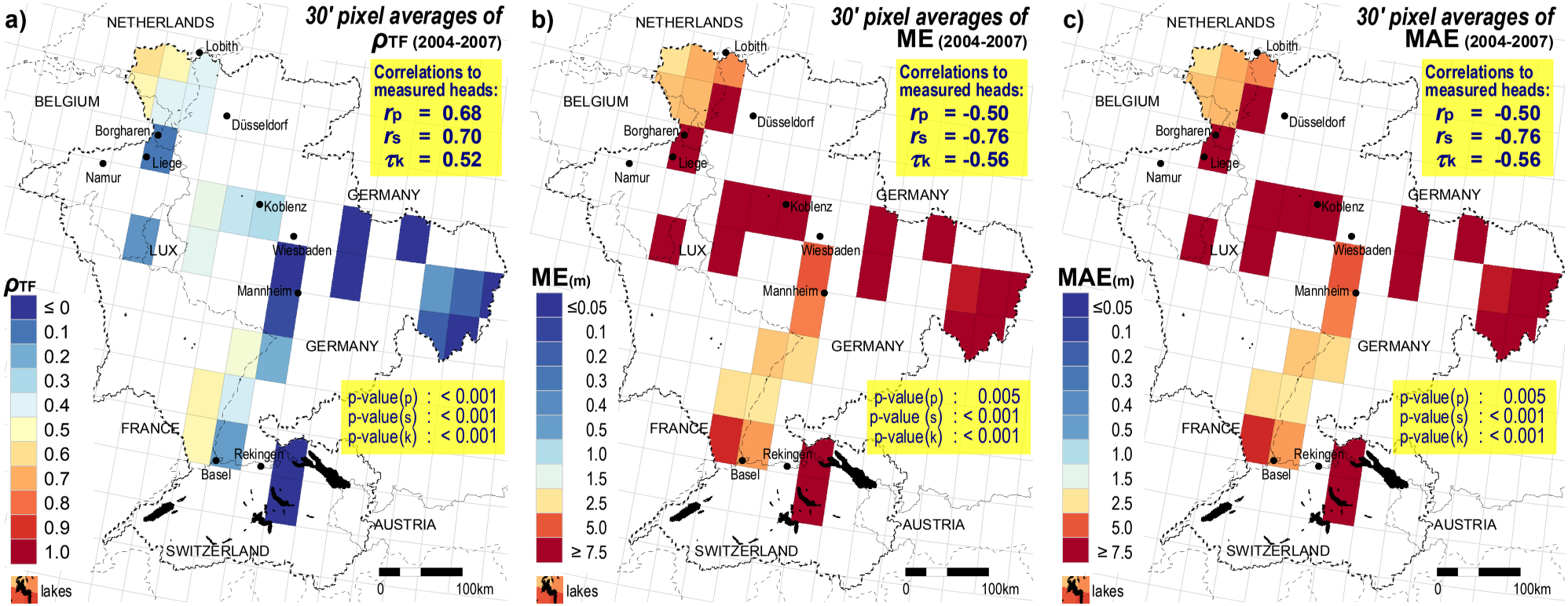

Figure 3.18 30 arc-minute pixel averages of TFN model performance measured in ρ_{TF} (a), ME (b) and MAE (c) for spatio-temporal predictions in the period 2004-2007 with transfer function parameters estimated using a digital elevation model. We show only the pixel average values calculated from at least 15 point-scale values. The upper yellow boxes contain the correlation coefficients of the field values to average measured heads (Fig. 2.2a): Pearson's correlation (r_p), Spearman's rho (r_s) and Kendall's tau (τ_k) coefficients. The lower yellow boxes contain their corresponding p-values.

show that the predictions are generally better for areas with shallow groundwater heads. The aforementioned conclusions are corroborated by the performance fields for the period 2004-2007, shown in Figs. 3.17b and 3.18a to c.

3.4 Discussion

3.4.1 Groundwater head forecasting in time

In the first exercise, we have shown that the time series of ERS SWI can be used as input for transfer function noise (TFN) models in order to make reasonably good temporal groundwater head predictions. This promising result may suggest for a further exploration to use other remotely sensed soil moisture time series, including the ones with higher temporal resolution, using a similar procedure used in this study.

Using a precipitation (excess) time series input, TFN modeling has been widely used for many purposes and applications: not only to predict groundwater heads (Bierkens et al., 2001), but also to fill in gaps of groundwater head measurement time series (Bierkens et al., 1999), to characterize groundwater regimes (van Geer and Defize, 1987) and to detect structural changes/interventions and outliers in groundwater head dynamics (Gehrels et al., 1994; Knotters and Bierkens, 2000). Based on the results of this study, we expect that ERS SWI can be used for similar purposes. It should be noted that ERS SWI time series (and other spaceborne remotely sensed soil moisture time series) offer a better spatial coverage and support than in situ observations of precipitation. Compared to TFN models using input time series of precipitation excess — i.e. the difference between precipitation and total evaporation and transpiration, a TFN model forced with with soil moisture time series may be considered more accurate since estimation of total evaporation and transpiration is unnecessary.

The TFN model with large support time series input of ERS SWI (half degree resolution) is clearly suitable for making groundwater head predictions in shallow phreatic groundwater areas where upper soil moisture fluctuations are the major cause of groundwater head fluctuations. However, the TFN model used may hardly explain groundwater head dynamics caused by local phenomena, such as anthropogenic causes (e.g. pumping operations) or nearby surface water level dynamics. Yet, if time series of such fluctuations are available, they can be incorporated in a more elaborated TFN model (e.g. van Geer and Defize, 1987; Gehrels et al., 1994; Knotters and Bierkens, 2000) in order to further improve groundwater head predictions.

Our study has not explored the possibility of using higher orders of TFN models with more parameters (i.e. longer model state and forcing input memories) that may provide even better predictions, specifically for areas where time-lags between ERS SWI_t and h_t are found in certain areas (see Chapter 2). Our study is also limited

by two relatively short periods of spaceborne soil moisture observations (1995-2000 and 2004-2007). Yet, there is a recent project, referred as Water Cycle Multimission Observation Strategy (WACMOS, `http://wacmos.itc.nl`), to set up a solid scientific basis for the creation of coherent long-term datasets of water relevant geo-information, including a harmonized soil moisture dataset from all microwave sensors. Within WACMOS, it is foreseen that a multi-decadal (more than 30 years) soil moisture dataset integrating all microwave observations that are available since 1978 will be created (see also Liu et al., 2011). If such a dataset is available, its implementation in a TFN modeling framework for relating it to groundwater head prediction will be interesting for groundwater studies.

3.4.2 Spatio-temporal prediction of groundwater head

Despite its limitations, our simple approach for generating spatio-temporal groundwater head predictions provides reasonably good results, specifically for shallow groundwater head areas. It is even capable to detect possible measurement outliers (see e.g. Fig. 3.14c and its discussion in Sect.3.3.2). Yet, clearly, there is still room for improvement in this study. For example, if available, we may include much more local information and knowledge, such as more detailed digital elevation models, more digital elevation map attributes (e.g. slopes and wetness indices) and soil types and attributes, including the high resolution ones, in order to obtain better estimates of TFN model parameters. This includes incorporating other forcing time series (e.g. surface water level time series that can solve the problem for pixels with HAND = 0). The technique used for estimating TFN model parameters can be improved as well. As an example, a geo-statistical based method, such as kriging, could be explored (see e.g. Bierkens et al., 2001, who implemented it in a regional precipitation-groundwater transfer function model).

Obviously, our approach still requires the availability of groundwater head measurement time series (although only few). Related to this issue, we suggest that future field campaigns of in-situ soil moisture observations, which will always be needed for the validation of remote sensing soil moisture observations, must be supported by groundwater head measurements. Rephrasing Becker (2006): it is a pity that there is still a lack of communication between soil moisture scientists and hydro-geologists, that is illustrated by the fact that hundreds of soil moisture samples were collected to depths of one meter during the field campaign of Soil Moisture Experiments (SMEX, `http://www.ars.usda.gov`) but depths to water table were not monitored. Another example of this schism could be illustrated from several studies using the REMEDHUS soil moisture station network (e.g. Ceballos et al., 2005; Martínez-Fernández and Ceballos, 2005) where groundwater head measurements are not mentioned. Also, the recently started project International Soil Moisture Network (Dorigo et al., 2011) does not incorporate any groundwater head measurements. If such soil moisture observations and datasets are supported by groundwater head measurements, an extension

of a remotely sensed soil moisture product to a groundwater related information is possible as shown in this study.

Although the current spatio-temporal method was not able to estimate the absolute value of groundwater heads, head variation in terms of timing and amplitude was predicted reasonably well, particularly in areas with shallow groundwater. The latter fact is particularly important when judging the suitability of remotely sensed soil moisture for groundwater assessment in ungauged or data poor groundwater basins. As GRACE is only able to detect storage change, not absolute storage (without any additional information), ERS SWI is only able to predict groundwater level variation, not its absolute level or depth either. However, ERS SWI (25-50 km) can do so at much higher resolution than GRACE (400 km). The downside of ERS SWI is that it only works for areas with shallow groundwater. If additional information about absolute groundwater heads can be derived — e.g. by occasional groundwater head observations in piezometers or by construction of a groundwater flow model based on globally available datasets on surface elevation, lithology, soil type and land use (e.g. Sutanudjaja et al., 2011) — then ERS SWI would certainly be useful to further improve model results by calibration and in an operational framework through data-assimilation. Here, GRACE and ERS SWI data are complementary. GRACE is able to inform on storage variations for the whole basin at lower resolution, whereas ERS SWI informs at higher resolution on groundwater level variations in areas with shallow groundwater, i.e. the areas where groundwater matters for the surface energy balance, agriculture and ecosystem.

3.5 Summary and conclusion

In this chapter, we used transfer function-noise models to predict groundwater heads using ERS SWI as model input. This was done in two modeling exercises. The first modeling exercise focussed on temporal forecasting of groundwater head dynamics, while the second one was to make spatio-temporal predictions of groundwater heads, including in areas where no groundwater head measurements are available. Results of both exercises are promising. The transfer function models can reproduce the observed groundwater head fluctuations reasonably well, especially in shallow groundwater areas where soil moisture dynamics are tightly connected to groundwater head fluctuations. We argue that ERS SWI products should be considered as an important source of information for the assessment of large-scale groundwater dynamics.

4 Large-scale groundwater modeling using global datasets

This chapter is based on:
Sutanudjaja, E. H., van Beek, L. P. H., de Jong, S. M., van Geer, F. C., Bierkens, M. F. P. (2011), Large-scale groundwater modeling using global datasets: a test case for the Rhine-Meuse basin, Hydrology and Earth System Sciences, 15, 2913-2935, doi:10.5194/hess-15-2913-2011.

Abstract

The current generation of large-scale hydrological models does not include a groundwater flow component. Large-scale groundwater models, involving aquifers and basins of multiple countries, are still rare mainly due to a lack of hydro-geological data which are usually only available in developed countries. In this study, we propose a novel approach to construct large-scale groundwater models by using global datasets that are readily available. As the test-bed, we use the combined Rhine-Meuse basin that contains groundwater head data used to verify the model output. We start by building a distributed land surface model (30 arc-second resolution — approximately 1 km at the equator) to estimate groundwater recharge and river discharge. Subsequently, a MODFLOW transient groundwater model is built and forced by the recharge and surface water levels calculated by the land surface model. Results are promising despite the fact that we still use an offline procedure to couple the land surface and MODFLOW groundwater models (i.e. the simulations of both models are separately performed). The simulated river discharges compare well to the observations. Moreover, based on our sensitivity analysis, in which we run several groundwater model scenarios with various hydro-geological parameter settings, we observe that the model can reasonably well reproduce the observed groundwater head time series. However, we note that there are still some limitations in the current approach, specifically because the offline-coupling technique simplifies the dynamic feedbacks between surface water levels and groundwater heads, and between soil moisture states and groundwater heads. Also the current sensitivity analysis ignores the uncertainty of the land surface model output. Despite these limitations, we argue that the results of the current model show a promise for large-scale groundwater modeling practices, including for data-poor environments and at the global scale.

4.1 Introduction

Groundwater is a vulnerable resource, and in many areas, groundwater is being consumed faster than it is being naturally replenished (e.g. Rodell et al., 2009; Wada et al., 2010). Given increased population and heightened variability and uncertainty in precipitation due to climate change, the pressure upon groundwater resources is expected to intensify. These issues make monitoring and predicting groundwater changes, especially over large areas, imperative.

Changes in groundwater resources and their causes can be inferred from groundwater models. A groundwater model has the ability to calculate and predict spatio-temporal groundwater head in a sufficiently fine resolution (e.g. 1 km resolution). However, large-scale groundwater models, especially for large aquifers and basins of multiple countries, are still rare, mainly due to lack of hydro-geological data. Some existing large-scale groundwater models, such as in the Death Valley area, USA (D'Agnese et al., 1999), and in the MIPWA region, the Netherlands (Snepvangers et al., 2008), were developed on the basis of highly detailed information (e.g. elaborate 3-D geological models). Such information may be available in developed countries but is seldom available in other parts of the world.

In this chapter, we propose a novel approach for constructing a large-scale groundwater model by using only readily available global datasets. Note that by large scale, we mean large extent area sizes, as defined by Bierkens et al. (2000), and not map scale or resolution. Here the model proposed is a MODFLOW transient groundwater model that is coupled to a distributed land surface model. The latter is used to estimate groundwater recharge and surface water levels that are used to force the groundwater model. As the test bed of this study, we use the combined Rhine-Meuse basin (total area: $\pm 200\,000$ km^2, see Figs. 2.1 and 2.2, and Sect. 2.2.1). This basin, located in Western Europe, is selected because it contains ample groundwater head data that can be used to verify the model output. However, while constructing the model, we use only globally available datasets that are listed as follows. We use the Global Land Cover Characteristics Data Base Version 2.0 (GLCC 2.0, `http://edc2.usgs.gov/glcc/globe_int.php`) and FAO soil maps (1995) in order to parameterize the land cover and upper sub-surface properties. For mapping hydro-geological features and estimating their aquifer properties, we make use of the global digital elevation model of HydroSHEDS (Lehner et al., 2008) and an estimate of groundwater depth based on a simple steady-state groundwater model (see Sect. 4.2.2). For climatological forcing, we use the global CRU datasets (Mitchell and Jones, 2005; New et al., 2002) that are combined with the ECMWF re-analysis data of ERA-40 (Uppala et al., 2005) and operational archive (`http://www.ecmwf.int/products/data/archive/descriptions/od/oper/index.html`).

The goal of this chapter is then to construct a large-scale groundwater model on the basis of readily available global datasets and to evaluate the model performance using

groundwater head observations. Here we do not intend to calibrate the model yet. Rather, we conduct a sensitivity analysis to study how changing aquifer properties influence the model outcome, specifically the resulting groundwater head time series. By this sensitivity analysis, we expect to gain insights into the model behaviour that can be used as the basis for improving the current model.

The chapter is organized as follows. In the following section, we explain the model concept and structure used in this study. Then, we present the methodology to evaluate the model outcome, including the sensitivity analysis procedure. Subsequently, the results and their analyses follow. The last part of this chapter is mainly devoted to a discussion about the prospects of large-scale groundwater assessment in data-poor environments and at the global scale, and to suggest ways to further improve this large-scale model.

4.2 Model description

4.2.1 General modeling procedure

The hydrological model developed in this study consists of two parts: (1) the land surface model (Sect. 4.2.2 and Appendix A), which conceptualizes the hydrological processes on and in the upper-soil or unsaturated-zone layer; and (2) the groundwater model (Sect. 4.2.3), which describes saturated flow in the deeper underground. The land surface model was adopted from the global hydrology model of PCR-GLOBWB (van Beek and Bierkens, 2009; van Beek et al., 2011) having two upper soil stores and a simple linear groundwater store (see Fig. 4.1a). In this study, we replaced the latter by the MODFLOW groundwater model (McDonald and Harbaugh, 1988).

We started this modeling exercise by modifying PCR-GLOBWB and performing the daily simulation of it to calculate groundwater recharge and river discharge. The river discharge was translated to monthly surface water levels by assuming channel dimensions and properties based on geomorphological relations to bankfull discharge (Lacey, 1930). These surface water levels and groundwater recharge were used to force a weekly transient groundwater model built in MODFLOW. The whole modeling procedure can be considered as an offline-coupling procedure between PCR-GLOBWB and MODFLOW because we separately and sequentially run both of them (see Fig. 4.1b). We chose this offline-coupling method to avoid expensive computational costs. This version, which takes about 1.0 h for one-year model simulation in a single PC with AMD Athlon Dual Core Processor $5200 + 2.71$ GHz 2GB RAM, is the first step into developing a fully coupled one. Using this offline-coupling version, we evaluated computational loads and identified weaknesses and possibilities in the modeling structure.

4.2.2 PCR-GLOBWB land surface model

PCR-GLOBWB (van Beek and Bierkens, 2009; van Beek et al., 2011) is a raster-based global hydrological model coded in PCRaster scripting languange (Wesseling et al., 1996). Here we briefly describe its main features and modifications implemented for the purpose of this thesis. The original PCR-GLOBWB (hereafter called as "PCR-GLOBWB-ORI") has $30' \times 30'$ cells (about 50 km at the equator), while the modified one used in this study (hereafter called as "PCR-GLOBWB-MOD") has the resolution of $30'' \times 30''$ (approximately 1 km $\times$ 1 km at the equator).

The full description of PCR-GLOBWB-MOD is provided in Appendix A, which mainly discusses the hydrological processes above and in the first two upper soil stores. These upper soil stores respectively represent the top 30 cm of soil (thickness $Z_1 \leq 30\,\text{cm}$) and the following 70 cm of soil ($Z_2 \leq 70\,\text{cm}$), in which the storages are respectively symbolized as S_1 and S_2 [L]. In both versions of PCR-GLOBWB (hereafter "PCR-GLOBWB" refers to both "PCR-GLOBWB-ORI" and "PCR-GLOBWB-MOD") the states and fluxes are calculated on a daily basis. Climate forcing data are also supplied on a daily resolution (see Appendix B about the forcing data used in this study). Following Fig. 4.1a, the specific local runoff Q_{loc} [$\text{L}\,\text{T}^{-1}$] in each land surface cell of PCR-GLOBWB consists of three components: direct runoff Q_{dr} [$\text{L}\,\text{T}^{-1}$], interflow Q_{sf} [$\text{L}\,\text{T}^{-1}$] and baseflow Q_{bf} [$\text{L}\,\text{T}^{-1}$]. Note that as the consequence of the offline-coupling procedure between the land surface model and MODFLOW, the linear reservoir concept of groundwater store (in which the storage is symbolized as S_3 [L]) is still used in PCR-GLOBWB-MOD, specifically for estimating Q_{bf}. In addition to Fig. 4.1, some tables related to the model are provided: Table 4.1 listing the model parameters, including the global datasets used to derive them; Table 4.2 listing the state and flux variables; and Table 4.3 summarizing the most important changes introduced in PCR-GLOBWB-MOD. It is important to note that contrary to a $30' \times 30'$ cell in PCR-GLOBWB-ORI, a $30'' \times 30''$ cell in PCR-GLOBWB-MOD has a uniform type of land cover, a uniform type of vegetation and a uniform type of soil. PCR-GLOBWB-MOD considers only the sub-grid elevation variability — based on the $3''$ (about 90 m at the equator) digital elevation map of HydroSHEDS (see Eq. A.9) — to estimate the fraction of saturated soil contributing to surface runoff.

As illustrated in Fig. 4.1a, besides precipitation P [$\text{L}\,\text{T}^{-1}$] and evaporation E [$\text{L}\,\text{T}^{-1}$] fluxes, important vertical fluxes are water exchanges between the stores 1 and 2, Q_{12} [$\text{L}\,\text{T}^{-1}$], and between the stores 2 and 3, Q_{23} [$\text{L}\,\text{T}^{-1}$]. Note that both Q_{12} and Q_{23} consist of downward percolation fluxes, $Q_{1\to2}$ and $Q_{2\to3}$ [$\text{L}\,\text{T}^{-1}$], and upward capillary rise fluxes, $Q_{2\to1}$ and $Q_{3\to2}$ [$\text{L}\,\text{T}^{-1}$]. However, in the current PCR-GLOBWB-MOD, to force one-way coupling from the land surface model to MODFLOW, we inactivate the upward capillary rise from the groundwater to second soil stores ($Q_{3\to2} = 0$), which is one of the limitations of the current modeling approach.

The land surface model simulation was performed for the period 1960–2008. In this study, we limited the channel discharge calculation of PCR-GLOBWB-MOD

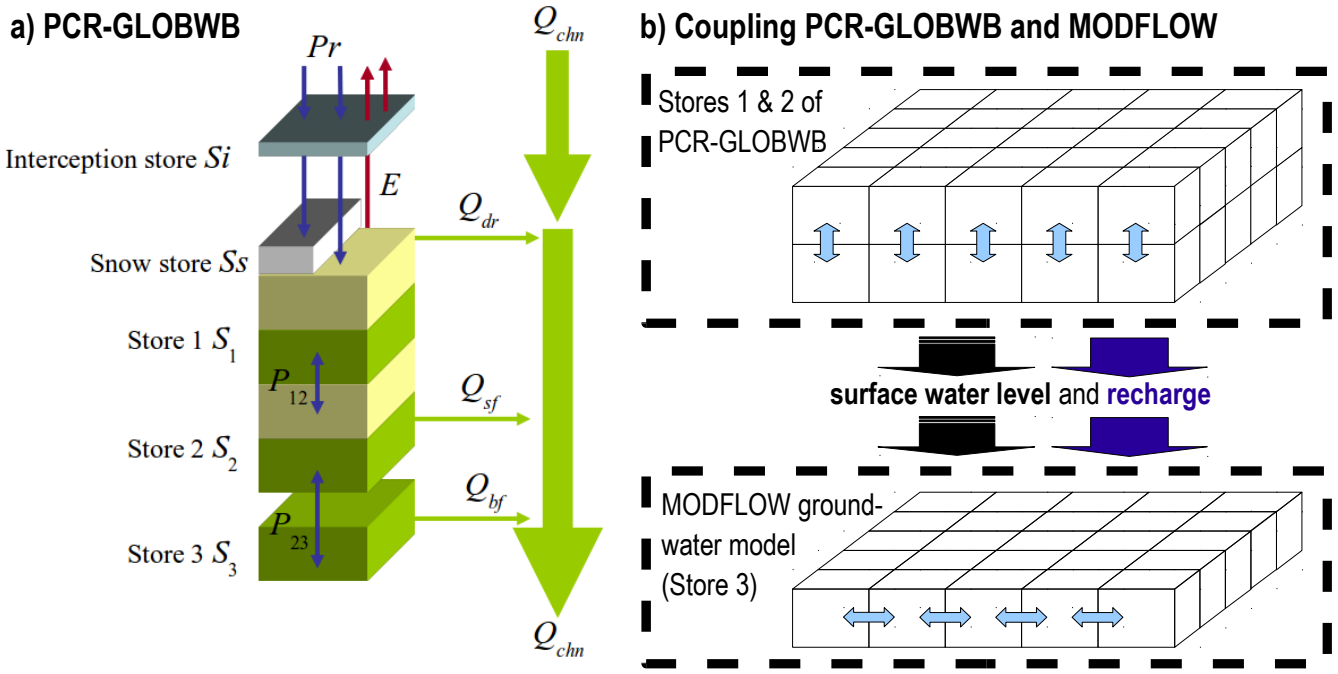

Figure 4.1 The modeling structure and strategy for this study: **(a)** the concept of the land surface model of PCR-GLOBWB (van Beek and Bierkens, 2009; van Beek et al., 2011): on the left, the soil compartment, divided in the two upper soil stores, S_1 and S_2, and the linear groundwater store, S_3, that is replaced by the MODFLOW (McDonald and Harbaugh, 1988) groundwater model; on the right, the total local gains from all cells are routed along the local drainage direction to yield the channel discharge, Q_{chn}. **(b)** The modeling strategy used to couple the PCR-GLOBWB and MODFLOW: first, we run the PCR-GLOBWB to calculate the monthly net recharge Q_{23} to groundwater store and channel discharge Q_{chn} that can be translated into surface water levels by assuming channel dimensions. Then, the monthly net recharge and surface water levels are used to force MODFLOW.

to monthly resolution. Therefore, we could neglect water residence time in channels (less than a week) and obtain monthly channel discharge time series Q_{chn} [$\text{L}^3\,\text{T}^{-1}$] by simply knowing the surface area A_{cell} [L^2] of each cell and accumulating the monthly values of the specific local runoff Q_{loc} from all cells along the drainage network.

4.2.3 Groundwater model

As mentioned earlier, a MODFLOW (McDonald and Harbaugh, 1988) based groundwater model is used to replace the groundwater store (S_3) in the land surface model. Here we built a simple MODFLOW model that considers only a single upper aquifer (see Sect. 4.2.3). The MODFLOW model was forced by the output of PCR-GLOBWB-

Table 4.1 List of model parameters used in the model.

Symbol	Description	Source or estimation method	Values	Unit
β	empirical exponent in the soil water retention curve	FAO soil map (1995)[a]	distributed	–
b	sub-grid elevation parameter	Eq. (A.9)	distributed	–
B_{chn} & D_{chn}	channel width and depths	Eqs. (4.4) and (4.5)	distributed	m
BRES	river and drainage bed resistance	Best guess estimate	1	day
$C_{\mathrm{f,min}}$ & $C_{\mathrm{f,max}}$	minimum and maximum vegetation cover fractions	GLCC 2.0 land cover map[b]	distributed	–
CFR	refreezing rate in the snow pack	Best guess estimate	0.05	day^{-1}
CRDR	river and drainage bed conductance	Eq. (4.8)	distributed	$\mathrm{m}^2\,\mathrm{day}{-1}$
CWH	liquid water holding capacity per unit snow storage Ss	Best guess estimate	0.10	–
DDF	degree-day factor in the snow pack	Best guess estimate	0.0055	$^{\circ}\mathrm{C}\,\mathrm{m}\,\mathrm{day}^{-1}$
DEM	elevation value from the digital elevation map/model	HydroSHEDS (Lehner et al., 2008)	distributed	m
f_{i}	a parameter updating $E_{\mathrm{p},0}$ after interception flux	Best guess estimate	1	–
f_{wat}	a boolean map indicating water bodies (1) or land surface cells (0)	GLCC 2.0 and levels 1 & 2 of GLWD (Lehner and Döll, 2004)	0 or 1	–
h_{veg}	vegetation height	GLCC 2.0 land cover map[c]	distributed	m
I_{nv} & I_{veg}	interception capacities per unit surface area in non vegetated and vegetated areas	Best guess estimate	0.001	m
J	groundwater recession coefficient	Eq. (A.27)	distributed	day^{-1}
Kc_{i}, Kc_{wat} & Kc_{s}	crop factors for wet interception, surface water and bare soil areas	Best guess estimate	1	–
Kc_{T}	crop factor for vegetation area based on the land cover type	Eq. (A.25)	distributed, monthly varying	–
KD	transmissivity	Best guess estimate	Sects. 4.2.3 & 4.3	$\mathrm{m}^2\,\mathrm{day}^{-1}$
$K_{\mathrm{sat},1}$ & $K_{\mathrm{sat},2}$[d]	saturated hydraulic conductivities	FAO soil map (1995)	distributed	$\mathrm{m}\,\mathrm{day}^{-1}$
L	hillslope length	DEM of HydroSHEDS	distributed	m
$\mathrm{LAI}_{\mathrm{min}}$ & $\mathrm{LAI}_{\mathrm{max}}$	minimum & maximum leaf area index	Table of Hagemann (2002)	distributed	–
n	Manning coefficient	Best guess estimate	0.045	$\mathrm{m}^{-1/3}\,\mathrm{s}$
$\psi_{50\,\%}$	soil matric suction at which transpiration is halved	Best guess estimate	3.33	m
ψ_{fc}	soil matric suction at field capacity	Best guess estimate	1	m
$\psi_{\mathrm{sat},1}$ & $\psi_{\mathrm{sat},2}$	soil matric suctions at saturation	FAO soil map (1995)	distributed	m
SC_1 & SC_2	soil water storage capacities	$(\theta_{\mathrm{sat},1}{\times}Z_1)$ & $(\theta_{\mathrm{sat},2}{\times}Z_2)$	distributed	m
RBOT & DELV	river bed and drain elevations	Sect. 4.2.3	distributed	m
Si_{max}	interception capacity	Eq. (A.1)	distributed, monthly varying	m
Sl	channel longitudinal slope	DEM of HydroSHEDS	distributed	–
Sy	aquifer specific yield or storage coefficient	Best guess estimate	Sects. 4.2.3 & 4.3	–
$\theta_{\mathrm{sat},1}$ & $\theta_{\mathrm{sat},2}$	effective soil moisture contents at saturation	FAO soil map (1995)	distributed	–
$\tan(\alpha)$	grid-average slope	DEM of HydroSHEDS	distributed	–
T_{LR}	temperature lapse rate	Best guess estimate	-0.65	$^{\circ}\mathrm{C}\,\mathrm{m}^{-1}$
W_{max}	grid-average soil storage	$SC_1 + SC_2$	distributed	m
W_{min}	grid-minimum soil storage	Best guess estimate	0	m
Z_1 & Z_2	soil thicknesses	FAO soil map (1995)	distributed	m

[a] The parameterization of FAO map (1995) based on Table of van Beek and Bierkens (2009).
[b] The parameterization of GLCC 2.0 land cover map based on Table of Hagemann (2002).
[c] The parameterization of the vegetation height h_{veg} based on Table of van Beek (2008).
[d] The subscripts 1 and 2 indicate the first and second soil stores.

Table 4.2 List of state and flux variables defined in the model.

Symbol	Description	Unit
d_{gw}	groundwater depth, difference between surface level elevation and groundwater head $= \mathrm{DEM} - h$	m
E_{i}	evaporation flux from the intercepted water	m day^{-1}
$E_{\mathrm{p,0}}$	reference potential evaporation energy (forcing data)	m day^{-1}
$E_{\mathrm{p,i}}$	potential evaporation energy for wet interception areas	m day^{-1}
$E_{\mathrm{p,s}}$	potential evaporation energy for bare soil areas	m day^{-1}
Es	total soil evaporation $= Es_1 + Es_{\mathrm{sl}}$	m day^{-1}
Es_1	soil evaporation from the first soil store	m day^{-1}
Es_{sl}	soil evaporation from the melt water store in the snow pack	m day^{-1}
E_{wat}	surface water evaporation	m day^{-1}
h	groundwater head	m
HRIV	monthly surface water levels/elevations	m
$K_1(s_1)$ & $K_2(s_2)$	hydraulic conductivities at specific degree of saturations s_1 and s_2*	m day^{-1}
$\psi_1(s_1)$ & $\psi_2(s_2)$	soil matric suctions (at specific degree of saturations s_1 and s_2)	m
P	total precipitation (forcing data)	m day^{-1}
P_{01}	infiltration flux to the first soil layer	m day^{-1}
P_{n}	net precipitation flux transferred to the soil	m day^{-1}
P_{rain}	liquid rainfall flux	m day^{-1}
Q_{12} & Q_{23}	net fluxes from the first to second soil stores: $Q_{12} = Q_{1\to2} - Q_{2\to1}$; and from the second soil to groundwater stores: $Q_{23} = Q_{2\to3} - Q_{3\to2}$	m day^{-1}
$Q_{1\to2}$ & $Q_{2\to3}$	downward components of percolation fluxes, from the first to second soil stores and from the second to groundwater stores	m day^{-1}
$Q_{2\to1}$ & $Q_{3\to2}$	upward seepage (capillary rise) fluxes, from the second to first soil stores and from the third groundwater to second stores. For this study, the latter is inactivated ($Q_{3\to2} = 0$).	m day^{-1}
Q_{bf}	baseflow	m day^{-1}
Q_{chn}	monthly average discharge from the land surface model output	m^3 s^{-1}
Q_{dr}	direct runoff	m day^{-1}
Q_{loc}	total local runoff from a land surface cell	m day^{-1}
Q_{sf}	interflow or shallow sub-surface flow	m day^{-1}
Q_{tot}	total local runoff expressed as a fluid volume per unit time	m^3 day^{-1} or m^3 s^{-1}
Q_{wat}	change in surface water storage	m day^{-1}
s_1 & s_2	degrees of saturation (S_1/SC_1 and S_2/SC_2)	–
S_1 & S_2	upper soil storages (first and second soil storages)	m
S_3	groundwater storage	m
Si	interception storage	m
Sn	snow flux	m day^{-1}
Ss	snow storage	m
Ss_{sl}	melt water storage in the snow pack	m
t & Δt	time and timestep	day
Ta	atmospheric temperature (forcing data)	K or °C
W_{act}	grid-average actual soil storage (Improved Arno Scheme) $= S_1 + S_2$	m
x	fraction of saturated soil	–

* The subscripts 1 and 2 indicate the first and second soil stores.

Table 4.3 Important changes in PCR-GLOBWB-MOD (compared to PCR-GLOBWB-ORI).

Item	Parameters or variables	PCR-GLOBWB-ORI	PCR-GLOBWB-MOD	Explanations of change
Cell size	-	$30' \times 30'$	$30'' \times 30''$	A fine resolution is needed to provide groundwater head fields.
Sub-grid variabilities	-	Considering variations of of elevation, land cover vegetation and soil.	Only sub-grid elevation variation is considered.	Variations of land cover, soil and vegetation are less important for a $30''$ cell.
Improved Arno Scheme	$W_{\min}$	$W_{\min} \geq 0$	$W_{\min} = 0$	$W_{\min}$ is less important for a $30''$ cell.
Interception	f_{i}, I_{nv} and I_{veg}	Only I_{veg} is used.	I_{nv} and f_{i} are introduced.	A broader definition is used in PCR-GLOBWB-MOD (see Sect. A.1).
Discharge routing	Q_{chn}	Using the kinematic wave method, daily Q_{chn} can be obtained.	We limit the discharge Q_{chn} analyses to monthly resolution.	Expensive computational cost needed by the kinematic wave method.
Capillary rise from groundwater to soil stores	$Q_{3\to2}$	$Q_{3\to2} \geq 0$	$Q_{3\to2} = 0$	One-way (offline) coupling between the land surface model and MODFLOW.

MOD, particularly the monthly recharge Q_{23} (see Sect. 4.2.3) and the monthly channel discharge Q_{chn} that is beforehand translated to surface water levels (see Sect. 4.2.3). We performed groundwater flow simulation for the period 1965–2008 using a weekly time step and monthly stress period, within which specific groundwater recharge and surface water levels are constant. Note that as there are no readily available global datasets about groundwater extraction by pumping, we did not include groundwater abstraction in our model yet.

Aquifer properties

To characterize the properties of the aquifer, we initially turned to two maps: (1) the global lithological map of Dürr et al. (2005) and (2) the UNESCO international hydrogeological map of Europe (`http://www.bgr.de/app/fishy/ihme1500/`). However, both maps are imprecise at $30''$ resolution employed here. The locality of units of the first map is not accurate, particularly after being checked with the $30''$ digital elevation map of HydroSHEDS that we used. For example, we found that the position of the Upper Rhine Graben area, a large and important groundwater body located in the

central part of the study area, is inaccurate. Moreover, the first map does not include small aquifer features that are often located surrounding rivers in narrow valleys. Although the second map includes these small aquifer features, it is as yet only a scanned map (not a digital one) with all its geocoding problems.

To overcome these difficulties, we developed a procedure that classifies the model area to shallow permeable sedimentary basin aquifers and deep less permeable mountainous aquifers. Briefly stated, the method uses a steady-state groundwater model to calculate steady-state groundwater heads, a digital elevation map (DEM) to estimate groundwater depths and a drainage direction map (LDD) to incorporate the influence of river networks, that are closely related to the occurrence of groundwater bodies in their surroundings. The method is summarized as follows:

1. First, for the entire model area, we assumed a set of uniform aquifer properties, transmissivity $KD = 100\,\mathrm{m^2\,day^{-1}}$ and specific yield $Sy = 0.25$, specifically for calculating the groundwater recession coefficient J in Eq. (A.28) of the land surface model.

2. Next, we ran the PCR-GLOBWB-MOD land surface model for a long period (1960–2008).

3. Subsequently, using the output of step 2, the long-term average recharge and discharge fields were calculated. The latter was translated to a surface water level field by using a relation between discharge and channel dimensions (see Sect. 4.2.3).

4. The average water level and discharge fields derived in the step 3 were used to force the groundwater model in order to estimate a field of steady-state groundwater head. Furthermore, using the $\mathrm{DEM}_{30''}$ [L] (where the subscript $30''$ indicates the spatial resolution), we could derive a steady-state field of "groundwater depth" d_{gw} [L], which is the difference between the surface level elevation and the calculated steady-state groundwater head.

5. We assumed that cells with steady-state groundwater depths d_{gw} of less than 25 m have productive aquifers. These shallow groundwater cells, located in valleys, were classified as the "sedimentary pocket/basin" cells that most likely contain permeable materials and productive groundwater bodies. To avoid the occurrence of isolated cells due to errors and limitations in the $\mathrm{DEM}_{30''}$ (such as "blocked" rivers in narrow valleys or gorges), we used the $\mathrm{LDD}_{30''}$ to assure that downstream cells of a sedimentary basin cell are also classified as sedimentary basin cells. Moreover, because MODFLOW uses a discretization that does not allow diagonal flow across the corners (see e.g. Wolf et al., 2008), we made sure that a sedimentary basin cell must have at least one neighbor in its left, right, upper, or lower extents. This is done in order to ensure the flow connectivity among the cells.

6. The remaining cells were subsequently classified as "mountainous area" cells, where groundwater bodies are most likely located at greater depths. Note that here we mean real groundwater bodies, not perched groundwater storage in regolith, which is modeled in the interflow module of the land surface model (see Sect. A.5).

7. For the sedimentary basin class, we assigned the relatively high values of transmissivity ($KD = 100\,\mathrm{m^2\,day^{-1}}$) and storage coefficient that is equal to the aquifer specific yield or ($Sy = 0.25$, see the following paragraph for further explanation). The relatively low values of transmissivity and storage coefficient are assigned for the mountainous area class ($KD = 25\,\mathrm{m^2\,day^{-1}}$ and $Sy = 0.02$).

8. Using the aquifer properties defined in the step 7, we repeated steps 2–7 to approximate the steady-state groundwater depth (shown in Fig. 4.2) and to subsequently define the final classification map – that was verified with the UNESCO international hydro-geological map of Europe (`http://www.bgr.de/app/fishy/ihme1500/`) – and its KD and Sy fields.

The fields of KD and Sy were stored in the "Block-Centered Flow" (BCF) package of MODFLOW (see McDonald and Harbaugh, 1988, Chapter 5). Here we defined a single aquifer layer, in which two conditions apply throughout the simulation:

1. The transmissivity KD is constant in time, independent of the actual thickness of the water table or the saturated zone. This condition is suitable for our model as groundwater head fluctuation is mostly expected to be only a small fraction of the thickness of the single aquifer layer defined in the model. This condition also implies that our MODFLOW cells are never 'dry' (i.e. the simulated groundwater heads never fall below the aquifer bottom elevation).

2. Sy is defined as the storage coefficient that remains constant in time (ignoring the fact that there might be a "transition" from a "confined groundwater" situation to a "phreatic water table" situation, or vice versa). Here we ignore the presence of confining layer and assume a phreatic groundwater throughout the simulation.

The main advantage of using this layer type is that it makes the MODFLOW iterative solver quickly converge throughout the simulation. Moreover, it circumvents the problem of having to define the aquifer top and bottom elevations, the information that is not globally available.

Attention is needed to convert the storage coefficient Sy for the variable $30'' \times 30''$ grid-size cells before using them in MODFLOW as MODFLOW normally uses a rectangular discretization with appropriate unit lengths (e.g. m). In the MODFLOW BCF package, the input values of Sy are commonly multiplied by the cell areas to

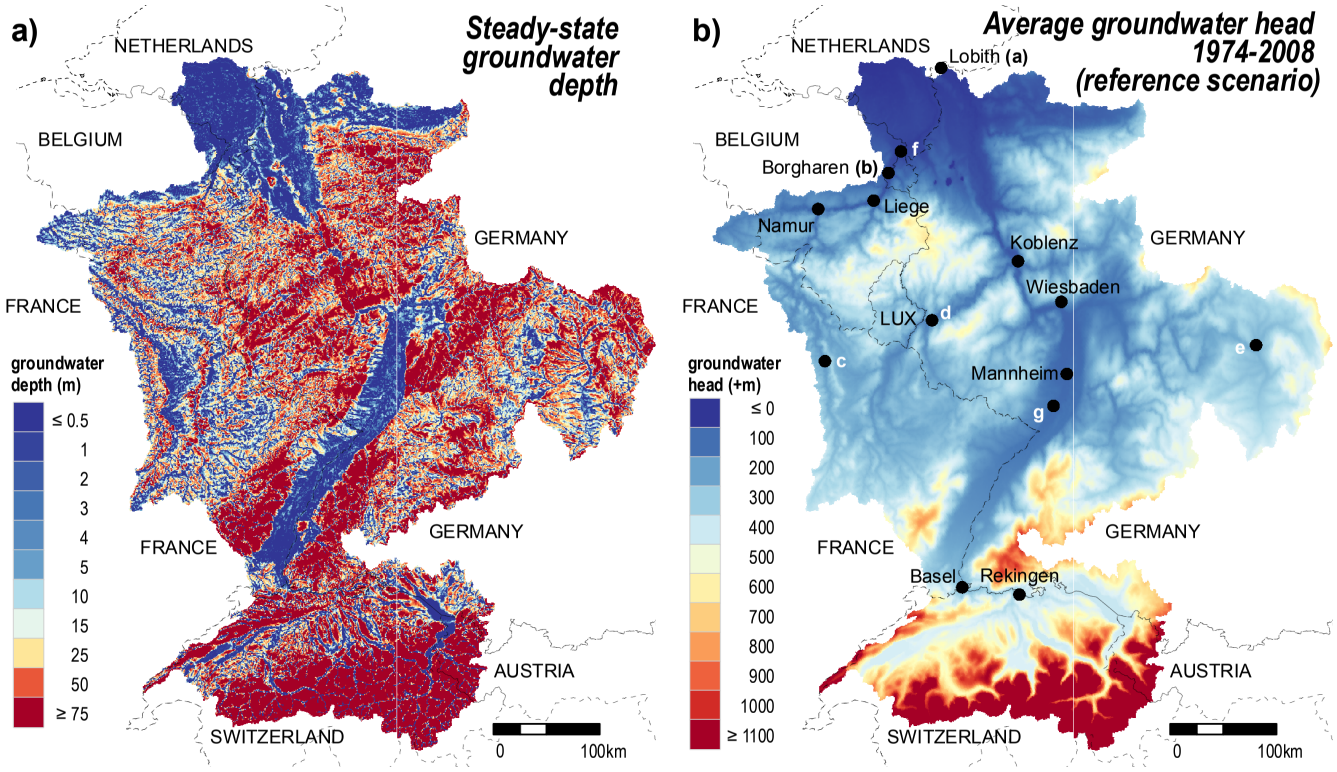

Figure 4.2 On the left (a): The approximate steady-state groundwater depth map that is used for aquifer classification. Here, we classified cells that have groundwater depth below 25 ,m and their downstream cells as the "sedimentary basin", where shallow productive aquifer pockets are usually located. Moreover, we also made sure that a sedimentary basin cell must have at least one neighboring cell in its left, right, upper, or lower extents. The remaining cells were classified as "mountainous areas", where groundwater depths are large (see Sect. 4.2.3). On the right (b): The average calculated groundwater head for the period 1974–2008, based on the reference scenario A01.0_B01.0. The alphabetical codes shown on the maps indicate the station locations for graphs in Fig. 4.3.

create so-called "storage capacities" (SC_{MF}, unit: m^2) that are used for the calculation (see McDonald and Harbaugh, 1988, Chapter 5, pages 5–24 and 5–25). The MODFLOW groundwater model that we built has the same resolution as the land surface model: $30'' \times 30''$. It means that our MODFLOW cells, which are not rectangular, have inappropriate length units and varying surface areas A_{cell} (m^2). Given this fact, we have to modify the input of Sy so that SC_{MF} has correct values and units:

$$Sy_{\mathrm{inp}} \;=\; Sy_{\mathrm{act}} \;\times\; \frac{A_{\mathrm{cell}}}{A_{\mathrm{MF}}} \tag{4.1}$$

where Sy_{inp} is the input supplied to the BCF package of MODFLOW, Sy_{act} is the actual storage coefficient and A_{MF} is the 'apparent' MODFLOW cell dimension, which is $30'' \times 30''$. Using these Sy_{inp} input values, the values of SC_{MF} (internally multiplied by A_{MF} in the BCF package) are:

$$\begin{aligned} SC_{\mathrm{MF}} \;=\; Sy_{\mathrm{inp}} \;\times\; A_{\mathrm{MF}} \;&=\; Sy_{\mathrm{act}} \;\times\; \frac{A_{\mathrm{cell}}}{A_{\mathrm{MF}}} \;\times\; A_{\mathrm{MF}} \\ &=\; Sy_{\mathrm{act}} \;\times\; A_{\mathrm{cell}} \end{aligned} \tag{4.2}$$

Note that the transmissivities KD ($\mathrm{m}^2\,\mathrm{day}^{-1}$) are not modified because the algorithm in the BCF package of MODFLOW never multiplies KD with the MODFLOW cell areas. However, to account for the difference between actual cell length and width (unit: m), an anisotropy factor can be introduced.

Boundary conditions and recharge

No-flow boundaries were assumed at the boundaries surrounding the basin, thus assuming that topographic and groundwater divides coincide. For the "large lakes" (see Fig. 1.1 for their locations), we assumed fixed-head boundary conditions, keeping water levels constant for the entire simulation period. Here we define "large lakes" by selecting, from the derived surface water body f_{wat} map (see Sect. A.8), only the lakes that have surface areas at least five times of $30'' \times 30''$ grid-cell. For each of those lakes, constant water levels are assumed based on the $\mathrm{DEM}_{30''}$ of HydroSHEDS.

The monthly time series of groundwater recharge Q_{23} obtained from the land surface model of PCR-GLOBWB-MOD were fed to the "Recharge" (RCH) package of MODFLOW. The actual unit of Q_{23} is $\mathrm{m\,day}^{-1}$. In the RCH package calculation, the input values of recharge are multiplied by the MODFLOW cell dimension so that they are expressed in a volume per unit time (see McDonald and Harbaugh, 1988, Chapter 7), which is $\mathrm{m}^3\,\mathrm{day}^{-1}$ in our case. Because our MODFLOW cell dimension is $30'' \times 30''$ (A_{MF}), the input of Q_{23} must be modified as follows:

$$Q_{23,\mathrm{inp}} \;=\; Q_{23,\mathrm{act}} \;\times\; \frac{A_{\mathrm{cell}}}{A_{\mathrm{MF}}} \tag{4.3}$$

where $Q_{23,\mathrm{inp}}$ is the input introduced to the RCH package of MODFLOW and $Q_{23,\mathrm{act}}$ is the actual recharge from the land surface model output (unit: $\mathrm{m\,day}^{-1}$).

Channel dimensions and surface water levels

We used the "RIVER" (RIV) and "DRAIN" (DRN) packages of MODFLOW to accommodate (offline) interaction between groundwater bodies and surface water networks. This interaction is governed by actual groundwater heads and surface water levels. The latter can be translated from the monthly discharge Q_{chn} by using assumed channel properties: the channel width B_{chn} [L], channel depth D_{chn} [L], Manning roughness coefficient n [$\text{L}^{-1/3}\,\text{T}$], and channel longitudinal slope Sl [−].

B_{chn} is derived using the formula of Lacey (1930) who postulated that the width of a natural channel at bankfull flow is proportional to the root of the discharge:

$$B_{\text{chn}} \;\approx\; P_{\text{bkfl}} \;=\; 4.8 \;\times\; Q_{\text{bkfl}}^{0.5} \tag{4.4}$$

where P_{bkfl} (unit: m) and Q_{bkfl} ($\text{m}^3\,\text{s}^{-1}$) are the wetted perimeter and flow at the bankfull condition, and 4.8 is a factor with unit $\text{s}^{0.5}\,\text{m}^{-0.5}$ (see Savenije, 2003). In large natural alluvial rivers, P_{bkfl} is slightly larger than B_{chn}. To calculate Q_{bkfl}, which, as a rule of thumb, occurs on average once every 1.5 yr, we used the monthly time series of Q_{chn} calculated from the land surface model.

D_{chn} is derived by combining the Lacey's formula with Manning's formula (Manning, 1891) and assuming a rectangular channel shape:

$$D_{\text{chn}} \;=\; \left(\frac{n \;\times\; Q_{\text{bkfl}}^{0.5}}{4.8 \;\times\; Sl^{0.5}}\right)^{3/5} \tag{4.5}$$

By subtracting D_{chn} from $\text{DEM}_{30''}$, we may estimate the channel or river bed elevation, RBOT. However, due to errors in $\text{DEM}_{30''}$, a few of pixels may have unrealistic RBOT elevations. Here we implemented median filters with various window sizes to smooth the longitudinal profile of RBOT.

Given the channel properties, RBOT, n, B_{chn} and Sl, the monthly water levels HRIV can be translated from the monthly discharge Q_{chn} by means of Manning's formula:

$$\text{HRIV} \;=\; \text{RBOT} \;+\; \left(\frac{n \;\times\; Q_{\text{chn}}}{B_{\text{chn}} \;\times\; Sl^{0.5}}\right)^{3/5} \tag{4.6}$$

RBOT and monthly HRIV are used as the input for the RIV package, the principle of which is:

$$\text{QRIV} \;=\; \begin{cases} \text{CRDR} \;\times\; (\text{HRIV} \;-\; h) & \text{if} \quad h \;>\; \text{RBOT} \\ \text{CRDR} \;\times\; (\text{HRIV} \;-\; \text{RBOT}) & \text{if} \quad h \;\leq\; \text{RBOT} \end{cases} \tag{4.7}$$

where QRIV [$\text{L}^3\,\text{T}^{-1}$] is the flow between the stream and aquifer, taken as positive if it is directed into the aquifer, h is the groundwater head, and CRDR [$\text{L}^2\,\text{T}^{-1}$] is the estimated river conductance:

$$\text{CRDR} \;=\; \frac{1}{\text{BRES}} \;\times\; P_{\text{chn}} \;\times\; L_{\text{chn}} \tag{4.8}$$

where BRES [T] is the bed resistance (taken as 1 day), P_{chn} [L] is the channel wetted perimeter (approximated by B_{chn}) and L_{chn} [L] is the channel length (approximated by the cell diagonal length).

The RIV package is defined only in cells with $B_{\text{chn}} \geq 2\,\text{m}$. To simulate smaller drainage elements, the DRN package is defined for all cells without RIV package:

$$\text{QDRN} = \begin{cases} \text{CRDR} \times (h - \text{DELV}) & \text{if } h > \text{DELV} \\ 0 & \text{if } h \leq \text{DELV} \end{cases} \tag{4.9}$$

where QDRN [$\text{L}^3\,\text{T}^{-1}$] is the flow between the drainage network and stream and DELV is the median drain elevation, which is assumed to be located half meter below the surface elevation $\text{DEM}_{30''}$.

4.3 Sensitivity analysis of aquifer properties

In groundwater modeling, the transmissivity KD and storage coefficient Sy are important parameters which are also subject to large uncertainty. In this chapter, which may be considered as our first attempt to model groundwater at a large scale, we did not perform a full calibration yet. However, we did investigate the sensitivity of the model outcome to changing aquifer properties. The list of the scenarios that we simulated is given in Table 4.4, in which the reference scenario has $KD_{\text{ref},1} = 100\,\text{m}^2\,\text{day}^{-1}$ and $Sy_{\text{ref},1} = 0.25$ for sedimentary basins and $KD_{\text{ref},2} = 25\,\text{m}^2\,\text{day}^{-1}$ and $Sy_{\text{ref},2} = 0.02$ for mountainous area class. The others have different aquifer properties. For example, the scenario "A02.0_B00.5" has transmissivities $2 \times KD_{\text{ref}}$ and storage coefficients $0.5 \times Sy_{\text{ref}}$.

For the sake of simplicity, we used only one fixed output from the land surface model for all scenarios. The monthly recharge Q_{23} and surface water level HRIV time series fields are the same for all scenarios. To verify the land surface model output, we first compared the modeled discharge in two stations: Lobith and Borgharen, located in the downstream parts of Rhine and Meuse, respectively. Note that the baseflow component of the modeled discharge evaluated here is Q_{bf} from the groundwater linear reservoir of the land surface model (Eq. (A.27)), not $-(\text{QRIV} + \text{QDRN})$ from the MODFLOW model (Eqs. (4.7) and (4.9)). In other words, although they are by definition the same, we ignored the discrepancies between the baseflow values of the land surface and groundwater models.

For each scenario, the simulated groundwater levels or heads h^{md} are compared to the piezometer data h^{dt}. We have collected more than 30 000 sets of head time series from several institutions in the Netherlands, Belgium, France, Germany and Switzerland and some individual partners. For model evaluation, we selected a subset of over about 6000 time series which are relatively recent (after 1979) and long records exceeding five years that contain seasonal variations (i.e there is at least a measurement

Table 4.4 List of the sensitivity analysis scenarios including their performance indicators presented in basin-scale average values.

Scenarios	KD	Sy	R_{cor}	QRE_{7525}
A00.5_B00.1	$0.5 \times KD_{\mathrm{ref}}$	$0.1 \times Sy_{\mathrm{ref}}$	NA	NA
A00.5_B00.2	$0.5 \times KD_{\mathrm{ref}}$	$0.2 \times Sy_{\mathrm{ref}}$	NA	NA
A00.5_B00.3	$0.5 \times KD_{\mathrm{ref}}$	$0.3 \times Sy_{\mathrm{ref}}$	0.42	254 %
A00.5_B00.5	$0.5 \times KD_{\mathrm{ref}}$	$0.5 \times Sy_{\mathrm{ref}}$	0.40	190 %
A00.5_B01.0	$0.5 \times KD_{\mathrm{ref}}$	$1 \times Sy_{\mathrm{ref}}$	0.36	133 %
A00.5_B02.0	$0.5 \times KD_{\mathrm{ref}}$	$2 \times Sy_{\mathrm{ref}}$	0.33	103 %
A01.0_B00.1	$1 \times KD_{\mathrm{ref}}$	$0.1 \times Sy_{\mathrm{ref}}$	NA	NA
A01.0_B00.2	$1 \times KD_{\mathrm{ref}}$	$0.2 \times Sy_{\mathrm{ref}}$	0.43	352 %
A01.0_B00.3	$1 \times KD_{\mathrm{ref}}$	$0.3 \times Sy_{\mathrm{ref}}$	0.42	276 %
A01.0_B00.5	$1 \times KD_{\mathrm{ref}}$	$0.5 \times Sy_{\mathrm{ref}}$	0.40	203 %
A01.0_B01.0*	$1 \times KD_{\mathrm{ref}}$	$1 \times Sy_{\mathrm{ref}}$	0.36	138 %
A01.0_B02.0	$1 \times KD_{\mathrm{ref}}$	$2 \times Sy_{\mathrm{ref}}$	0.32	103 %
A02.0_B00.1	$2 \times KD_{\mathrm{ref}}$	$0.1 \times Sy_{\mathrm{ref}}$	NA	NA
A02.0_B00.2	$2 \times KD_{\mathrm{ref}}$	$0.2 \times Sy_{\mathrm{ref}}$	0.43	339 %
A02.0_B00.3	$2 \times KD_{\mathrm{ref}}$	$0.3 \times Sy_{\mathrm{ref}}$	0.42	261 %
A02.0_B00.5	$2 \times KD_{\mathrm{ref}}$	$0.5 \times Sy_{\mathrm{ref}}$	0.40	188 %
A02.0_B01.0	$2 \times KD_{\mathrm{ref}}$	$1 \times Sy_{\mathrm{ref}}$	0.36	128 %
A02.0_B02.0	$2 \times KD_{\mathrm{ref}}$	$2 \times Sy_{\mathrm{ref}}$	0.32	98 %
A05.0_B00.1	$5 \times KD_{\mathrm{ref}}$	$0.1 \times Sy_{\mathrm{ref}}$	0.43	472 %
A05.0_B00.2	$5 \times KD_{\mathrm{ref}}$	$0.2 \times Sy_{\mathrm{ref}}$	0.43	313 %
A05.0_B00.3	$5 \times KD_{\mathrm{ref}}$	$0.3 \times Sy_{\mathrm{ref}}$	0.42	242 %
A05.0_B00.5	$5 \times KD_{\mathrm{ref}}$	$0.5 \times Sy_{\mathrm{ref}}$	0.40	176 %
A05.0_B01.0	$5 \times KD_{\mathrm{ref}}$	$1 \times Sy_{\mathrm{ref}}$	0.36	116 %
A05.0_B02.0	$5 \times KD_{\mathrm{ref}}$	$2 \times Sy_{\mathrm{ref}}$	0.32	89 %
A10.0_B00.1	$10 \times KD_{\mathrm{ref}}$	$0.1 \times Sy_{\mathrm{ref}}$	0.43	437 %
A10.0_B00.2	$10 \times KD_{\mathrm{ref}}$	$0.2 \times Sy_{\mathrm{ref}}$	0.42	291 %
A10.0_B00.3	$10 \times KD_{\mathrm{ref}}$	$0.3 \times Sy_{\mathrm{ref}}$	0.41	222 %
A10.0_B00.5	$10 \times KD_{\mathrm{ref}}$	$0.5 \times Sy_{\mathrm{ref}}$	0.40	160 %
A10.0_B01.0	$10 \times KD_{\mathrm{ref}}$	$1 \times Sy_{\mathrm{ref}}$	0.37	110 %
A10.0_B02.0	$10 \times KD_{\mathrm{ref}}$	$2 \times Sy_{\mathrm{ref}}$	0.33	84 %

* The scenario A01.0_B01.0 is the reference scenario.
NA indicates the scenarios that failed to converge, specifically the ones with low KD and low Sy.
KD: aquifer transmissivities; Sy: specific yields or storage coefficients;
R_{cor}: cross-correlation coefficients between calculated and measured groundwater head time series;
QRE_{7525}: the relative error of inter-quantile range of the calculated head time series (see Eq. 4.10).

datum for each season: winter, spring, summer and autumn). Moreover, based on the information from the data suppliers, we only selected the time series belonging to the top aquifer. Figure 4.5a shows the selected measurement station locations. Note that for stations located in the same pixel, we did not upscale them to the pixel resolution because they usually have different time spans. It means that all measurements are at the point scale, not at the $30'' \times 30''$ as the model resolution, and our evaluation is therefore on the conservative side because of lack of scale adjustment.

To verify the model performance of each scenario, specifically in every measurement station, we compared and evaluated modeled and observed head time series using several measures. First, we calculated the bias between both mean values, $\left[\bar{h}^{\mathrm{md}} - \bar{h}^{\mathrm{dt}}\right]$, and the bias between both median values, $\left[h_{50}^{\mathrm{md}} - h_{50}^{\mathrm{dt}}\right]$. Also, we calculated the cross-correlation coefficient R_{cor} between the model results and measurement data. The latter performance indicator — calculated without considering any lags — evaluates the timing of modeled time series to measurement time series. Finally, to evaluate the time series amplitude, we calculated the (relative) inter-quantile range error, QRE_{7525}:

$$\mathrm{QRE}_{7525} = \frac{\mathrm{IQ}_{7525}^{\mathrm{md}} - \mathrm{IQ}_{7525}^{\mathrm{dt}}}{\mathrm{IQ}_{7525}^{\mathrm{dt}}} \tag{4.10}$$

where $\mathrm{IQ}_{7525}^{\mathrm{md}}$ and $\mathrm{IQ}_{7525}^{\mathrm{dt}}$ are the inter-quantile ranges of the model result and measurement data time series. While evaluating mean and median biases, cross-correlations and inter-quantile range errors, we only used dates for which measurement data exist.

With so many observation points used (> 6000 points), we decided to analyze all performance indicators (biases, cross-correlations and inter-quantile range errors) at the sub-basin scale. We sub-divided the model areas into several sub-basins, by using the local drainage direction map. Then, in each sub-basin, we calculated the sub-basin averages of $\left|\bar{h}^{\mathrm{md}} - \bar{h}^{\mathrm{dt}}\right|$, $\left|h_{50}^{\mathrm{md}} - h_{50}^{\mathrm{dt}}\right|$, R_{cor} and $|\mathrm{QRE}_{7525}|$.

4.4 Results

Figure 4.3a and 4.3b show the river discharges calculated by the land surface model and the measurement data in two locations, in Lobith (downstream of Rhine) and Borgharen (Meuse), both are in the Netherlands. The figures show that the discharge can be reasonably simulated by the model, except the summer discharge in Borgharen which is generally overestimated. This overestimation can be explained by the fact that our model did not include water extraction in Monsin, located about 25 km upstream of Borgharen. In Monsin, especially during the summer, some water from the Meuse River is diverted to sustain the navigation function of the Scheldt River, which is located outside the Rhine-Meuse basin (de Wit, 2001).

Some examples of comparison of simulated head time series to measurement data are presented in Fig. 4.3c–4.3g. Here, instead of plotting actual head h^{md} and h^{dt} values,

we plotted the model results and measurement data in their anomalies related to their mean values, $\bar{h}^{\mathrm{md}}$ and $\bar{h}^{\mathrm{dt}}$. Note that, while calculating $\bar{h}^{\mathrm{md}}$ and $\bar{h}^{\mathrm{dt}}$, we only used the dates for which measurement data exist. For the examples shown in Fig. 4.3c–4.3g, we can conclude that the model is able to capture both the timing and the amplitude of observed heads quite well.

An alternative straightforward way to evaluate the model outcome is by making scatter-plots between both mean values, $\bar{h}^{\mathrm{dt}}$ and $\bar{h}^{\mathrm{md}}$ – as shown in Fig. 4.4a, and between both medians, h_{50}^{dt} and h_{50}^{md} – as shown in Fig. 4.4b. From both scatter-plots, we see that model result average and median values correlate very well to measurement data average and median values. However, these scatter-plots do not provide information about the spatial distribution of the biases between the model results and measurement data. Moreover, such scatter-plots are pre-dominantly influenced to areas with high densities in measurement stations, which are mainly in the lowland and valley areas of the basins. Also, some data suppliers supplied enormous number of data, while others supplied only few points (see Fig. 4.5a). Areas with sparse measurement stations may not be well-represented in the scatter-plots.

Moreover, the scatter-plots in Fig. 4.4 — especially their calculated correlation coefficients between observed and modeled time series (R = 0.9962) — should be carefully interpreted because the absolute values of groundwater head time series are strongly influenced by the surface elevation of the study area (including its range and variation). Here, analyzing the biases between observed and modeled head time series is preferred than the scatter-plots of Fig. 4.4. Figure 4.5b shows the sub-basin-scale mean absolute biases ($\left|\bar{h}^{\mathrm{dt}} - \bar{h}^{\mathrm{md}}\right|$) of the reference scenario A01.0_B01.0. Note that, due to the uneven station location distribution, we performed the analyses at the sub-basin scale. From Fig. 4.5b, we observe that there are large biases in some sub-basins. Explanations for these biases are model structure errors (e.g. only a single layer aquifer model used and no pumping activities simulated), parameter errors (e.g. no calibration, only two classes for classifying aquifer and only homogeneous aquifer properties assigned for each class) and discrepancies in resolutions and elevation references between the model results and point measurement data. Related to the elevation references, we acknowledge that we did not do perform any correction to the DEM of HydroSHEDS used in the model and station elevation information provided by data suppliers, who most likely do not use the same elevation references. This issue may be considered as one of the limitations of the current study. However, given the nature of a large-scale groundwater model, which covers multiple basins and countries, we have to accept that it is still difficult to define the same and consistent elevation reference for the whole model area. Moreover, the accuracy of the DEM of HydroSHEDS used, which is the most recent derivation product of SRTM mission (`http://www2.jpl.nasa.gov/srtm/`), should be considered limiting since the target value of the SRTM standard accuracy is 16 m. In MODFLOW, an accurate DEM is important, particularly because it is needed as the input to define drainage bed (RBOT and DELV) and surface water level (HRIV) elevations, which

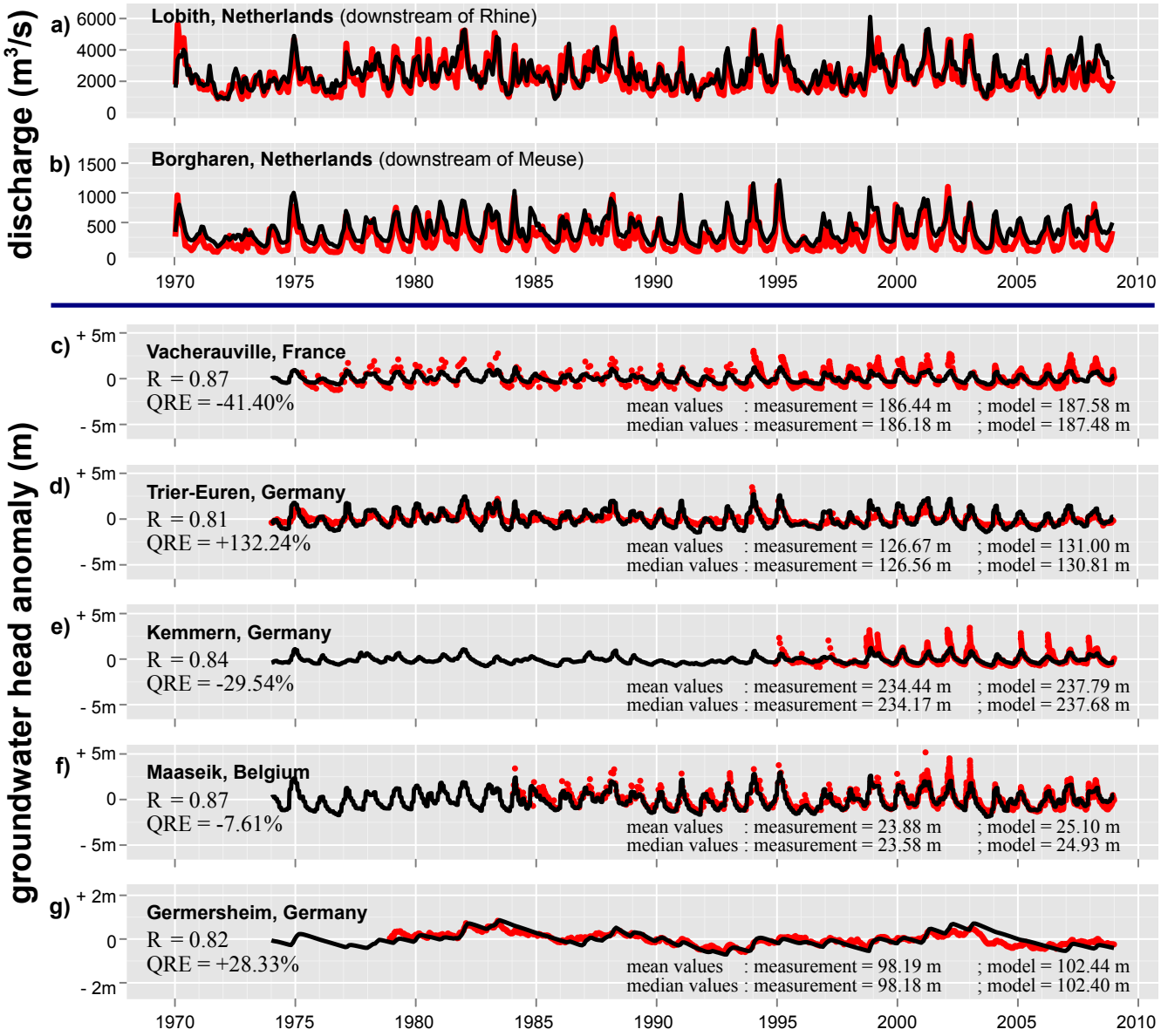

Figure 4.3 The comparison between measurement data (red) and model output (black): **(a)** the discharge in Lobith, located downstream of the Rhine. **(b)** The discharge in Borgharen, located downstream of Meuse. **(c, d, e, f, and g)** Groundwater head anomaly comparisons based on the reference scenario A01.0_B01.0 at several locations indicated in Fig. 4.2b. Note that for Figs. 4.3c, d, e, f and g, we plotted the simulated and measuread groundwater head time series in their anomalies related to their mean values. The mean and median values of each time series are also given in the graph.

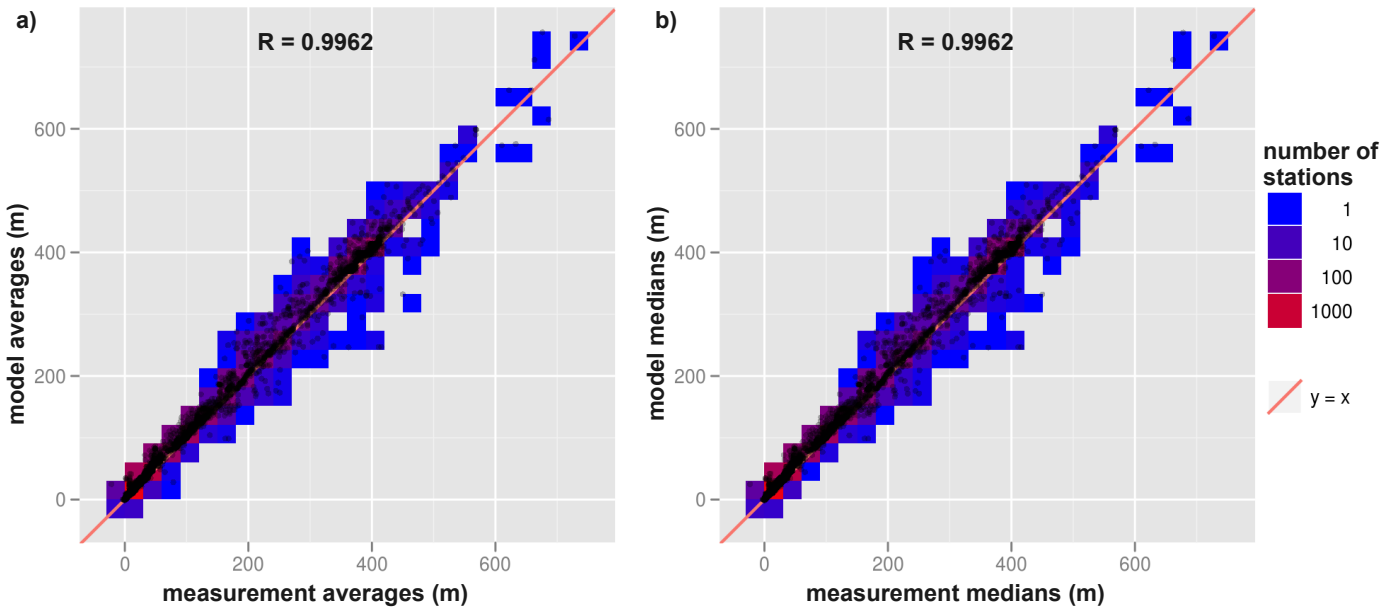

Figure 4.4 The scatter-plots comparing between: **(a)** model result averages vs. measurement data averages; **(b)** model result median values vs. measurement data median values.

serve as the model boundary conditions by means of the RIV and DRN packages (see Eqs. (4.6), (4.7), and (4.9)).

Figures 4.6 and 4.7 show the sub-basin scale averages of R_{cor}, which indicate the timing punctuality, and $|\mathrm{QRE}_{7525}|$, which indicate the magnitude of amplitude error. Both figures present results from several scenarios with different aquifer properties (KD and Sy). We see that mostly the amplitude error $|\mathrm{QRE}_{7525}|$ (Fig. 4.7) is sensitive to different aquifer properties, while the timing agreement R_{cor} (Fig. 4.6) is less sensitive. The latter may be due to the fact that although we varied KD and Sy for our MODFLOW groundwater model input, we used the same land surface model output (the same recharge Q_{23} and surface water levels HRIV time series) for all scenarios. It seems that, to achieve better time series timing, we should have extended our sensitivity analysis by also looking at the uncertainty of our land surface model outcome. The sensitivity of $|\mathrm{QRE}_{7525}|$ and the insensitivity of R_{cor} to the aquifer properties variation can be observed from Table 4.4, that summarizes the (entire) basin-scale average values for each scenario. Note that to calculate these basin-scale average values, we used the surface areas of sub-basins as weight factors. From our sensitivity analysis, we see that the basin-scale average values of $|\mathrm{QRE}_{7525}|$ vary from 80 % to above 450 %, while the basin-scale average values of R_{cor} vary only from 0.32 to 0.43.

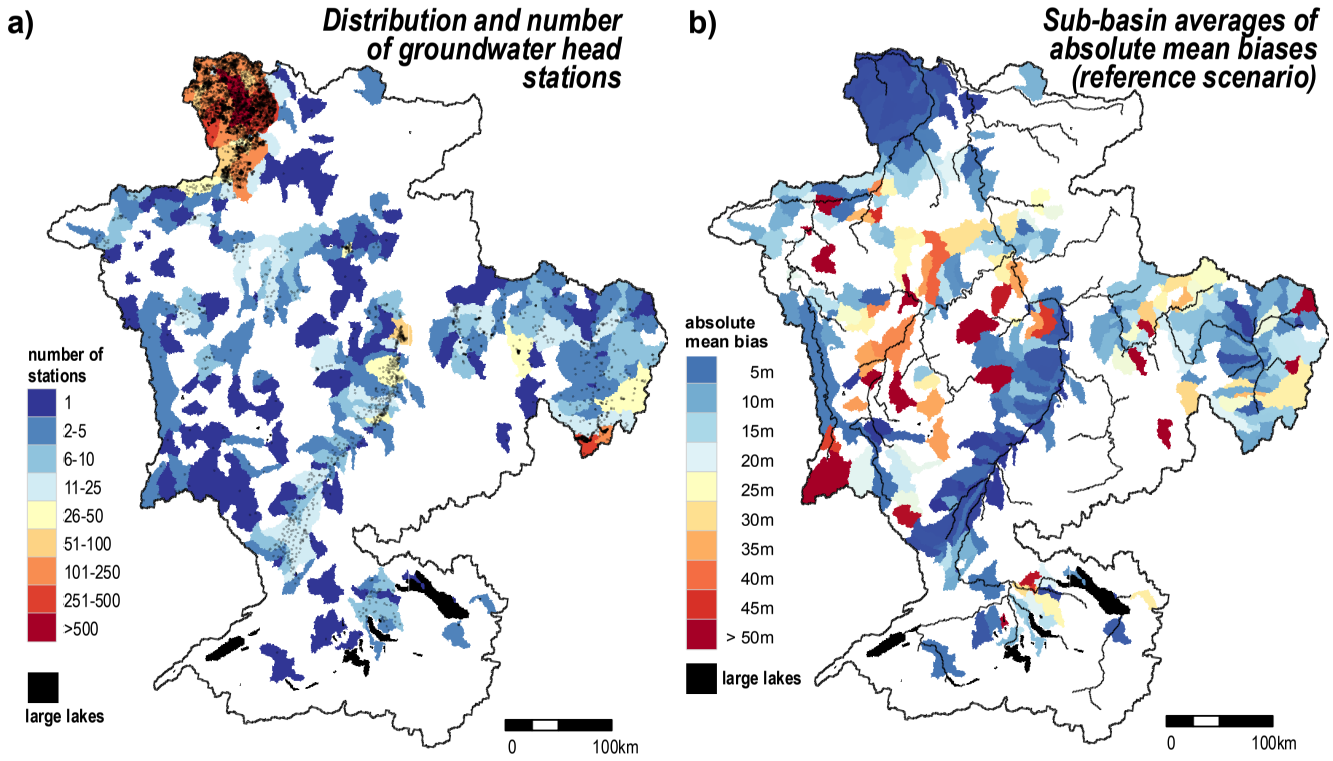

Figure 4.5 On the left (a): The sub-basins used to analyze the model performance. The locations and the number of head measurement stations in each of sub-basin are also illustrated. On the right (b): The sub-basin averages of absolute mean biases, based on the reference scenario A01.0_B01.0.

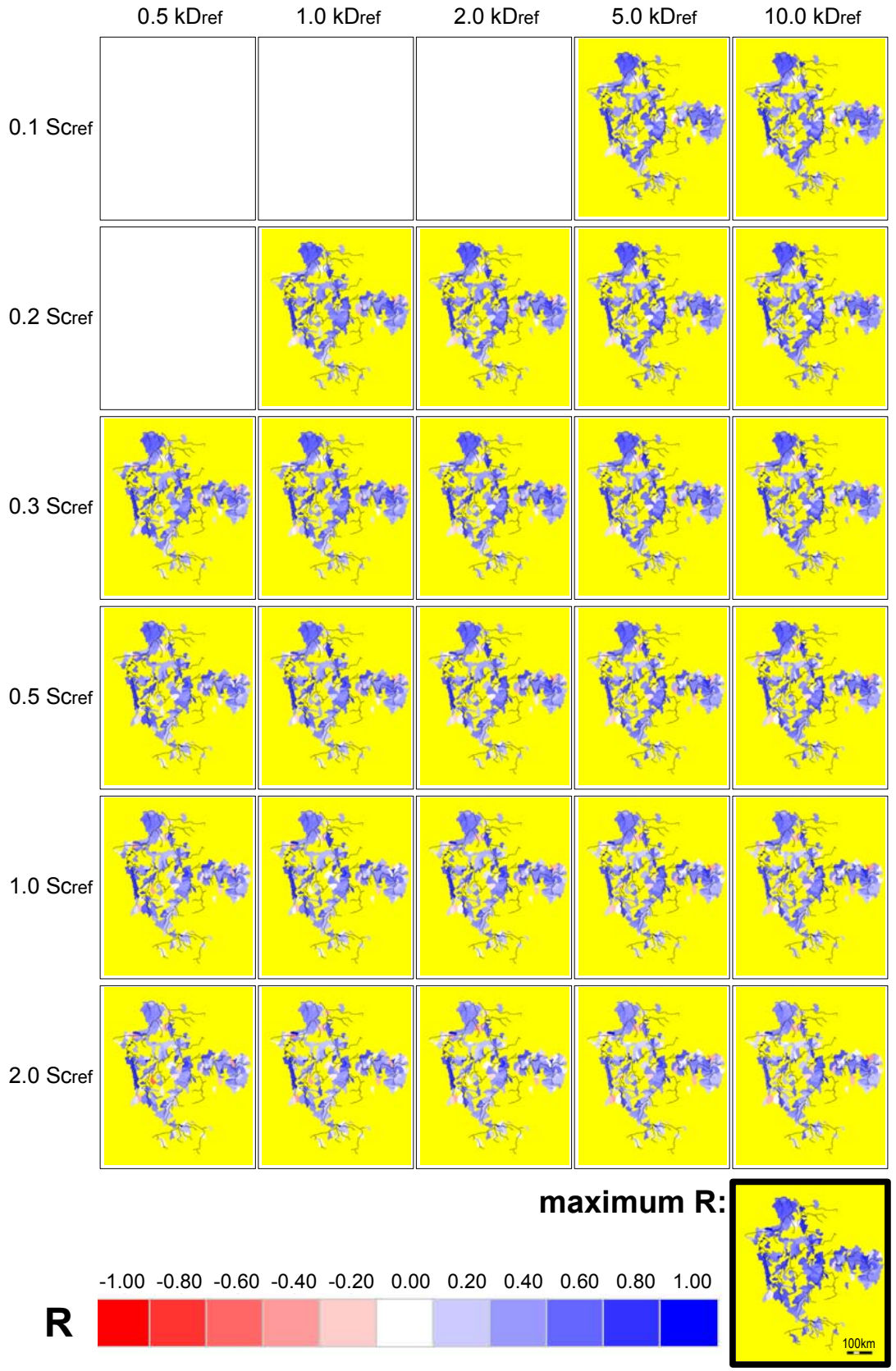

Figure 4.6 The sub-basin average of timing agreement indicators, R_{cor}, for all scenarios. To distinguish near zero values (white), we use a yellow background. The lower right corner map is a composite map of the maximum values of all scenarios. Note: some scenarios with small tranmissivities KD and storage coefficients Sy failed to converge.

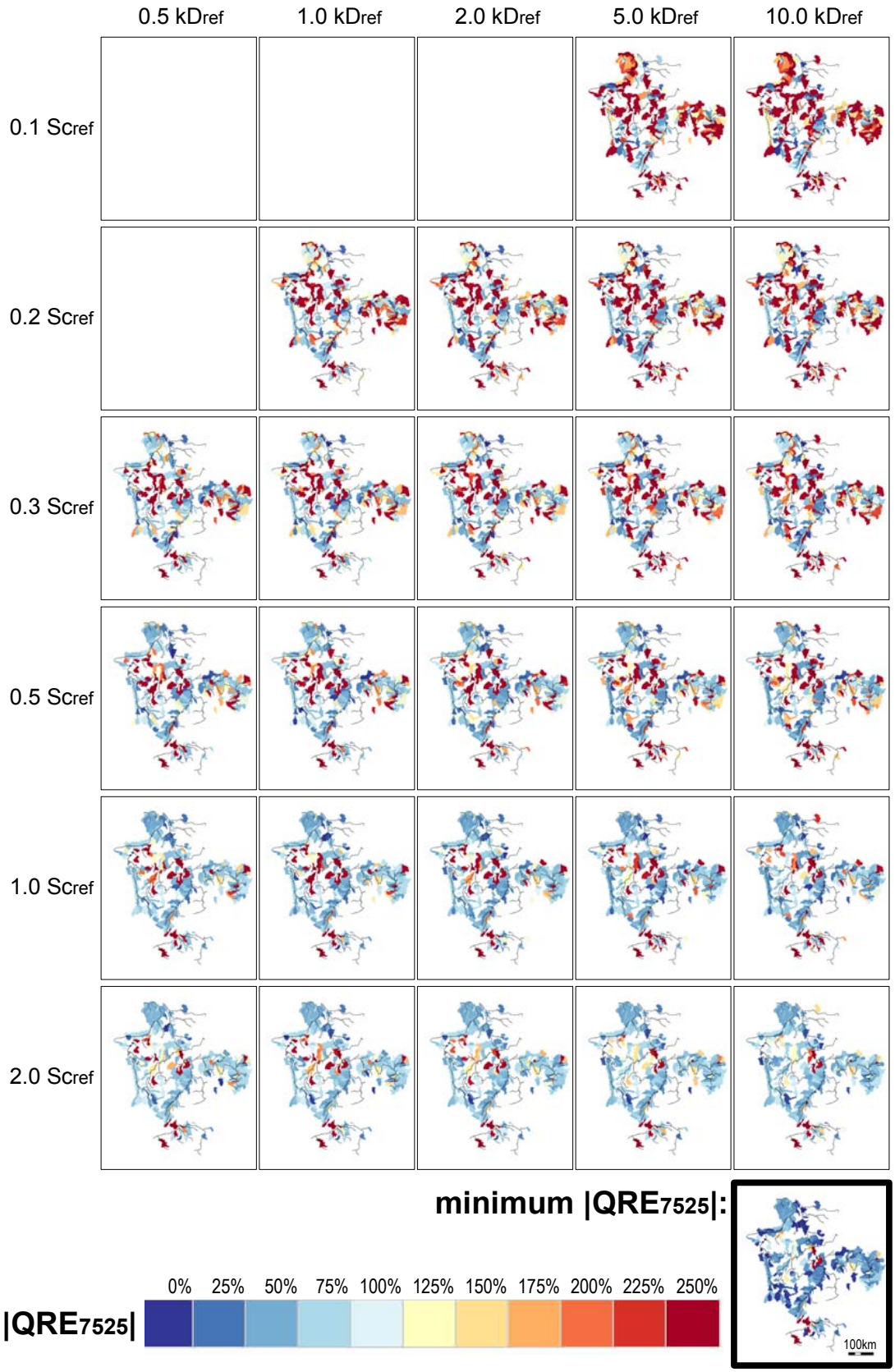

Figure 4.7 The sub-basin average of amplitude error indicators, $|\mathrm{QRE}_{7525}|$, for all scenarios. The lower right corner map is a composite map of the minimum values of all scenarios. Note: some scenarios with small tranmissivities KD and storage coefficients Sy failed to converge.

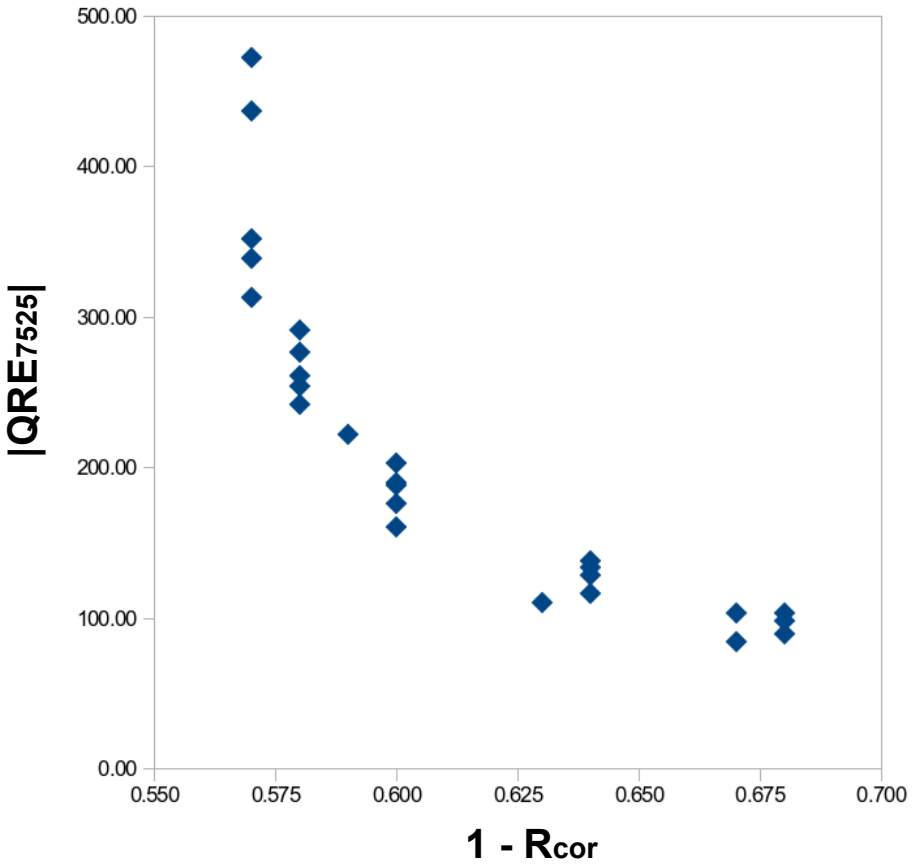

Figure 4.8 The scatter-plots of two model performance indicators (in (entire) basin-scale average values) from all scenarios with varying aquifer properties: $|\mathrm{QRE}_{7525}|$ (y-axis, in percentage) and $(1 - R_{\mathrm{cor}})$ (x-axis).

To further explore the results, we plotted the basin scale values of $|\mathrm{QRE}_{7525}|$ against $(1 - R_{\mathrm{cor}})$ in Fig. 4.8. Ideally, a scenario should have both values near zero or its point in Fig. 4.8 is located near the origin of the axes. From Fig. 4.8, we encounter that different combinations of KD and Sy values can lead to similar performance of R_{cor}. Moreover, we also see a pareto optimal front developing while looking into two performance indicators at the same time. It implies that the performance indicators, R_{cor} and $|\mathrm{QRE}_{7525}|$, behave oppositely, in the sense that, moving through the parameter space, a performance indicator improves whereas the other deteriorates. This condition can be regarded as an inability of the model to reproduce simultaneously different aspects of observed groundwater heads, which are related to model structural limitations that should be investigated in the future.

Yet, despite the aforementioned limitations, we can still observe that our groundwater model can reasonably reproduce the time series of observed groundwater head time

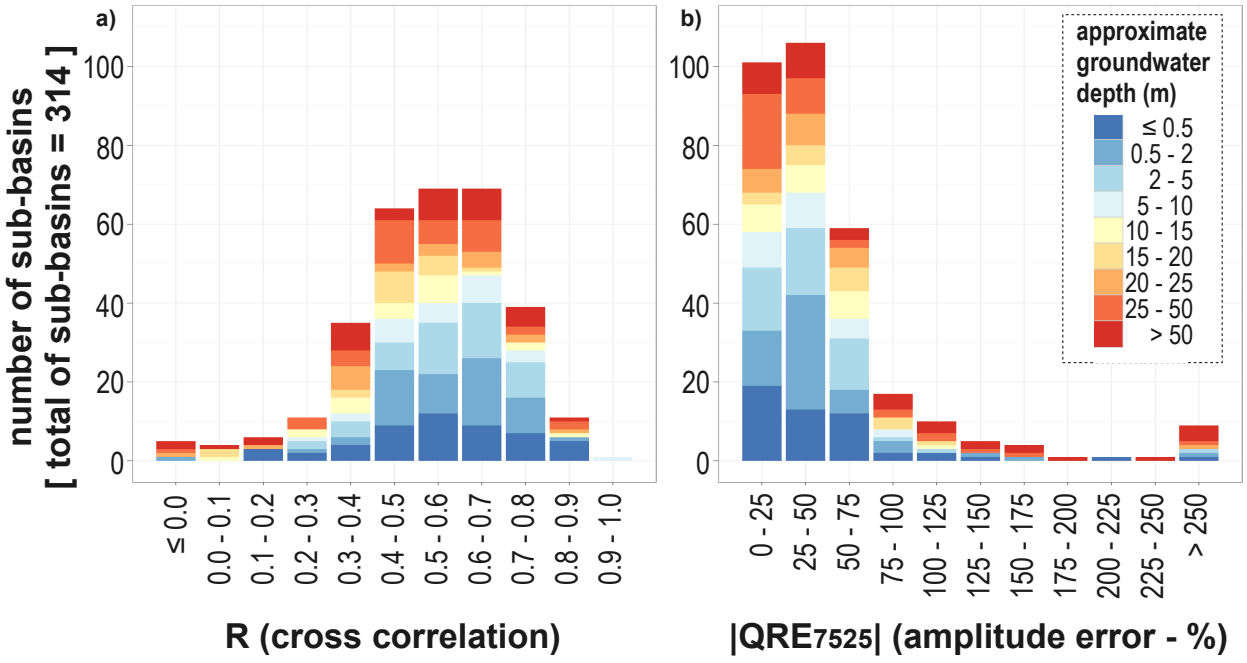

Figure 4.9 Histograms of maximum values of all maps in Fig. 4.6 (cross correlation R_{cor}) and minimum values of all maps in Fig. 4.7 (amplitude error $|\mathrm{QRE}_{7525}|$). Each bar in the histogram is clustered based on approximate groundwater depths that are calculated by averaging the 34-yr 1974–2008 average modeled groundwater heads of all scenarios. Note that, to calculate these average depths, we used only cells with measuring stations.

series. Figure 4.9a and 4.9b shows the histogram of the maximum values of R_{cor} and the minimum values of $|\mathrm{QRE}_{7525}|$ that are selected from the sub-basin scale values of all scenarios (from Figs. 4.6 and 4.7). We observed that more than 50 % of sub-basins have relatively good timing agreements ($R_{\mathrm{cor}} > 0.5$), and more than 50 % of sub-basins have relatively small amplitude errors ($|\mathrm{QRE}_{7525}| < 50$ %). They include not only shallow groundwater areas, but also areas with deep groundwater heads (see the lower right corners figures of Figs. 4.6 and 4.7). These facts indicate that the results of our current model are promising.

4.5 Conclusions and discussion

This study shows that it is possible to build a simple and reasonably accurate large-scale groundwater model by using only global datasets. It suggests a promising prospect for large-scale groundwater modeling practice, including in data-poor en-

vironments. Although the model may not be suitable for karstic aquifer areas – for which MODFLOW is not suitable for modeling groundwater flow – PCR-GLOBWB-MOD can be applied in several areas that contain large sedimentary basins or pockets, such as the basins of Nile, Danube, Mekong, Yellow and Ganges-Brahmaputra Rivers.

The promising results of this study open an opportunity to improve common existing global large-scale hydrological models, such as the original version of PCR-GLOBWB (van Beek and Bierkens, 2009; van Beek et al., 2011), WASMOD-M (Widén-Nilsson et al., 2007) and VIC (Liang et al., 1994), which do not have the ability to calculate spatio-temporal groundwater heads; therefore, do not incorporate any lateral flows in their groundwater compartments. Although groundwater heads and lateral groundwater flows may not be important for current common global hydrological models, which usually have a spatial resolution of 25–50 km, their inclusion is relevant for future global hydrological models that may have spatial resolutions of down to 1 km (Wood et al., 2011).

Several authors (Bierkens and van den Hurk, 2007; Fan et al., 2007; Miguez-Macho et al., 2007; Anyah et al., 2008; Miguez-Macho et al., 2008; Maxwell and Kollet, 2008; Fan and Miguez-Macho, 2011, 2010) have suggested that groundwater lateral flows can be important for regional climate conditions. For instance, Bierkens and van den Hurk (2007) have shown that rainfall persistence may be partly explained by groundwater confluence to discharge zones that remain wet throughout the year to sustain evaporation for longer periods of time. However, for our study area that has humid climate and relatively high drainage density, the importance of groundwater lateral flows to regional climate has to be confirmed. In such areas where rainfall may be mostly transferred as hillslope and channel flows, groundwater lateral flow or groundwater confluence to discharge zones may only be important during a long dry spell. This issue may still not be resolved from our current study, but we argue that any further investigation about it can be done by using a model such as presented here.

We realize that there are several weaknesses in the current approach. The most obvious one is the fact that we do not use a full coupling between the land surface model and the groundwater model parts. Consequently, the soil moisture of the upper soil stores calculated by the land surface model, do not interactively correlate to groundwater heads simulated with the groundwater model (as capillary rise is ignored). The omission of this interaction makes the groundwater store not have the ability to sustain soil moisture states and to fulfill evaporation demands (especially during dry seasons).

We also ignore the fluctuations of water levels in large lakes. Moreover, we disable the direct and interactive connection between the channel/surface water flows and groundwater tables. It should be also noted that the current model ignores the fact that overland flows may occur as the consequence of rising water tables above the land surface elevation (especially for phreatic aquifer locations). Such overland flow might

be accommodated by using additional MODFLOW packages (e.g. Restrepo et al., 1998). However, they are currently irreconcilable with PCR-GLOBWB-MOD in its current form as the capillary rise from the groundwater store has been disabled. All of the aforementioned weaknesses must be addressed while building the next generation of this model that includes full coupling between the land surface model and the groundwater model parts.

We also acknowledge that the current version of PCR-GLOBWB-MOD is still not suitable for areas under heavy anthropogenic water extraction as there are no global datasets on pumping activities that can be meaningfully resolved at the model resolution ($30'' \times 30''$). As far as we know, Wada et al. (2010) and Wada et al. (2011) are the only studies that estimated global groundwater abstraction, but at a very coarse resolution of $30' \times 30'$. However, our model is still useful to assess impacts under an uncertain future climate, such as changing precipitation and temperature. Moreover, if such datasets of water pumping abstraction rate are provided, they can be readily incorporated in our model.

In this study, the sensitivity analysis of the groundwater head output is still limited to the uncertainty of our aquifer properties in the groundwater model, not considering the uncertainty of the land surface model outcome. In a future study, we may want to extend the sensitivity analysis by running several scenarios with varying soil properties of the first and second soil stores (unsaturated zone) to produce several recharge and surface water level time series and using them to force the groundwater model. However, considering aforementioned weaknesses discussed previously, this extended sensitivity analysis may not be meaningful if we do not use the fully coupled model. In such a fully coupled model, the dynamic feedback between surface water levels and groundwater heads, and between soil moisture states and groundwater heads are expected to influence the behaviour of resulting groundwater head time series.

Moreover, for such a fully coupled large-scale model, model evaluation and calibration can be reasonably done by comparing the model soil moisture states and remote sensing soil moisture products, such as AMSR-E (e.g. Njoku et al., 2003) and ERS (Wagner et al., 1999b), which are also available for the entire globe. By doing this, we anticipate that a large-scale groundwater model may be evaluated and calibrated without extensive head measurement data that are hardly available in other parts of the world. Thus, it allows the construction and verification of large-scale groundwater models in data-poor environments.

5 The suitability of using ERS spaceborne soil moisture time series to calibrate a large-scale groundwater model

This chapter is based on:
Sutanudjaja, E. H., van Beek, L. P. H., de Jong, S. M., van Geer, F. C., Bierkens, M. F. P., Calibrating a large-scale groundwater model using soil moisture and discharge measurements, in preparation for Water Resources Research.

Abstract

We explore the possibility of using remotely-sensed soil moisture data to calibrate the performance of a large-scale, physically-based and fully-coupled groundwater-land surface model. The model used in this study is PCR-GLOBWB-MOD, which has a spatial resolution of 30 arc-second (approximately 1 km at the equator) and operates at a daily basis. We apply a brute-force calibration procedure by running more than three thousand runs with varying model parameter values. Results of all runs are evaluated against two in-situ discharge measurements located near the basin outlets, more than four thousand point-scale groundwater head observations from piezometers and the European Remote Sensing Soil Water Index (ERS SWI) time series. The latter, derived from satellite signals, provides spatio-temporal expressions of the first meter profile soil moisture content at a spatial resolution of 30 arc-minute (approximately 50 km at the equator). Results indicate that ERS SWI time series can be used for the calibration of upper soil saturated hydraulic conductivities that determine groundwater recharge. However, discharge measurements should be included to obtain full calibration of the coupled land surface-groundwater model, specifically to resolve equifinality problems of fitting soil moisture dynamics and to constrain aquifer transmissivities and runoff-infiltration partitioning processes. The combined and step-wise approach using both in-situ discharge observations and remotely-sensed soil moisture data in model calibration yields a model that is able to fit both discharge and soil moisture reasonably well, as well as predicting groundwater head dynamics with acceptable accuracy.

5.1 Introduction

The current generation of large-scale hydrological models generally lacks a groundwater model component simulating lateral groundwater flow. Large-scale groundwater models are rare partly due to a lack of in-situ groundwater head data required for their calibration. In the limited areas where they are available, groundwater head measurements are sparsely located or available over limited spatial extent. Moreover, ground-based groundwater head observations give only information for a few locations with limited spatial support (i.e. point scale). Consequently, calibrating large-scale groundwater models using in-situ groundwater head data is difficult.

The main strength of spaceborne remote sensing observations, which has the ability to provide spatially and temporally exhaustive maps of earth surface properties, is their global coverage. Since the last decades, many studies have shown the possibilities of earth observation for hydrological purposes and spaceborne remote sensing has been increasingly used for mapping hydrological states and fluxes, such as precipitation (e.g. Kummerow et al., 2000), soil moisture (Njoku et al., 2003; Wagner et al., 1999b), snow cover (Dankers and de Jong, 2004; Immerzeel et al., 2009), land surface temperature (Wan and Li, 1997) and evaporation (Bastiaanssen et al., 1998a,b; Su, 2002; Mu et al., 2007; Jung et al., 2010). However, their benefits for groundwater hydrology applications are still limited. Up to now, only the space gravity satellite Gravity Recovery and Climate Experiment (GRACE, Tapley et al., 2004) from the National Aeronautics and Space Administration (NASA) has been recognized as a groundwater assessment tool, specifically to detect groundwater storage changes (e.g. Rodell et al., 2009). Yet, a major drawback of GRACE is its coarse resolution of 400 km, severely hampering its regional scale application. Nevertheless, Becker (2006) argues that groundwater behavior may be inferred from remotely-sensed surface expressions, such as elevation, surface temperature and soil moisture. Indeed, in a recent application Alkhaier et al. (2012b) suggest that remotely-sensed evaporation and land surface temperature correlate well with groundwater depth and can be physically connected by means of a soil water and heat flux model (see also Alkhaier et al., 2012a). Moreover, Chapter 2 of this thesis shows that there is correlation between the time series of shallow groundwater head dynamics and the time series of the spaceborne soil moisture product European Remote Sensing Soil Water Index (ERS SWI). In this chapter, we intend to explore the potential to use remotely-sensed soil moisture data — having a better spatial resolution (25-50 km) than the GRACE product — to support groundwater studies (see also Jackson, 2002).

More specifically, the objective of this chapter is to investigate whether the global coverage soil moisture time series ERS SWI (Wagner et al., 1999b) can be used to calibrate a large-scale physically-based coupled groundwater-land surface model called PCR-GLOBWB-MOD (Sutanudjaja et al., 2011, see also Chapter 4). The underlying idea is that the combination of setting up a coupled groundwater-land surface model using only globally-available datasets (Chapter 4) and calibrating it

with globally-available remote sensing data can make large-scale groundwater modeling feasible throughout the world. As a test-bed, we used the combined Rhine-Meuse basin (Sect. 2.2.1 and Fig. 2.2) having a good coverage of ERS SWI, discharge and ample groundwater head observations. We implemented a brute-force calibration by running more than three thousand runs with different parameter sets. From these runs, we evaluated model results and identified the optimal parameter sets that result in good performance based on two observation types: spaceborne soil moisture-based ERS SWI time series and in-situ discharge measurements; as well as the combination of both. We further analyzed the benefits of using each observation in model calibration by verifying the model results to 4250 point-scale groundwater head observations.

This chapter is organized as follows. The following Sect. 5.2 describes the coupled groundwater-land surface model used in this study. Subsequently, Sect. 5.3 explains the brute-force calibration procedure, including the methodology used to evaluate the model performance and the observation data used. Next, the results are presented and discussed in Sect. 5.4. Finally, Sect. 5.5 summarizes the findings.

5.2 Model structure: the online coupled groundwater-land surface model of PCR-GLOBWB-MOD

A detailed description of PCR-GLOBWB-MOD (Sutanudjaja et al., 2011) can be found in Chapter 4 (and Appendix A). Briefly stated, PCR-GLOBWB-MOD, having a spatial resolution of 30 arc-second ($30'' \times 30''$, approximately equal to 1 km $\times$ 1 km at the equator), is the land surface model PCR-GLOBWB (van Beek and Bierkens, 2009; van Beek et al., 2011) coupled to a MODFLOW (McDonald and Harbaugh, 1988) groundwater model. The land surface model conceptualizes the hydrological processes above soil surface and in two unsaturated zone soil layers (in which their storages are symbolized as S_1 and S_2 [L]), while the groundwater model contains a groundwater store (S_3 [L]) conceptualizing deeper saturated flows (see Fig. 4.1).

This Sect. 5.2 illustrates the main features of the model and reports the modifications introduced in this Chapter 5. In the previous version of PCR-GLOBWB-MOD in Chapter 4 — hereafter referred as "PCR-GLOBWB-MOD$_{\mathrm{OFF}}$" (with the subscript OFF indicating 'offline coupling'), there is still no direct coupling between the land surface model and groundwater model (since the simulations of both models were performed separately and sequentially, see Sect. 4.2.1). In PCR-GLOBWB-MOD$_{\mathrm{OFF}}$, there is no interactive coupling between channel/surface water level and groundwater head dynamics (see Sect 4.5). The water level fluctuations in large lakes are also ignored in PCR-GLOBWB-MOD$_{\mathrm{OFF}}$ (see Sect. 4.2.3). Moreover, as capillary rise from the groundwater store is ignored (see Sect. 4.2.2), the groundwater level simulated in PCR-GLOBWB-MOD$_{\mathrm{OFF}}$ cannot sustain the soil moisture states of the upper soil stores and thus cannot fulfill high evaporation demand (during dry condtion). In

this Chapter 5, we introduce the fully-coupled version of the model — referred as "PCR-GLOBWB-MOD$_{\mathrm{ONL}}$" (with the subscript ONL indicating 'online coupling') — described in the following sections.

5.2.1 Activating capillary rises from the groundwater bodies

In the upper stores S_1 and S_2 (Fig. 4.1), representing the top 30 cm of soil (thickness $Z_1 \leq 30\,\mathrm{cm}$) and the following 70 cm of soil ($Z_2 \leq 70\,\mathrm{cm}$), PCR-GLOBWB-MOD (hereafter "PCR-GLOBWB-MOD" refers to both "PCR-GLOBWB-MOD$_{\mathrm{OFF}}$" and "PCR-GLOBWB-MOD$_{\mathrm{ONL}}$") includes water balance calculation on the daily basis, a snow module based on the HBV model (Bergström, 1995), an improved sub-grid saturation variability of the Arno scheme (Todini, 1996; Hagemann and Gates, 2003) and an interflow module based on Sloan and Moore (1984).

Besides precipitation P [$\mathrm{L\,T^{-1}}$] and evaporation E [$\mathrm{L\,T^{-1}}$], important vertical fluxes in the land surface model are water exchanges between the first and second stores, Q_{12} [$\mathrm{L\,T^{-1}}$], and between the second and groundwater stores, Q_{23} [$\mathrm{L\,T^{-1}}$]. Q_{12} and Q_{23} consist of downward percolation fluxes, $Q_{1\to2}$ and $Q_{2\to3}$ [$\mathrm{L\,T^{-1}}$], and upward capillary rise fluxes, $Q_{2\to1}$ and $Q_{3\to2}$ [$\mathrm{L\,T^{-1}}$]. These fluxes are driven by degrees of saturation of both stores, s [-], calculated either as $s_1 = S_1/SC_1$ and $s_2 = S_2/SC_2$ (where SC [L] indicates water storage capacities); or $s_1 = \theta_1/\theta_{\mathrm{sat},1}$ and $s_2 = \theta_2/\theta_{\mathrm{sat},2}$ (where the subscript sat indicates saturation and θ [$-$] is effective moisture content defined as $\theta = S/Z$ and $\theta_{\mathrm{sat}} = SC/Z$).

If there is enough water available in S_1, percolation rate $Q_{1\to2}$ equals the unsaturated conductivity, $K_1(s_1)$ [LT-1]. If s_1 is smaller than s_2 ($s_1 < s_2$), capillary rise occurs with the amount of $Q_{2\to1} = K_2(s_2)\times(1 - s_1)$. $K(s)$ is calculated based on (Campbell, 1974): $K(s) = K_{\mathrm{sat}} \times s^{2\beta+3}$, where β [-] is a parameter in the soil matric suction ψ [L] function of Clapp and Hornberger (1978): $\psi(s) = \psi_{\mathrm{sat}} \times s^{-\beta}$ (see Sect. A.4).

In the offline coupled version PCR-GLOBWB-MOD$_{\mathrm{OFF}}$, the capillary rise flux from the groundwater store is neglected ($Q_{3\to2} = 0$). In this new and online coupled version PCR-GLOBWB-MOD$_{\mathrm{ONL}}$, we activate this flux ($Q_{3\to2} \geq 0$). Here, the Gardner-Eagleson approach (Gardner, 1958; Eagleson, 1978; Soylu et al., 2011) is adopted to estimate capillary rise as a function of groundwater table position. Given the assumptions of a steady state condition with a suction head at the surface is (negatively) large (i.e. dry soil surface), the maximum capillary rise flux rate, $\mathrm{CR}_{\mathrm{max}}$ [LT-1], is given as:

$$\mathrm{CR}_{\mathrm{max}} \;=\; K_{\mathrm{sat},2}\left[1 + \frac{3}{2 + 6/\beta_2}\right]\left(\frac{|\psi_{\mathrm{sat},2}|}{Z_{\mathrm{gw}}}\right)^{2+3/\beta_2} \tag{5.1}$$

where the index 2 indicates the second soil layer, Z_{gw} [L] is the difference between surface level (from the digital elevation model) and groundwater head h [L] (calculated from the MODFLOW groundwater model). Equation 5.1 is used to estimate the

maximum $Q_{3\rightarrow2}$ and limited by $K_{\text{sat},2}$, which is also used if the groundwater is at or above the surface ($Z_{\text{gw}} \leq 0$). Moreover, we limit the capillary rise fluxes, $Q_{3\rightarrow2}$ and $Q_{2\rightarrow1}$, such that both of them do not result in any of the upper soil storages exceeding the equilibrium water content, W_{equ} [L]. The form of this equilibrium soil moisture profile is given as (Clapp and Hornberger, 1978; Koster et al., 2000):

$$s_{\text{equ}}(z) \;=\; \left(\frac{\psi_{\text{sat}} - z}{\psi_{\text{sat}}}\right)^{(-1/\beta)} \tag{5.2}$$

where s_{equ} [$-$] is the degree of saturation at a height z above the water table. The equilibrium soil storage W_{equ} is determined by integrating $s_{\text{equ}}(z)$ from the groundwater table to the surface level.

5.2.2 Local runoff and surface water routing

The local runoff in each 30 arc-second cell basically consists of three components: interflow Q_{sf} [LT^{-1}] and direct runoff Q_{dr} [LT^{-1}] (both from the land surface model part, see Eq. A.13) and A.8), as well as baseflow Q_{bf} [LT^{-1}] (from the groundwater model part, see Sect. 5.2.3). By multiplying the local runoff with the surface area of each 30 arc-second cell, the local runoff can be expressed in a water volume per unit time Q_{tot} [L^3T^{-1}] (Eq. A.32). Subsequently, to obtain the channel discharge Q_{chn} [L^3T^{-1}], Q_{tot} from all 30 arc-second cells are first accumulated along the drainage network. Then, to take account of travel time through channels, the unit hydrograph method (Soil Conservation Service (SCS), 1972; Sólyom and Tucker, 2004) is used to route the channel discharge:

$$Q_{\text{chn,rt}} \;=\; \sum_{n=0}^{N} f_n \times Q_{\text{chn}}\,(t-n) \tag{5.3}$$

where the subscript rt indicates the discharge after routing procedure implemented, t and $(t-n)$ are the current and previous daily time steps (until N days), and f_n [$-$] are the weights ($\sum f_n = 1$) given by considering the time of concentration at the most distant point of the basin to reach the cell.

For the surface water bodies classified as "large lakes" (see Fig. 1.1 for their locations), PCR-GLOBWB-MOD_{ONL} simulates their water level changes. These water level changes are simulated by assuming fixed surface lake areas and based on water balance calculation considering not only local precipitation input and open water evaporation loss, but also water exchange between groundwater bodies and lakes (see Sect. 5.2.3), incoming inflow from upstream areas of lakes (including from other upstream lakes) and outflow in lake outlets. The latter is calculated in analogy to a weir formula as the discharge through a rectangular cross section (Bos, 1989; van Beek and Bierkens, 2009):

$$Q_{\text{LAK}} \;=\; 1.70 \times C \times B_{\text{LAK}} \times \left[\max\left(0, h_{\text{LAK}} - h_0\right)\right]^{1.5} \Delta t \tag{5.4}$$

where Q_{LAK} [$\mathrm{L^3T^{-1}}$] is the lake outflow, C [$\mathrm{L^{4/3}T^{-1}}$] is a correction factor, h_{LAK} [L] and h_0 [L] are respectively the lake water level and sill elevation of the outlet, and B_{LAK} [L] is the breadth outlet approximated by the bankfull width formula of Eq. 4.4. Note that this calculated outlet discharge Q_{LAK} is added and routed to the discharge (Eq. 5.3) of the downstream channels and lakes. Here, for each daily time step, the routing procedure is performed sequentially and serially — along the drainage network — from the most upstream pixels and lakes to the most downstream ones.

5.2.3 Groundwater model

The link between the land surface model part of PCR-GLOBWB-MOD — written in the PCRaster scripting languange (Wesseling et al., 1996) — and the MODFLOW groundwater model is provided by a PCRaster-MODFLOW extension developed by Schmitz et al. (2009). Using this extension, a single layer MODFLOW groundwater model is constructed and forced with the output from the land surface model part of PCR-GLOBWB-MOD, specifically the net groundwater recharge ($Q_{23} = Q_{2\rightarrow3} - Q_{3\rightarrow2}$) and the routed discharge $Q_{\mathrm{chn,rt}}$ that is beforehand translated to surface water levels HRIV [L] (Sect. 4.6). The "recharge" (RCH) package is used to introduce Q_{23}, while the "river" (RIV) and "drain" (DRN) packages are used to introduce HRIV as the boundary conditions of the MODFLOW model (Eqs. 4.7 and 4.9). To incorporate the influence of changes of water levels in large lakes (see Fig. 1.1 for their locations) and quantify water exchange between lakes and groundwater bodies, the RIV package is used with the assumption of very deep lake bed elevations such that groundwater heads are always above lake bed levels ($h \gg$ RBOT, see Eq. 4.7).

The implementation of RIV and DRN packages gives the possibility to quantify flows between streams and aquifers, symbolized as $-(\mathrm{qRIV} + \mathrm{qDRN})$ [$\mathrm{LT^{-1}}$] (with the negative sign is introduced as MODFLOW uses a positive sign for flows entering the aquifer). The amount of $-(\mathrm{qRIV} + \mathrm{qDRN})$, which depends on the difference between groundwater head h and surface water level HRIV, is the main component of the baseflow Q_{bf}, especially for channels in flat sedimentary pockets where groundwater flow is relatively slow. However, the magnitude of $-(\mathrm{qRIV} + \mathrm{qDRN})$ is basically too small to satisfy the baseflow from mountainous areas, where the main flow sources often consist of many springs tapping groundwater located higher up in valleys that are not explicitly resolved at a 30 arc-second resolution. To include this fast baseflow component, feeding tributaries to main rivers, it is assumed that the groundwater above the flood plain is drained based on a linear reservoir concept. Hence, the total baseflow Q_{bf} is expressed as follows:

$$Q_{\mathrm{bf}} = -(\mathrm{qRIV} + \mathrm{qDRN}) + (J \times S_{3,\mathrm{fpl}}) \tag{5.5}$$

where J [$\mathrm{T^{-1}}$] is a recession coefficient based on Kraaijenhoff van de Leur (1958) (see Eq. A.28). $S_{3,\mathrm{fpl}}$ [L] is the groundwater storage above the flood plain calculated as:

$$S_{3,\mathrm{fpl}} = \max(0, h - \mathrm{DEM_{fpl}} + \mathrm{BUFF}) \times Sy \tag{5.6}$$

where $\mathrm{DEM_{fpl}}$ [L] is the assumed flood plain elevation in a cell and BUFF [L] is the buffer zone (below the flood plain) that can be released as baseflow, while Sy [−] is the assumed specific yield. The consequence of incorporating this fast-response flow component — represented by the second term of Eq. 5.6: $J \times S_{3,\mathrm{fpl}}$ — is that the water balance of the model must be closed by subtracting this component from the input of the MODFLOW recharge package, $\mathrm{RCH_{inp}}$ [$\mathrm{LT^{-3}}$]:

$$\mathrm{RCH_{inp}} \;=\; (Q_{23} - J \times S_{3,\mathrm{fpl}}) \times A_{\mathrm{cell}} \tag{5.7}$$

where A_{cell} [$\mathrm{L^2}$] is the surface area of each 30 arc-second cell.

Note that all states and fluxes are calculated at daily basis, where a time-explicit scheme is used to solve Eqs. 5.1 to 5.7 with values of h and $-(\mathrm{qRIV} + \mathrm{qDRN})$ from the previous day.

5.3 Brute-force model calibration

5.3.1 General calibration strategy

We implemented a brute-force calibration procedure by first simulating a large number of runs with different parameter values (explained in Sect. 5.3.2). Using various observations and objective functions (defined in Sect. 5.3.3), we evaluated and compared the model fits or performances of 3045 runs. The "best fit" or "optimal" parameter sets were then identified as the "calibrated" parameter sets. As discharge data are traditionally used to calibrate hydrological models, we first identified the calibrated parameter sets based on discharge time series. For all 3045 runs, we also checked the model fits with the remotely-sensed ERS SWI soil moisture time series. The runs with optimal or calibrated parameter sets based on ERS SWI time series were thus also identified.

While evaluating the model performance of all 3045 runs, we analyzed how well unique parameter sets can be identified by inspecting the objective function behaviors — based on observed discharge and SWI data — and their parameter spaces. By combining the analyses based on discharge and soil moisture, we then performed a step-wise calibration procedure to identify the parameter sets that are able to simultaneously reproduce observed discharge and SWI time series (see further explanation in Sect. 5.4.3).

Subsequently, we compared the runs with the calibrated parameter sets based on observed discharge, SWI and the combination of both of them. To this end, we validated or verified the modeled groundwater head time series of each calibration scenario to the observed groundwater head time series. This verification is intended to investigate whether each observation type (i.e. discharge and SWI) and the combination (of both) could be used to calibrate the groundwater part of the coupled model.

5.3.2 Model parameters and runs

We performed the brute-force calibration procedure by simulating more than three thousand model runs with different parameter values of minimum (local) soil water capacities $W_{\min}$ [L], upper soil saturated conductivities $K_{\text{sat},1}$ and $K_{\text{sat},2}$ [LT^{-1}] and aquifer transmissivities KD [L^2T^{-1}]. The latter is a MODFLOW groundwater model parameter that also governs the value of the linear recession coefficient J (see Eqs. 5.5 and A.28). The parameters $K_{\text{sat},1}$ and $K_{\text{sat},2}$ are defined in the land surface model part of PCR-GLOBWB and mainly control direct runoff (Q_{dr}) and interflow (Q_{sf}) magnitudes and water exchange fluxes between the upper soil stores Q_{12} and groundwater stores Q_{23} (see Fig. 4.1, and Sect. 5.2.1 and Appendix A, especially Sects. A.3 to A.5). The parameter $W_{\min}$, which is used in the improved Arno scheme conceptualization (Todini, 1996; Hagemann and Gates, 2003; van Beek and Bierkens, 2009), controls the partitioning of rainfall into direct runoff and infiltration to the soil (see Eq. A.8). For $W_{\min} = 0$ (assumed in PCR-GLOBWB-MOD_{OFF}, see Tables 4.1 and 4.3), direct runoff always occurs after each rainfall event. If $W_{\min} > 0$, no direct runoff occurs as long as the total upper soil storages do not exceed $W_{\min}$.

We started this brute-force calibration procedure by defining the REFERENCE run. Figures 5.1a, 5.1b and 5.2c respectively show the spatially-distributed values of parameters $K_{\text{sat},1}$, $K_{\text{sat},2}$ and KD used in this REFERENCE run, for which $W_{\min} = 0$ is uniformly introduced within the study area. The values of $K_{\text{sat},1}$, $K_{\text{sat},2}$, KD and $W_{\min}$ used in the REFERENCE run, as well as the values of the other model parameters (i.e. snow module parameters, soil thicknesses, etc.), were generally adopted from the values used in Chapter 4 (Table 4.1) — except the aquifer transmissivities KD and specific yields Sy that are given in Table 5.1. The values of KD are adopted from Gleeson et al. (2011) who attributed the global lithological map of Dürr et al. (2005) with the geometric mean permeability of each lithology class in the map. The lithological map used is given in Fig. 2.1c. Note that compared with the original map of Dürr et al. (2005), we simplified the number of classes into five and performed a series of corrections to include sedimentary pockets in narrow rivers and to correct the position of large aquifer bodies (see Sect. 4.2.3). For the values of Sy in Table 5.1, which are also spatially-distributed and based on the lithological map in Fig. 2.1c, we refer to Freeze and Cherry (1979).

Table 5.2 lists the pre-factors used to vary KD, $K_{\text{sat},1}$ and $K_{\text{sat},2}$ and $W_{\min}$ and defined in more than three thousand model runs. All pre-factors refer to the REFERENCE parameter set (i.e. $f_W = 0$, $f_K = 0$ and $f_{KD} = 0$, used for the REFERENCE run). In total, there are 3045 parameter sets. Note that to limit the number of runs, we fixed the other model parameters (i.e. aquifer specific yield Sy, soil thicknesses Z, etc.). Moreover, to vary the parameter values of one run over the others, we used only three non-spatially distributed pre-factors (uniformly introduced within the study area), f_W, f_K and f_{KD}, listed in Table 5.2.

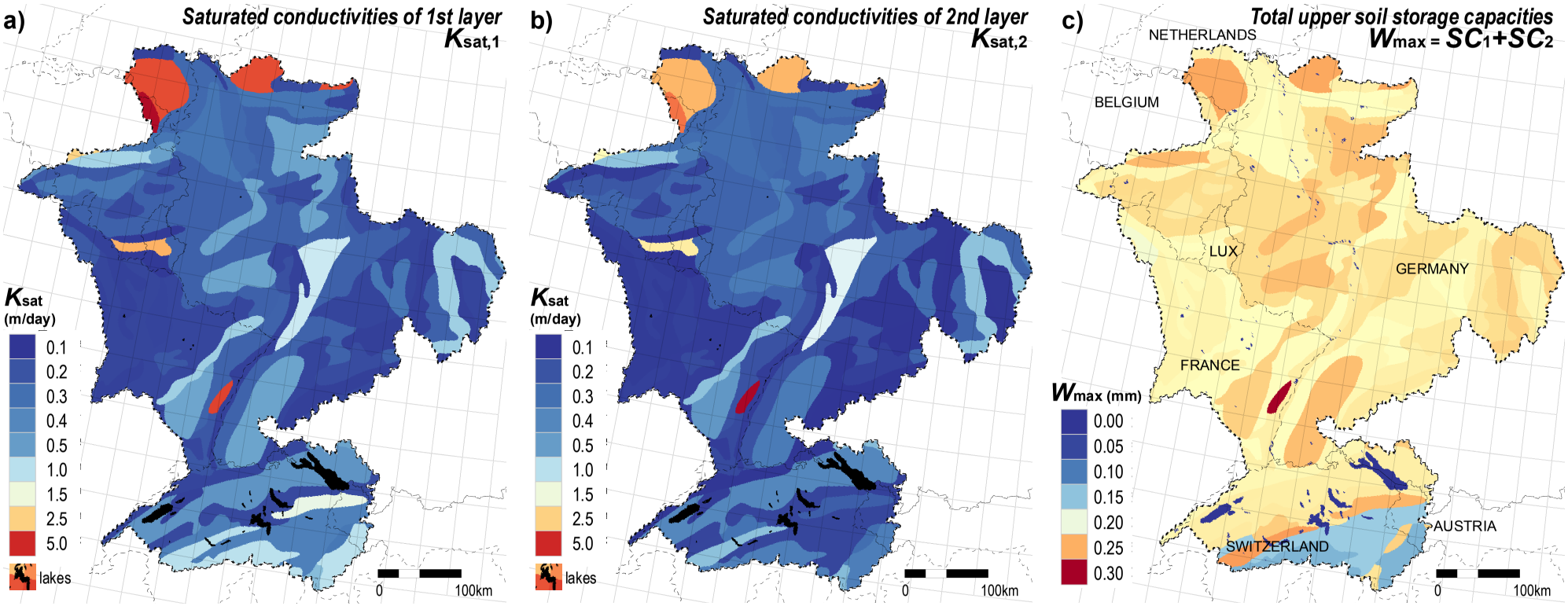

Figure 5.1 The fields of saturated conductivities (K_{sat}) of the first (a) and second (b) soil layers used in the REFERENCE run, and the total water storage capacities ($W_{\text{max}} = SC_1 + SC_2$) of the entire soil layer (c).

Table 5.1 The aquifer parameter values used in the reference run.

Lithology/aquifer class	Transmissivity KD [m^2/day]	Specific yield [−]
Non-consolidated sediments	533.52	0.25
Carbonate sedimentary rocks	67.17	0.10
Volcanic rocks	13.40	0.05
Crystalline rocks	0.50	0.02
Siliciclastic sedimentary rocks	13.40	0.05

Table 5.2 The parameter values used in the brute-foce calibration

Pre-factors	Parameter values	Number of discrete values
$f_W \in \{0, 0.25, 0.5, 0.75, 1\}$	$W_{\min} = f_W \times W_{\max} = f_W \times (SC_1 + SC_2)$	5
$f_{KD} \in \{-2.5, -2.25, -2, ..., 0, ..., 2, 2.25, 2.5\}$	$\log(KD) = f_{KD} + \log(KD_{\text{ref}})$	21
$f_K \in \{-3.5, -3.25, -3, ..., 0, ..., 3, 3.25, 3.5\}$	$\log(K_{\text{sat},1}) = f_K + \log(K_{\text{sat},1,\text{ref}})$	29
	$\log(K_{\text{sat},2}) = f_K + \log(K_{\text{sat},2,\text{ref}})$	
		Total number of scenarios: 3045

The subscript ref indicates the REFERENCE run with the parameters $W_{\min} = 0$, $KD = KD_{\text{ref}}$ (Fig. 5.2a), and $K_{\text{sat},1} = K_{\text{sat},1,\text{ref}}$ and $K_{\text{sat},2} = K_{\text{sat},2,\text{ref}}$ (Figs. 5.1a and b.)

The pre-factor f_W is used to vary $W_{\min}$ based on the following expression:

$$W_{\min} \;=\; f_W \times W_{\max} = f_W \times (SC_1 + SC_2) \tag{5.8}$$

where $W_{\max}$ is the total storage capacities of both soil layers $(SC_1 + SC_2)$. Because $W_{\max}$ is a spatially-variable field, as illustrated in Fig. 5.1c, the field of $W_{\min}$ in all 3045 parameter sets are always spatially variable, except for $f_W = 0$.

The pre-factor f_K is used to vary simultaneously $K_{\text{sat},1}$ and $K_{\text{sat},2}$ in the following expressions:

$$\log(K_{\text{sat},1}) \;=\; f_K + \log(K_{\text{sat},1,\text{ref}}) \tag{5.9}$$

$$\log(K_{\text{sat},2}) \;=\; f_K + \log(K_{\text{sat},2,\text{ref}}) \tag{5.10}$$

with the subscript ref indicating the fields used in reference run (Fig. 5.1). In each parameter set, Eqs. 5.9 and 5.10 imply that both soil layers have the same f_K. However, because the reference values of $K_{\text{sat},1,\text{ref}}$ and $K_{\text{sat},2,\text{ref}}$ are not the same (see Figs. 5.1a and b), the resulting fields of $K_{\text{sat},1}$ and $K_{\text{sat},2}$ are not the same. Given the spatially variable fields of $K_{\text{sat},1,\text{ref}}$ and $K_{\text{sat},2,\text{ref}}$, the fields of $K_{\text{sat},1}$ and $K_{\text{sat},2}$ for all runs are always spatially variable.

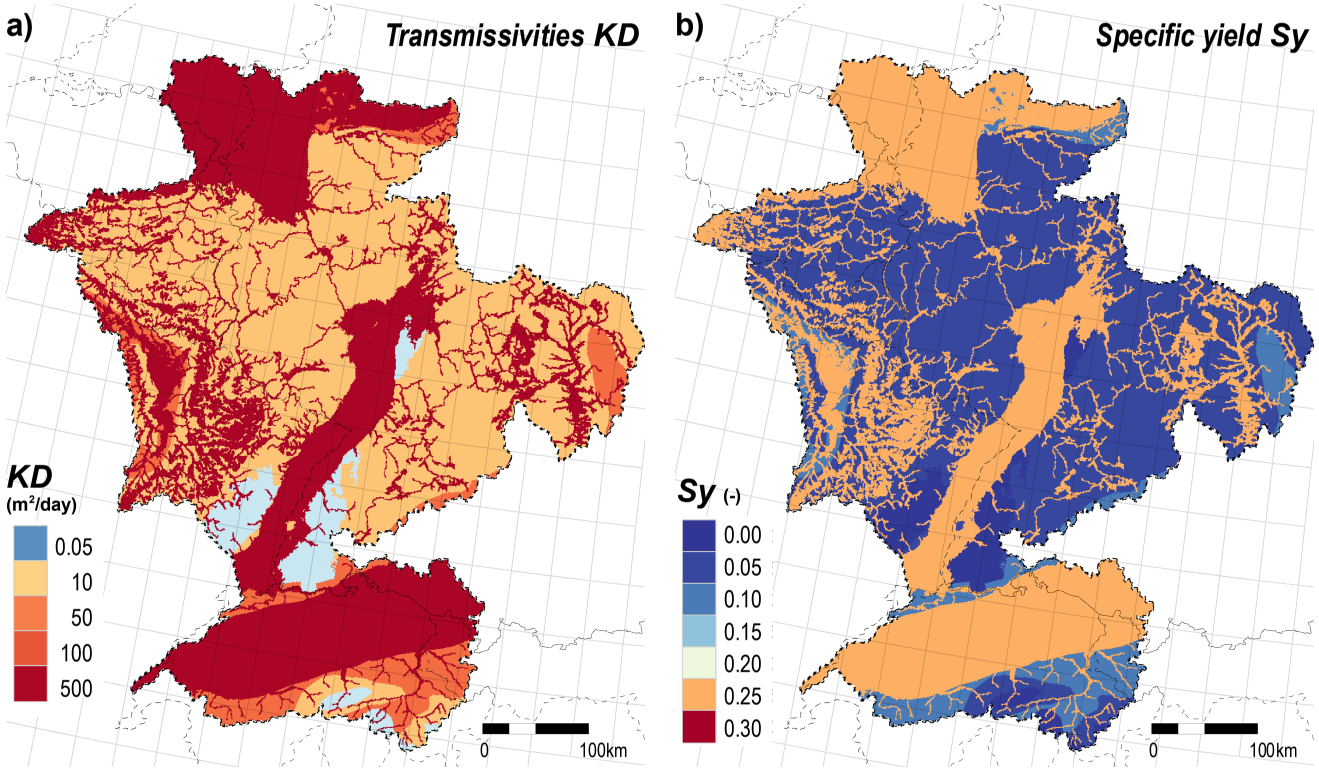

Figure 5.2 The fields of aquifer transmissivities KD used in the reference run (a) and aquifer specific yield Sy (b).

The pre-factor f_{KD} is used to vary KD:

$$\log(KD) = \max\left[\log(KD_{\min}), f_{KD} + \log(KD_{\text{ref}})\right] \tag{5.11}$$

where $KD_{\min}$ is the minimum aquifer transmissivity (taken as 0.05 m^2/day) that can be defined in a parameter set and assumed such that the convergence in the MODFLOW calculation is guaranteed. Equation 5.11 implies that, given the spatially variable field of KD_{ref}, the field of KD for all runs are always spatially variable.

For the study presented in this Chapter 5, the simulations of PCRGLOBWB-MOD_{ONL} were performed for the period 1992-2000. This period is much shorter than the PCRGLOBWB-MOD_{OFF} simulation in Chapter 4 (1965-2008, see Sects. 4.2.3), as PCRGLOBWB-MOD_{ONL} requires much more expensive computation time. This is mainly due to the fact that the MODFLOW simulation for PCRGLOBWB-MOD_{ONL} is done at a daily basis, while the MODFLOW calculation for the previous version PCRGLOBWB-MOD_{OFF} in Chapter 4 was done at a weekly basis. Using a single PC with AMD Athlon Dual Core Processor $5200 + 2.71$ GHz 2GB RAM, a simulation of a single run of PCRGLOBWB-MOD_{ONL} (for the period 1992-2000) takes about 60 h (apart from the requirement to simulate 3045 runs). To tackle this large computation time, we used the LISA Compute Cluster from the SARA Computing and Networking Services (`http://www.sara.nl/`) to simulate all 3045 runs. Note that although the simulations of PCRGLOBWB-MOD_{ONL} in this study were performed for the period 1992-2000, we used only the period 1995-2000 to evaluate the simulation results, as the period 1992-1994 was used as the spin-up period. In the following we describe the observation data and objective functions used for evaluating the model result of each of 3045 run.

5.3.3 Model evaluation criteria

Using discharge measurement time series

The modeled discharge time series, Q_{mod} (i.e. the routed channel discharge $Q_{\text{chn,rt}}$ in Eq. 5.3), were evaluated to the observed discharge time series, Q_{obs}, at two downstream locations: Lobith (Rhine) and Borgharen (Meuse). In both location, we determined the Nash and Sutcliffe (1970) efficiency coefficients NS_{eff}:

$$\text{NS}_{\text{eff}} = 1 - \frac{\sum\left(Q_{\text{obs},t} - Q_{\text{mod},t}\right)^2}{\sum\left(Q_{\text{obs},t} - \overline{Q_{\text{obs}}}\right)^2} \tag{5.12}$$

with $\overline{Q_{\text{obs}}}$ indicating the average of observed time series and t indicating the time index. The evaluation of discharge performance was performed at a daily resolution. Because our model simulations did not include water extraction from the river, biases between simulated and observed discharge time series might be expected (see Sect. 4.4 discussing surface water extraction in Monsin, located about 25 km upstream of

Borgharen). Hence, we also calculated the discharge efficiency coefficients $\mathrm{NS}_{\mathrm{ano}}$ by beforehand removing the biases between two times series:

$$\mathrm{NS}_{\mathrm{ano}} \;=\; 1 - \frac{\sum \left((Q_{\mathrm{obs},t} - \overline{Q_{\mathrm{obs}}}) - (Q_{\mathrm{mod},t} - \overline{Q_{\mathrm{mod}}}) \right)^2}{\sum \left(Q_{\mathrm{obs},t} - \overline{Q_{\mathrm{obs}}} \right)^2} \tag{5.13}$$

with $\overline{Q_{\mathrm{mod}}}$ indicating the average of modeled time series.

Using ERS Soil Water Index

The European Remote Sensing Soil Water Index (ERS SWI) fields provide the spatio-temporal profile soil moisture content in the first meter of soil. Wagner et al. (1999b) derived the ERS SWI time series from the ERS Surface Soil Moisture (SSM) time series, which are retrieved 3-4 times per week from the ERS scatterometers (see Sect. 2.2.2). By employing an exponential low-pass filter to SSM time series, SWI time series were derived and provided in the relative units (0-100%). SWI time series are available at 25-50 km and 10 day resolution. For this study, we resampled them to 30 arc-minute (approximately 50 km at the equator) and monthly resolution. This resampling is necessary in order to reduce the number of missing SWI values that usually occur during the winter (see Fig. 2.2c).

For evaluating model performance in terms of soil moisture dynamics, we compared the time series of the modeled saturation degree of the (entire) upper soil stores of PCRGLOBWB-$\mathrm{MOD}_{\mathrm{ONL}}$ to ERS SWI. The saturation degree from the model, presented in the relative unit (0-100%), is calculated as $s_{12} = (S_1 + S_2) \,/\, (SC_1 + SC_2)$. Comparisons were done at 30 arc-minute and monthly resolution.

As a measure of model performance, we considered the cross correlation coefficient — symbolized as ρ_{SM} — between the ERS SWI and s_{12} time series. We also evaluated the mean absolute error of modeled soil moisture time series. However, due to the uncertainty and discrepancy between the reference values of remotely-sensed SWI (assumed to vary between wilting level and field capacity conditions based on the documentation in `http://www.ipf.tuwien.ac.at/radar/index.php?go=ascat`) and simulated s_{12} (ranging from zero to full saturation conditions), the cumulative distribution function (cdf) matching technique (see e.g. Liu et al., 2011) was implemented in order to rescale s_{12} against SWI time series. Using this technique, which is also a way to remove the bias between both time series, we rescaled the actual values s_{12} to the scaled ("corrected") values $s_{12}^{'}$ [−] such that the cdf curves of $s_{12}^{'}$ and SWI match:

$$\mathrm{cdf}\left(s_{12}^{'}\right) \;=\; \mathrm{cdf}\,(\mathrm{SWI}) \tag{5.14}$$

To implement the principle in Eq. 5.14, we first derived the empirical cumulative distribution function of s_{12} time series, $\mathrm{ecdf}\,(s_{12})$. Next, corresponding to the calculated probabilities in $\mathrm{ecdf}\,(s_{12})$, we produced the sample quantiles of SWI time series which

were further assumed as the scaled or "corrected" time series s'_{12}. Subsequently, for each model run, we evaluated the mean absolute error between s'_{12} and SWI time series — symbolized as $\mathrm{MAE}_{\mathrm{SM-CDF}}$. The correlation coefficient between s'_{12} and SWI time series — symbolized as $\rho_{\mathrm{SM-CDF}}$ — was also calculated as another metric of each model run performance.

Using groundwater head measurement time series

The modeled and observed groundwater head time series were compared in 4250 stations at monthly resolution. We only used and evaluated the time series that consist of at least 50 monthly values in the period 1995-2000. In each station, we calculated the correlation coefficient between the monthly modeled and observed time series — symbolized as ρ_{HEAD}. Also, we calculated the mean absolute error of predicted time series. Note, as discussed in Sect. 4.4, biases between modeled and observed groundwater head time series are expected, especially due to the discrepancies in resolution and elevation references of 30 arc-second resolution model results and point-scale measurement data. Hence, to evaluate the error of predicted groundwater head time series, we preferred to calculate the mean absolute error $\mathrm{MAE}_{\mathrm{ano}}$ using the anomaly time series of the modeled and observed groundwater head time series.

Combining ρ_{HEAD} and $\mathrm{MAE}_{\mathrm{ano}}$, we also calculated the following objective function to evaluate the performance of simulated groundwater head time series, HP:

$$\mathrm{HP} \;=\; \frac{\mathrm{MAE}_{\mathrm{ano}}}{1+\rho_{\mathrm{HEAD}}} \tag{5.15}$$

Equation 5.15 suggests that a low correlation between simulated and measured groundwater head time series (ρ_{HEAD}) will penalize the prediction error ($\mathrm{MAE}_{\mathrm{ano}}$). HP will approach zero (i.e. $\mathrm{HP} \to 0$) for a perfect fit between simulated and measured time series ($\mathrm{MAE}_{\mathrm{ano}} \to 0$) and become very large ($\mathrm{HP} \to \infty$) for a perfect negative correlation between simulated and measured time series ($\rho_{\mathrm{HEAD}} \to -1$).

5.4 Results and discussion

This Sect. 5.4 discusses the results of all model runs performed in this study. In Sect. 5.4.1, the results of 3045 runs are analyzed based on discharge observations. Sect. 5.4.2 presents the evaluation of the model results based on ERS SWI time series. Next, based on the analyses in Sects. 5.4.1 and 5.4.2, calibration scenarios are defined in Sect. 5.4.3. Subsequently, the results of all calibration scenarios are verified to 4250 observed groundwater head time series and discussed in Sect. 5.4.4.

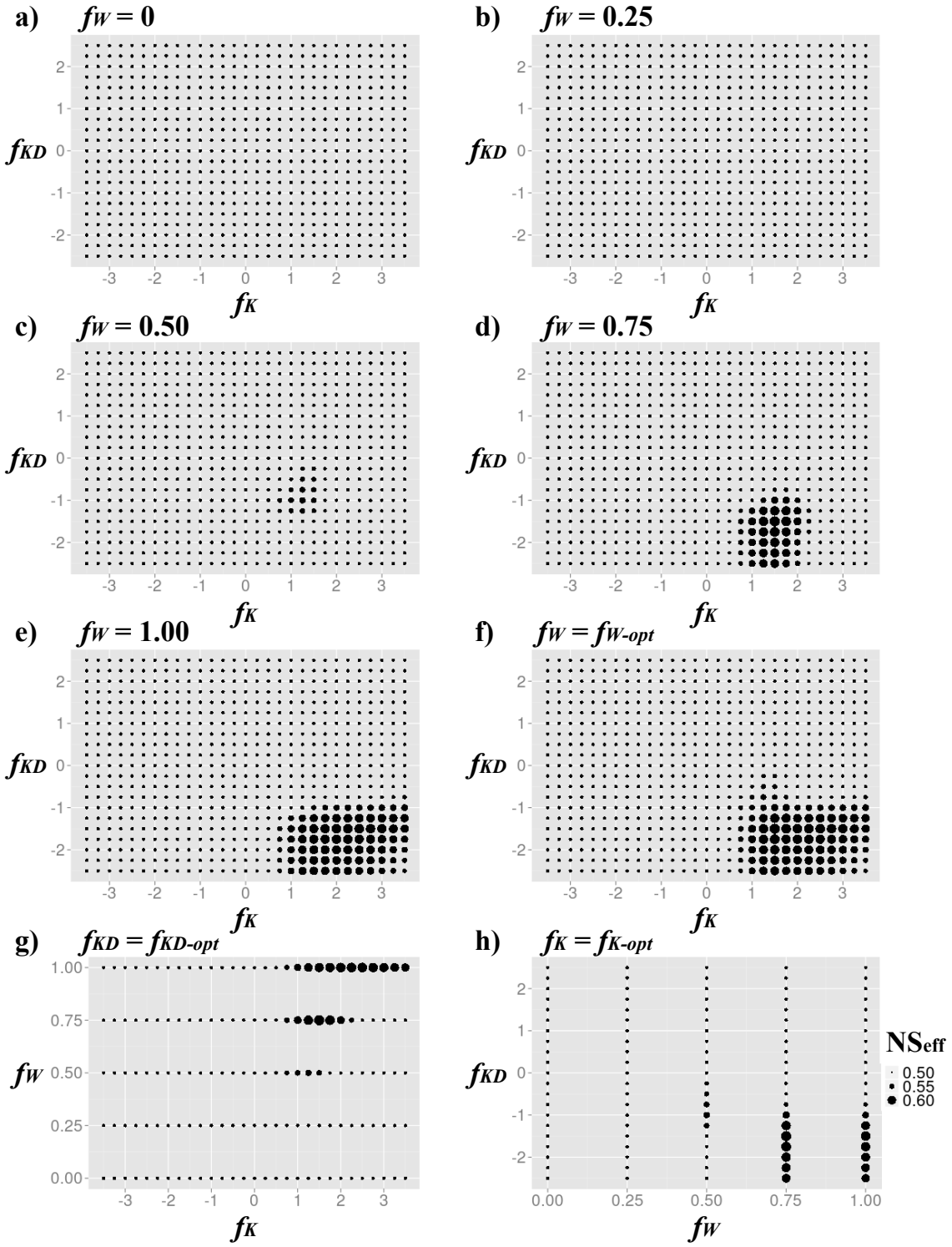

Figure 5.3 Pre-factor spaces corresponding to Rhine (Lobith) daily discharge efficient coefficients NS_{eff} indicated by areas of circles (see text for more explanation). Note that the subscript *opt* in f, g and h indicates a pre-factor value (i.e. f_W in f, f_{KD} in g and f_W in h) that gives the highest performance in a pre-factor space of the other two pre-factors (i.e. f_K and f_{KD} in f, f_K and f_W in g and f_W and f_{KD} in h.

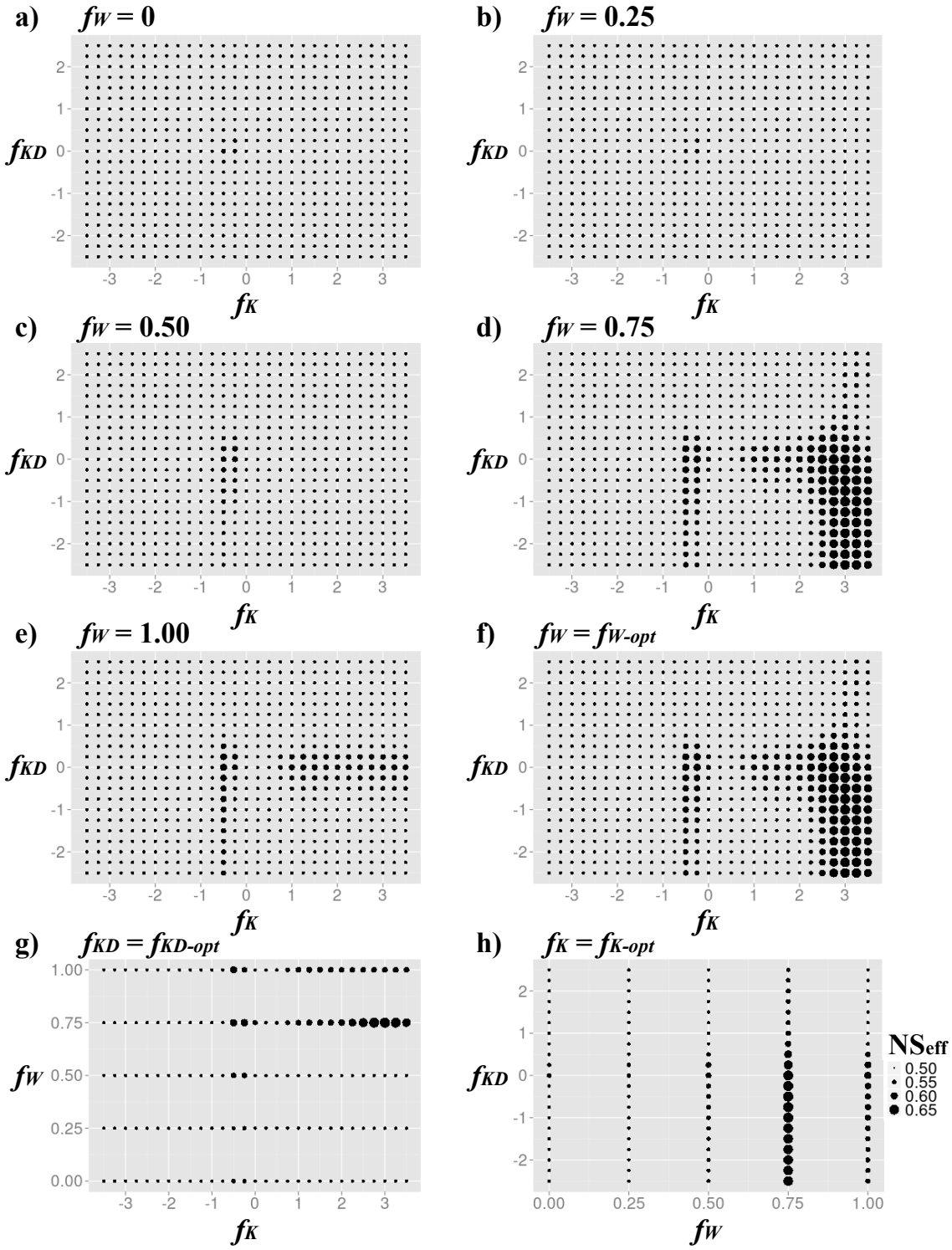

Figure 5.4 Pre-factor spaces corresponding to Meuse (Borgharen) daily discharge efficient coefficients NS_{eff} indicated by areas of circles (see text for more explanation). Note that the subscript *opt* in f, g and h indicates a pre-factor value (i.e. f_W in f, f_{KD} in g and f_W in h) that gives the highest performance in a pre-factor space of the other two pre-factors (i.e. f_K and f_{KD} in f, f_K and f_W in g and f_W and f_{KD} in h.

5.4.1 Model evaluation using in-situ daily discharge measurement time series

To summarize the results of all 3045 runs, Fig. 5.3 presents the "pre-factor spaces" (or commonly known as "parameter spaces") corresponding to daily discharge efficient coefficients NS_{eff} at Lobith (Rhine basin). The magnitudes of NS_{eff} — indicated by the areas/sizes of the circles — are plotted for all combinations of pre-factors. Figures 5.3a, b, c, d and e show NS_{eff} for all combinations f_K and f_{KD}, with $f_W = 0$ (a), $f_W = 0.25$ (b), $f_W = 0.5$ (c), $f_W = 0.75$ (d) and $f_W = 1$ (e), respectively. Comparing those five plots, we observe that good discharge performance can be obtained only if high values of f_W are used ($f_W \geq 0.75$). Besides high values of f_W, from Fig. 5.3d ($f_W = 0.75$) and Fig. 5.3d ($f_W = 1$), we find that high values of f_W and low values of f_{KD} are needed to provide good discharge performance. Fig. 5.3f presents the maximum values of NS_{eff}, which are the composite of all combinations of f_K and f_{KD} in Fig. 5.3a to e. Similarly to Fig. 5.3f, we present the pre-factor spaces of f_K and f_W in Fig. 5.3g and the pre-factor spaces of f_W and f_{KD} in Fig. 5.3h. Note that the subscript *opt* in Figs. 5.3f, g and h indicates a pre-factor value (i.e. f_W in Fig. 5.3f, f_{KD} in Fig. 5.3g and f_W in Fig. 5.3h) that give the highest NS_{eff} in a pre-factor space of the other two pre-factors (i.e. f_K and f_{KD} in Fig. 5.3f, f_K and f_W in Fig. 5.3g and f_W and f_{KD} in Fig. 5.3h). From Figs. 5.3f, g and h, it is clear that that the combinations of high values of f_W, high values of f_K and low values of f_{KD} provide good discharge performance.

For the discharge performance at Borgharen (Meuse basin), a similar presentation (as in Fig. 5.3 and explained in the previous paragraph) is given in Fig. 5.4. From Fig. 5.4, it is also evident that combinations of high f_W, high f_K and low f_{KD} again result in good discharge performance. Therefore, for both Rhine and Meuse basins, we can conclude that combinations of high local minimum soil capacities $W_{\min}$, high upper soil saturated conductivities K_{sat} and low aquifer transmissivities KD generally yield good fits of modeled to observed discharge time series. With a combination of high K_{sat} and $W_{\min}$, excess precipitation (after interception) tends to first infiltrate into the soil and the flow to river as sub-surface flow components (i.e. interflow Q_{sf} and baseflow Q_{bf}), as expected in a humid temperate zones (see e.g. Savenije, 2010), including in our study area. In other words, this suggests the importance of preferential flow (in the study area), which is not incorporated in PCR-GLOBWB-MOD and a subject for its future development. As the current PCR-GLOBWB-MOD model structure only includes soil matrix flow (mainly based on Campbell, 1974; Clapp and Hornberger, 1978), high values of K_{sat} are needed to simulate such preferential flow mechanism.

The pre-factor spaces can also be represented by two-dimensional scatter-plots between pre-factors (given in x-axis) and model performance indicators (y-axis), as plotted in Fig. 5.5a for the Rhine basin and in Fig. 5.5b for the Meuse basin. In these scatter-plots, the pre-factors f_W, f_K and f_{KD} are presented against NS_{eff} (calculated using original daily discharge time series, see Eq. 5.12) and NS_{ano} (calculated using

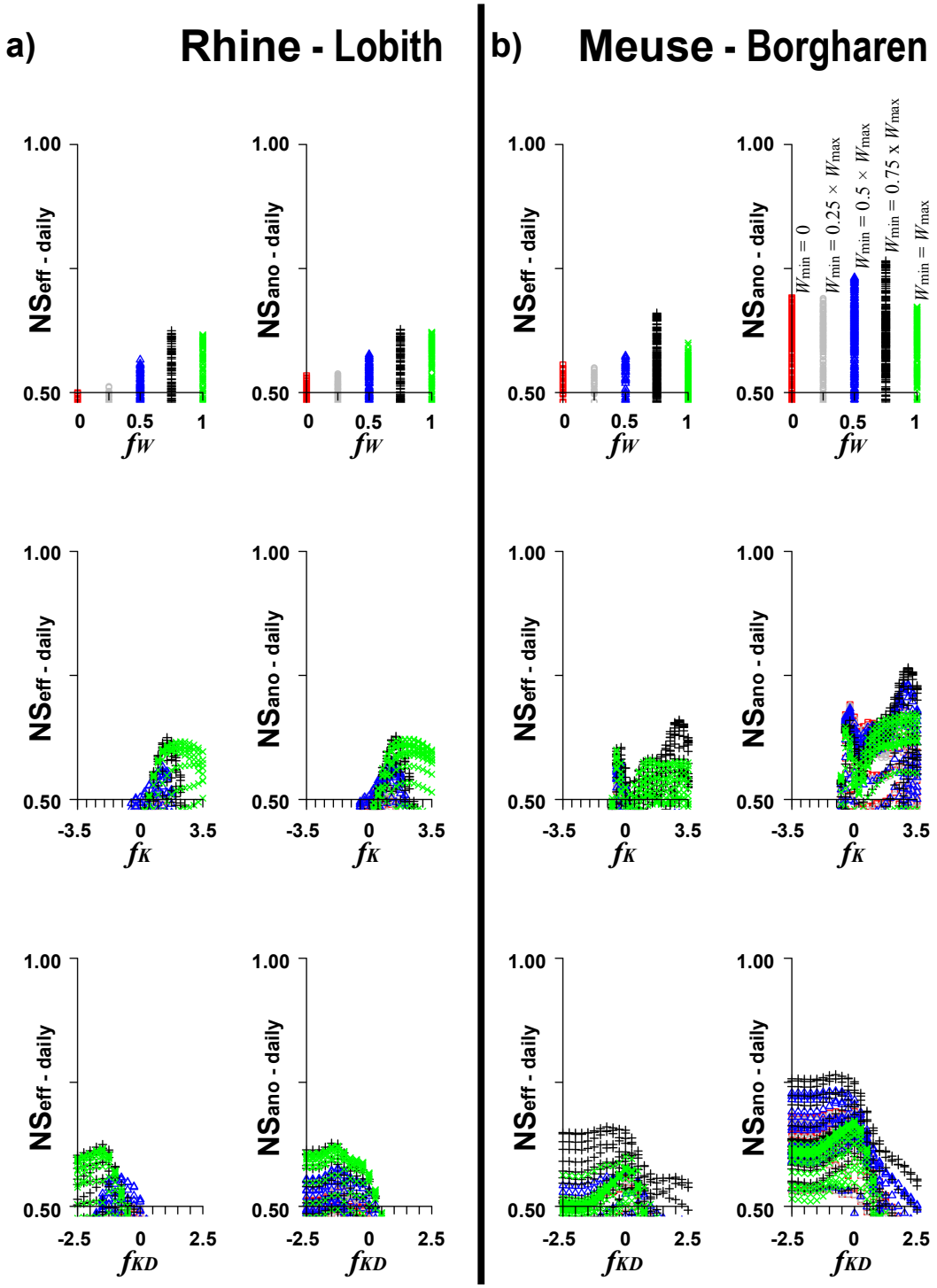

Figure 5.5 Scatter-plots of model performance indicators NS_{eff} and NS_{ano} (y-axes) based on the daily discharge observations in Lobith, Rhine basin (a) and Borgharen, Meuse basin (b) vs. pre-factors f_W, f_K and f_{KD} (x-axes). Note that colors and dot shapes indicate different values of f_W (see the plot on the right upper corner).

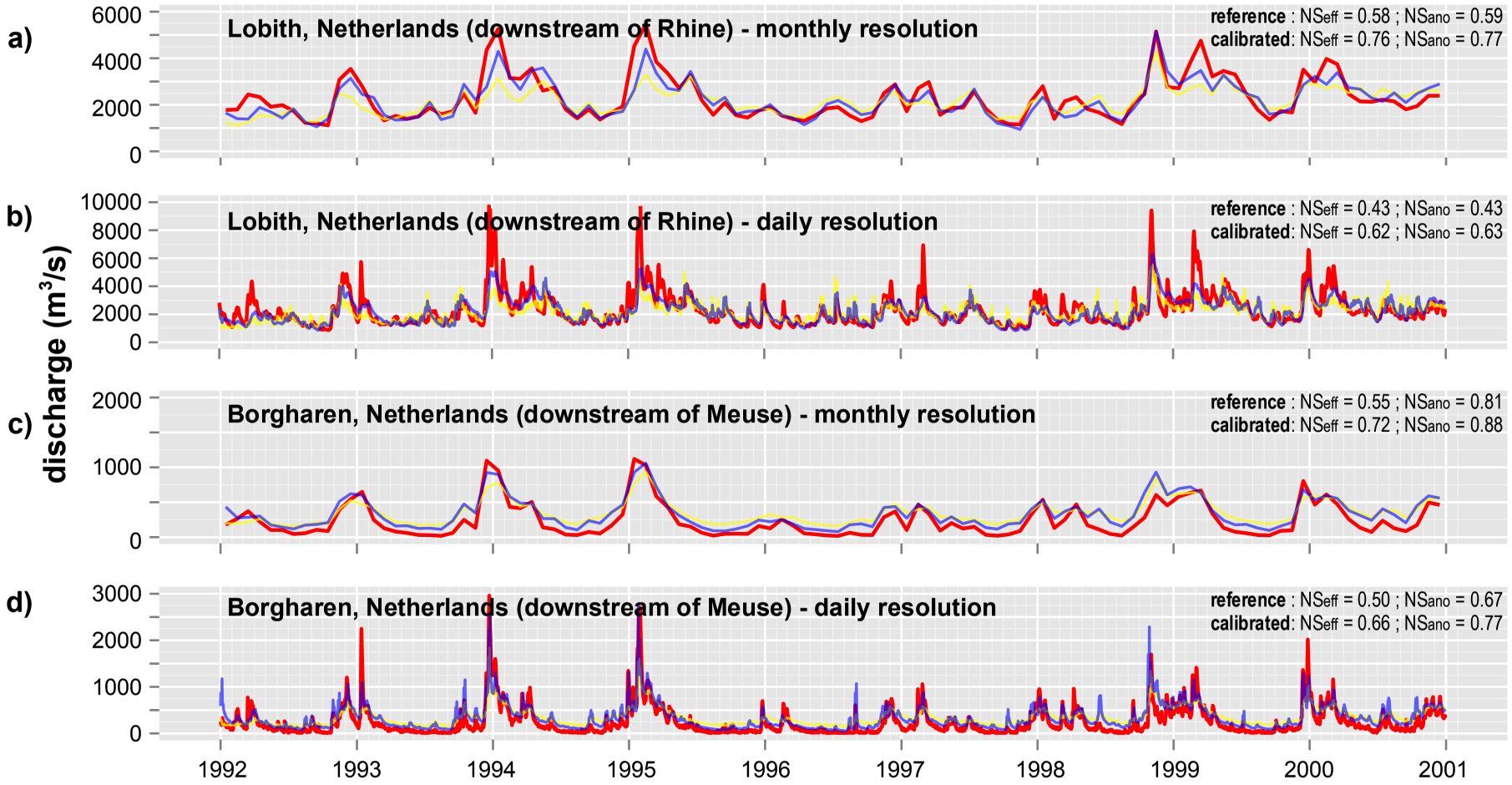

Figure 5.6 Comparisons between measured discharge (red) and simulated discharge (yellow and blue) time series. The yellow lines represent the results of the simulations of the reference run (uncalibrated), while the blue lines represent the results of the best simulations based on daily discharge observations near the basin outlets (see text for more explanations).

time series of daily discharge anomalies, see Eq. 5.13). For the Rhine basin (Fig. 5.5a), we find that the scatter-plots for NS_{eff} are generally similar as the scatter-plots for NS_{ano}. However, for the Meuse basin (Fig. 5.5a), the values of NS_{ano} are higher than the values of NS_{eff}. This confirms the bias (between simulated and observed time series) that is attributable to surface water extraction (as mentioned in Sect. 5.3.3).

From all scatter-plots in Figs. 5.5a and b, as well as from the parameter spaces in Figs. 5.3 and 5.4, all pre-factors are identifiable. We can distinguish parameter ranges leading to better and worse performance, as well as their global optima. For the Rhine basin, the optimal discharge performance is obtained for the parameter set $f_W = 0.75$, $f_K = 1.5$ and $f_{KD} = -1.5$. The run with this parameter set can reproduce the observed discharge time series reasonably well, as illustrated in Fig. 5.6a (at monthly resolution: $NS_{eff} = 0.76$ and $NS_{ano} = 0.77$) and Fig. 5.6b (at daily resolution: $NS_{eff} = 0.62$ and $NS_{ano} = 0.63$), except the fact that some extreme peaks cannot properly be simulated. This lack of fit is most likely due to errors in the input forcing data and other parameters, such as snow module and soil thickness parameters which were not calibrated. For the Meuse basin, the optimal parameter set is a combination of $f_W = 0.75$, $f_K = 3$ and $f_{KD} = -0.75$. The modeled discharge time series at Borgharen of this run, illustrated in Fig. 5.6c (monthly resolution, $NS_{eff} = 0.72$ and $NS_{ano} = 0.88$) and Fig. 5.6d (daily resolution, $NS_{eff} = 0.66$ and $NS_{ano} = 0.77$), indicate a reasonably good performance. As expected, its major drawback is the fact that the low flow events during summer months cannot be properly simulated as the model simulation did not incorporate water extraction from the river (see Sect. 5.3.3).

5.4.2 Model evaluation using ERS Soil Water Index time series

Evaluation for pixels located in the Dutch and Flemish lowlands

Figure 5.7 shows the scatter-plots between the pre-factors used (x-axes: f_W, f_K and f_{KD}) and soil moisture performance indicators (y-axes: objective functions ρ_{SM}, ρ_{SM-CDF} and MAE_{SM-CDF}) for pixel 21 (half arc-degree resolution), located in a low lying area (see Fig. 2.2 for the location). For all objective functions ρ_{SM}, ρ_{SM-CDF} and MAE_{SM-CDF} in Fig. 5.7, we observe that the pre-factors f_W and f_{KD} are not identifiable. Hence, it is difficult to calibrate the parameters W_{min} and KD if we rely only on ERS SWI time series. In Fig. 5.7, the pre-factor f_K is better identifiable. It indicates the possibilities to use SWI time series to calibrate the upper soil hydraulic conductivities K_{sat} and thus indirectly tune groundwater recharge Q_{23} (see Sect. 5.2). We can distinguish parameter ranges leading to good and poor performance from the point of view of their simulated soil moisture dynamics.

However, although f_K can be identified somewhat better, it remains weakly identifiable because there are two distinct local optima (i.e. maxima for ρ_{SM} and ρ_{SM-CDF}, and minima for MAE_{SM-CDF}) observed in Fig. 5.7. From all scatter-plots between the pre-factor f_K and objective functions ρ_{SM}, ρ_{SM-CDF} and MAE_{SM-CDF} (in Fig. 5.7),

we find that there are two local optima: located at around $f_K = -2$ (considered as "global optimum") and at around $f_K = 2.75$ (considered as "local optimum").

Similar to Figs. 5.3 and 5.4 for discharge, Fig. 5.8 shows the pre-factor spaces corresponding to the magnitudes of ρ_{SM} (indicated by circles areas) for pixel 21. From Fig. 5.8, it is evident that f_W and f_{KD} are not identifiable and there are multiple optima for f_K. The occurrence of multiple optima of f_K indicates that the estimation of pre-factor f_K is not trivial if we rely only on ERS SWI for model calibration.

The above-mentioned phenomena found for pixel 21 are exemplary for the other pixels located in low-lying and flat regions, i.e. sedimentary basin areas and having shallow groundwater tables (see Figs. 2.1b and 2.2a), particularly in the Dutch and Flemish lowlands). As illustration for other pixels located in this region, Fig. 5.9a and Fig. 5.9b present the scatter-plots between the objective functions (i.e. ρ_{SM}, $\rho_{\mathrm{SM-CDF}}$ and $\mathrm{MAE}_{\mathrm{SM-CDF}}$) and pre-factor f_K for pixels 25 and 39, respectively. These scatter-plots are quite similar with the ones for pixel 21 presented in Fig. 5.7, in which there are two optima observed. Note that pre-factors f_W and f_{KD} are not identifiable for pixels 25 and 39, as well as for the other pixels in the entire study area (like the case for pixel 21, illustrated in Figs. 5.7 and 5.8). Therefore, for the sake of simplicity, the scatter-plots of f_W and f_{KD} for the other pixels (besides pixel 21) are not presented.

Evaluation for pixels located in the Upper Rhine Graben

The Upper Rhine Graben is an intermediate sedimentary basin region between the Dutch lowlands and mountainous areas of Rhine basin (see Sect. 2.2.1 and Fig. 2.1). For the pixels located in the Upper Rhine Graben, we refer to Fig. 5.9c and Fig. 5.9d, showing the scatter-plots between the objective functions (i.e. ρ_{SM}, $\rho_{\mathrm{SM-CDF}}$ and $\mathrm{MAE}_{\mathrm{SM-CDF}}$) and pre-factor f_K for pixels 95 and 112, respectively. These plots show that the pre-factors f_K are somewhat less identifiable compared to the ones for pixels 21, 25 and 39 (Figs. 5.7, 5.9a and 5.9b). This fact is also illustrated in the pre-factor spaces of pixel 95 in Fig. 5.10 showing that it is difficult to identify the optimal f_K. The difficulty in identifying the optimal f_K for such pixels is most likely caused by the spatial heterogeneity of their landscape properties. As illustrated in the elevation and groundwater head maps in Figs. 2.1a and b, most of the pixels located in the Upper Rhine Graben (see Fig. 2.2b for the pixel locations) are mixtures of sedimentary basin (with shallow groundwater) and mountainous areas (with deep groundwater).

Evaluation for pixels located in mountainous areas

To represent pixels located in mountainous areas (see Fig. 2.1b), we present the pre-factor spaces (corresponding to the objective function ρ_{SM}) for pixel 91 in Fig. 5.11, pixel 97 in Fig. 5.12 and pixel 117 in Fig. 5.13. Their scatter-plots for pre-factor f_K are presented in Fig. 5.14a (pixel 91), Fig. 5.14b (pixel 97) and Fig. 5.14c (pixel

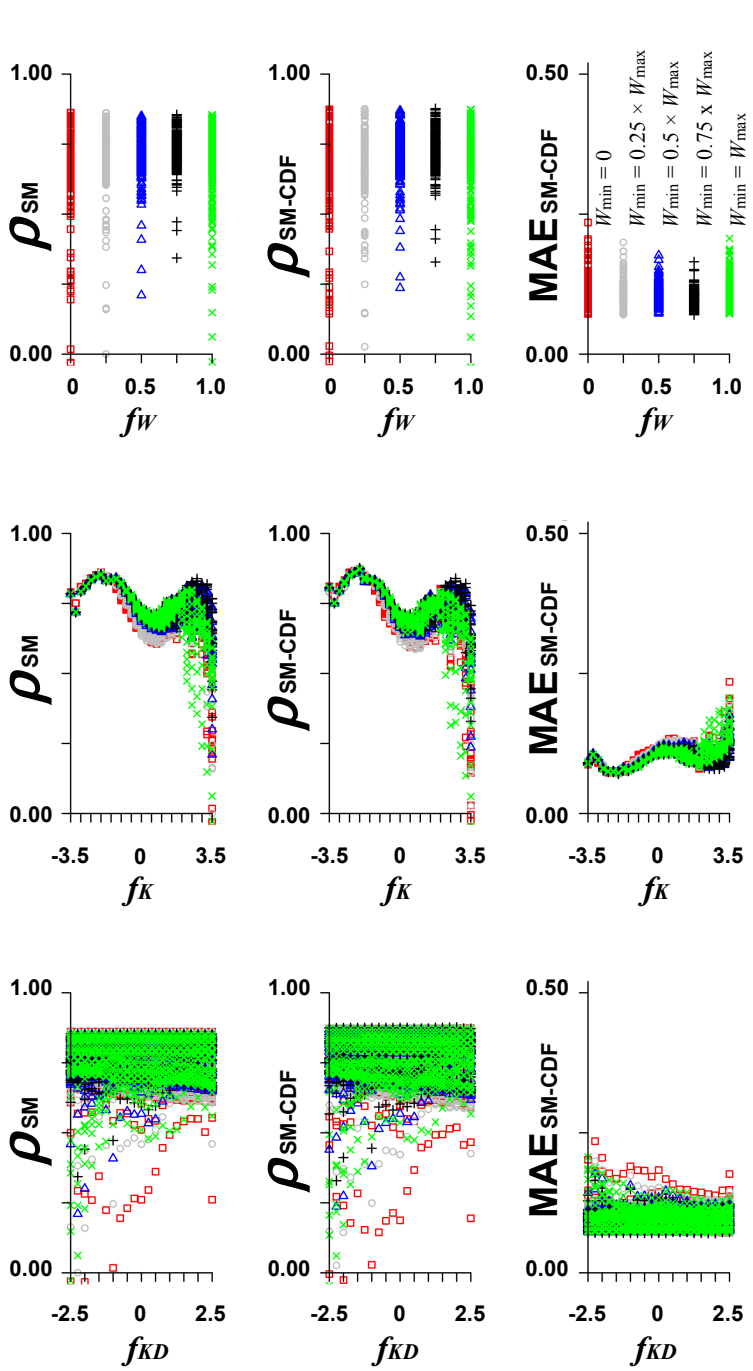

Figure 5.7 Scatter-plots of soil moisture performance indicators ρ_{SM}, $\rho_{\mathrm{SM-CDF}}$ and $\mathrm{MAE}_{\mathrm{SM-CDF}}$ vs. pre-factors f_W, f_K and f_{KD} for pixel 21 (see Fig. 2.2b for the pixel location). Note that colors and dot shapes indicate different values of f_W (see the plot on the right upper corner).

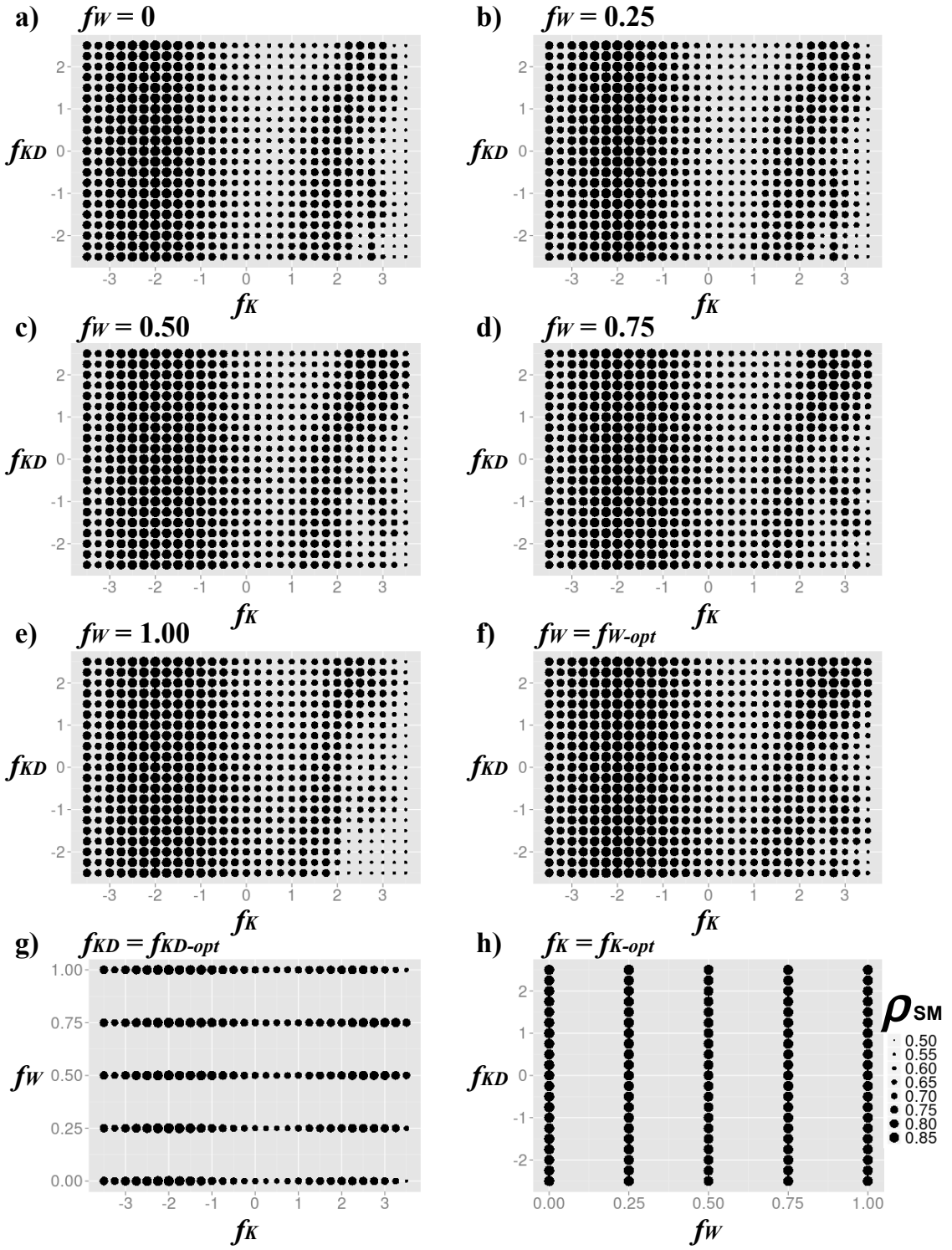

Figure 5.8 Pre-factor spaces corresponding to ρ_{SM} — indicated by areas of circles — for pixel 21 (see Fig. 2.2b for the pixel location and see text for more explanation). Note that the subscript *opt* in f, g and h indicates a pre-factor value (i.e. f_W in f, f_{KD} in g and f_W in h) that give the highest performance in a pre-factor space of the other two pre-factors (i.e. f_K and f_{KD} in f, f_K and f_W in g and f_W and f_{KD} in h).

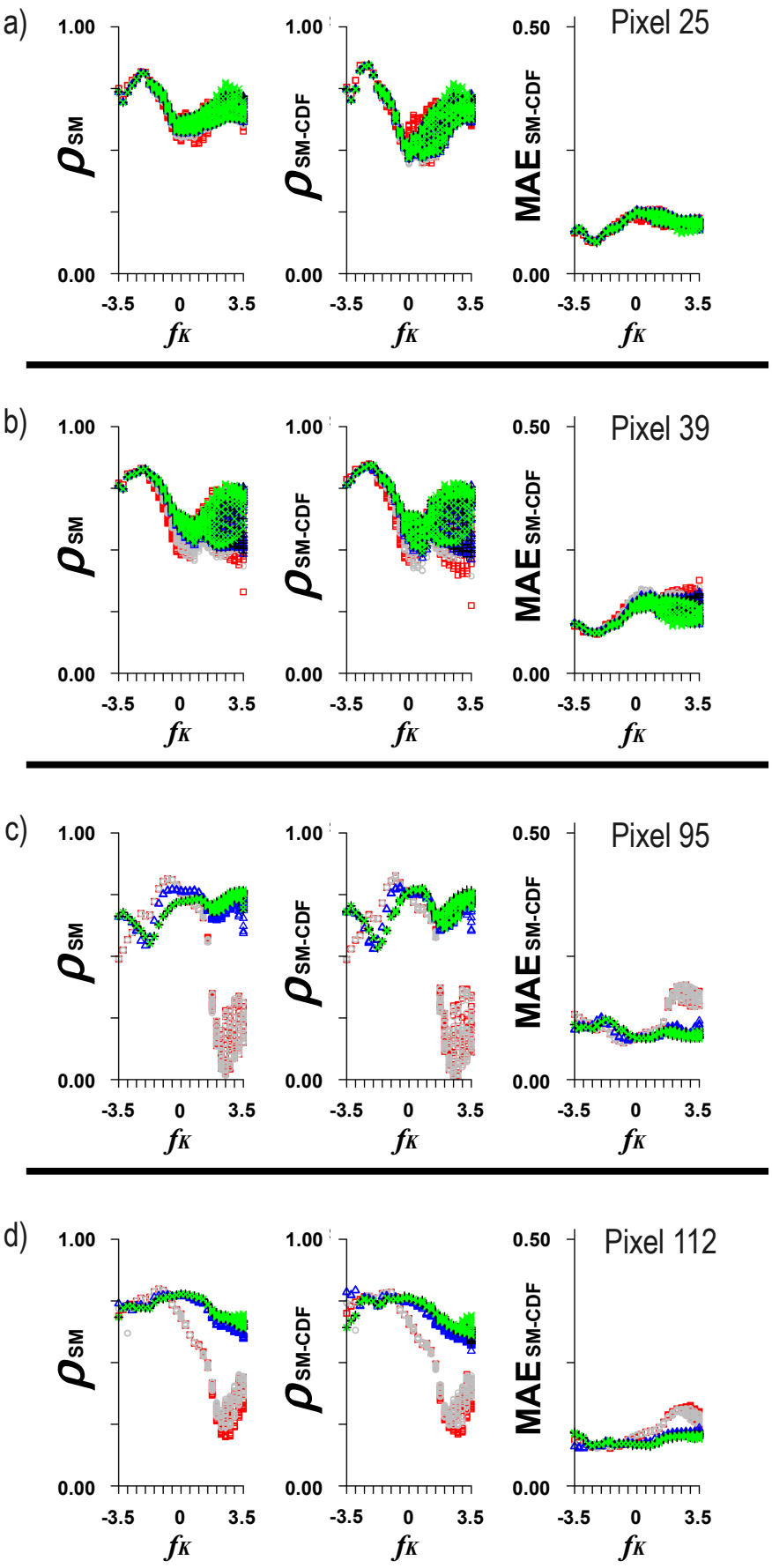

Figure 5.9 Scatter-plots of soil moisture performance indicators vs. pre-factor f_K for pixels 25, 39, 95 and 112 (see Fig. 2.2b for the pixel locations). Note that colors and dot shapes indicate different values of f_W, as indicated in Fig. 5.7.

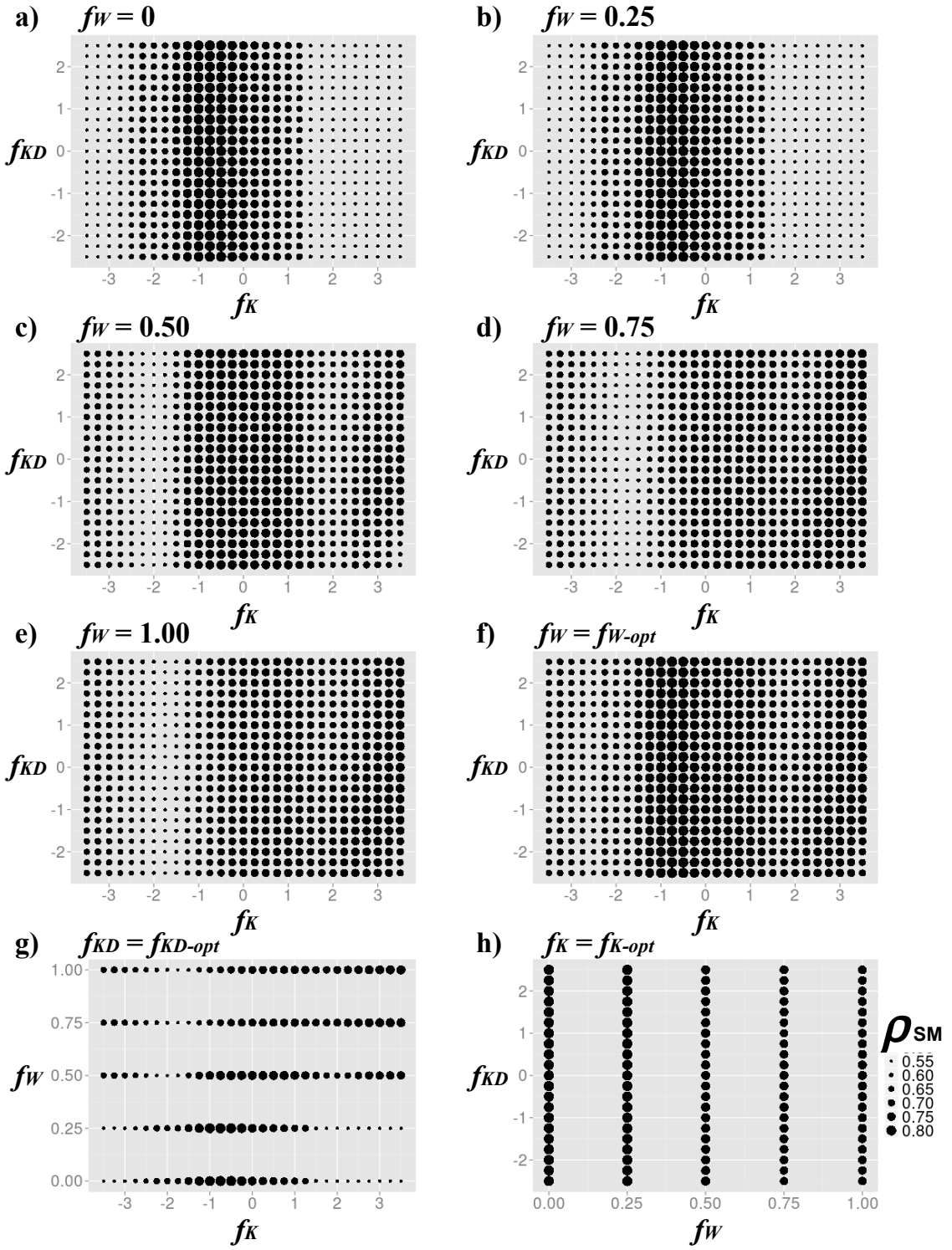

Figure 5.10 Pre-factor spaces corresponding to ρ_{SM} — indicated by areas of circles — for pixel 95 (see Fig. 2.2b for the pixel location and see text for more explanation). Note that the subscript *opt* in f, g and h indicates a pre-factor value (i.e. f_W in f, f_{KD} in g and f_W in h) that give the highest performance in a pre-factor space of the other two pre-factors (i.e. f_K and f_{KD} in f, f_K and f_W in g and f_W and f_{KD} in h).

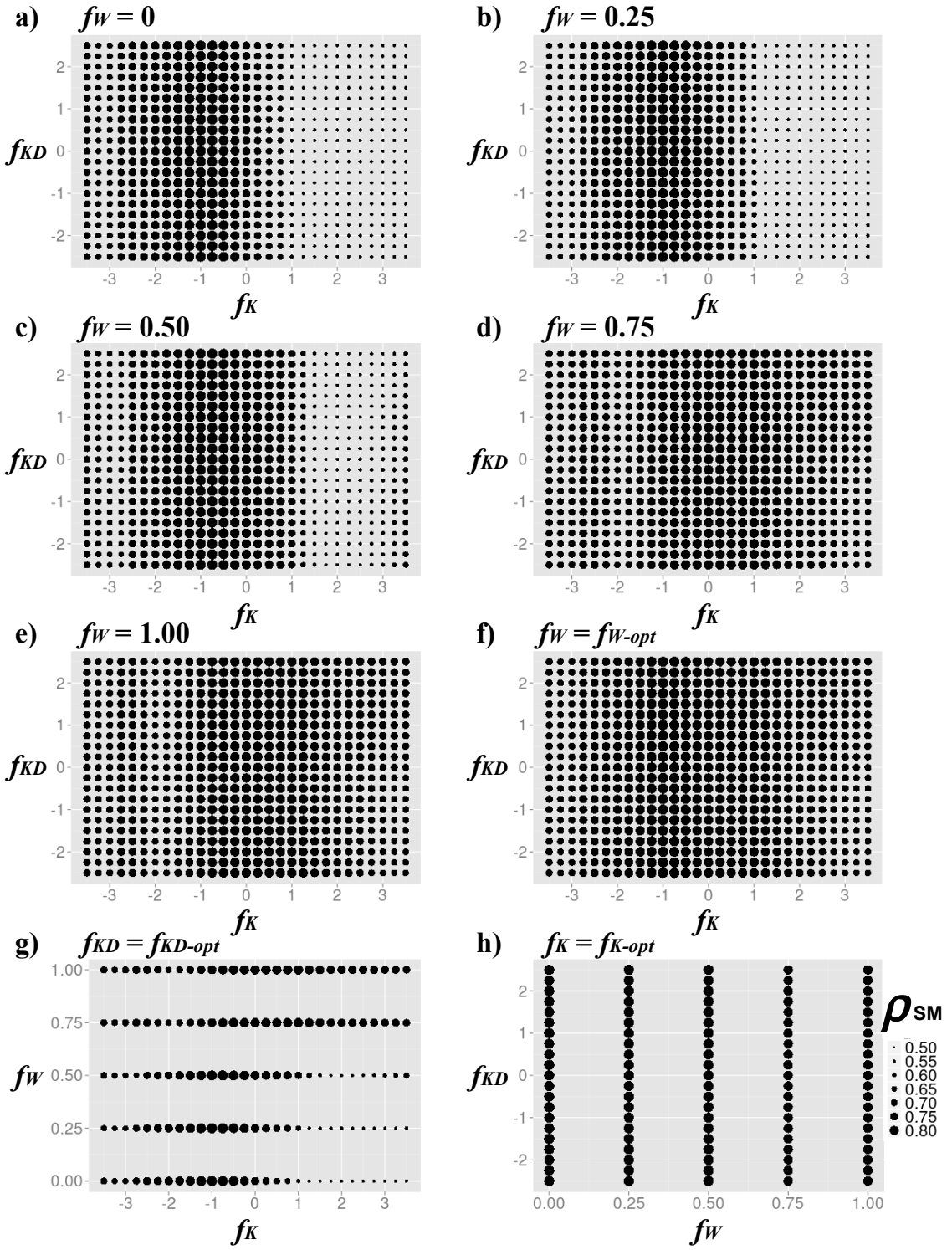

Figure 5.11 Pre-factor spaces corresponding to ρ_{SM} — indicated by areas of circles — for pixel 91 (see Fig. 2.2b for the pixel location and see text for more explanation). Note that the subscript *opt* in f, g and h indicates a pre-factor value (i.e. f_W in f, f_{KD} in g and f_W in h) that give the highest performance in a pre-factor space of the other two pre-factors (i.e. f_K and f_{KD} in f, f_K and f_W in g and f_W and f_{KD} in h).

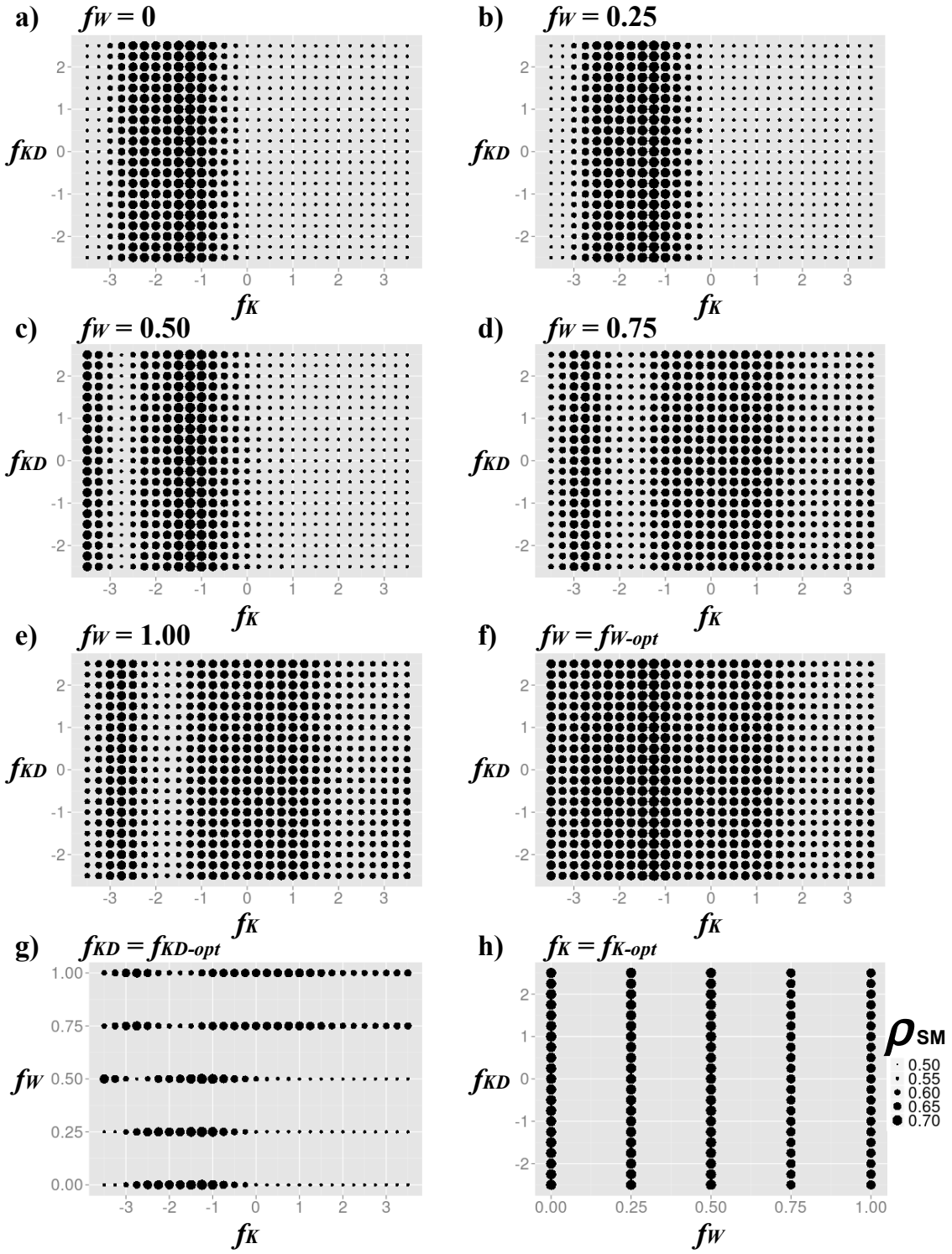

Figure 5.12 Pre-factor spaces corresponding to ρ_{SM} — indicated by areas of circles — for pixel 97 (see Fig. 2.2b for the pixel location and see text for more explanation). Note that the subscript *opt* in f, g and h indicates a pre-factor value (i.e. f_W in f, f_{KD} in g and f_W in h) that give the highest performance in a pre-factor space of the other two pre-factors (i.e. f_K and f_{KD} in f, f_K and f_W in g and f_W and f_{KD} in h).

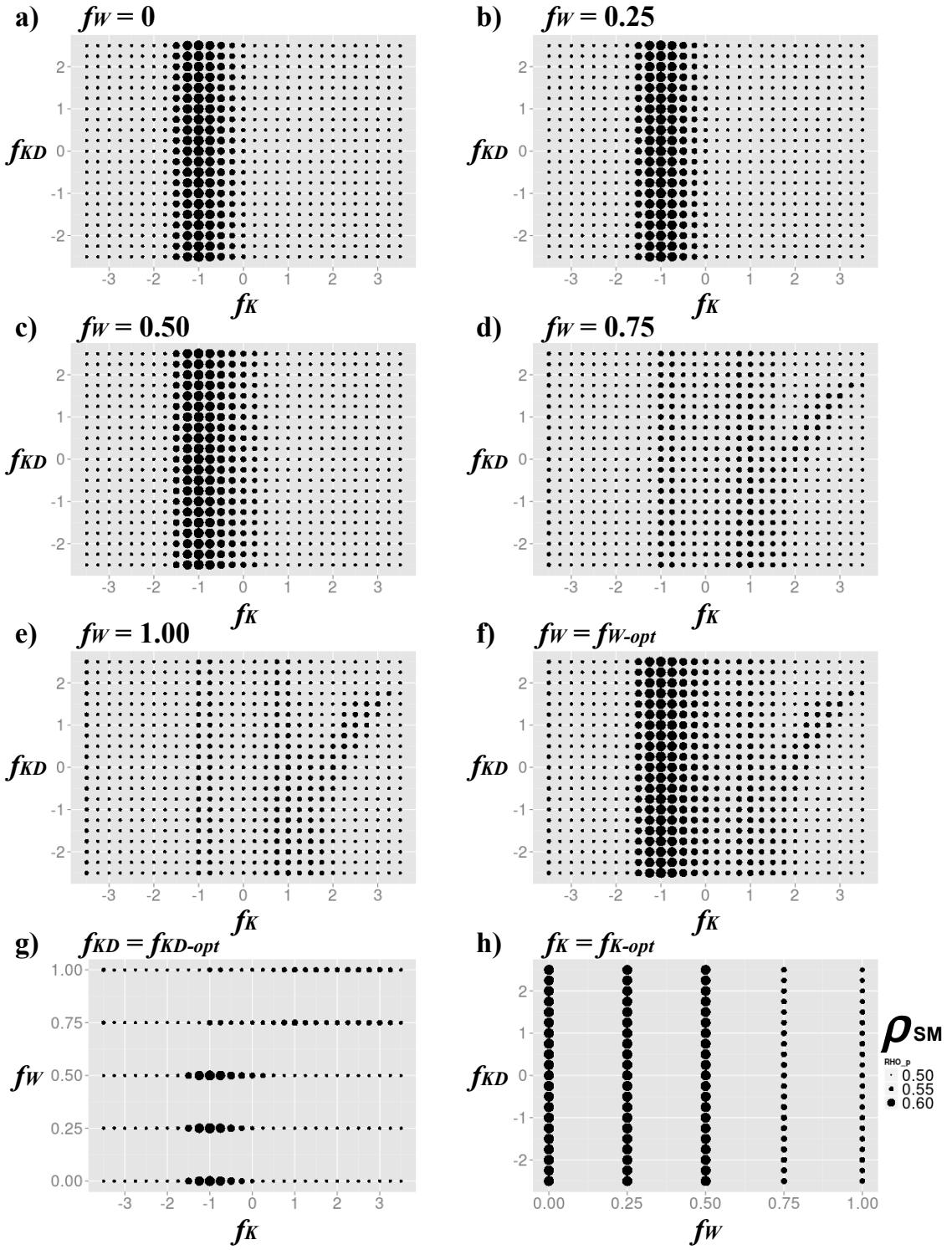

Figure 5.13 Pre-factor spaces corresponding to ρ_{SM} — indicated by areas of circles — for pixel 117 (see Fig. 2.2b for the pixel location and see text for more explanation). Note that the subscript *opt* in f, g and h indicates a pre-factor value (i.e. f_W in f, f_{KD} in g and f_W in h) that give the highest performance in a pre-factor space of the other two pre-factors (i.e. f_K and f_{KD} in f, f_K and f_W in g and f_W and f_{KD} in h).

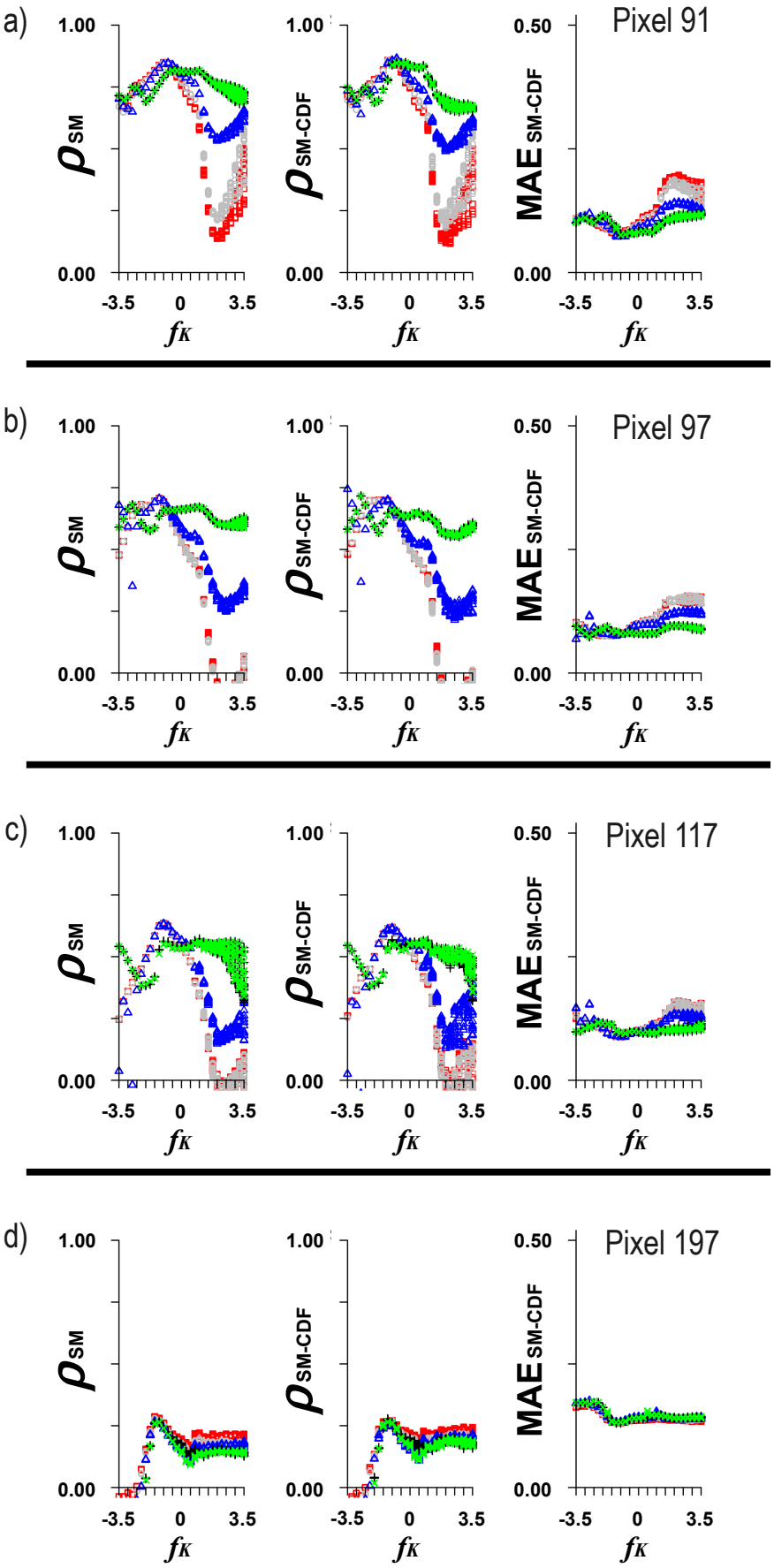

Figure 5.14 Scatter-plots of soil moisture performance indicators vs. pre-factor f_K for pixels 91, 97, 117 and 197 (see Fig. 2.2b for the pixel locations). Note that colors and dot shapes indicate different values of f_W, as indicated in Fig. 5.7.

117). For both pixels 91 and 97, we find that the pre-factors f_W and f_{KD} are not identifiable, as illustrated in Figs. 5.11h and 5.12h . In term of f_K, we find that the pre-factors f_K are identifiable for low f_W values ($f_W \leq 0.5$, see Figs. 5.11a to c and Figs. 5.12a to c). Yet, as pre-factors f_W are increased ($f_W > 0.5$), the pre-factors f_K become less identifiable (Figs. 5.11d and e and Figs. 5.12d and e). Based on these facts, we consider that the pre-factors f_K are not identifiable (see also Figs. 5.11f to h and Figs. 5.12f to h). Note that as indicated in Fig. 5.11g and Fig. 5.12g, we find a mutual dependence between increasing f_K and increasing f_W in order to maintain high ρ_{SM}. This suggests that there are multiple solutions leading to an equal performance. This equifinality is also clear from the scatter-plots in Fig. 5.14a and Fig. 5.14b.

From the pre-factor space of ρ_{SM} in Fig. 5.13, the pre-factor f_K for pixel 117 is relatively identifiable, particularly for low f_W ($f_W \leq 0.5$ (see Figs. 5.12a, b and c, and Figs. 5.13f, g and h). However, the values of ρ_{SM} are considerably low ($\rho_{\mathrm{SM}} < 0.65$), indicating the problem in matching simulated soil moisture dynamics to ERS SWI time series. This low performance is most likely due to errors in the remote sensing data. It is known that scatterometer signals from mountainous regions often contain artefacts (Wagner, 1998; Wagner et al., 1999a) and therefore consequently affect the accuracy of SWI time series. As another example, the scatter-plots of pixel 197 (also in a mountainous region) in Fig. 5.14d show even worse performance ($\rho_{\mathrm{SM}} < 0.35$).

Following all above-mentioned analyses, we conclude that it is difficult to find optimal pre-factor sets for pixels located in mountainous areas. This indicates the limitation of using SWI series for the model calibration in mountainous areas.

Study area-averages of soil moisture performance indicators

We also calculated the study area-averages of performance indicators ρ_{SM}, $\rho_{\mathrm{SM-CDF}}$ and $\mathrm{MAE}_{\mathrm{SM-CDF}}$. These average values, calculated for all 3045 runs, are given in the scatter-plots in Fig. 5.15. Note that to calculate these averages, we used the surface area of each half arc-degree pixel as the weight factor. From Fig. 5.15, it is evident that that the pre-factors f_W and f_{KD} are not identifiable, while the pre-factor f_K is relatively identifiable. Yet, as indicated by the maximum values of ρ_{SM} and $\rho_{\mathrm{SM-CDF}}$, we observe relatively weak performance ($\rho_{\mathrm{SM}} < 0.65$ and $\rho_{\mathrm{SM-CDF}} < 0.65$). This low performance is not surprising because the study area is dominated by mountainous areas (see Fig. 2.1), where ERS SWI time series most-likely contain artefacts.

5.4.3 Defining calibration scenarios (developed based on Sects. 5.4.1 and 5.4.2)

As mentioned in Sect. 5.3.3, this study aims to investigate the value of using various observations types for calibrating the coupled groundwater-land surface model PCR-GLOBWB-MOD. Using the results discussed in Sects. 5.4.1 and 5.4.2, we define

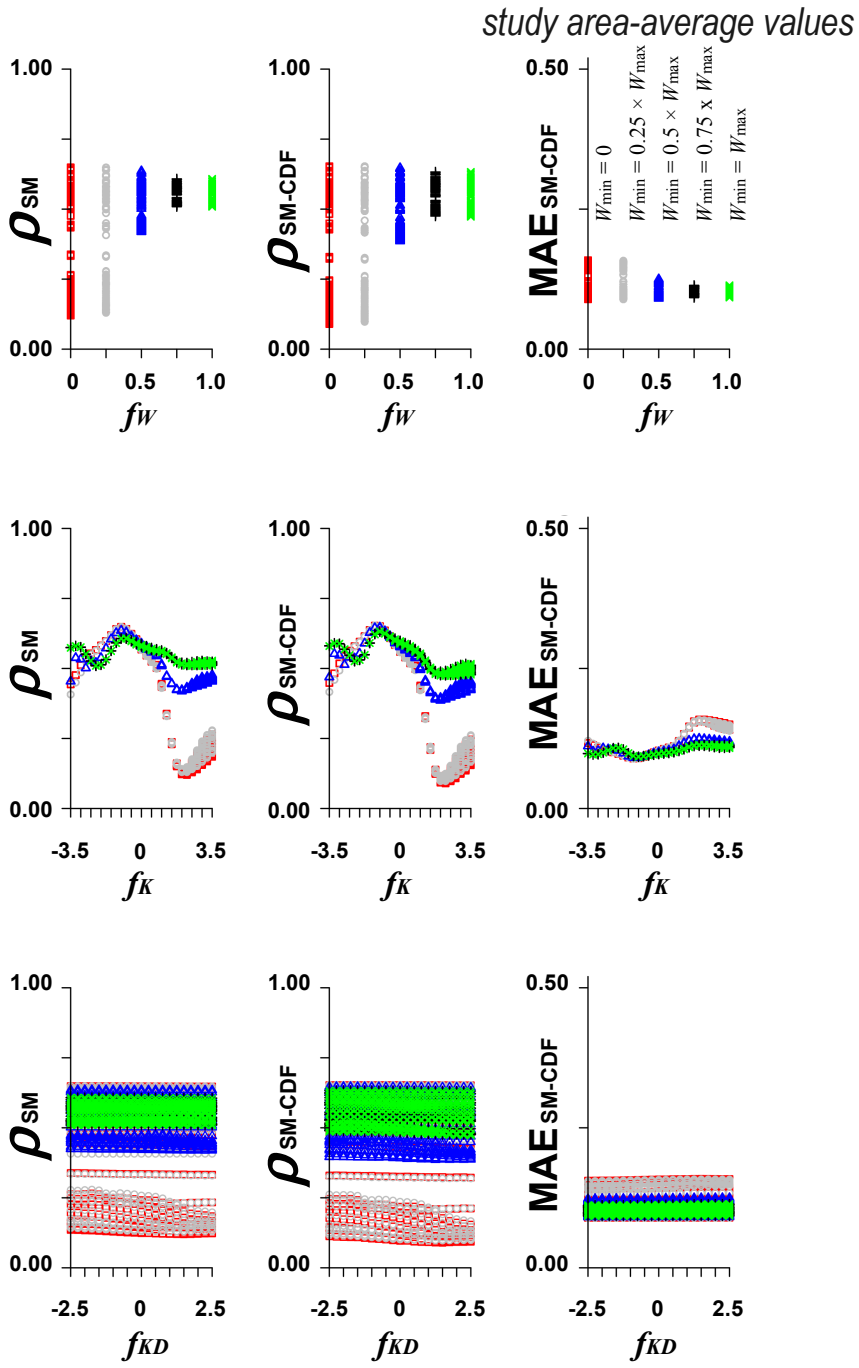

Figure 5.15 Scatter-plots of soil moisture performance indicators (ρ_{SM}, $\rho_{\mathrm{SM-CDF}}$ and $\mathrm{MAE}_{\mathrm{SM-CDF}}$) calculated using study area-average values vs. pre-factors f_W, f_K and f_{KD} (see text for explanation). Note that colors and dot shapes indicate different values of f_W (see the plot on the right upper corner).

four calibration scenarios namely RM-DISCHARGE, SM-RM-BASIN, SM-PIXEL and SM-DISCHARGE. In this Sect. 5.4.3, we describe the procedure to describe each scenario. In Sect. 5.4.4, we further verify the performance of each calibration scenario with groundwater head observations.

The first one, RM-DISCHARGE, is the scenario for which the coupled model is calibrated using daily discharge measurements. For this scenario, we combined two best runs (selected from 3045 runs) based on measurements in Lobith and Borgharen (see Sect. 5.4.1). More specifically, we made a new model run in which the combination of $f_W = 0.75$, $f_K = 1.5$ and $f_{KD} = -1.5$ (which gives the highest $\mathrm{NS_{eff}}$ and $\mathrm{NS_{ano}}$ in Fig. 5.5a) was assigned for the area belonging to Rhine basin and the combination of $f_W = 0.75$, $f_K = 3$ and $f_{KD} = -0.75$ (which provides the highest $\mathrm{NS_{eff}}$ and $\mathrm{NS_{ano}}$ in Fig. 5.5b) was assigned for the Meuse basin. Using this combined pre-factor set, we simulated a new model run RM-DISCHARGE that provides simulated discharge time series with efficiency coefficients as good as obtained by the two best runs (based on discharge data) discussed in Sect. 5.4.1 and presented in Fig. 5.6 ($\mathrm{NS_{eff}} = 0.62$ and $\mathrm{NS_{ano}} = 0.63$ for the discharge at Lobith and $\mathrm{NS_{eff}} = 0.66$ and $\mathrm{NS_{ano}} = 0.77$ for the discharge at Borgharen).

The second and third scenarios, SM-RM-BASIN and SM-PIXEL, are the scenarios calibrated on ERS SWI time series. The procedure of defining the SM-RM-BASIN and SM-PIXEL scenarios is based on the expectation: a "global optimum" pre-factor set — identified during model evaluation to ERS SWI time series (discussed in Sect. 5.4.2) — will lead the model to provide well-simulated groundwater head dynamics. Here, we identified one single run (selected from 3045 runs) resulting in the highest ρ_{SM}. Note that we decided to use only ρ_{SM} because we observe that there are significant correlations among the objective functions ρ_{SM}, $\rho_{\mathrm{SM-CDF}}$ and $\mathrm{MAE_{SM-CDF}}$, as illustrated in Fig. 5.16 (see also the similarities observed in the scatter-plots presented in Figs. 5.7, 5.9, 5.14 and 5.15). Hence, it is sufficient to analyze one of the objective functions for identifying the "best" run with the best soil moisture fit.

For identifying the SM-RM-BASIN scenario, we used the study area-average value of ρ_{SM}, specifically to identify the "best" run with the highest ρ_{SM} from the scatter-plots in Fig. 5.15. Unfortunately, the SM-RM-BASIN scenario results in low discharge performance, with $\mathrm{NS_{eff}} = 0.01$ and $\mathrm{NS_{ano}} = 0.04$ for the daily discharge simulation at Lobith and $\mathrm{NS_{eff}} = 0.13$ and $\mathrm{NS_{ano}} = 0.25$ for the daily discharge simulation at Borgharen. This fact indicates that following a global optimum of soil moisture performance does not necessarily lead to good discharge performance.

For identifying SM-PIXEL, we used the (half arc-degree) pixel values of ρ_{SM}. As the study area covers 136 half-arc degree pixels (see Fig. 2.2b), there are 136 ERS SWI time series that can be used to identify 136 different pre-factor sets corresponding to different maximum values of ρ_{SM} (at different half-arc degree pixels). For every half arc-degree pixel, using such a scatter-plot given in Fig. 5.7 (an example for pixel 21), we identified the "best" run and its pre-factor set (i.e. f_W, f_K and f_{KD} that leads to

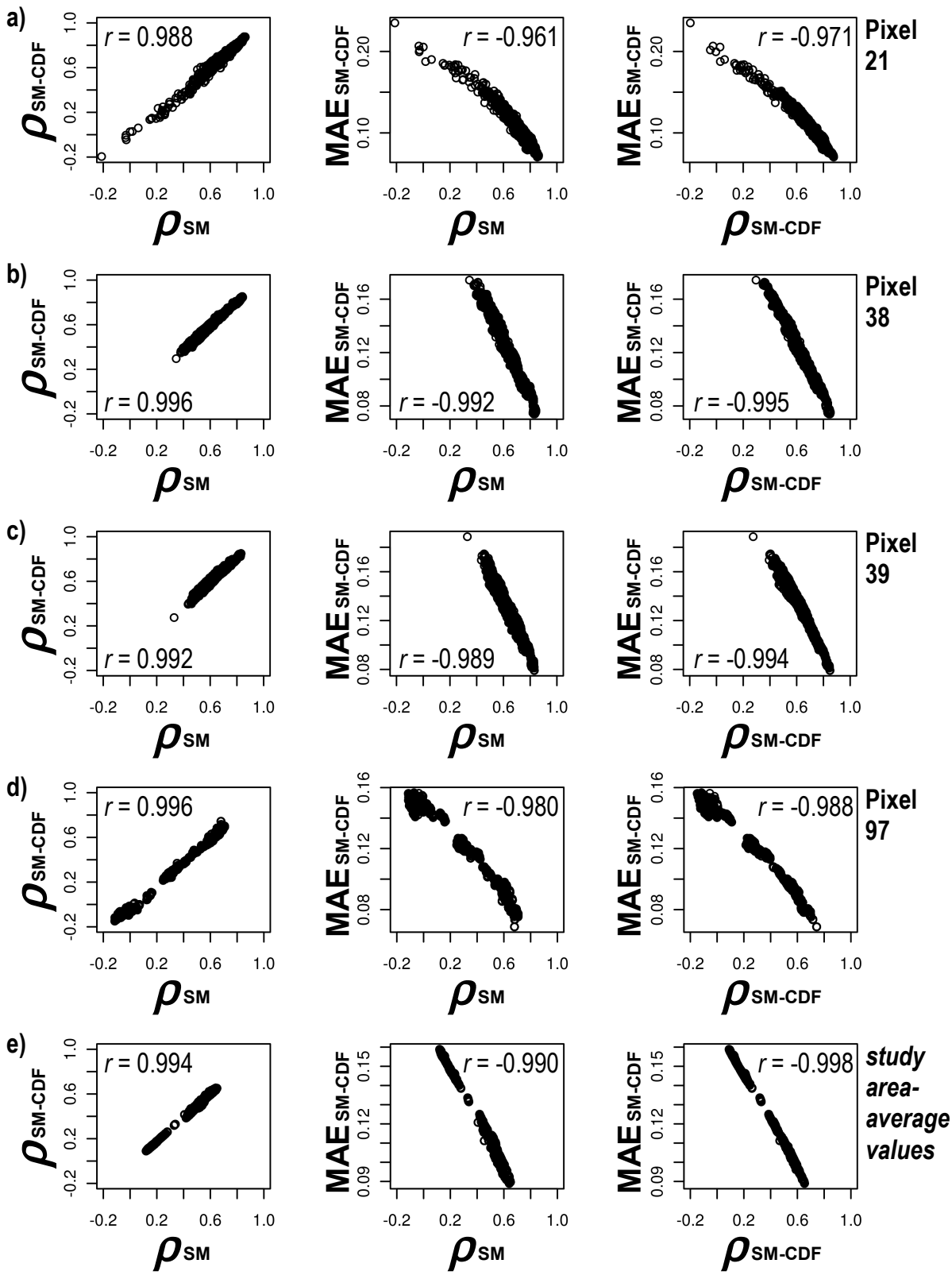

Figure 5.16 Scatter-plots among soil moisture performance indicators showing their significant correlations (all p-values < 0.001), calculated for pixel 21 (a), pixel 38 (b), pixel 39 (c), pixel 97 (d) (see Fig. 2.2b for the pixel locations) and using study area-average objective functions (e).

the highest ρ_{SM}). As this procedure is repeated for all half arc-degree pixels, the identified pre-factor sets are spatially-variable and varying among half arc-degree pixels. Note that SM-PIXEL is not a single run, but a collection of runs representing the "best results" that we can get from the point of view of matching simulated soil moisture dynamics to SWI time series. To get an overview of the discharge performance of this scenario, we combined the spatially-variable optimal pre-factor sets identified previously and performed a new model run using this combined pre-factor set (which are varying among half arc-degree pixels). Unfortunately, this run results in low discharge performance with negative discharge efficient coefficients, $\mathrm{NS}_{\mathrm{eff}} = -1.17$ and $\mathrm{NS}_{\mathrm{ano}} = -0.97$ for its daily discharge simulation at Lobith (Rhine) and $\mathrm{NS}_{\mathrm{eff}} = -0.69$ and $\mathrm{NS}_{\mathrm{ano}} = -0.48$ for its daily discharge simulation at Borgharen (Meuse). Based on this fact, we conclude that pursuing optimal soil moisture performance does not necessarily lead to good discharge performance.

The fourth calibration scenario, SM-DISCHARGE, is the scenario for which a stepwise calibration procedure is implemented based on the combination of discharge and ERS SWI time series. Because the pre-factors f_W and f_{KD} are generally not identifiable from the evaluation to ERS SWI time series (as discussed in Sect. 5.4.2), we fixed f_W and f_{KD} as defined in RM-DISCHARGE, i.e. $f_W = 0.75$ for the entire study area, $f_{KD} = -1.5$ for the Rhine basin and $f_{KD} = -0.75$ for the Meuse basin. For the pre-factor f_K, we assigned different values in distributed half arc-degree pixels using the following procedure. First, we considered only the pixels that have $\rho_{\mathrm{SM}} \geq 0.75$ (from any runs discussed during model evaluation to ERS SWI time series, Sect. 5.4.2). For the pixels with all runs giving $\rho_{\mathrm{SM}} < 0.75$ (mainly in mountainous areas where SWI time series may contain artefacts, such as pixel 197, Fig. 5.14d), we fixed f_K based on the discharge calibration scenario, RM-DISCHARGE, i.e. $f_K = 1.5$ in the Rhine basin and $f_K = 3$ in the Meuse basin. For the pixels having $\rho_{\mathrm{SM}} \geq 0.75$ (i.e. in low-lying and flat regions with shallow groundwater), we considered only the local optima that are higher than or equal to the reference value ($f_K \geq 0$). The latter constraint is a simplification based on the discharge analysis in Sect. 5.4.1 showing that high saturated conductivities are required to generate a simulation with good discharge performance.

As illustrations of implementing the aforementioned procedure, we assigned $f_K = 2.75$ for pixel 21 (see Fig. 5.7); $f_K = 2.5$ for pixel 25, $f_K = 2.5$ for pixel 39, $f_K = 3.5$ for pixel 95 and $f_K = 0$ for pixel 112 (see Fig. 5.9); and $f_K = 1$ for pixel 91, $f_K = 1.5$ for pixel 97, $f_K = 1.5$ for pixel 117 and $f_K = 1.5$ for pixel 197 (see Fig. 5.14). Note that, as this procedure repeated for all half arc-degree pixels, the pre-factor f_K of this scenario are basically spatially-variable (among half arc-degree pixels).

The simulated discharge of the SM-DISCHARGE scenario results in a good performance with $\mathrm{NS}_{\mathrm{eff}} = 0.62$ and $\mathrm{NS}_{\mathrm{ano}} = 0.62$ for its daily discharge simulation at Lobith (Rhine) and $\mathrm{NS}_{\mathrm{eff}} = 0.66$ and $\mathrm{NS}_{\mathrm{ano}} = 0.77$ for its daily simulated discharge at Borgharen (Meuse). These efficiency coefficients are as good as obtained by the RM-DISCHARGE scenario and the best runs (based on discharge) discussed in Sect. 5.4.1.

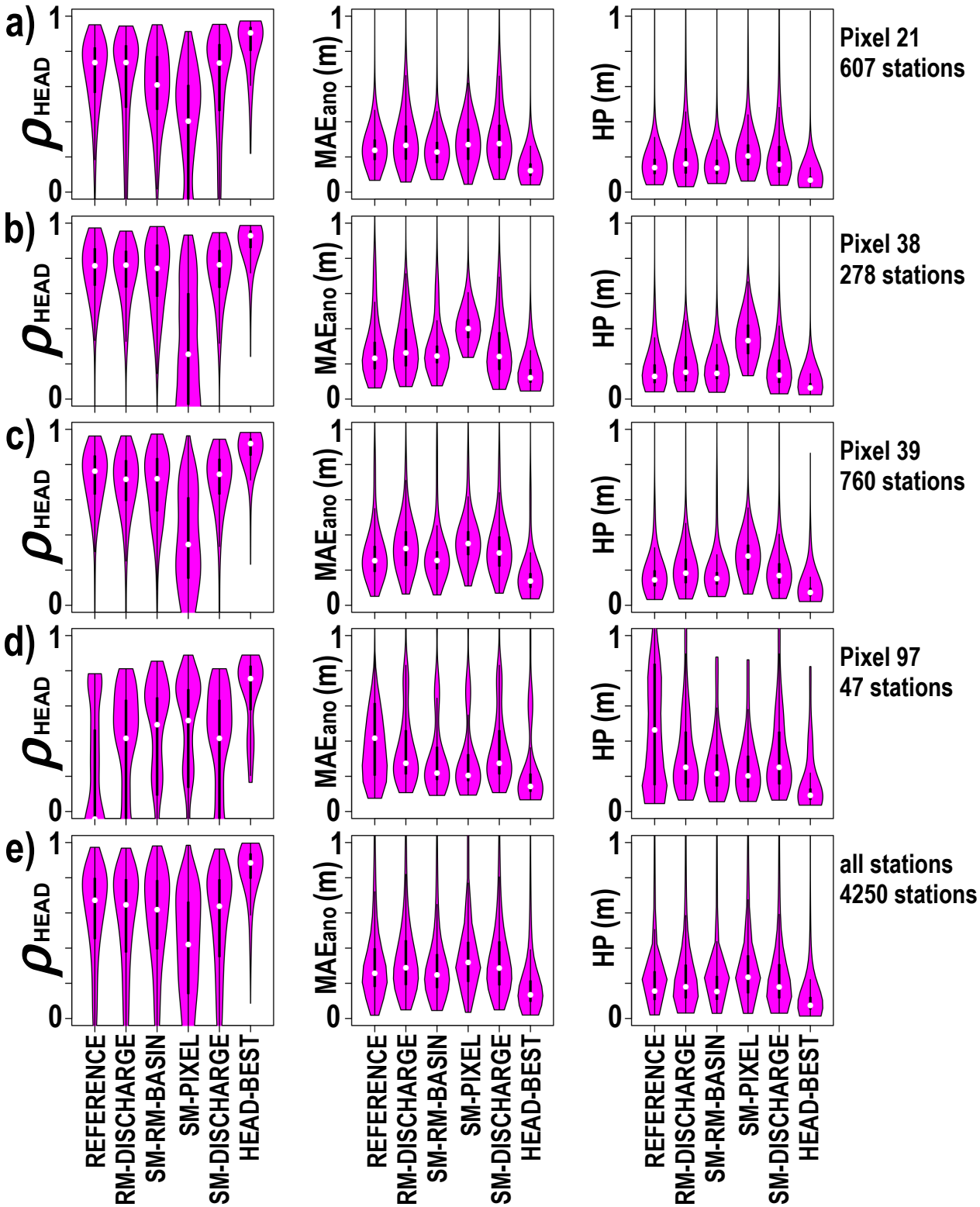

Figure 5.17 Violin plots summarizing groundwater head performance in measurement stations located in pixel 21 (a), pixel 38 (b), pixel 39 (c), pixel 97 (d) (see Fig. 2.2b for the pixel locations) and in the entire study area (e).

5.4.4 Verification to observed groundwater head time series

To validate the performance of all calibration scenarios defined in Sect. 5.4.3, we evaluated their simulated groundwater head time series at 4250 stations. Figures 5.17a to d present the groundwater head performance indicators of all calibration scenarios — measured in ρ_{HEAD}, $\mathrm{MAE}_{\mathrm{ano}}$ and HP — for groundwater head stations located in pixels 21, 38, 39 and 97 — arbitrarily chosen in order to illustrate overall phenomena found in this study. Figure 5.17e presents ρ_{HEAD}, $\mathrm{MAE}_{\mathrm{ano}}$ and HP for all groundwater head stations used in this study. In these figures, besides the four scenarios described in Sect. 5.4.3, there are two other scenarios: REFERENCE and HEAD-BEST. The REFERENCE scenario represents the uncalibrated model run (having $f_W = 0$, $f_K = 0$ and $f_{KD} = 0$), while the HEAD-BEST scenario represents the "best results" based on groundwater head observations (see the following paragraphs). For each of them, we made the violin plots summarizing the groundwater head performance indicators of ρ_{HEAD}, $\mathrm{MAE}_{\mathrm{ano}}$ and HP for the head observations in a given pixel (Figs. 5.17a to d) and for the entire study area (Fig. 5.17e). A violin plot is a modified box plot with their sides showing the shape of its density trace (or "smoothed histogram") and indicating the distributional characteristics of data (for more detailed explanation, see Hintze and Nelson, 1998). In the violin plots that we made, the median is shown as a circle, and 25th and 75th percentiles are indicated as the low and high ends of bold lines. The whisker (or thin line) extends to the most extreme data which are no more than 1.5 times the inter-quantile range of the data (see also Tukey, 1977). Hence, the shapes of the distribution curves above and below the whisker ends represent the outlier distributions.

The first group in the violin plots, REFERENCE, presents the results from the simulation using the initial estimates of model parameters (without calibration). In general, we observe that the groundwater head results of the reference run are already good. In term of ρ_{HEAD}, which is an indicator of timing agreement between simulated and observed groundwater head time series, there are 3034 stations (71%) having $\rho_{\mathrm{HEAD}} > 0.5$ and there are 1897 stations (45%) having $\rho_{\mathrm{HEAD}} > 0.7$. In term of $\mathrm{MAE}_{\mathrm{ano}}$, which is an indicator of error (unit: m) of simulated groundwater head time series, there are 2044 stations (48%) having $\mathrm{MAE}_{\mathrm{ano}} < 0.25$ m. In term of HP, which is an alternative indicator of prediction error (unit: m) that is penalized if low ρ_{HEAD} occurs (see Eq. 5.15), there are 3109 stations (73%) having HP < 0.25 m.

For defining HEAD-BEST, we identified the best run — selected from 3045 runs that we simulated — for each groundwater head station, i.e. the highest ρ_{HEAD}, as well as the lowest $\mathrm{MAE}_{\mathrm{ano}}$ and HP, by evaluating the results of 3045 runs to observed head time series. Note that, as this is done separately for each groundwater head station, HEAD-BEST is not a single run, but a collection of runs. Hence, the violin plots of HEAD-BEST represent ("by proxy") the "best results" that we can get from the point of view of matching simulated groundwater head time series to observations. In this group, there are 4060 stations (96%) having $\rho_{\mathrm{HEAD}} > 0.5$ and 3706 stations (87%)

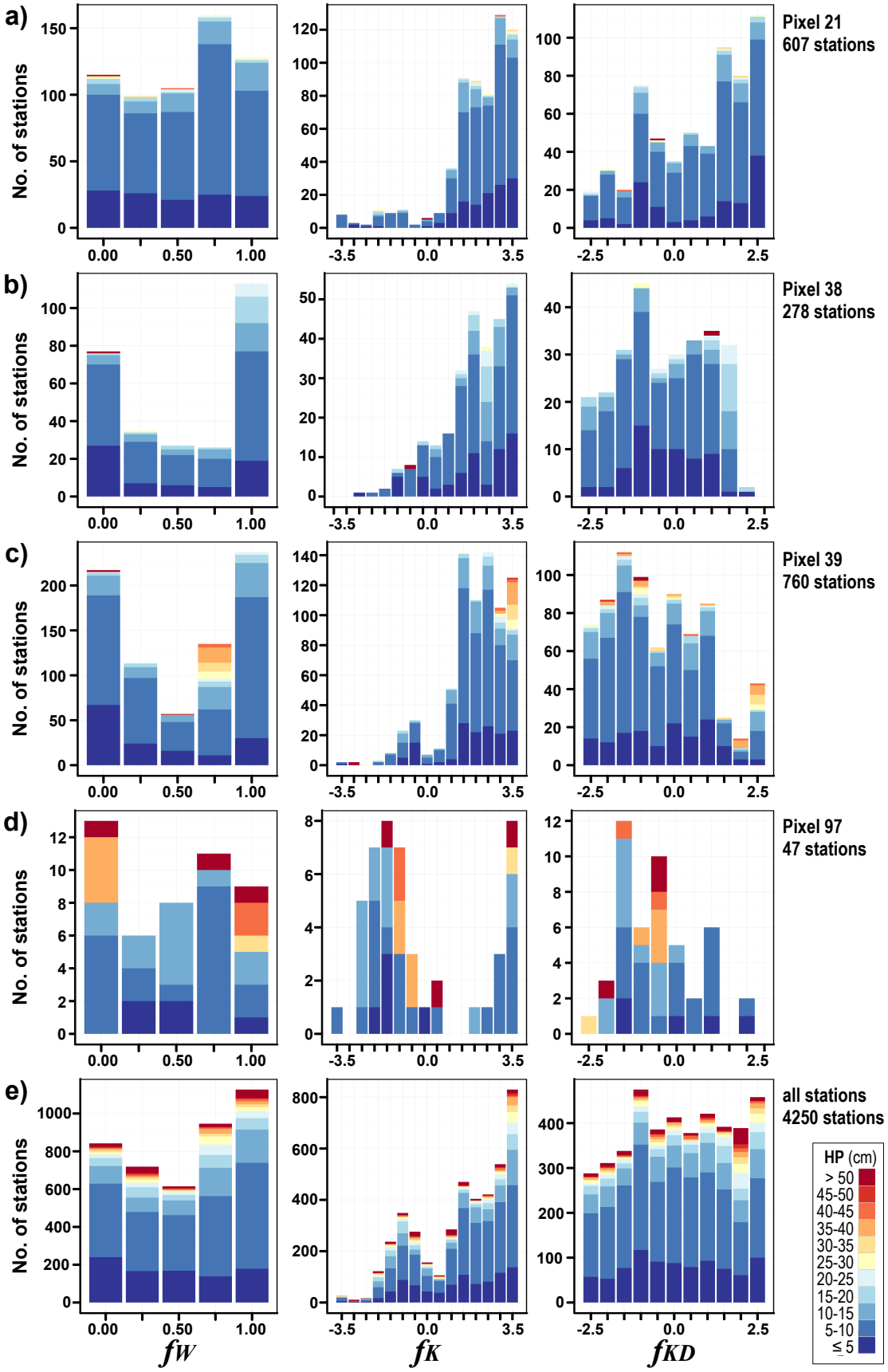

Figure 5.18 Histograms of pre-factors of the scenario HEAD-BEST based on the objective function HP for the groundwater head measurement stations located in the pixels 21 (a), 38 (b), 39 (c), 97 (d) and in the entire study area (e).

having $\rho_{\mathrm{HEAD}} > 0.7$, and there are 3400 stations (80%) having $\mathrm{MAE}_{\mathrm{ano}} < 0.25$ m and 3849 stations (91%) having HP < 0.25 m. Note that such numbers can still be improved if we also tune or vary other model parameters (e.g. varying aquifer specific yields Sy).

The second group, RM-DISCHARGE, is the scenario calibrated based on discharge measurements (located near the basin outlets). From the violin plots in Fig. 5.17d (pixel 97), we find improvements after the model was calibrated based on the discharge measurements. However, from Fig. 5.17a (pixel 21), Fig. 5.17b (pixel 38), Fig. 5.17c (pixel 39) and Fig. 5.17e (for the entire study area), we find that there are hardly any improvements obtained. For the entire study area, there are 2773 stations (65%) having $\rho_{\mathrm{HEAD}} > 0.5$ and 1770 stations (42%) having $\rho_{\mathrm{HEAD}} > 0.7$, and there are 1774 stations (41%) having $\mathrm{MAE}_{\mathrm{ano}} < 0.25$ m and 2809 stations (67%) having HP $<$ 0.25 m. These numbers are almost the same as the ones of REFERENCE and indicate both REFERENCE and RM-DISCHARGE perform an equally good performance in term of simulating groundwater head dynamics. Yet, it should be noted that in term of discharge, RM-DISCHARGE gives a much better simulation (see Sect. 5.4.3).

The SM-RM-BASIN and SM-PIXEL scenarios were calibrated on (only) ERS SWI time series using the objective function ρ_{SM}, which is the indicator of timing agreement between simulated soil moisture and ERS SWI time series. Given their highest values of ρ_{SM} (from 3045 runs), this scenario may be considered as the "best runs" in simulating soil moisture dynamics. For SM-RM-BASIN scenario, for which we used the study-area average of ρ_{SM} while analyzing soil moisture performance, there are hardly any improvements obtained (relatively to REFERENCE), except for pixel 97 (Fig. 5.17d). For this calibration scenario, there are 2743 stations (65%) having $\rho_{\mathrm{HEAD}} > 0.5$ and 1611 stations (38%) having $\rho_{\mathrm{HEAD}} > 0.7$, and there are 2170 stations (51%) having $\mathrm{MAE}_{\mathrm{ano}} < 0.25$ m and 3219 stations (75%) having HP < 0.25 m. These numbers are almost the same as the ones of REFERENCE and RM-DISCHARGE and indicate all of them have an equally good performance in simulating groundwater head dynamics. However, as discussed previously in Sect. 5.4.3, it should be noted that only RM-DISCHARGE provides a reasonably well discharge simulation.

For SM-PIXEL scenario, in which we used the half-arc degree value of ρ_{SM} while analyzing and identifying the best soil moisture performance, we find that the groundwater head performance generally decreases, as indicated in Fig. 5.17 (except for pixel 97, Fig. 5.17d). For the entire study area, there are only 1765 stations (42%) having $\rho_{\mathrm{HEAD}} > 0.5$ and only 870 stations (20%) having $\rho_{\mathrm{HEAD}} > 0.7$, and there are only 452 stations (11%) having $\mathrm{MAE}_{\mathrm{ano}} < 0.25$ m and only 2266 stations (53%) having HP < 0.25 m. These numbers are much lower than the ones from REFERENCE and RM-DISCHARGE, as well as SM-RM-BASIN. These facts indicate that pursuing locally optimal soil moisture performance does not necessarily lead to good groundwater head performance.

The SM-DISCHARGE calibration scenario was defined by using the observed discharge and ERS SWI time series for the model calibration. From the violin-plots in Fig. 5.17d (pixel 97), we observe that the results of the scenario SM-DISCHARGE is better than the REFERENCE and as equally good as RM-DISCHARGE and SM-RM-BASIN. Yet, in general, as indicated in Fig. 5.17a (pixel 21), Fig. 5.17b (pixel 38), Fig. 5.17c (pixel 39) and Fig. 5.17e (for the entire study area), we find that there are limited improvements. However, from the positive side, it should be noted that the SM-DISCHARGE calibration is the only one that is able to reproduce both soil moisture and discharge reasonably well (Sect. 5.4.3), while at the same time producing acceptable head predictions. For SM-DISCHARGE, there are 2709 stations (64%) having $\rho_{\mathrm{HEAD}} > 0.5$ and 1748 stations (41%) having $\rho_{\mathrm{HEAD}} > 0.7$, and there are 1772 stations (42%) having $\mathrm{MAE}_{\mathrm{ano}} < 0.25$ m and 2852 stations (67%) having HP < 0.25 m. These numbers are almost the same as the ones from REFERENCE and RM-DISCHARGE. This indicates that all scenarios provide an equally good performance in simulating groundwater head dynamics. The fact that there are no improvements gained in SM-DISCHARGE is most likely because we adopted basin-uniform pre-factors f_{W} and f_{KD} of RM-DISCHARGE. Such calibrations of f_{W} and f_{KD} can be improved if we use spatially-variable pre-factors, specifically in order to incorporate local or finer resolution variation. Moreover, the coarse resolution of ERS SWI products (half arc-degree) limits the possibility to capture finer resolution of f_K values (within a half arc-degree pixel). In Fig. 5.18, we plotted the histograms of pre-factors of the scenario HEAD-BEST that result in the lowest HP indicators. Figures 5.18a to d present the distributions of pre-factors of groundwater head stations located in pixels 21, 38, 39 and 97 — arbitrarily chosen in order to illustrate overall phenomena found in this study. Figure 5.18e presents the distribution of pre-factors of all groundwater head stations used in this study. Based on the histograms in Fig. 5.18, it is shown that there are wide variations (within a pixel) of pre-factors that cannot be captured by all calibration scenarios.

5.5 Conclusions

The possibility to calibrate a large-scale coupled groundwater-land surface model by using the soil moisture remote sensing product ERS SWI is explored in this chapter. It is shown that ERS SWI time series may be used to tune the upper soil saturated hydraulic conductivities determining the recharge to the deeper groundwater zone. By comparing the results of different model runs with different upper soil conductivities, we can distinguish parameter ranges leading to good and poor simulated soil moisture dynamics. However, it is also shown that it is difficult to fully calibrate such models by relying on remotely-sensed ERS SWI time series only. When discharge measurement is included, a more accurate model calibration is obtained because it resolves multiple optima or equifinality problems that occur while fitting soil moisture dynamics and it better constrains aquifer transmissivities and runoff-infiltration

partitioning processes. The combined and step-wise calibration approach using both discharge observations and remotely-sensed soil moisture data yields a model that is able to fit both discharge and soil moisture reasonably well, as well as predicting the dynamics of groundwater heads with acceptable accuracy. Yet, groundwater head measurements, if available, can be used to improve the accuracy, especially to capture local variation and fine-scale heterogeneity (e.g. of soil moisture and groundwater head dynamics), which cannot be captured by the current generation of spaceborne soil moisture product (25-50 km resolution).

6 Summary and outlook

6.1 Introduction

Predicting the behavior of hydrological systems over large areas requires large numbers of data that are often difficult to acquire on the ground. Consequently, satellite-based remote sensing has become a powerful tool in surface hydrology. However, groundwater hydrology has yet to realize the benefits of remote sensing although several scientists have noticed that surface expressions of groundwater can be monitored from space (Jackson, 2002; Becker, 2006). The main objective of this study is to explore the potential of spaceborne remote sensing applications for large scale groundwater modeling. The potential for remote sensing of groundwater is explored here in the context of active microwave-based sensors. In this study, we focus on a half-arc degree (approximately equal to 50 km at the equator) and monthly soil moisture time series product called the European Remote Sensing Soil Water Index (ERS SWI) — representing the first meter profile soil moisture content (Wagner et al., 1999b). As a test-bed, we used the combined Rhine Meuse basin, located in the humid temperate zone in Western Europe. This well-documented basin is relatively large, covering $\pm$ 200 000 km^2 and supported by a good coverage of ERS SWI and thousands of in-situ groundwater head measurement time series, which makes it suitable for large scale groundwater hydrology studies.

This study explores the potential of employing ERS SWI time series in two types of models: an empirical black-box transfer function-noise (TFN) model and a physically-based, large-scale, coupled groundwater-land surface model called PCR-GLOBWB-MOD. In exploring the possibility of using ERS SWI time series in both models, the following research questions were defined in this study and briefly discussed in the following sections:

1. Is there correlation between ERS Soil Water Index time series and groundwater head dynamics?
2. If this correlation exists, can ERS Soil Water Index time series be used as the input of transfer function-noise models for predicting groundwater head in space and time?
3. Is it possible to build a large-scale, physically-based and coupled land surface-groundwater model using only global datasets?
4. Can ERS Soil Water Index time series be used to support the calibration of a large-scale groundwater model?

6.2 Is there correlation between ERS Soil Water Index time series and groundwater head dynamics?

In Chapter 2, we investigated whether there is correlation between groundwater head time series and ERS SWI time series for the Rhine-Meuse basin. We considered areas with shallow and deep groundwater depth and we studied the correlation between the ERS SWI and groundwater head time series by accounting for lag time, i.e. response time of water from the upper unsaturated soil zone to saturated groundwater bodies. Results show that there is a significant correlation between the ERS SWI and groundwater head time series. The correlation is apparent especially for areas with shallow groundwater depth. Moreover, for most areas particularly the ones with deep groundwater depth, the correlation becomes more apparent if the response time is taken into account and a time delay is added to the correlation analysis.

The results of this study are promising for spaceborne microwave remote sensing applications to support large scale groundwater assessment, particularly relevant for groundwater modeling applications and offers possibilities for making groundwater head predictions. Due to the correlation between ERS SWI and field-measured shallow groundwater head time series predicting shallow groundwater head variations based on ERS SWI dynamics should be feasible. This possibility is demonstrated in Chapter 3 and briefly summarized in the following Sect. 6.3.

6.3 Can ERS Soil Water Index time series be used as the input of transfer function-noise models for predicting groundwater head in space and time?

Chapter 3 explores the possibility of using ERS SWI time series to predict the groundwater head. The ERS SWI time series were used as the input of a transfer function-noise (TFN) model. We performed two modeling exercises. The first was focused on temporal forecasting of groundwater head dynamics, while the second one was to make spatio-temporal prediction of groundwater head.

For the first exercise, the parameters of the TFN model were calibrated based on groundwater head time series in the period 1995-2000 by embedding the model in a Kalman filter algorithm. TFN models were calibrated separately at all locations where groundwater head measurement time series are available. Once calibrated, the TFN forecasts were validated for the period 2004-2007 in order to assess their forecasting skill. For the second exercise, we selected calibrated TFN model parameters — derived in the first exercise — from a subset of locations and used them to fit regression models with a digital elevation map as input. With these regression models, TFN model parameters were spatially predicted. Subsequently, using

these estimated parameters, spatio-temporal prediction of groundwater head was performed (also with the TFN model and ERS SWI time series as the model input) and evaluated against all available groundwater head observations.

Results of both exercises were promising. The TFN models can reproduce the observed groundwater head fluctuations reasonably well, especially in shallow groundwater areas where soil moisture dynamics are tightly connected to groundwater head fluctuations. Our results show that ERS SWI time series should be considered as an important source of information for the assessment of large scale groundwater dynamics.

6.4 Is it possible to build a large scale, physically-based and coupled land surface-groundwater model by using only global datasets?

In this study, we develop an approach to construct large scale groundwater models by using global datasets that are readily available. The model proposed is called PCR-GLOBWB-MOD. Briefly stated, PCR-GLOBWB-MOD, which has a spatial resolution of $30'' \times 30''$ (approximately equal to 1 km $\times$ 1 km at the equator) and operates based on daily basis water balance, is the modified land surface model of PCR-GLOBWB (van Beek and Bierkens, 2009; van Beek et al., 2011) coupled to a MODFLOW (McDonald and Harbaugh, 1988) groundwater model.

In Chapter 4, we started building the model by modifying the PCR-GLOBWB land surface model and performed the daily simulation of it to estimate groundwater recharge and river discharge. Subsequently, a single layer MODFLOW transient groundwater model was created and forced by the recharge and surface water levels calculated by the land surface model. Results were promising. The simulated river discharges compare well to the observations. Moreover, based on our sensitivity analysis, in which we ran several groundwater model runs with various hydro-geological parameter settings, we observed that the model can reproduce the observed groundwater head time series reasonably well. It shows that it is possible to build a simple and reasonably accurate large scale groundwater model by using only readily available global datasets. It brings a promise for large scale groundwater modeling practices, including for data-poor environments and at the global scale.

For the model developed in Chapter 4 — referred as PCR-GLOBWB-MOD$_{\mathrm{OFF}}$, we noted that there are still some limitations, specifically because the used offline-coupling technique simplifies the dynamic feedback between surface water level and groundwater head, and between soil moisture state and groundwater head. In Chapter 5 (specifically Sect. 5.2), we introduce the online-coupled groundwater-land surface model PCR-GLOBWB-MOD$_{\mathrm{ONL}}$. This fully-coupled version incorporates a two-way

feedback interaction between channel/surface water levels and groundwater head dynamics. Moreover, through a two-way coupling between groundwater and soil moisture, the simulated groundwater head can sustain the soil moisture state of the upper soil stores and thus can fulfill high evaporation demands (during dry seasons and/or in arid areas). The performance of the PCR-GLOBWB-MOD$_{\mathrm{ONL}}$ is evaluated at Chapter 5 and summarized in the following Sect. 6.5.

6.5 Can ERS Soil Water Index time series be used to evaluate the performance of a large scale, physically-based and coupled land surface-groundwater model?

Chapter 5 explores the suitability of using ERS SWI time series to calibrate the fully coupled groundwater-land surface model PCR-GLOBWB-MOD$_{\mathrm{ONL}}$. Contrary to "black-box" TFN models used in Chapter 3, the PCR-GLOBWB-MOD$_{\mathrm{ONL}}$ model is a physically-based model, in which model parameters are initially estimated based on physical properties (e.g. soil physical properties). However, such estimates are often uncertain and should be tuned by evaluating the model results against available observations.

In Chapter 5, a brute force calibration procedure was applied for calibrating the coupled groundwater-land surface model PCR-GLOBWB-MOD$_{\mathrm{ONL}}$. More than three thousand model runs with varying parameter sets were used. Results of all runs were evaluated against basin outlet discharge measurements, ERS SWI time series and in-situ groundwater head observations. From this study, we concluded that ERS SWI time series can be used in the calibration of upper soil saturated hydraulic conductivity that determines groundwater recharge. However, we find that it is not possible to calibrate the complete model using soil moisture time series only. Discharge measurements should be included to acquire a more accurate model calibration, specifically in order to tackle multiple optima problems when fitting soil moisture dynamics and to constrain aquifer transmissivities and runoff-infiltration partitioning processes.

6.6 Outlook

In the first part of this study (Chapters 2 and 3), we used soil moisture ERS Soil Water Index (SWI) time series to predict the groundwater head in space and time using an empirical transfer function-noise (TFN) model. In the second part of this study (Chapters 4 and 5), we developed a large-scale, physically-based groundwater-land surface model called PCR-GLOBWB-MOD using only global datasets and explored the possibilities and limitations to constrain the model by using ERS Soil Water Index time series. Both parts demonstrate the integration of remote sensing products with

groundwater models and in-situ groundwater head observations. This section serves as the epilogue of this study by discussing its prospective applications (Sect. 6.6.1) and exploring future research topics (Sect. 6.6.2).

6.6.1 Possible applications

Chapter 3 demonstrates the use of ERS SWI time series in an empirical transfer function-noise (TFN) model to predict groundwater head. Using time series of precipitation (excess), TFN models have been widely used for many applications: not only to predict groundwater head (Bierkens et al., 2001), but also to fill in gaps of groundwater head measurement time series (Bierkens et al., 1999), to characterize groundwater regimes (van Geer and Defize, 1987) and to detect structural changes/interventions and outliers in groundwater head dynamics (Gehrels et al., 1994; Knotters and Bierkens, 2000). Following the successful results of Chapter 3 in predicting groundwater head, we expect that ERS SWI, offering a better spatial coverage and support than in-situ observations of precipitation, can be used for the other aforementioned purposes. Note that compared to TFN models using precipitation excess (i.e. the difference between precipitation and total evaporation and transpiration) time series as input, TFN models forced with with soil moisture time series may be considered more accurate since estimation of actual evaporation and transpiration is unnecessary. Moreover, the global coverage of satellite-based soil moisture products make the application of TFN models feasible in data-poor areas.

Chapters 4 and 5 demonstrate the possibility to build a simple and reasonably accurate large-scale groundwater-land surface PCR-GLOBWB-MOD model by using only global datasets. It suggests a promising prospect for implementing PCR-GLOBWB-MOD in many areas of the world, including in data-poor regions. The PCR-GLOBWB-MOD can be applied in several areas with large sedimentary basins, such as the basins of Nile, Danube, Mekong, Yellow and Ganges-Brahmaputra Rivers. The inclusion of the well-known MODFLOW (McDonald and Harbaugh, 1988) groundwater model code in PCR-GLOBWB-MOD also opens an opportunity to improve existing global hydrological models, such as the original version of PCR-GLOBWB (van Beek and Bierkens, 2009; van Beek et al., 2011), WASMOD-M (Widén-Nilsson et al., 2007) and VIC (Liang et al., 1994), which are not yet capable to simulate groundwater head dynamics and thus do not incorporate groundwater lateral flow. Using the methods suggested in Sects. 4.2 (offline coupling) and 5.2 (online coupling), such global hydrological models can be coupled with a MODFLOW groundwater model. Although groundwater lateral flow may not be important for current global hydrological models, which usually have a spatial resolution of 50 km, its inclusion is relevant for future global hydrological models with finer resolutions down to 1 km (Wood et al., 2011).

6.6.2 Further research topics

Analyzing the influence of vegetation, soil and other hydrological factors

It is known that scatterometer signals and their derived products, including ERS SWI time series, can be influenced by the presence of vegetation (Wagner et al., 1999a, 2003; Wanders et al., 2012). In this study, we did not investigate the influence of vegetation on ERS SWI time series on the relation between ERS SWI time series and groundwater dynamics. Moreover, the influence of variations of soil textures and properties (e.g. porosity and conductivity) were also not explored. In Chapter 2, we limited the correlation analysis between ERS SWI and groundwater head dynamics by only distinguishing areas with shallow and deep groundwater depths. More detailed investigations concerning the influence of vegetation, soil and other hydrological factors should be endeavored in further study. This can best be done by identifying a smaller size study area (not the entire basin) which is supported by detailed information on surface water and groundwater regimes and supplemented with high-resolution vegetation maps, soil maps and hydro-geological information, including the lithology and stratification. A smaller well-defined study area will allow us to further investigate the potential and limitation of using ERS SWI for predicting groundwater head (Chapter 3) and their suitability for calibrating a physically-based groundwater-land surface model (Chapter 5).

Incorporating human influence

Another obvious thing that was not considered is anthropogenic influence, e.g. water management, irrigation, surface and groundwater extraction, artificial groundwater recharge, etc. In this study, we intentionally excluded the downstream areas in the Netherlands where water management intervention is dominant. Groundwater and surface-water extraction or pumping activities were also ignored. As only soil moisture time series used as forcing input, TFN models used in this study will work mainly in shallow groundwater areas where soil moisture dynamics are tightly connected to groundwater head fluctuations. However, such TFN models can be improved by including other forcing time series, including pumping rates and surface water management regimes (van Geer and Defize, 1987; Knotters and Bierkens, 2000; Berendrecht et al., 2003). Similarly, the current physically-based model PCR-GLOBWB-MOD should be improved by incorporating the above-mentioned forcing time series.

Using other spaceborne products

The ERS SWI product used in this study is only one of many currently available spaceborne soil moisture time series. For further study, explorations to use other readily-available soil moisture time series are strongly encouraged. By implementing the methods described in this study, we should try to use, for example, an improved

version of ERS SWI proposed by de Lange et al. (2008), who derived SWI using a one dimensional water flow model and incorporating the influence of soil texture. We could also explore the possibility to use the Surface Soil Moisture (SSM) product of ERS and the other products from other spaceborne missions, such as the ones from the missions of Advanced Microwave Scanning Radiometer-Earth Observation System (AMSR-E, Njoku et al., 2003; de Jeu and Owe, 2003) and Soil Moisture and Ocean Salinity (SMOS, Kerr et al., 2001). Moreover, there is a recent project, referred as Water Cycle Multi-Mission Observation Strategy (WACMOS, `http://wacmos.itc.nl`), to set up a solid scientific basis for the creation of coherent long-term datasets of water relevant geo-information, including a harmonized soil moisture dataset from all microwave sensors. Within WACMOS, it is foreseen that a multi-decadal (more than 30 years) soil moisture dataset integrating all microwave observations that are available since 1978 will be created (see also Liu et al., 2011). If such a dataset is available, its implementation in similar methods used in this study will be of interest to groundwater studies.

Besides soil moisture based products, gravity-based missions of Gravity Recovery and Climate Experiment (GRACE, Tapley et al., 2004) and Gravity Field and Steady-state Ocean Circulation Explorer (GOCE, Drinkwater et al., 2003, 2007), should also be explored. Future studies should also anticipate future missions that will results in better products with better spatial and temporal resolutions.

In-situ observations

Although satellite missions bring many promises, we still have to acknowledge the importance of in-situ observations for hydrology studies. As shown in Chapter 5, it is obvious that we need discharge data to calibrate some model parameters. Hence, it is still important to encourage an initiative as done by Global Runoff Data Centre (`http://www.bafg.de/GRDC`) to organize an international archive of discharge data.

We also suggest that field campaigns for soil moisture observations — always needed for the validation of current and future remote sensing soil moisture products — must be supported by in-situ groundwater head observations. It is unfortunate that, for example, hundreds of soil moisture samples were collected during the field campaign of Soil Moisture Experiments (SMEX, `http://www.ars.usda.gov`) but groundwater head was not measured (Becker, 2006). Another example of this schism could be illustrated from several studies using the REMEDHUS soil moisture station network (e.g. Ceballos et al., 2005; Martínez-Fernández and Ceballos, 2005) where groundwater head measurements are not mentioned. Also, the project of International Soil Moisture Network (Dorigo et al., 2011) does not incorporate any groundwater head measurements. If such soil moisture observations are supported by in-situ head measurements, an extension of the use of remotely sensed soil moisture products for groundwater hydrological studies is definitely possible as shown in this study.

Appendix A The land surface model of PCR-GLOBWB-MOD

This appendix is adopted from:
Sutanudjaja, E. H., van Beek, L. P. H., de Jong, S. M., van Geer, F. C., Bierkens, M. F. P. (2011), Large-scale groundwater modeling using global datasets: a test case for the Rhine-Meuse basin, Hydrology and Earth System Sciences, 15, 2913-2935, doi:10.5194/hess-15-2913-2011.

This Appendix A briefly describes the main features of the land-surface model of PCR-GLOBWB-MOD (which has the spatial resolution of $30'' \times 30''$) and explains the modifications from its original version PCR-GLOBWB-ORI ($30' \times 30'$), of which van Beek and Bierkens (2009) and van Beek et al. (2011) provide the detailed description. Note that as stated in Sect. 4.2.2, the terms "PCR-GLOBWB-ORI" and "PCR-GLOBWB-MOD" refer to the original and modified versions, while 'PCR-GLOBWB' refers to both versions.

A.1 Interception

PCR-GLOBWB includes an interception storage, Si [L], which is subject to evaporation. Precipitation, P [$\mathrm{L\,T^{-1}}$], which falls either as snow, Sn [$\mathrm{L\,T^{-1}}$] (if atmospheric temperature is below the water freezing temperature, $Ta < 0°\mathrm{C}$), or liquid rainfall, P_{rain} [$\mathrm{L\,T^{-1}}$] (if $Ta \geq 0°\mathrm{C}$), fills the interception storage up to a certain threshold. In PCR-GLOBWB-MOD, we use the interception definition as suggested by Savenije (2004), asserting that interception accounts not only for evaporation fluxes from leaf interception, but also any fast evaporation fluxes as precipitation may be intercepted on other places, such as rocks, bare soils, roads, litters, organic top soil layers, etc. Thus, the interception capacity is parameterized as:

$$Si_{\mathrm{max,m}} = [1 - C_{\mathrm{f,m}}]\ I_{\mathrm{nv}} + C_{\mathrm{f,m}}\ I_{\mathrm{veg}}\ \mathrm{LAI_m} \tag{A.1}$$

where Si_{max} [L] is the interception capacity of each grid-cell consisting of the fractions C_{f} [−] of vegetation cover. I_{nv} and I_{veg} [L] are parameters defining the interception capacities per unit surface area in non-vegetated and vegetated areas. LAI [−] is the leaf area index, defined as the ratio of total upper leaf surface of vegetation divided by the surface area of the land on which the vegetation grows. Equation (A.1), used in PCR-GLOBWB-MOD, is slightly different than its original version PCR-GLOBWB-ORI, which limits the interception capacity only to leaf canopies represented by the

second term of Eq. (A.1) ($C_{\mathrm{f,m}}\, I_{\mathrm{veg}}\, \mathrm{LAI_m}$). The first term of Eq. (A.1) ($[1 - C_{\mathrm{f,m}}]\, I_{\mathrm{nv}}$), introduced in PCR-GLOBWB-MOD, represents the interception capacity in the non-vegetated fraction.

The subscript m, which is the monthly index, indicates that $Si_{\mathrm{max,m}}$, $C_{\mathrm{f,m}}$ and $\mathrm{LAI_m}$ show monthly or seasonal variations due to vegetation phenology. Their variations are according to a growth factor f_{m} [−] which is a function of monthly temperature T_{m} [Θ]:

$$f_{\mathrm{m}} \;=\; 1 \;-\; \left[\frac{T_{\mathrm{max}} \;-\; T_{\mathrm{m}}}{T_{\mathrm{max}} \;-\; T_{\mathrm{min}}}\right]^2 \tag{A.2}$$

where T_{max} and T_{min} are the maximum temperature and minimum temperature assumed for the growing and dormancy seasons, and the monthly temperature T_{m} fields are taken from the 10′ CRU-CL2.0 dataset (New et al., 2002), containing 12 monthly fields representing the average climatology conditions over 1961–1990. Using f_{m}, the seasonal parameters $C_{\mathrm{f,m}}$ and $\mathrm{LAI_m}$ are modeled as:

$$\mathrm{LAI_m} \;=\; \mathrm{LAI_{min}} \;+\; f_{\mathrm{m}} \;\times\; (\mathrm{LAI_{max}} \;-\; \mathrm{LAI_{min}}) \tag{A.3}$$

$$C_{\mathrm{f,m}} \;=\; C_{\mathrm{f,min}} \;+\; f_{\mathrm{m}} \;\times\; (C_{\mathrm{f,max}} \;-\; C_{\mathrm{f,min}}) \tag{A.4}$$

The maximum and minimum values of LAI and C_{f} are assigned based on the land cover map of GLCC 2.0 (`http://edc2.usgs.gov/glcc/globe_int.php`), the global ecosystem classification of Olson (1994a,b) and the improved land surface parameter table of Hagemann (2002).

The fast evaporation flux from the intercepted water, E_{i} [$\mathrm{L\,T^{-1}}$], is limited by either available evaporation energy for wet interception areas $E_{\mathrm{p,i}}$ [$\mathrm{L\,T^{-1}}$] or available water in Si:

$$E_{\mathrm{p,i}} \;=\; E_{\mathrm{p,0}} \;\times\; Kc_{\mathrm{i}} \tag{A.5}$$

$$E_{\mathrm{i}}\, \Delta t \;=\; \min\; (Si,\; E_{\mathrm{p,i}}\, \Delta t) \tag{A.6}$$

where $E_{\mathrm{p,0}}$ [$\mathrm{L\,T^{-1}}$] is the reference potential evaporation (FAO Penman-Monteith, Allen et al., 1998), Kc_{i} [−] is the "crop factor" for interception areas and Δt [T] is the timestep (one day).

A.2 Snow pack

If $Ta < 0$°C, the surplus precipitation above Si_{max} falls as snow and feeds the snow storage, Ss [L], which is modeled with a degree-day-factor (DDF [$\mathrm{L\,\Theta^{-1}\,T^{-1}}$]) method adapted from the HBV model (Bergström, 1995). Snow may melt (if $Ta \geq 0$°C) and melt water may refreeze (if $Ta < 0$°C) with linear rate CFR [$\mathrm{T^{-1}}$] or evaporate (if enough energy is available). Melt water can also be stored in a liquid water storage of the snow pack, Ss_{sl} [L], up to a certain maximum holding capacity that is proportionally to Ss and controlled by a factor CWH [−]. Any surplus above this holding capacity is transferred to the soil.

A.3 Direct or surface runoff

If $Ta \geq 0°\mathrm{C}$, the net input liquid flux transferred to soil, P_n [$\mathrm{L\,T^{-1}}$], consists of the surplus precipitation above the interception capacity Si_max (falling as liquid rainfall) and excess melt water from the snow pack. In principle, P_n infiltrates if soil is not saturated and causes direct runoff if soil is saturated. However, this principle cannot be straightforwardly implemented because we have to account for the variability of soil saturation within a $30'' \times 30''$ cell. Here we adopted the Improved Arno Scheme concept (Hagemann and Gates, 2003), in which the total soil water storage capacity of a cell consists of the aggregate of many different soil water storage capacities. Following this concept, van Beek and Bierkens (2009) derived Eq. (A.7) to estimate the fractional saturation of a PCR-GLOBWB grid-cell, x [$-$], as a function of grid-average values W [L]:

$$x \;=\; 1 \;-\; \left(\frac{W_\mathrm{max} \;-\; W_\mathrm{act}}{W_\mathrm{max} \;-\; W_\mathrm{min}}\right)^{\frac{b}{b+1}} \tag{A.7}$$

where W_min is the grid-(local)-minimum capacity, W_act and W_max are respectively the grid-average-actual water storage and water capacity for the entire soil profile ($W_\mathrm{act} = S_1 + S_2$ and $W_\mathrm{max} = SC_1 + SC_2$, where SC [L] is the soil water capacity for each layer).

Based on Eq. (A.7), the net input flux P_n is divided into direct runoff, Q_dr [$\mathrm{L\,T^{-1}}$], and infiltration flux into the first soil layer, P_{01} [$\mathrm{L\,T^{-1}}$]. The direct runoff is given by:

$$Q_\mathrm{dr}\Delta t = \begin{cases} 0 & \text{if } P_\mathrm{n}\Delta t + W_\mathrm{act} \leq W_\mathrm{min} \\ P_\mathrm{n}\Delta t - \Delta W_\mathrm{act} + \\ \Delta W\left[\left(\frac{\Delta W_\mathrm{act}}{\Delta W}\right)^{\frac{1}{b+1}} - \frac{P_\mathrm{n}\Delta t}{(b+1)\Delta W}\right]^{b+1} & \text{if } W_\mathrm{min} < P_\mathrm{n}\Delta t + W_\mathrm{act} \leq W_\mathrm{max} \\ P_\mathrm{n}\Delta t - \Delta W_\mathrm{act} & \text{if } P_\mathrm{n}\Delta t + W_\mathrm{act} > W_\mathrm{max} \end{cases} \tag{A.8}$$

with $\Delta W = W_\mathrm{max} - W_\mathrm{min}$ and $\Delta W_\mathrm{act} = W_\mathrm{max} - W_\mathrm{act}$.

Equation (A.8) states that an event P_n, for a given cell and a given period Δt, only generates runoff Q_dr if it brings W_act above W_min. It implies that W_min is an important parameter governing runoff generation response time, especially for a large and highly variable $30' \times 30'$ cell of PCR-GLOBWB-ORI consisting of several land cover, vegetation and soil types. However, W_min is less important for a relatively small $30'' \times 30''$ cell of PCR-GLOBWB-MOD, for which we assumed a uniform type of land cover, a uniform type of vegetation and a uniform type of soil. Here, for the sake

of simplicity, we assumed $W_{\min} = 0$ for all cells in PCR-GLOBWB-MOD. However, PCR-GLOBWB-MOD still considers the sub-grid elevation variability in a $30'' \times 30''$ cell by the existence of parameter b that accounts for the fact that for a given soil wetness, we expect that more runoff is produced in mountainous regions than in flat regions (see e.g. Hagemann and Gates, 2003; van Beek and Bierkens, 2009):

$$b \;=\; \max\left(\frac{\sigma_{\mathrm{h}} \;-\; \sigma_{\min}}{\sigma_{\mathrm{h}} \;+\; \sigma_{\max}},\; 0.01\right) \tag{A.9}$$

where σ_{h} is the standard deviation of orography within a $30'' \times 30''$ cell calculated from the $3''$ DEM of HydroSHEDS (Lehner et al., 2008), and $\sigma_{\min}$ and $\sigma_{\max}$ are the model-area minimum and maximum values of the standard deviations of orography at the grid resolution.

Through this scheme, the amount of infiltration P_{01} transferred to the first soil store is equal to the difference between P_{n} and Q_{dr} ($P_{01} = P_{\mathrm{n}} - Q_{\mathrm{dr}}$). However, we also have to consider that the infiltration rate cannot exceed the saturated hydraulic conductivity of the first layer, $K_{\mathrm{sat},1}$ [$\mathrm{L\,T^{-1}}$]. In this case, if $P_{01} > K_{\mathrm{sat},1}$, its excess is passed to the direct runoff Q_{dr}.

A.4 Vertical water exchange between soil and groundwater stores

Net vertical fluxes between the first and second stores Q_{12} [$\mathrm{L\,T^{-1}}$] are driven by degrees of saturation of both layers, s [$-$]. They are calculated either as $s_1 = S_1/SC_1$ and $s_2 = S_2/SC_2$; or $s_1 = \theta_1/\theta_{\mathrm{sat},1}$ and $s_2 = \theta_2/\theta_{\mathrm{sat},2}$, where the subscript sat indicates saturation and θ [$-$] is the effective moisture content defined as the fraction of storage over thickness ($\theta_1 = S_1/Z_1$ and $\theta_2 = S_2/Z_2$). In principle, Q_{12} consists of a downward percolation $Q_{1\to2}$ [$\mathrm{L\,T^{-1}}$], and a capillary rise $Q_{2\to1}$ [$\mathrm{L\,T^{-1}}$]. If there is enough water in S_1, percolation $Q_{1\to2}$ is equal to the first store unsaturated hydraulic conductivity, $K_1(s_1)$ [$\mathrm{L\,T^{-1}}$]. If $s_1 < s_2$, capillary rise may occur with the amount of $Q_{2\to1} = K_2(s_2) \times (1 - s_1)$, where $K_2(s_2)$ [$\mathrm{L\,T^{-1}}$] is the second store unsaturated hydraulic conductivity and $(1 - s_1)$ is the moisture deficit in the first store. The unsaturated hydraulic conductivity of each layer, $K(s)$, which depends on the degree of saturation s, is calculated based on the relationship suggested by Campbell (1974):

$$K(s) \;=\; K_{\mathrm{sat}} \;\times\; s^{2\beta+3} \tag{A.10}$$

where β [$-$] is a soil water retention curve parameter based on the model of Clapp and Hornberger (1978):

$$\psi \;=\; \psi_{\mathrm{sat}} \;\times\; s^{-\beta} \tag{A.11}$$

with ψ being the soil matric suction [L]. Equations (A.10) and (A.11), in which the subscripts 1 and 2 are removed, are used for both soil stores. To assign all soil

parameters (i.e. β, k_{sat}, ψ_{sat}, θ_{sat} and Z – see Table 4.1), we used the FAO soil map (1995) and a soil parameter table derived by van Beek and Bierkens (2009) based on the database of Global Soil Data Task (2000).

Net vertical fluxes between the second and groundwater stores, Q_{23} [$\text{L}\,\text{T}^{-1}$], also consist of percolation $Q_{2\to3}$ [$\text{L}\,\text{T}^{-1}$] and capillary rise $Q_{3\to2}$ [$\text{L}\,\text{T}^{-1}$]. Ideally, the flux $Q_{3\to2}$ [$\text{L}\,\text{T}^{-1}$] should exist and its amount is controlled by moisture contents and groundwater heads. However, in the offline coupling version of PCR-GLOBWB-MOD, to force one-way coupling of the land surface model to MODFLOW, the capillary rise from the groundwater store is inactivated ($Q_{3\to2}=0$), which is one of the limitations of offline coupling of the modeling approach.

In Chapter 5, we introduce the online coupling version of PCR-GLOBWB-MOD enabling the capillary rise from the groundwater store ($Q_{3\to2} \geq 0$) to sustain the soil moisture states of the upper soil stores and thus cannot fulfill high evaporation demand (during dry condtion). Here, the Gardner-Eagleson approach (Gardner, 1958; Eagleson, 1978; Soylu et al., 2011) is adopted to estimate capillary rise as a function of groundwater table position (see especially Sect. 5.2.1 for more detailed explanation).

A.5 Interflow or shallow sub-surface flow

In shallow soil deposits covering bed rocks and in regolith soil developed in mountainous areas, interflow or sub-surface storm flow is an important runoff component as perched groundwater bodies usually occur during wet periods. In PCR-GLOBWB, we model the interflow, Q_{sf} [$\text{L}\,\text{T}^{-1}$], as releasing water from the second store based on a simplified approach of Sloan and Moore (1984):

$$LQ_{\text{sf}}(t) = \left[1 - \frac{\Delta t}{\text{TCL}}\right] LQ_{\text{sf}}\ (t - \Delta t) + \frac{\Delta t}{\text{TCL}}\ L\ [Q_{12}(t) - Q_{23}(t)] \tag{A.12}$$

where (t) and $(t-\Delta t)$ indicate the actual time and previous time, $LQ_{\text{sf}}(t)$ [$\text{L}^2\,\text{T}^{-1}$] is the interflow per unit hillslope width, and L [L] is the average hillslope length, defined as half the average distance between stream channels. The parameter TCL [T] is a characteristic response time given by:

$$\text{TCL} = \frac{L \times (\theta_{\text{sat},2} - \theta_{\text{fc},2})}{2 \times K_{\text{sat},2} \times \tan(\alpha)} \tag{A.13}$$

where θ_{fc} [$-$] is the moisture content at field capacity and $\tan(\alpha)$ [$-$] is the grid-average slope for each cell. To derive $\tan(\alpha)$ in each cell of PCR-GLOBWB-MOD, we used the $3''$ DEM of HydroSHEDS. To derive θ_{fc} [$-$], we used Eq. (A.11) and assumed the matric suction ψ_{fc} (at field capacity) equals 1 m. To derive L, we derived

the channel network map of the Rhine-Meuse basin using the 3″ DEM and LDD of HydroSHEDS. First, we calculated a generalized divergence map ∇Sl (a generalized curvature) using 3×3 moving windows as outlined by Zevenbergen and Thorne (1987). Subsequently, by tracking from the most upstream 3″ cells, we located "channel head" cells, which are the inflection points from hillslope landscape cells – that are dominated by mass wasting and generalized by positive ∇Sl – to valley cells – that are areas of topographic convergence and generalized by negative ∇Sl (Montgomery and Foufoula-Georgiou, 1993; Howard, 1994). Then, we assumed every cell located downstream of these channel head cells to have streams with the total length equals to its cell diagonal length. Considering errors that may exist in DEM, we added a condition that cells having drainage contributing area higher than 2500 of 3-arc second cells (about $25\,\mathrm{km}^2$ at the equator) are channeled. Having derived the channel network map, we calculated L, which is approximately equal to half the reciprocal of drainage density, $1/2D_d$ (see e.g. Rodriguez-Iturbe and Rinaldo, 1997).

A.6 Soil evaporation and plant transpiration

Soil evaporation, Es $[\mathrm{L\,T^{-1}}]$, may originate from two places: (1) from the first store (in which the storage is S_1); and (2) from the melt water store in the snow pack (Ss_{sl}). The flux from Ss_{sl}, which is symbolized by Es_{sl} $[\mathrm{L\,T^{-1}}]$, is always prioritized over that from S_1, which is symbolized by Es_1 $[\mathrm{L\,T^{-1}}]$. The total of both is limited by the potential evaporation energy left after interception flux, $E_{\mathrm{p,s}}$ $[\mathrm{L\,T^{-1}}]$ ($Es_{\mathrm{sl}} + Es_1 \leq E_{\mathrm{p,s}}$). In PCR-GLOBWB-MOD, these principles are summarized by:

$$E_{\mathrm{p,s}} = (E_{\mathrm{p,0}} - f_{\mathrm{i}}\, E_{\mathrm{i}}) \times Kc_{\mathrm{s}} \times (1 - C_{\mathrm{f}}) \tag{A.14}$$

$$Es_{\mathrm{sl}}\, \Delta t = \min\,(Ss_{\mathrm{sl}},\; E_{\mathrm{p,s}}\, \Delta t) \tag{A.15}$$

where f_{i} $[-]$ is a parameter for updating $E_{\mathrm{p,0}}$ after the interception flux E_{i} (taken as 1) and Kc_{s} $[-]$ is a "crop factor" coefficient assumed for bare soil areas. In addition, Es_1 in the saturated area x is limited by the saturated conductivity $K_{\mathrm{sat,1}}$, while the one in the unsaturated area $(1 - x)$ is limited by the unsaturated conductivity $K_1(s_1)$:

$$\begin{aligned} Es_1 = (1 - x) \times \min\,(K_1\,(s_1),\; E_{\mathrm{p,s}} - Es_{\mathrm{sl}}) + \\ x \times \min\,(K_{\mathrm{sat,1}},\; E_{\mathrm{p,s}} - Es_{\mathrm{sl}}) \end{aligned} \tag{A.16}$$

Transpirations occurs due to root abstraction from both first and second soil stores. Their total flux, T_{12} $[\mathrm{L\,T^{-1}}]$, is limited to the potential energy left after interception flux, $E_{\mathrm{p,T}}$ $[\mathrm{L\,T^{-1}}]$ (hereafter called as potential transpiration). Under fully saturation, roots can experience lack of aeration preventing themselves to uptake water. Therefore, we consider that transpiration only takes place in unsaturated area $(1 - x)$. In PCR-GLOBWB-MOD, these principles are summarized by:

$$E_{\mathrm{p,T}} = (E_{\mathrm{p,0}} - f_{\mathrm{i}}\, E_{\mathrm{i}})\; Kc_{\mathrm{T}}\, C_{\mathrm{f}} \tag{A.17}$$

$$T_{12} = f_{\mathrm{T}}\, E_{\mathrm{p,T}}\, (1 - x) \tag{A.18}$$

where Kc_{T} [−] is the crop factor assumed for each land cover type and f_{T} [−] is a reducing factor due to lack of soil moisture (water stress) that was derived based on the Improved Arno Scheme concept by van Beek and Bierkens (2009):

$$f_{\mathrm{T}} \;=\; \frac{1}{1 \;+\; \left(\theta_{\mathrm{E}}/\theta_{50\,\%}\right)^{-3\;\beta_{50\,\%}}} \tag{A.19}$$

where the parameters $\theta_{50\,\%}$ [−] and $\beta_{50\,\%}$ [−] are the degree of saturation at which the potential transpiration is halved and the corresponding coefficient of its soil water retention curve, and θ_{E} [−] is a state variable representing the average degree of saturation over the unsaturated fraction $(1-x)$. Note that all θ_{E}, $\theta_{50\,\%}$ and $\beta_{50\,\%}$ are the effective values for the entire soil profile (the first and second soil stores):

$$\theta_{\mathrm{E}} \;=\; \frac{W_{\max} \;+\; b\Delta W \;\left[1 \;-\; \frac{b\;+\;1}{b}\;\left(\frac{\Delta W_{\mathrm{act}}}{\Delta W}\right)^{\frac{1}{b+1}}\right]}{W_{\max} \;+\; b\;\Delta W\;\left[1 \;-\; \left(\frac{\Delta W_{\mathrm{act}}}{\Delta W}\right)^{\frac{1}{b+1}}\right]} \tag{A.20}$$

$$\theta_{50\,\%} \;=\; \frac{SC_1 R_{\mathrm{f},1}\left(\frac{\psi_{50\,\%}}{\psi_{\mathrm{sat},1}}\right)^{-\frac{1}{\beta}} + SC_2 R_{\mathrm{f},2}\left(\frac{\psi_{50\,\%}}{\psi_{\mathrm{sat},2}}\right)^{-\frac{1}{\beta}}}{SC_1 R_{\mathrm{f},1} \;+\; SC_2 R_{\mathrm{f},2}} \tag{A.21}$$

$$\beta_{50\,\%} \;=\; \frac{SC_1\;R_{\mathrm{f},1}\;\beta_1 + SC_2\;R_{\mathrm{f},2}\;\beta_2}{SC_1 R_{\mathrm{f},1} \;+\; SC_2 R_{\mathrm{f},2}} \tag{A.22}$$

where $\psi_{50\,\%}$ [L] is the matric suction at which potential transpiration is halved (taken as 3.33 m), and R_{f} [−] is the root fractions per soil layer. Here we simplified that the root fractions are proportionally distributed according to the layer thicknesses, $R_{\mathrm{f},1} = Z_1/\left(Z_1 + Z_2\right)$ and $R_{\mathrm{f},2} = Z_2/\left(Z_1 + Z_2\right)$.

The distribution of the total transpiration T_{12} to the fluxes from both stores, T_1 and T_2 [$\mathrm{L\,T^{-1}}$], is based on the root fractions, $R_{\mathrm{f},1}$ and $R_{\mathrm{f},2}$, and available S_1 and S_2:

$$T_1 \;=\; \frac{R_{\mathrm{f},1}\;S_1}{R_{\mathrm{f},1}\;S_1 \;+\; R_{\mathrm{f},2}S_2} \;\times\; T_{12} \tag{A.23}$$

$$T_2 \;=\; \frac{R_{\mathrm{f},2}\;S_2}{R_{\mathrm{f},1}S_1 \;+\; R_{\mathrm{f},2}S_2} \;\times\; T_{12} \tag{A.24}$$

Within a time step, T_1 has the same priority as Es_1 and Q_{12}, while T_2 has the same priority as Q_{12} and Q_{sf}. If the available storages are limited to accommodate total fluxes, all fluxes are reduced proportionally to their sizes.

Crop factors Kc_{T} [−] in Eq. (A.17), based on land cover types, are calculated as (Allen et al., 1998):

$$Kc_{\mathrm{T,m}} \;=\; Kc_{\min} \;+ [Kc_{\mathrm{full}} \;-\; Kc_{\min}] \times [1 \;-\; \exp\left(-0.7\;\mathrm{LAI_m}\right)] \tag{A.25}$$

where $Kc_{\min}$ and Kc_{full} are crop factors assumed under minimum and full vegetation cover conditions. The first was taken as 0.2, while the latter was calculated as:

$$Kc_{\mathrm{full}} \;=\; 1.0 \;+\; 0.1 \;\times\; h_{\mathrm{veg}} \;\leq\; 1.2 \tag{A.26}$$

where h_{veg} is the height of vegetation in meter based on the table of van Beek (2008).

A.7 Baseflow and specific runoff from a land surface cell

In the land surface model part of PCR-GLOBWB-MOD, we still use the groundwater linear reservoir (in which the storage is S_3 [L]) to calculate the baseflow Q_{bf} [$\mathrm{L\,T^{-1}}$]:

$$Q_{\mathrm{bf}} \;=\; S_3 \; J \tag{A.27}$$

where J [$\mathrm{T^{-1}}$] is the reservoir coefficient based on Kraaijenhoff van de Leur (1958):

$$J \;=\; \frac{\pi^2 (KD)}{4 \; Sy \; \mathrm{L}^2} \tag{A.28}$$

with KD [$\mathrm{L^2\,T^{-1}}$] and Sy [$-$] being the aquifer transmissivity and specific yield.

The local runoff in a land surface cell, Q_{loc} [$\mathrm{L\,T^{-1}}$], is given as:

$$Q_{\mathrm{loc}} \;=\; Q_{\mathrm{dr}} \;+\; Q_{\mathrm{sf}} \;+\; Q_{\mathrm{bf}} \tag{A.29}$$

For the cells with "urban" and "glacier ice" land covers, Q_{loc} consists of only Q_{dr} because they are considered as impermeable areas where no infiltration can occur. Equation (A.29) is not valid for a "surface water" cell, which is described in Sect. A.8.

A.8 Surface water bodies and surface water accumulation in the land surface model

For cells classified as surface water, we assumed that the storage change Q_{wat} [$\mathrm{L\,T^{-1}}$] is influenced by the precipitation, P, and open water evaporation, E_{wat} [$\mathrm{L\,T^{-1}}$]:

$$Q_{\mathrm{wat}} \;=\; P \;-\; E_{\mathrm{wat}} \tag{A.30}$$

$$E_{\mathrm{wat}} \;=\; E_{\mathrm{p,0}} \;\times\; Kc_{\mathrm{wat}} \tag{A.31}$$

where Kc_{wat} [$-$] is the "crop factor" coefficient assumed for surface water bodies.

Knowing the cell areas for all grid-cells, A_{cell} [$\mathrm{L^2}$], and combining Q_{wat} and Q_{loc}, we can express the total local runoff in a water volume per unit time Q_{tot} [$\mathrm{L^3\,T^{-1}}$]:

$$Q_{\mathrm{tot}} \;=\; A_{\mathrm{cell}} \;\times\; [(1 \;-\; f_{\mathrm{wat}}) \; Q_{\mathrm{loc}} \;+\; f_{\mathrm{wat}} \; Q_{\mathrm{wat}}] \tag{A.32}$$

where f_{wat} [$-$] is either one for surface water cells or zero for non-surface water cells. To get the f_{wat} field, we integrated the surface water bodies identified in the GLCC 2.0 land cover map and the levels 1 and 2 of the Global Lakes and Wetlands Database (Lehner and Döll, 2004).

For the simulation in Chapter 4, we limit the discharge analysis to monthly resolution. Here, we could neglect water residence time in channels (less than a week) and obtain monthly discharge time series Q_{chn} [$\mathrm{L^3\,T^{-1}}$] by simply accumulating the monthly values of Q_{tot} along the drainage network. However, for the simulation in Chapter 5, the discharge calculation is expanded to daily resolution and referred to Sect. 5.2.2.

Appendix B Climatological forcing data

This appendix is adopted from:
Sutanudjaja, E. H., van Beek, L. P. H., de Jong, S. M., van Geer, F. C., Bierkens, M. F. P. (2011), Large-scale groundwater modeling using global datasets: a test case for the Rhine-Meuse basin, Hydrology and Earth System Sciences, 15, 2913-2935, doi:10.5194/hess-15-2913-2011.

Climate time series maps, consisting of temperature Ta, precipitation P, and reference potential evaporation $E_{\mathrm{p},0}$, are supplied on a daily basis to force the land surface model. For this study, we used the monthly CRU data (Mitchell and Jones, 2005; New et al., 2002) in combination with: (1) the EMCWF ERA-40 re-analysis data (Uppala et al., 2005), for the period 1960–1999 (Sect. B.1); and (2) the EMCWF operational archive (http://www.ecmwf.int/products/data/archive/descriptions/od/oper/index.html), for 2000–2008 (Sect. B.2).

B.1 Period 1960–1999

For the period 1960–1999, we used the monthly CRU-TS2.1 dataset (Mitchell and Jones, 2005), covering 1901–2002, and the daily ERA-40 reanalysis dataset (Uppala et al., 2005), covering 1957–2002. First, we re-sampled ERA-40 maps into half-degree (30′) resolution, which is the resolution of CRU-TS2.1. These re-sampled ERA-40 daily time series fields were subsequently used to downscale the monthly CRU-TS 2.1 into daily resolution. To get finer spatial resolution maps, we used the 10′ CRU-CL2.0 dataset (New et al., 2002), containing 12 monthly fields representing the average climatology over the period 1961–1990. For precipitation P, this algorithm is summarized by:

$$P_{30',\mathrm{d}} = \frac{P_{\text{ERA-40, }30',\mathrm{d}}}{P_{\text{ERA-40, }30',\mathrm{m}}} \times P_{\text{CRU-TS2.1},30',\mathrm{m}} \tag{B.1}$$

$$P_{\mathrm{fn},10',\mathrm{d}} = \frac{P_{\text{CRU-CL2.0},10',\mathrm{m}}}{P_{\text{CRU-CL2.0},30',\mathrm{m}}} \times P_{30',\mathrm{d}} \tag{B.2}$$

where the subscripts 10′ and 30′ indicate the spatial resolutions, the subscripts m and d indicate the monthly and daily resolutions, the subscripts CRU-CL2.0, CRU-TS2.1 and ERA-40 indicate the dataset names and the subscript fn stands for the final derived forcing data supplied to the model.

Equation (B.1), used for temporal downscaling from monthly to daily fields, and Eq. (B.2), used for spatial downscaling from 30′ to 10′, were also used to derive the daily 10′ forcing temperature fields, $Ta_{10',\mathrm{d}}$. For this temperature downscaling, the unit must be in Kelvin (K) in order to avoid zero and near zero values in the denominators. To improve the spatial resolution of the snow coverage (simulated by the snow pack), the forcing temperature fields were downscaled into 30″ resolution:

$$Ta_{\mathrm{fn},30'',\mathrm{d}} \;=\; Ta_{10',\mathrm{d}} \;+\; T_{\mathrm{LR}} \times (\mathrm{DEM}_{30''} - \mathrm{DEM}_{10'}) \tag{B.3}$$

where T_{LR} $[\Theta\,\mathrm{L}^{-1}]$ is the temperature lapse rate, $\mathrm{DEM}_{30''}$ is taken from the 30″ digital elevation map of HydroSHEDS (Lehner et al., 2008) and $\mathrm{DEM}_{10'}$ is its aggregated version at 10′ resolution.

For monthly reference potential evaporation $E_{\mathrm{p},0}$, we used the dataset of van Beek (2008), which is available at 30′, covering 1901–2002 and derived based on the FAO Penman-Monteith method (Allen et al., 1998). To derive monthly $E_{\mathrm{p},0}$ fields, van Beek used relevant climatological fields of CRU-TS2.1, such as cloud cover, vapour pressure, and average, minimum and maximum temperature fields. For wind speed fields, the CRU-CL1.0 (New et al., 1999) dataset, containing average monthly wind speeds over 1961–1990, was used as there are no wind speed fields defined in CRU-TS2.1. For PCR-GLOBWB-MOD, the 30′ monthly reference potential evaporation fields of van Beek (2008) – symbolized as $E_{\mathrm{p},0,*,30',\mathrm{m}}$ – were downscaled into 10' resolution fields using the monthly $Ta_{\text{CRU-CL2.0},10',\mathrm{m}}$ (unit: K), and into daily resolution using the daily $Ta_{10',\mathrm{d}}$ (K):

$$E_{\mathrm{p},0,10',\mathrm{m}} \;=\; \frac{Ta_{\text{CRU-CL2.0},10',\mathrm{m}}}{Ta_{\text{CRU-CL2.0},30',\mathrm{m}}} \;\times\; E_{\mathrm{p},0,*,30',\mathrm{m}} \tag{B.4}$$

$$E_{\mathrm{p},0,\mathrm{fn},10',\mathrm{d}} \;=\; \frac{Ta_{10',\mathrm{d}}}{Ta_{10',\mathrm{m}}} \;\times\; E_{\mathrm{p},0,10',\mathrm{m}} \tag{B.5}$$

B.2 Period 2000–2008

For the precipitation and temperature forcing during 2000–2008, we used the ECMWF operational archive (`http://www.ecmwf.int/products/data/archive/descriptions/od/oper/index.html`) that was constrained to the long term averages and trends of the CRU-TS2.1 data:

1. For each year y, the annual mean of the CRU-TS2.1 forcing data, $F_{\text{CRU-TS2.1,y}}$ (which may be either precipitation or temperature) was calculated. Then, the 1961–1980 long-term mean of $F_{\text{CRU-TS2.1,y}}$ – symbolized as $\bar{F}_{\text{CRU-TS2.1,61-80}}$ – was also calculated.

2. Next, for the period 1981–2002, we calculated the anomaly time series A_{y}:

$$A_{\mathrm{y}} \;=\; F_{\text{CRU-TS2.1,y}} - \bar{F}_{\text{CRU-TS2.1,61-80}} \tag{B.6}$$

3. Furthermore, the trend of A_{y} time series was regressed with a linear model:

$$A_{\mathrm{y}}^{\mathrm{trend}} \;=\; b_0 \;+\; b_1 \;\times\; \mathrm{y} \tag{B.7}$$

where $A_{\mathrm{y}}^{\mathrm{trend}}$ is the model prediction, while b_0 and b_1 are the intercept and slope parameters.

4. Subsequently, the 2000–2008 long-term mean, $\bar{F}^{\mathrm{trend}}_{\text{CRU-TS2.1,00-08}}$, was estimated using Eq. (B.7), $\bar{F}_{\text{CRU-TS2.1,61-80}}$ and the year y = 2004, which is taken as the representative of the period 2000–2008:

$$\begin{aligned} \bar{F}^{\mathrm{trend}}_{\text{CRU-TS2.1,00-08}} \;&=\; \bar{F}_{\text{CRU-TS2.1,61-80}} \\ &\quad +\; (b_0 \;+\; b_1 \;\times\; 2004) \end{aligned} \tag{B.8}$$

5. As done in the step 1, the long-term average of annual means of the ECMWF operational archive doatasets (hereafter called as "ECMWF-OA") for the period 2000–2008 – symbolized as $\bar{F}_{\text{ECMWF-OA,00-08}}$ – was calculated.

6. Next, the bias between $\bar{F}_{\text{ECMWF-OA,00-08}}$ and $\bar{F}^{\mathrm{trend}}_{\text{CRU-TS2.1,00-08}}$, was identified and used to correct the ECMWF operational archive datasets:

$$F^{\mathrm{corrected}}_{\text{ECMWF-OA,m}} \;=\; F_{\text{ECMWF-OA,m}} \;+\; \Delta\bar{F} \tag{B.9}$$

$$\Delta\bar{F} \;=\; \bar{F}^{\mathrm{trend}}_{\text{CRU-TS2.1,00-08}} - \bar{F}_{\text{ECMWF-OA,00-08}} \tag{B.10}$$

where $F_{\text{ECMWF-OA,m}}$ are the original ECMWF-OA fields and $F^{\mathrm{corrected}}_{\text{ECMWF-OA,m}}$ are their corrected ones that are used to force the land surface model (2000–2008).

7. The aforementioned procedure is done at monthly and half arc-degree resolution, for both precipitation P and temperature Ta fields. To obtain finer resolutions, Eqs. (B.1), (B.2) and (B.3) were used.

To obtain monthly reference potential evaporation $E_{\mathrm{p,0}}$ fields over the period 2000–2008, for most of which no CRU-TS2.1 datasets are available, we defined a procedure to select the corresponding data from the monthly dataset of van Beek (2008), $E_{\mathrm{p,0,*,30',m}}$, that covers the period 1901-2002. The procedure – repeated for each $30' \times 30'$ cell, and every month m and year y in 2000–2008 – is summarized as:

1. For the month m, we identified the corresponding year y-CRU from the 1901-2002 CRU-TS2.1 dataset in which the precipitation $P_{\text{CRU-TS2.1,m,y-CRU}}$ and temperature $Ta_{\text{CRU-TS2.1,m,y-CRU}}$ are similar to $P^{\mathrm{corrected}}_{\text{ECMWF-OA,m,y}}$ and $Ta^{\mathrm{corrected}}_{\text{ECMWF-OA,m,y}}$.

2. Next, we assumed that the monthly reference potential evaporation $E_{\mathrm{p,0,30',m,y}}$ (where y is in the interval $[2000, 2008]$) is the same as the one of van Beek (2008) for the month m and year y-CRU, $E_{\mathrm{p,0,*,m,y\text{-}CRU}}$ (where y-CRU is in the interval $[1901, 2002]$).

3. To get finer resolutions, Eqs. (B.4) and (B.5) were used.

References

Abbott, M., J. Bathurst, J. Cunge, P. O'Connell and J. Rasmussen (1986a), An introduction to the European Hydrological System - Systeme Hydrologique Europeen, "SHE", 1: History and philosophy of a physically-based, distributed modelling system. Journal of Hydrology 87, 45–59. URL http://dx.doi.org/10.1016/0022-1694(86)90114-9.

Abbott, M., J. Bathurst, J. Cunge, P. O'Connell and J. Rasmussen (1986b), An introduction to the European Hydrological System - Systeme Hydrologique Europeen, "SHE", 2: Structure of a physically-based, distributed modelling system. Journal of Hydrology 87, 61–77. URL http://dx.doi.org/10.1016/0022-1694(86)90115-0.

Alkhaier, F., G. N. Flerchinger and Z. Su (2012a), Shallow groundwater effect on land surface temperature and surface energy balance under bare soil conditions: modeling and description. Hydrology and Earth System Sciences 16, 1817–1831. URL http://dx.doi.org/10.5194/hess-16-1817-2012.

Alkhaier, F., Z. Su and G. N. Flerchinger (2012b), Reconnoitering the effect of shallow groundwater on land surface temperature and surface energy balance using MODIS and SEBS. Hydrology and Earth System Sciences 16, 1833–1844. URL http://dx.doi.org/10.5194/hess-16-1833-2012.

Allen, R. G., L. S. Pereira, D. Raes and M. Smith (1998), Crop evapotranspiration: Guidelines for computing crop requirements. UN-FAO, Rome, Italy. URL http://www.fao.org/docrep/X0490E/X0490E00.htm.

Anyah, R. O., C. P. Weaver, G. Miguez-Macho, Y. Fan and A. Robock (2008), Incorporating water table dynamics in climate modeling: 3. Simulated groundwater influence on coupled land-atmosphere variability. Journal of Geophysical Research 113, D07103. URL http://dx.doi.org/10.1029/2007JD009087.

Bakker, M., E. Anderson, T. Olsthoorn and O. Strack (1999), Regional groundwater modeling of the Yucca Mountain site using analytic elements. Journal of Hydrology 226, 167–178. URL http://dx.doi.org/10.1016/S0022-1694(99)00149-3.

Bastiaanssen, W. G. M., M. Menenti, R. A. Feddes and A. A. M. Holtslag (1998a), A remote sensing surface energy balance algorithm for land (SEBAL). 1. Formulation. Journal of Hydrology 212-213, 198–212. URL http://dx.doi.org/10.1016/S0022-1694(98)00253-4.

Bastiaanssen, W. G. M., H. Pelgrum, J. Wang, Y. Ma, J. F. Moreno, G. J. Roerink and T. van der Wal (1998b), A remote sensing surface energy balance algorithm for land (SEBAL).: 2. Validation. Journal of Hydrology 212-213, 213 – 229. URL http://dx.doi.org/10.1016/S0022-1694(98)00254-6.

Becker, M. W. (2006), Potential for Satellite Remote Sensing of Ground Water. Ground Water 44, 306–18. URL http://dx.doi.org/10.1111/j.1745-6584.2005.00123.x.

Berendrecht, W., A. Heemink, F. van Geer and J. Gehrels (2003), Decoupling of modeling and measuring interval in groundwater time series analysis based on response characteristics. Journal of Hydrology 278, 1–16. URL http://dx.doi.org/10.1016/S0022-1694(03)00075-1.

Bergström, S. (1995), The HBV model. In: V. Singh, ed., Computer Models of Watershed Hydrology, Water Resources Publications, Highlands Ranch, CO.

Beven, K. J. (1993), Prophecy, reality and uncertainty in distributed hydrological modelling. Advances in Water Resources 16, 41–51. URL http://dx.doi.org/10.1016/0309-1708(93)90028-E.

Bierkens, M., P. A. Finke and P. de Willigen (2000), Upscaling and Downscaling Methods for Environmental Research. Kluwer Academic Publishers, Dordrecht, The Netherlands.

Bierkens, M. F. P. and B. J. J. M. van den Hurk (2007), Groundwater convergence as a possible mechanism for multi-year persistence in rainfall. Geophysical Research Letters 34, L02402. URL http://dx.doi.org/10.1029/2006GL028396.

Bierkens, M. F. P., M. Knotters and F. C. van Geer (1999), Calibration of transfer function-noise models to sparsely or irregularly observed time series. Water Resources Research 35, 1741–1750. URL http://dx.doi.org/10.1029/1999WR900083.

Bierkens, M. F. P., M. Knotters and T. Hoogland (2001), Space-time modeling of water table depth using a regionalized time series model and the Kalman Filter. Water Resources Research 37, 1277–1290. URL http://dx.doi.org/10.1029/2000WR900353.

Bos, M. G. (1989), Discharge measurement structures (Third revised edition). International Institute for Land Reclamation and Improvement (ILRI), Wageningen, The Netherlands.

Box, G. E. P. and G. M. Jenkins (1976), Time Series Analysis: Forecasting and Control. Holden-Day, San Francisco.

Brocca, L., F. Melone, T. Moramarco, W. Wagner and S. Hasenauer (2010), ASCAT soil wetness index validation through in situ and modeled soil moisture data in central Italy. Remote Sensing of Environment 114, 2745–2755. URL http://dx.doi.org/10.1016/j.rse.2010.06.009.

Campbell, G. (1974), A simple method for determining unsaturated conductivity from moisture retention data. Soil Science 117, 311–314.

Ceballos, A., K. Scipal, W. Wagner and J. Martnez-Fernndez (2005), Validation of ERS scatterometer-derived soil moisture data in the central part of the Duero Basin, Spain. Hydrological Processes 19, 1549–1566. URL http://dx.doi.org/10.1002/hyp.5585.

Clapp, R. B. and G. M. Hornberger (1978), Empirical equations for some soil hydraulic properties. Water Resources Research 14, 601–604. URL http://dx.doi.org/10.1029/WR014i004p00601.

D'Agnese, F. A., C. C. Faunt, M. C. Hill and A. K. Turner (1999), Death valley regional ground-water flow model calibration using optimal parameter estimation methods and geoscientific information systems. Advances in Water Resources 22, 777–790. URL http://www.sciencedirect.com/science/article/B6VCF-3X4WKTG-2/2/ae57e8ad74f238a406ad86696bccd51c.

Dankers, R. and S. M. de Jong (2004), Monitoring snow-cover dynamics in Northern Fennoscandia with SPOT VEGETATION images. International Journal of Remote Sensing 25, 2933–2949. URL http://dx.doi.org//10.1080/01431160310001618374.

de Jeu, R. A. M. and M. Owe (2003), Further validation of a new methodology for surface moisture and vegetation optical depth retrieval. International Journal of Remote Sensing 24, 4559–4578. URL http://dx.doi.org/10.1080/0143116031000095934.

de Jong, S. M. and V. G. Jetten (2007), Estimating spatial patterns of rainfall interception from remotely sensed vegetation indices and spectral mixture analysis. International Journal of Geographical Information Science 21, 529–545. URL http://dx.doi.org/10.1080/13658810601064884.

de Lange, R., R. Beck, N. van de Giesen, J. Friesen, A. de Wit and W. Wagner (2008), Scatterometer-Derived Soil Moisture Calibrated for Soil Texture With a One-Dimensional Water-Flow Model. Geoscience and Remote Sensing, IEEE Transactions on 46, 4041–4049. URL http://dx.doi.org/10.1109/TGRS.2008.2000796.

de Wit, M. (2001), Effect of climate change on the hydrology of the river Meuse. National Institute for Public Health and the Environment (RIVM), Bilthoven, The Netherlands.

Dooge, J. (1973), Linear theory of hydrologic systems. Technical bulletin No. 1468, United States Department of Agriculture, Agricultural Research Service.

Dorigo, W. A., W. Wagner, R. Hohensinn, S. Hahn, C. Paulik, A. Xaver, A. Gruber, M. Drusch, S. Mecklenburg, P. van Oevelen, A. Robock and T. Jackson (2011), The International Soil Moisture Network: A data hosting facility for global in situ soil moisture measurements. Hydrology and Earth System Sciences 15, 1675–1698. URL http://www.hydrol-earth-syst-sci.net/15/1675/2011/.

Drinkwater, M. R., R. Floberghagen, R. Haagmans, D. Muzi and A. Popescu (2003), GOCE: ESA's first Earth Explorer Core mission. In: G. B. Beutler, M. R. Drinkwater, R. Rummel and R. von Steiger, eds., Earth Gravity Field from Space – from Sensors to Earth Sciences, vol. 18 of *Space Sciences Series*, Kluwer Academic Publishers, Dordrecht, The Netherlands, 419–432.

Drinkwater, M. R., R. Haagmans, D. Muzi, A. Popescu, R. Floberghagen, M. Kern and M. Fehringer (2007), The GOCE gravity mission: ESA's First Core Earth Explorer. In: Proceedings of the 3rd International GOCE User Workshop, 6-8 November 2006, Frascati, Italy, ESA SP-627, 1–8.

Dürr, H. H., M. Meybeck and S. H. Dürr (2005), Lithologic composition of the Earth's continental surfaces derived from a new digital map emphasizing riverine material transfer. Global Biogeochemical Cycles 19, GB4S10. URL http://dx.doi.org/10.1029/2005GB002515.

Eagleson, P. S. (1978), Climate, soil, and vegetation: 3. A simplified model of soil moisture movement in the liquid phase. Water Resources Research 14, 722–730. URL http://dx.doi.org/10.1029/WR014i005p00722.

Fan, Y. and G. Miguez-Macho (2010), Potential groundwater contribution to Amazon evapotranspiration. Hydrology and Earth System Sciences 14, 2039–2056. URL http://dx.doi.org/10.5194/hess-14-2039-2010.

Fan, Y. and G. Miguez-Macho (2011), A simple hydrologic framework for simulating wetlands in climate and earth system models. Climate Dynamics 37, 253–278. URL http://dx.doi.org/10.1007/s00382-010-0829-8.

Fan, Y., G. Miguez-Macho, C. P. Weaver, R. Walko and A. Robock (2007), Incorporating water table dynamics in climate modeling: 1. Water table observations and equilibrium water table simulations. Journal of Geophysical Research 112, D10125. URL http://dx.doi.org/10.1029/2006JD008111.

Food and Agriculture Organization of the United Nations (FAO) (1995), Digital Soil Map of the World, Version 3.5. FAO, Rome, Italy.

Freeze, R. and R. Harlan (1969), Blueprint for a physically-based, digitally-simulated hydrologic response model. Journal of Hydrology 9, 237–258. URL http://dx.doi.org/10.1016/0022-1694(69)90020-1.

Freeze, R. A. and J. A. Cherry (1979), Groundwater. Prentice-Hall, Englewood Cliffs, New Jersey.

Gambolati, G., P. Gatto and R. A. Freeze (1974), Predictive Simulation of the Subsidence of Venice. Science 183, 849–851.

Gardner, W. R. (1958), Some steady-state solutions of the unsaturated moisture flow equation with application to evaporation from a water table. Soil Science 85, 228–32.

Gehrels, J., F. van Geer and J. de Vries (1994), Decomposition of groundwater level fluctuations using transfer modelling in an area with shallow to deep unsaturated zones. Journal of Hydrology 157, 105–138. URL http://dx.doi.org/10.1016/0022-1694(94)90101-5.

Gleeson, T., L. Smith, N. Moosdorf, J. Hartmann, H. H. Dürr, A. H. Manning, L. P. H. van Beek and A. M. Jellinek (2011), Mapping permeability over the surface of the earth. Geophys. Res. Lett. 38, L02401. URL http://dx.doi.org/10.1029/2010GL045565.

Gleick, P. H. (1996), Water resources. In: S. H. Schneider, ed., Encyclopedia of Climate and Weather, vol. 2, Oxford University Press, 817–823.

Global Soil Data Task (2000), Global Soil Data Products CD-ROM (IGBP-DIS).

Hagemann, S. (2002), An improved land surface parameter dataset for global and regional climate models. Max-Planck-Institut für Meteorologie, Hamburg, Germany. URL https://www.mpimet.mpg.de/fileadmin/publikationen/Reports/max_scirep_336.pdf.

Hagemann, S. and L. D. Gates (2003), Improving a subgrid runoff parameterization scheme for climate models by the use of high resolution data derived from satellite observations. Climate Dynamics 21, 349–359. URL http://dx.doi.org/10.1007/s00382-003-0349-x.

Haitjema, H. M. and S. Mitchell-Bruker (2005), Are Water Tables a Subdued Replica of the Topography? Ground Water 43, 781–786. URL http://dx.doi.org/10.1111/j.1745-6584.2005.00090.x.

Hansen, M. C., S. V. Stehman, P. V. Potapov, T. R. Loveland, J. R. G. Townshend, R. S. DeFries, K. W. Pittman, B. Arunarwati, F. Stolle, M. K. Steininger, M. Carroll and C. DiMiceli (2008), Humid tropical forest clearing from 2000 to 2005 quantified by using multitemporal and multiresolution remotely sensed data. Proceedings of the National Academy of Sciences 105, 9439–9444. URL http://dx.doi.org/10.1073/pnas.0804042105.

Hintze, J. L. and R. D. Nelson (1998), Violin Plots: A Box Plot-Density Trace Synergism. The American Statistician 52, 181–184.

Hipel, K. and A. McLeod (1994), Time Series Modelling of Water Resources and Environmental Systems. Developments in Water Science No. 45, Elsevier.

Howard, A. (1994), A detachment-limited model of drainage basin evolution. Water Resources Research 30, 2261–2285. URL http://dx.doi.org/10.1029/94WR00757.

Hubbert, M. K. (1940), The Theory of Ground-Water Motion. The Journal of Geology 48, 785–944.

Immerzeel, W. W., P. Droogers, S. M. de Jong and M. F. P. Bierkens (2009), Large-scale monitoring of snow cover and runoff simulation in Himalayan river basins using remote sensing. Remote Sensing of Environment 113, 40–49. URL http://dx.doi.org/10.1016/j.rse.2008.08.010.

Jackson, T. (2002), Remote sensing of soil moisture: implications for groundwater recharge. Hydrogeology Journal 10, 40–51. URL http://dx.doi.org/10.1007/s10040-001-0168-2.

Jung, M., M. Reichstein, P. Ciais, S. I. Seneviratne, J. Sheffield, M. L. Goulden, G. Bonan, A. Cescatti, J. Chen, R. de Jeu, A. J. Dolman, W. Eugster, D. Gerten, D. Gianelle, N. Gobron, J. Heinke, J. Kimball, B. E. Law, L. Montagnani, Q. Mu, B. Mueller, K. Oleson, D. Papale, A. D. Richardson, O. Roupsard, S. Running, E. Tomelleri, N. Viovy, U. Weber, C. Williams, E. Wood, S. Zaehle and K. Zhang (2010), Recent decline in the global land evapotranspiration trend due to limited moisture supply. Nature 467, 951–954. URL http://dx.doi.org/10.1038/nature09396.

Kerr, Y., P. Waldteufel, J.-P. Wigneron, J. Martinuzzi, J. Font and M. Berger (2001), Soil moisture retrieval from space: the Soil Moisture and Ocean Salinity (SMOS) mission. Geoscience and Remote Sensing, IEEE Transactions on 39, 1729–1735.

Knotters, M. and M. F. Bierkens (2001), Predicting water table depths in space and time using a regionalised time series model. Geoderma 103, 51–77. URL http://dx.doi.org/10.1016/S0016-7061(01)00069-6.

Knotters, M. and M. F. P. Bierkens (2000), Physical basis of time series models for water table depths. Water Resources Research 36, 181–188. URL http://dx.doi.org/10.1029/1999WR900288.

Kollet, S. J. and R. M. Maxwell (2006), Integrated surface groundwater flow modeling: A free-surface overland flow boundary condition in a parallel groundwater flow model. Advances in Water Resources 29, 945 – 958. URL http://dx.doi.org/10.1016/j.advwatres.2005.08.006.

Kollet, S. J. and R. M. Maxwell (2008), Capturing the influence of groundwater dynamics on land surface processes using an integrated, distributed watershed model. Water Resour. Res. 44, W02402. URL http://dx.doi.org/10.1029/2007WR006004.

Koster, R. D., M. J. Suarez, A. Ducharne, M. Stieglitz and P. Kumar (2000), A catchment-based approach to modeling land surface processes in a general circulation model: 1. Model structure. Journal of Geophysical Research 105, 24809–24822. URL http://dx.doi.org/10.1029/2000JD900327.

Kraaijenhoff van de Leur, D. (1958), A study of non-steady groundwater flow with special reference to a reservoir coefficient. De Ingénieur 70, 87–94.

Kummerow, C., J. Simpson, O. Thiele, W. Barnes, A. T. C. Chang, E. Stocker, R. F. Adler, A. Hou, R. Kakar, F. Wentz, P. Ashcroft, T. Kozu, Y. Hong, K. Okamoto, T. Iguchi, H. Kuroiwa, E. Im, Z. Haddad, G. Huffman, B. Ferrier, W. S. Olson, E. Zipser, E. A. Smith, T. T. Wilheit, G. North, T. Krishnamurti and K. Nakamura (2000), The status of the Tropical Rainfall Measuring Mission (TRMM) after two years in orbit. Journal of Applied Meteorology 39, 1965–1982. URL http://dx.doi.org/10.1175/1520-0450(2001)040<1965:TSOTTR>2.0.CO;2.

Lacey, G. (1930), Stable channels in alluvium. Proceedings of the Institution of Civil Engineers, London 229, 259–292.

Lam, A., D. Karssenberg, B. J. J. M. van den Hurk and M. F. P. Bierkens (2011), Spatial and temporal connections in groundwater contribution to evaporation. Hydrology and Earth System Sciences 15, 2621–2630. URL http://dx.doi.org/10.5194/hess-15-2621-2011.

Lehner, B. and P. Döll (2004), Development and validation of a global database of lakes, reservoirs and wetlands. Journal of Hydrology 296, 1–22. URL http://dx.doi.org/10.1016/j.jhydrol.2004.03.028.

Lehner, B., K. Verdin and A. Jarvis (2008), New global hydrography derived from spaceborne elevation data. Eos 89. URL http://dx.doi.org/10.1029/2008EO100001.

Liang, X., D. P. Lettenmaier, E. F. Wood and S. J. Burges (1994), A simple hydrologically based model of land surface water and energy fluxes for general circulation models. Journal of Geophysical Research 99, 14415–14428. URL http://dx.doi.org/10.1029/94JD00483.

Liu, Y. Y., R. M. Parinussa, W. A. Dorigo, R. A. M. De Jeu, W. Wagner, A. I. J. M. van Dijk, M. F. McCabe and J. P. Evans (2011), Developing an improved soil moisture dataset by blending passive and active microwave satellite-based retrievals. Hydrology and Earth System Sciences 15, 425–436. URL http://www.hydrol-earth-syst-sci.net/15/425/2011/.

Manning, R. (1891), On the flow of water in open channels and pipes. Transactions of the Institution of Civil Engineers of Ireland 20, 161–207.

Martínez-Fernández, J. and A. Ceballos (2005), Mean soil moisture estimation using temporal stability analysis. Journal of Hydrology 312, 28–38. URL http://dx.doi.org/10.1016/j.jhydrol.2005.02.007.

Maxwell, R. M. and S. J. Kollet (2008), Interdependence of groundwater dynamics and land-energy feedbacks under climate change. Nature Geoscience 1, 665–669. URL http://dx.doi.org/10.1038/ngeo315.

McDonald, M. and A. Harbaugh (1988), A modular three-dimensional finite-difference ground-water flow model: Techniques of Water-Resources Investigations of the United States Geological Survey, Book 6. URL http://pubs.water.usgs.gov/twri6a1.

Miguez-Macho, G., Y. Fan, C. P. Weaver, R. Walko and A. Robock (2007), Incorporating water table dynamics in climate modeling: 2. Formulation, validation, and soil moisture simulation. Journal of Geophysical Research 112, D13108. URL http://dx.doi.org/10.1029/2006JD008112.

Miguez-Macho, G., H. Li and Y. Fan (2008), Simulated water table and soil moisture climatology over North America. Bulletin of the American Meteorological Society 89, 663–672. URL http://dx.doi.org/10.1175/BAMS-89-5-663.

Mitchell, T. D. and P. D. Jones (2005), An improved method of constructing a database of monthly climate observations and associated high-resolution grids. International Journal of Climatology 25, 693–712. URL http://dx.doi.org/10.1002/joc.1181.

Montgomery, D. and E. Foufoula-Georgiou (1993), Channel network source representation using digital elevation models. Water Resources Research 29, 3925–3934. URL http://dx.doi.org/10.1029/93WR02463.

Mu, Q., F. A. Heinsch, M. Zhao and S. W. Running (2007), Development of a global evapotranspiration algorithm based on MODIS and global meteorology data. Remote Sensing of Environment 111, 519–536. URL http://dx.doi.org/10.1016/j.rse.2007.04.015.

Myneni, R., S. Hoffman, Y. Knyazikhin, J. Privette, J. Glassy, Y. Tian, Y. Wang, X. Song, Y. Zhang, G. Smith, A. Lotsch, M. Friedl, J. Morisette, P. Votava, R. Nemani and S. Running (2002), Global products of vegetation leaf area and fraction absorbed PAR from year one of MODIS data. Remote Sensing of Environment 83, 214–231. URL http://dx.doi.org/10.1016/S0034-4257(02)00074-3.

Nash, J. and J. Sutcliffe (1970), River flow forecasting through conceptual models part I — A discussion of principles. Journal of Hydrology 10, 282–290. URL http://dx.doi.org/10.1016/0022-1694(70)90255-6.

New, M., M. Hulme and P. Jones (1999), Representing Twentieth-Century Space-Time Climate Variability. Part I: Development of a 1961-90 Mean Monthly Terrestrial Climatology. Journal of Climate 12, 829–856. URL http://dx.doi.org/10.1175/1520-0442(1999)012<0829:RTCSTC>2.0.CO;2.

New, M., D. Lister, M. Hulme and I. Makin (2002), A high-resolution data set of surface climate over global land areas. Climate Research 21, 1–25.

Njoku, E., T. Jackson, V. Lakshmi, T. Chan and S. Nghiem (2003), Soil moisture retrieval from AMSR-E. Geoscience and Remote Sensing, IEEE Transactions on 41, 215–229. URL http://dx.doi.org/10.1109/TGRS.2002.808243.

Nobre, A., L. Cuartas, M. Hodnett, C. Renn, G. Rodrigues, A. Silveira, M. Waterloo and S. Saleska (2011), Height Above the Nearest Drainage - A hydrologically relevant new terrain model. Journal of Hydrology 404, 13–29. URL http://dx.doi.org/10.1016/j.jhydrol.2011.03.051.

Olson, J. (1994a), Global ecosystem framework-definitions. Tech. Rep., USGS EROS Data Center Internal Report, Sioux Falls, SD.

Olson, J. (1994b), Global ecosystem framework-translation strategy. Tech. Rep., USGS EROS Data Center Internal Report, Sioux Falls, SD.

Olsthoorn, T. N. (2008), Do a Bit More with Convolution. Ground Water 46, 13–22. URL http://dx.doi.org/10.1111/j.1745-6584.2007.00342.x.

Olsthoorn, T. N. and P. T. W. J. Kamps (1996), Groundwater model calibration for the Amsterdam Water Supply dune area. IAHS Publ. 237, 105–114.

Olsthoorn, T. N. and P. T. W. J. Kamps (2006), Challenges to Calibration: Facing an Increasingly Critical Environment. Ground Water 44, 876–879. URL http://dx.doi.org/10.1111/j.1745-6584.2006.00247.x.

Oude Essink, G. H. P., E. S. van Baaren and P. G. B. de Louw (2010), Effects of climate change on coastal groundwater systems: A modeling study in the Netherlands. Water Resources Research 46, W00F04. URL http://dx.doi.org/10.1029/2009WR008719.

Rennó, C. D., A. D. Nobre, L. A. Cuartas, J. V. Soares, M. G. Hodnett, J. Tomasella and M. J. Waterloo (2008), HAND, a new terrain descriptor using

SRTM-DEM: Mapping terra-firme rainforest environments in Amazonia. Remote Sensing of Environment 112, 3469–481. URL http://dx.doi.org/10.1016/j.rse.2008.03.018.

Restrepo, J., A. Montoya and J. Obeysekera (1998), A Wetland Simulation Module for the MODFLOW Ground Water Model. Ground Water 36, 764–770. URL http://dx.doi.org/10.1111/j.1745-6584.1998.tb02193.x.

Rodell, M., J. Chen, H. Kato, J. Famiglietti, J. Nigro and C. Wilson (2007), Estimating groundwater storage changes in the Mississippi River basin (USA) using GRACE. Hydrogeology Journal 15, 159–166. URL http://dx.doi.org/10.1007/s10040-006-0103-7.

Rodell, M., I. Velicogna and J. S. Famiglietti (2009), Satellite-based estimates of groundwater depletion in India. Nature 460, 999–1002. URL http://dx.doi.org/10.1038/nature08238.

Rodriguez-Iturbe, I. and A. Rinaldo (1997), Fractal River Basins: Chance and Self-Organization. Cambridge University Press.

Savenije, H. H. G. (2003), The width of a bankfull channel; Lacey's formula explained. Journal of Hydrology 276, 176–183. URL http://dx.doi.org/10.1016/S0022-1694(03)00069-6.

Savenije, H. H. G. (2004), The importance of interception and why we should delete the term evapotranspiration from our vocabulary. Hydrological Processes 18, 1507–1511. URL http://dx.doi.org/10.1002/hyp.5563.

Savenije, H. H. G. (2010), HESS Opinions "Topography driven conceptual modelling (FLEX-Topo)". Hydrology and Earth System Sciences 14, 2681–2692. URL http://dx.doi.org/10.5194/hess-14-2681-2010.

Schmitz, O., D. Karssenberg, W. van Deursen and C. Wesseling (2009), Linking external components to a spatio-temporal modelling framework: Coupling MODFLOW and PCRaster. Environmental Modelling & Software 24, 1088–1099. URL http://dx.doi.org/10.1016/j.envsoft.2009.02.018.

Scibek, J. and D. M. Allen (2006), Modeled impacts of predicted climate change on recharge and groundwater levels. Water Resources Research 42, W11405. URL http://dx.doi.org/10.1029/2005WR004742.

Scipal, K., C. Scheffler and W. Wagner (2005), Soil moisture-runoff relation at the catchment scale as observed with coarse resolution microwave remote sensing. Hydrology and Earth System Sciences 9, 173–183. URL http://www.hydrol-earth-syst-sci.net/9/173/2005/.

Sivapalan, M., G. Blschl, L. Zhang and R. Vertessy (2003), Downward approach to hydrological prediction. Hydrological Processes 17, 2101–2111. URL http://dx.doi.org/10.1002/hyp.1425.

Sloan, P. G. and I. D. Moore (1984), Modeling subsurface stormflow on steeply sloping forested watersheds. Water Resources Research 20, 1815–1822. URL http://dx.doi.org/10.1029/WR020i012p01815.

Snepvangers, J., B. Minnema, W. Berendrecht, P. Vermeulen, A. Lourens, W. van der Linden, M. Duijn, J. van Bakkel, W.-J. Zaadnoordijk, M. Boerefijn, M. Meeuwissen and V. Lagendijk (2008), MIPWA : Water managers develop their own high-resolution groundwater model tools. IAHS Publ. 320, 108–113.

Soil Conservation Service (SCS) (1972), National Engineering Handbook, Section 4: Hydrology. United States Department of Agriculture.

Sólyom, P. B. and G. E. Tucker (2004), Effect of limited storm duration on landscape evolution, drainage basin geometry, and hydrograph shapes. Journal of Geophysical Research 109, F03012. URL http://dx.doi.org/10.1029/2003JF000032.

Soylu, M. E., E. Istanbulluoglu, J. D. Lenters and T. Wang (2011), Quantifying the impact of groundwater depth on evapotranspiration in a semi-arid grassland region. Hydrology and Earth System Sciences 15, 787–806. URL http://dx.doi.org/10.5194/hess-15-787-2011.

Stephenson, G. R. and R. A. Freeze (1974), Mathematical simulation of subsurface flow contributions to snowmelt runoff, Reynolds Creek Watershed, Idaho. Water Resources Research 10, 284–294. URL http://dx.doi.org/10.1029/WR010i002p00284.

Strassberg, G., B. R. Scanlon and D. Chambers (2009), Evaluation of groundwater storage monitoring with the GRACE satellite: Case study of the High Plains aquifer, central United States. Water Resour. Res. 45, W05410. URL http://dx.doi.org/10.1029/2008WR006892.

Su, Z. (2002), The Surface Energy Balance System (SEBS) for estimation of turbulent heat fluxes. Hydrology and Earth System Sciences 6, 85–100. URL http://dx.doi.org/10.5194/hess-6-85-2002.

Sutanudjaja, E. H., L. P. H. van Beek, S. M. de Jong, F. C. van Geer and M. F. P. Bierkens (2011), Large-scale groundwater modeling using global datasets: a test case for the Rhine-Meuse basin. Hydrology and Earth System Sciences 15, 2913–2935. URL http://dx.doi.org/10.5194/hess-15-2913-2011.

Swenson, S., J. Famiglietti, J. Basara and J. Wahr (2008), Estimating profile soil moisture and groundwater variations using GRACE and Oklahoma Mesonet soil moisture data. Water Resources Research 44, W01413. URL http://dx.doi.org/10.1029/2007WR006057.

Tapley, B. D., S. Bettadpur, J. C. Ries, P. F. Thompson and M. M. Watkins (2004), GRACE Measurements of Mass Variability in the Earth System. Science 305, 503–505. URL http://dx.doi.org/10.1126/science.1099192.

Todini, E. (1996), The ARNO rainfall-runoff model. Journal of Hydrology 175, 339–382. URL http://dx.doi.org/10.1016/S0022-1694(96)80016-3.

Tóth, J. (1962), A theory of groundwater motion in small drainage basins in Central Alberta, Canada. Journal of Geophysical Research 67, 4375–4388. URL http://dx.doi.org/10.1029/JZ067i011p04375.

Tukey, J. W. (1977), Exploratory Data Analysis. Addison-Wesley, Reading, Massachusetts.

Uppala, S. M., P. W. Kallberg, A. J. Simmons, U. Andrae, V. D. Bechtold, M. Fiorino, J. K. Gibson, J. Haseler, A. Hernandez, G. A. Kelly, X. Li, K. Onogi, S. Saarinen, N. Sokka, R. P. Allan, E. Andersson, K. Arpe, M. A. Balmaseda, A. C. M. Beljaars, L. Van De Berg, J. Bidlot, N. Bormann, S. Caires, F. Chevallier, A. Dethof, M. Dragosavac, M. Fisher, M. Fuentes, S. Hagemann, E. Holm, B. J. Hoskins, L. Isaksen, P. A. E. M. Janssen, R. Jenne, A. P. McNally, J. F. Mahfouf, J. J. Morcrette, N. A. Rayner, R. W. Saunders, P. Simon, A. Sterl, K. E. Trenberth, A. Untch, D. Vasiljevic, P. Viterbo and J. Woollen (2005), The ERA-40 re-analysis URL http://edoc.mpg.de/256471.

van Beek, L. (2008), Forcing PCR-GLOBWB with CRU data. Tech. Rep., Department of Physical Geography, Utrecht University, Utrecht, The Netherlands. URL http://vanbeek.geo.uu.nl/suppinfo/vanbeek2008.pdf.

van Beek, L. and M. Bierkens (2009), The Global Hydrological Model PCR-GLOBWB: Conceptualization, Parameterization and Verification. Tech. Rep., Department of Physical Geography, Utrecht University, Utrecht, The Netherlands. URL http://vanbeek.geo.uu.nl/suppinfo/vanbeekbierkens2009.pdf.

van Beek, L. P. H., Y. Wada and M. F. P. Bierkens (2011), Global monthly water stress: 1. Water balance and water availability. Water Resources Research 47, W07517. URL http://dx.doi.org/10.1029/2010WR009791.

van Geer, F. C. and P. Defize (1987), Detection of natural and artifical causes of groundwater fluctuations. IAHS Publ. 168, 597–606.

von Asmuth, J. R. and M. Knotters (2004), Characterising groundwater dynamics based on a system identification approach. Journal of Hydrology 296, 118–134. URL http://dx.doi.org/10.1016/j.jhydrol.2004.03.015.

von Asmuth, J. R., M. F. P. Bierkens and K. Maas (2002), Transfer function-noise modeling in continuous time using predefined impulse response functions. Water Resources Research 38, 1287. URL http://dx.doi.org/10.1029/2001WR001136.

Wada, Y., L. P. H. van Beek, C. M. van Kempen, J. W. T. M. Reckman, S. Vasak and M. F. P. Bierkens (2010), Global depletion of groundwater resources. Geophysical Research Letters 37, L20402. URL http://dx.doi.org/10.1029/2010GL044571.

Wada, Y., L. P. H. van Beek, D. Viviroli, H. H. Dürr, R. Weingartner and M. F. P. Bierkens (2011), Global monthly water stress: 2. Water demand and severity of water stress. Water Resources Research 47, W07518. URL http://dx.doi.org/10.1029/2010WR009792.

Wada, Y., L. P. H. van Beek, F. C. Sperna Weiland, B. F. Chao, Y.-H. Wu and M. F. P. Bierkens (2012), Past and future contribution of global groundwater depletion to sea-level rise. Geophysical Research Letters 39, L09402. URL http://dx.doi.org/10.1029/2012GL051230.

Wagner, W. (1998), Soil Moisture Retriecval from ERS scatterometer data. Ph.D. thesis, Vienna University of Technology, Austria.

Wagner, W., G. Lemoine, M. Borgeaud and H. Rott (1999a), A study of vegetation cover effects on ERS scatterometer data. Geoscience and Remote Sensing, IEEE Transactions on 37, 938–948.

Wagner, W., G. Lemoine and H. Rott (1999b), A method for estimating soil moisture from ERS Scatterometer and soil data. Remote Sensing of Environment 70, 191–207. URL http://dx.doi.org/10.1016/S0034-4257(99)00036-X.

Wagner, W., K. Scipal, C. Pathe, D. Gerten, W. Lucht and B. Rudolf (2003), Evaluation of the agreement between the first global remotely sensed soil moisture data with model and precipitation data. Journal of Geophysical Research 108, 4611. URL http://dx.doi.org/10.1029/2003JD003663.

Wagner, W., V. Naeimi, K. Scipal, R. de Jeu and J. Martnez-Fernndez (2007), Soil moisture from operational meteorological satellites. Hydrogeology Journal 15, 121–131. URL http://dx.doi.org/10.1007/s10040-006-0104-6.

Wan, Z. and Z.-L. Li (1997), A physics-based algorithm for retrieving land-surface emissivity and temperature from EOS/MODIS data. Geoscience and Remote Sensing, IEEE Transactions on 35, 980–996. URL http://dx.doi.org/10.1109/36.602541.

Wanders, N., D. Karssenberg, M. F. P. Bierkens, R. M. Parinussa, R. A. M. de Jeu, J. van Dam and S. M. de Jong (2012), Observation uncertainty of satellite soil moisture products determined with physically-based modeling. Remote Sensing of Environment 127, 341–356. URL http://dx.doi.org/10.1016/j.rse.2012.09.004.

Welsh, W. (2000), GABFLOW: A Steady State Groundwater Flow Model of the Great Artesian Basin. Land and Water Sciences Division, Bureau of Rural Sciences, Department of Agriculture, Fisheries and Forestry, Australia.

Welsh, W. (2006), Great Artesian Basin transient groundwater model. Bureau of Rural Sciences, Department of Agriculture, Fisheries and Forestry, Australia.

Wesseling, C. G., D. Karssenberg, W. P. A. van Deursen and P. A. Burrough (1996), Integrating dynamic environmental models in GIS: The development of a Dynamic Modelling language. Transactions in GIS 1, 40–48. URL http://dx.doi.org/10.1111/j.1467-9671.1996.tb00032.x.

Widén-Nilsson, E., S. Halldin and C. yu Xu (2007), Global water-balance modelling with WASMOD-M: Parameter estimation and regionalisation. Journal of Hydrology 340, 105–118.

Wolf, J., R. Barthel and J. Braun (2008), Modeling Ground Water Flow in Alluvial Mountainous Catchments on a Watershed Scale. Ground Water 46, 695–705. URL http://dx.doi.org/10.1111/j.1745-6584.2008.00456.x.

Wood, E. F., J. K. Roundy, T. J. Troy, L. P. H. van Beek, M. F. P. Bierkens, E. Blyth, A. de Roo, P. Döll, M. Ek, J. Famiglietti, D. Gochis, N. van de Giesen, P. Houser, P. R. Jaffé, S. Kollet, B. Lehner, D. P. Lettenmaier, C. Peters-Lidard, M. Sivapalan, J. Sheffield, A. Wade and P. Whitehead (2011), Hyperresolution global land surface modeling: Meeting a grand challenge for monitoring Earth's terrestrial water. Water Resources Research 47, W05301. URL http://dx.doi.org/10.1029/2010WR010090.

Zevenbergen, L. and C. Thorne (1987), Quantitative analysis of land surface topography. Earth Surface Processes and Landforms 12, 47–56. URL http://dx.doi.org/10.1002/esp.3290120107.

Zhao, M. and S. W. Running (2010), Drought-Induced Reduction in Global Terrestrial Net Primary Production from 2000 Through 2009. Science 329, 940–943. URL http://dx.doi.org/10.1126/science.1192666.

Summary

In this thesis, the possibilities of using spaceborne remote sensing for large-scale groundwater modeling are explored. We focus on a soil moisture product called the European Remote Sensing Soil Water Index (ERS SWI, Wagner et al., 1999) — representing the upper profile soil moisture. As a test-bed, we used the Rhine-Meuse basin, covering about ± 200 000 km^2 and having more than four thousand in-situ groundwater head observations. The thesis explores the potential of using SWI in an empirical transfer function-noise (TFN) model and in a physically-based model PCR-GLOBWB-MOD.

We first show that there is correlation between observed groundwater head dynamics and SWI dynamics, which is apparent mostly for shallow groundwater areas. For deep groundwater areas, the correlation may become apparent if delay time is considered. Given such correlation, groundwater head prediction based on SWI time series should be feasible. Hence, we performed two exercises in which SWI time series were used as TFN model input. For the first exercise — focusing on temporal forecasting, the TFN model parameters were calibrated based on head measurements in the period 1995-2000. Subsequently, the forecasts were validated in the period 2004-2007. In the second exercise — focusing on spatio-temporal prediction, the TFN model parameters were predicted by using a digital elevation map. Using these estimated parameters, spatio-temporal groundwater head prediction was created. Both exercises show that observed groundwater head dynamics can be well simulated, especially for shallow groundwater where head fluctuations are dominated by meteorological forcing, which is reflected in SWI soil moisture dynamics.

In this thesis, we also introduce a physically-based and coupled groundwater-land surface model PCR-GLOBWB-MOD (1 km resolution), built by using only globally available datasets. We started building it by modifying PCR-GLOBWB land surface model (van Beek et al., 2011) and then performing its daily simulation to estimate groundwater recharge and river discharge. Subsequently, a MODFLOW groundwater model (McDonald and Harbaugh, 1988) was created and forced by the recharge and water levels calculated by the land surface model. Results are promising despite the fact that an offline coupling procedure was still used (i.e. both models were separately and sequentially simulated). The PCR-GLOBWB-MOD model simulation can reproduce the observed discharge and groundwater head reasonably well.

We also introduce the online-coupled version of PCR-GLOBWB-MOD, including two-way feedback between surface water and groundwater dynamics and two-way feedback interaction between groundwater and upper soil stores. The latter enables groundwater to sustain upper soil moisture states and fulfill evaporation demand (during dry conditions). For this online coupled PCR-GLOBWB-MOD model, we explored

the possibility of using the remotely-sensed SWI soil moisture data to calibrate it. We performed more than three thousand runs with various parameter sets and evaluated their results against discharge, SWI and groundwater head measurements. From these runs, we conclude that SWI time series can be used for calibrating upper soil saturated hydraulic conductivities that determine groundwater recharge. However, discharge measurements should be included to calibrate the complete model, specifically to resolve equifinality problems of fitting soil moisture dynamics and to constrain aquifer transmissivities and runoff-infiltration partitioning processes. The combined calibration approach using both SWI and discharge data yielded a model that was able to fit both soil moisture and discharge, as well as predicting the dynamics of groundwater heads with acceptable accuracy.

Although there is room for improvement, the results of this study show that with the combination of globally available datasets and remote sensing products, large-extent groundwater modeling is in reach for data-poor environments (e.g. developing countries) and eventually for the entire globe.

Samenvatting: Toepassing van bodemvocht remote sensing in grootschalige grondwatermodellering

In gebieden waar geen metingen op de grond beschikbaar zijn wordt bij het vaststellen van de hydrologische toestand steeds gebruik gemaakt van remote sensing: data uit satellieten (aardobservatie). Echter in bij het vaststellen van grondwaterstanden, van belang voor landbouw en ecosystemen, wordt van remote sensing nauwelijks gebruikt gemaakt.

In dit proefschrift wordt de mogelijkheid om microgolf remote sensing bodemvochtproducten te gebruiken voor grootschalige grondwatermodellering onderzocht. Het focust op het product van de Europese Remote Sensing satellieten, *Soil Water Index* (SWI, Wagner et al., 1999) dat het bodemvochtprofiel van de onverzadigde zone beschrijft. Als studiegebied is het Rijn-Maas stroomgebied gekozen wat een oppervlak van $\pm$ 200 000 km^2 beslaat en waar een zeer groot aantal stijghoogtemetingen aanwezig zijn. We bestuderen het gebruik van SWI door middel van een empirisch transfer/ruis (TFN) model en een fysisch-gebaseerd hydrologisch model, PCR-GLOBWB-MOD.

Eerst tonen we aan dat er correlatie bestaat tussen SWI-dynamiek en grondwaterstanddynamiek, met name in gebieden met ondiepe grondwater. Voor gebieden met diep grondwater wordt de correlatie pas zichtbaar als rekening gehouden wordt met een vertragingstijd tussen de onverzadigde zone en het grondwater. Gezien deze correlatie, is een voorspelling van grondwaterstanden gebaseerd op SWI mogelijk. Op grond van deze resultaten zijn twee studies uitgevoerd waarin SWI-tijdreeksen als TFN-model input worden gebruikt. De eerste studie richt zich op het voorspellen van de grondwaterstand op een meetlocatie. Hiervoor zijn de parameters gekalibreerd op de metingen van stijghoogten in de periode van 1995-2000. Daarna zijn de voorspellingen gevalideerd op de metingen in de periode van 2004-2007. In de tweede studie, die zich op ruimtelijke-temporele voorspelling van grondwaterstanden richt, worden de parameters van TFN-model geschat met behulp van een digitale hoogtekaart. Door het gebruik van deze geschatte parameterskunnen wij een ruimtelijke-temporele stijghoogten voorspelling doen. Beide studies tonen aan dat de stijghoogtemetingen goed worden gereproduceerd. Dit geldt vooral in het ondiepe grondwater waar grondwaterdynamiek wordt gedomineerd door weersvariaties, gereflecteerd in bodemvochtdynamiek.

In dit proefschrift introduceren we tevens een fysisch-gebaseerd en gekoppeld grondwater-landoppervlak model PCR-GLOBWB-MOD (met een resolutie van 1 km) dat mondiaal beschikbare datasets gebruikt. Het bestaat uit het PCR-GLOBWB landoppervlakmodel (van Beek et al., 2011) en MODFLOW grondwatermodel (McDonald en Harbaugh, 1988). Eerst wordt de dagelijkse simulatie van het landoppervlakmodel aangepast om grondwateraanvullling en rivierafvoer te berekenen. Vervolgens hebben

wij grondwateraanvullling en oppervlaktewaterstanden uit het landoppervlaktemodel geconfigureerd als input voor het grondwatermodel. De simulatieresultaten zijn veelbelovend, ondanks het feit dat we nog steeds een offline koppelingsmethode tussen beide modellen gebruiken (d.w.z. dat beide modellen opeenvolgend zijn uitgevoerd). Hieruit blijkt dat het PCR-GLOBWB-MOD model redelijk goed de metingen van de rivierafvoeren en grondwaterstanden kan reproduceren.

Binnen deze studie is ook een online-gekoppelde versie van PCR-GLOBWB-MOD ontwikkeld met een koppeling in twee richtingen tussen de oppervlaktewater- en stijghoogte-dynamiek en tussen het grondwater en bovenste bodemlagen. Hier levert het grondwater door middel van capillaire naleveringaanvulling voor het bodemvocht in situaties met hoge verdamping (bijvoorbeeld in de zomer). Met deze online-gekoppelde versie van PCR-GLOBWB-MOD onderzoeken we de mogelijkheid om het SWI-bodemvocht te gebruiken voor het kalibreren van PCR-GLOBWB-MOD. We simuleren meer dan drieduizend scenarios met verschillende parametersets en de resultaten zijn gevalueerd aan de hand van rivierdebiet-, SWI- en stijghoogteobservaties. Hieruit wordt geconcludeerd dat SWI geschikt is voor het ijken van de toplaag-doorlatendheid. Het is echter niet mogelijk om het volledige model te kalibreren met slechts SWI-data. Rivierafvoermetingen zijn noodzakelijk om de equifinaliteit van de bodemvocht-dynamiek op te lossen en om het doorlaatvermogen van de aquifer en de overvlakteafvoer-infiltratie partitioneringsprocessen te beperken.

Hoewel er ruimte voor verbetering is, toont deze studie aan dat door gebruik te maken van mondiaal datasets en remote sensing-producten, grootschalige grondwatermodellering — ook in data-arme ontwikkelingslanden — binnen handbereik ligt.

Ringkasan: Penggunaan data kelembaban tanah berdasarkan teknologi penginderaan jauh untuk pemodelan aliran air tanah skala makro

Untuk daerah-daerah yang jarang atau tidak tersedia data pengukuran lapangan (seperti di banyak negara berkembang), analisa dan evaluasi kondisi hidrologi dapat memanfaatkan teknologi penginderaan jauh, termasuk data-data dari satelit. Namun, studi mengenai kondisi aliran air tanah, yang sangat penting untuk ekosistem alam dan sektor pertanian, masih sangat jarang memanfaatkan teknologi penginderaan jauh.

Disertasi ini mengkaji potensi pemanfaatan teknologi penginderaan jauh untuk pemodelan dan evaluasi aliran air tanah. Dalam thesis ini, kami menggunakan data *Soil Water Index* (SWI) dari Universitas Teknologi Wina, Austria, yang berasal dari pengamatan satelit *European Remote Sensing*. Data SWI yang disajikan dalam deret waktu ini berupa nilai-nilai fluktuasi kelembaban tanah atau kadar air dalam tanah pada lapisan tanah atas (sampai dengan sekitar satu meter di bawah permukaan tanah). Untuk penelitian ini, kami menggunakan daerah aliran sungai Rhine dan sungai Meuse (total luas area: $\pm$ 200 000 km^2) di Eropa Barat.

Pada bagian pertama dari disertasi ini, kami menggunakan metode statistik untuk memprediksi tinggi muka air tanah berdasarkan data fluktuasi SWI. Metode ini bekerja dengan baik terutama di lokasi-lokasi yang memiliki permukaan air tanah dangkal dan didominasi oleh variasi cuaca. Prediksi tinggi muka air tanah pada daerah tersebut cukup akurat karena terdapat hubungan (korelasi) antara fluktuasi muka air tanah berdasarkan data pengukuran lapangan dan fluktuasi kelembaban tanah berdasarkan data SWI.

Bagian kedua dari penelitian ini mengkaji mengenai kemungkinan penggunaan data SWI untuk mengkalibrasi model hidrologi aliran air tanah. Di dalam proses pembuatan model ini, kami hanya menggunakan data-data yang tersedia di seluruh dunia (contoh: peta tutupan lahan dunia, peta tanah dunia, peta lithologi dunia dan lain sebagainya) sehingga metoda pembuatan model ini dapat diterapkan di mana saja. Hasil dari model ini ternyata sangat menjanjikan. Model ini mampu memberikan hasil simulasi debit sungai dan tinggi muka air tanah yang sesuai dengan data pengukuran lapangan. Dan meskipun data SWI tidak dapat digunakan untuk mengkalibrasi parameter lapisan air tanah (akuifer), data SWI bisa dimanfaatkan dalam proses kalibrasi konduktivitas hidraulik lapisan tanah atas yang menentukan jumlah resapan air tanah.

Berdasarkan hasil penelitian ini, kami berharap pemodelan dan evaluasi kondisi aliran air tanah skala makro bisa dilakukan di mana saja (termasuk di negara-negara berkembang) dengan mengkombinasikan data-data yang tersedia di seluruh dunia dan data-data yang berasal dari satelit.

Acknowledgements

This study is funded by the Netherlands Organization for Scientific Research NWO (contract: SRON GO-AO/10). We acknowledge the Microwave Remote Sensing Group of Institute of Photogrammetry and Remote Sensing, Vienna University of Technology, Austria (IPF TU Wien, http://www.ipf.tuwien.ac.at/radar) for providing the ERS SWI data. We are also indebted to many institutions that provided groundwater head data, such as the central portal to Data and Information of the sub-surface of the Netherlands (DINOLoket, http://www.dinoloket.nl); the Flanders sub-soil database, Belgium (DOV, http://dov.vlaanderen.be); the Wallonia Operational Directorate-General for Agriculture, Natural Resources and the Environment, Belgium (DGARNE, http://environnement.wallonie.be); the BRGM French Geological Survey (the French Groundwater National Portal, http://www.ades.eaufrance.fr); the Baden-Württemberg State Environment Agency, Germany (LUBW, http://www.lubw.baden-wuerttemberg.de); the Rhineland-Palatinate State Environment Agency, Germany (LUWG Rheinland Pfalz, http://www.luwg.rlp.de); the North Rhine Westphalia State Environment Agency, Germany (LANUV NRW, http://www.lanuv.nrw.de); the Bavarian Environment Agency, Germany (Bayerisches LfU, http://www.lfu.bayern.de); the National Groundwater Monitoring NAQUA of the Swiss Federal Office for the Environment FOEN (http://www.bafu.admin.ch); and the AWEL Office for Waste, Water, Energy and Air of the Canton Zurich, Switzerland (http://www.awel.zh.ch); and some individuals, such as Harrie-Jan Hendricks-Franssen and Sebastian Stoll. For the discharge data, we acknowledge the Global Runoff Data Centre (GRDC, Koblenz, Germany, http://grdc.bafg.de) and the Waterbase portal (http://waterbase.nl) of Rijkwaterstaat (the Dutch Directorate General for Public Works and Water Management). We also received support from the Dutch Research Institute Deltares, Utrecht, and the Geological Survey of the Netherlands TNO, Utrecht, that allowed us to use their GRID parallel computing system. We also thank SARA Computing and Networking Services (www.sara.nl) for their support in using the Lisa Compute Cluster.

Dankwoord

A Ph.D. degree is clearly a great achievement in my life (assuming everything goes well on the D-day). For this huge step, I would like to express my acknowledgements to many people. Yet, I found that it was very difficult to write this section. Honestly, I even considered to skip writing this part. I was afraid that I would have missed many names that have been very important for me (not only during this Ph.D. life, but also before I even started it). At the end, I decided to write few paragraphs (as follows), but without mentioning any names.

Special thanks to all members of the evaluation committee. It is a huge honor to have all of you assessing my thesis.

I would like to acknowledge my biggests debts to all promotors who have trusted me to do this research and give freedom to pursue my own ideas. They have become my mentors who are always very kind and patient. Their enthusiasm always inpires me. I am thankful for their motivation and support, especially during every frustation and difficult time (e.g. computer burglary).

I also owe to all PCR-GLOWB-MOD and PCRaster team. Their brilliant ideas and efforts in initiating and developing the model and software made my Ph.D. life much easier. I thank them for their patience and support throughout the project.

Special thanks to all staff members and colleagues at the Department of Physical Geography, Utrecht University. I also owe to many people in TNO and Deltares Utrecht. I thank all my room-mates (at the university and TNO/Deltares) that "dare" to share the room with me. I thank the GEO-ICT team and GIS room team of Faculty of Geosiences, Utrecht University: They did not only provide me with technical supports, but also baptized me as a "computer nerd" by initiating our own computer cluster.

I would also like to express my gratitude to all my friends: not only the ones living in The Netherlands, but also anywhere in the world. It is clearly impossible to list all of your names. And it is even much more impossible to list all wonderful things that you have done to me and all inspirations that you have shared with me. I feel very blessed to be your friend.

To all my family members: thanks for your loves. And I hope that I am a good son, brother, uncle, nephew, cousin and grandson (etc) for all of you. Finally, I praise my LORD, JESUS CHRIST. Ad maiorem de Gloriam.

Cornelius Edwin Husni Sutanudjaja, Utrecht, October 2012

About the author

Edwin Sutanudjaja is the son of Handrianto Sutanudjaja and Lindawaty. He has one older sister, Elisa, one little brother, Paulus, and one little sister, Paula. Edwin was born on 16 June 1981 in Cirebon (West Java, Indonesia), where he spent his childhood time and attended his primary school 'Santa Maria'.

When Edwin was fifteen, his father sent him to Jakarta, where he attended his high school 'Kolese Kanisius'. In 1999, he then moved to the city of Bandung and started his bachelor study at the Department of Civil Engineering, Bandung Institute of Technology (ITB). In 2004, he obtained his bachelor degree specialized in the field of water resources engineering. Following his bachelor study, he worked for a civil engineering consultant in Bandung for about a year. Edwin then went to Meulaboh (Aceh) in September 2005 to join an international NGO involved in tsunami relief work, mainly for building houses, water and sanitation facilities.

In September 2006, he moved to The Netherlands to start his master study at the Department of Water Management, Delft University of Technology (TU Delft). During this master study, Edwin received the Huygens Scholarship. He did his internship and thesis researches (between August 2007 and August 2008) at the Dutch Research Institute Deltares (before 2008: Netherlands Organization for Applied Scientific Research TNO) in Utrecht. In August 2008, Edwin obtained his master degree (with distinction) specialized in in the field of geo-hydrology.

Following his master study, Edwin joined the Department of Physical Geography, Utrecht University to work on a Ph.D. research focusing on large-scale groundwater modeling and remote sensing. During this research, he had a fascinating time: not only in programming his modeling scripts and writing papers (and eventually this thesis), but also traveling abroad to present his research results. He was awarded a travel grant to attend the 2012 AGU Chapman Conference on Remote Sensing of the Terrestrial Water Cycle in Kona, Hawaii, USA.

Edwin now still works at the Department of Physical Geography, Utrecht University. Since September 2012, he has started a post-doctoral research on the development of a high-resolution global hydrological model.

List of publications

First-authored papers

Sutanudjaja, E. H., van Beek, L. P. H., de Jong, S. M., van Geer, F. C., Bierkens, M. F. P. (2011), Large-scale groundwater modeling using global datasets: a test case for the Rhine-Meuse basin, Hydrology and Earth System Sciences, 15, 2913-2935, doi:10.5194/hess-15-2913-2011.

Sutanudjaja, E. H., van Beek, L. P. H., de Jong, S. M., van Geer, F. C., Bierkens, M. F. P. (2012), Calibrating a large-scale groundwater model using spaceborne remote sensing products: a test-case for the Rhine-Meuse basin. IAHS (International Association of Hydrological Sciences) Publ. 355.

Sutanudjaja, E. H., de Jong, S. M., van Geer, F. C., Bierkens, M. F. P., Using ERS spaceborne microwave soil moisture observations to predict groundwater heads in space and time, submitted to Remote Sensing of Environment.

Sutanudjaja, E. H., van Beek, L. P. H., de Jong, S. M., van Geer, F. C., Bierkens, M. F. P., Calibrating a large-scale groundwater model using soil moisture and discharge measurements, in preparation for Water Resources Research.

Selected conference abstracts

Sutanudjaja, E. H., van Beek, L. P. H., de Jong, S. M., van Geer, F. C., Bierkens, M. F. P. (2010), Large scale groundwater modeling using globally available datasets: a test for the Rhine-Meuse basin. Poster presentation presented at 2010 General Assembly, EGU (European Geosciences Union), Vienna, Austria, 2-7 May.

Sutanudjaja, E. H., de Jong, S. M., van Geer, F. C., Bierkens, M. F. P. (2010), Correlating microwave remote sensing with groundwater head measurement time series. Poster presentation presented at 2010 Fall Meeting, AGU (American Geophysical Union), San Francisco, California, USA, 13-17 December.

Sutanudjaja, E. H., van Beek, L. P. H., de Jong, S. M., van Geer, F. C., Bierkens, M. F. P. (2011), Calibrating a large-scale groundwater model using spaceborne remote sensing products: a test-case for the Rhine-Meuse basin. Oral presentation presented at ModelCARE2011 conference, Leipzig, Germany, 18-22 September.

Sutanudjaja, E. H., van Beek, L. P. H., de Jong, S. M., van Geer, F. C., Bierkens, M. F. P. (2012), Using space-borne remote sensing products to calibrate a large-scale groundwater model: a test case for the Rhine-Meuse basin. Poster presentation presented at 2012 AGU Chapman Conference on Remote Sensing of the Terrestrial Water Cycle, Kona, Hawaii, USA, 19-22 February.

Sutanudjaja, E. H., de Jong, S. M., van Geer, F. C., Bierkens, M. F. P. (2012), Can we monitor groundwater head variation from space? Coupling ERS spaceborne microwave observations to groundwater dynamics. Oral presentation presented at 2012 General Assembly, EGU, Vienna, Austria, 22-27 April.

Sutanudjaja, E. H., de Jong, S. M., van Geer, F. C., Bierkens, M. F. P. (2012), Using ERS spaceborne microwave based soil moisture products to predict groundwater heads in space and time. Oral presentation presented at Prediction in Ungauged Basin (PUB) Symposium 2012, IAHS, Delft, The Netherlands, 23-25 October.

Sutanudjaja, E. H., van Beek, L. P. H., de Jong, S. M., van Geer, F. C., Bierkens, M. F. P. (2012), Building and calibrating a large-extent and high resolution coupled groundwater-land surface model using globally available datasets. Oral presentation presented at 2012 Fall Meeting, AGU, San Francisco, California, USA, 3-7 December.